Controlling Plasma Reactivity Transfer to Gases, Solids and Liquids

by

Juliusz A. Kruszelnicki

A dissertation submitted in partial fulfillment
of the requirements for the degree of
Doctor of Philosophy
(Nuclear Engineering and Radiological Sciences)
in the University of Michigan
2021

Doctoral Committee:

Professor Mark J. Kushner, Chair
Professor Herek L. Clack
Professor John E. Foster
Professor Bryan R. Goldsmith
Professor Ryan D. McBride

Juliusz Kruszelnicki

jkrusze@umich.edu

ORCID iD: 0000-0003-4596-1780

DEDICATION

For Justyna, Kamila and Eliza

ACKNOWLEDGMENTS

Throughout my time at the University of Michigan, I was lucky to meet numerous extraordinary people. Without their input, my work would not have been possible.

Firstly, I would like to thank my advisor – Professor Mark J. Kushner. He guided me throughout my pursuit of a PhD – sharing his tremendous insight into not only physics, chemistry, and computational science, but also into life as a scientist and beyond. I would also like to thank my committee members – Professors John E. Foster, Ryan D. McBride, Herek L. Clack and Bryan R. Goldsmith. The numerous discussions with them enlightened many aspects of plasma physics and catalysis or me.

Secondly, I would like to thank my many colleagues and lab mates: Peng Tian, Wei Tian, Chad Huard, Michael Logue, Soheila Mohades, Guy Parsey, Aram Markosyan, Chenhui Qu, Steven Lanham, Amanda Lietz, Shuo Huang, Xifeng Wang, Jordyn Polito, Mackenzie Meyer, Kseniia Konina, and Florian Krueger, Astrid Raisanen and Tugba Piskin. Many of my best ideas were a direct result of conversations with them. In addition, I would like to thank Julia Falkovitch-Khan, whose tireless work has helped my coworkers and myself out of many crises. Furthermore, I would like to thank my collaborators – Dr. Kenneth Engeling, Dr. Savio Poovathingal, Runchu Ma, and Prof. Wenjung Ning. A special thanks also belongs to Dr. Janis Lai, whose continuous support, advice, and friendship were invaluable assets throughout the pursuit of my degree.

Thirdly, I want to extend my thanks to the US Department of Energy – Office of Fusion Energy Science, the US National Science Foundation, Michigan Institute of Plasma Science and Engineering, and the Plasma Science Center for making my work possible via financial support.

Lastly, I would like to thank my sisters – Justyna, Kamila and Eliza – whose continuous support and encouragement enabled me to complete this work. They stood by me during difficult moments and helped me celebrate the happy ones. Nothing would have been possible without their love.

Table of Contents

List of Figures

List Of Tables

ABSTRACT

Plasma discharges at atmospheric pressure enable efficient conversion of the kinetic energy of electrons to chemical reactivity. In the process of breaking of bonds of molecular gases, plasmas produce high densities of reactive species. These species can then be utilized to treat flue gases and waste water. However, currently deployed systems suffer from poor energy efficiencies and throughputs, largely due to the lack of understanding of the underlying physics and chemistries. In this work, computational modeling was performed to investigate the transfer of reactivity (relative capacity to undergo or produce a chemical reaction) from plasmas to gases (via Packed Bed Reactors (PBRs)), solids (metallic catalysts, porous media) and liquid (micron-scale aerosols). The work was performed using the plasma hydrodynamics model – *nonPDPSIM*. Necessary changes and additions to the code included addition of source terms to the surface heating module, implementation of an updated mesh generator, and parallelization of radiation transport routines.

The evolution and properties of plasmas in PBRs were characterized. Three plasma modalities were shown to exist, each leading to different rates of production of reactive species. Chemical selectivity could be achieved by choosing the packing fraction and materials that lead to preferential formation of one of the modalities over others – for example, formation of Surface Ionization Waves in air preferentially increases dissociation of nitrogen over oxygen. When metallic catalysts were added to the PBR, the discharge modalities changed, causing increased fluxes of charged species to the surfaces of the catalysts. This was, in part, due to realignment of charges within the metallic

particles, which induced high local electric fields, and electric field emission of electrons. The high fluxes could lead to heating and self-cleaning of the catalysts, which would explain some of the plasma-catalytic synergies observed in experimental literature. Lastly, the interactions of liquid aerosols with Dielectric Barrier Discharges were investigated. The diameter of the droplets was shown to address diffusion transport limits of both ions and neutrals by maximizing the surface-to-volume ratio. Large surface areas enable rapid solvation from the gas-phase while small volume led to fast saturation of liquid-phase reactive species. Different species were shown to have different saturation time-scales, depending on the droplet size, pointing to an additional control mechanism of liquid-chemistry and selectivity. For example, for a 10 μm droplet, ozone (Henry's law constant, $h_0 \approx 0.3$) saturates within one tenth of a millisecond. On the other hand, hydrogen peroxide ($h_0 \approx 1.9\times10^6$) requires up to 10 seconds to saturate a droplet of the same size.

Chapter 1 Introduction

Plasma is a form of matter comprised of electrons, ions, and neutral (ground and excited) species. Depending on system parameters, plasmas can be classified into low- and high-temperature regimes. In the low temperature regime, plasmas are commonly employed within the microprocessor manufacturing industry, material processing, pollution mitigation and high voltage control [1–4]. Furthermore, exciting new technologies utilizing low temperature plasmas (LTPs) are currently being developed to include plasma-based gas pollutant mitigation, plasma catalysis, and plasma medicine [5,6]. However, further understanding of plasma behaviors and interactions within these systems is required to advance development of practical systems. For this purpose, computational modeling of plasma-chemical systems was employed and is the central focus of this thesis.

General introduction to plasmas and low temperature regime are provided in Section 1.1, followed by more specific descriptions of particular applications, including – including Packed Bed Reactors (Section 1.2), Plasma/Liquid reactors (Section 1.3), and Plasma/Catalysts (Section 1.4). Further motivation for this work is then provided in Section 1.5. Lastly, the remaining chapters of this thesis are introduced and described in Section 1.6.

1.1 Basics of Plasma Physics

Majority of matter in the universe is believed to exist in the plasma state [7]. The constituents of a plasma can include negatively charged species (electrons and anions), positively

charged species (cations) and neutrals. As a result, plasmas respond – and can be influenced by – to electromagnetic fields, exhibiting collective behavior. Plasmas can be further classified based on their densities, temperatures and ionization fractions (amongst other parameters), each leading to differing simplifying assumptions. In Fig. 1.1, it can be seen that plasmas span over 30 orders of magnitude in density and 6 orders of magnitude in temperature. Fully ionized plasmas include fusion reactors, and star/solar plasmas [8–12]. Very low temperature plasmas include auroras and some flames [13,14]. Lastly, the regimes which are the focus of this work are the Low Temperature Plasmas which exist on earth in the form of lightning, neon signs and laboratory-based reactors, and in particular, at atmospheric pressures [2,15–18]. These plasmas have the following characteristic parameters:

- Ionization fraction between 5×10^{-10} - 5×10^{-5}.
- Electron temperatures between 1 eV and 20 eV.
- Ion and gas temperatures between 300 K and few 1000s K.

Typically, three criteria must be met for matter to be considered a plasma:

I. The Debye Length (λ_D) must be much smaller than the characteristic length (or size) or the plasma discharge. The Debye Length is the distance over which plasma can display non-uniformity (or the shielding distance) and is one of the primary plasma parameters. Within the area of low temperature plasmas, it is defined as:

$$\lambda_D = \sqrt{\left(\frac{\varepsilon_0 k_B T_e}{e^2 n_0}\right)} \tag{1.1}$$

Where ε_0 is the permittivity of free space, k_B is Boltzmann's constant, T_e is the electron temperature, e is the electron charge, and n_e is the electron density. Within Atmospheric Pressure Low Temperature Plasmas

(APLTPs), the Debye Length are typically between a micron and a millimeter.

II. The number of charged particles within the Debye sphere must be much greater than 1. The number of particles in the Debye sphere is number within a spherical volume with a radius of a Debye Length:

$$N_D = n\frac{4}{3}\pi\,\lambda_D^3 \tag{1.2}$$

where *n* is the number density of charged species.

III. Lastly, as charged species move due to their kinetic energy, they separate from one another. This produces an attractive electric field between positive and negative charges, forcing them to turn direction. This process produces a characteristic plasma oscillation. In LTP systems, this oscillation has a frequency given by Eq. 1.3:

$$\omega_{pe} = \sqrt{\frac{e^2 n_0}{\varepsilon_0 m_e}} \tag{1.3}$$

where n_0 is the plasma density, *e* is the electron charge, m_e is the electron mass, and ε_0 is the permittivity of free space. Simultaneously, as particles oscillate, they may undergo a collision with other particles within the system. The time between these collisions is

$$\tau_{col} = 1/nv\sigma \tag{1.4}$$

Where σ is the collision cross-section and *v* is the velocity. For a plasma to display collective behavior, a particle must be able to complete many oscillations between collisions. The third parameter is therefore: the time between collisions (τ_{col}) must

be greater than the time required for an electron to oscillate $\left(\frac{1}{\omega_{pe}}\right)$. Within APLTP, these timescales are between picoseconds and nanoseconds.

Plasmas studied herein are nonthermal – meaning that the electrons and ions are not in a thermal equilibrium with the background gases. As a result, the concepts of electron temperature and electron energy distribution function (EEDF) is of high importance. Simply put, temperature is the average kinetic energy of the particles. Whereas in thermal plasmas, the energies of its constituents may be assumed to follow a Maxwellian distribution, this is not the case in APLTPs [19]. This change in distribution is caused by preferential sinks due to specific kinetic reactions between electrons and background gas. Due to the large disparity in masses between electrons and atoms/molecules (approximately 3 orders of magnitude), only limited fraction of electron energy can be transferred via elastic reactions, and electrons must be treated in a unique fashion. On the other hand, electron-impact ionization (≈10-20 eV), molecular dissociation (≈5-15 eV) and vibrational and electronic excitation (few eV) can preferentially deplete the tail of the electron energy distribution. As a result, the EEDF within LTPs has to be calculated while taking into account the background gas kinetics, densities, pressures and temperatures.

There are many approaches to calculating the EEDF in the LTP regime. These include Monte-Carlo (MC), Particle-in-Cell (PIC) and Fluid approaches [20–24]. The latter is utilized within this work. The EEDF is found by solving Boltzmann's Equation (Eq. 1.5):

$$\frac{\partial f}{\partial t} + \vec{v} \cdot \nabla_{\vec{r}} f + \frac{\vec{F}}{m} \cdot \nabla_{\vec{v}} f = \left(\frac{\partial f}{\partial t}\right)_{coll} \tag{1.5}$$

where f is the electron velocity distribution function as a function of time and space, m is the electron mass, $\vec{v}$ is the velocity, $\nabla_{\vec{r}}$ and $\nabla_{\vec{v}}$ are the gradients in space velocity, respectively and $\vec{F}$

is the force on the particle due to applied electric field and Coulombic interactions between particles. This equation is solved based on background gases in the system, producing a set of electron transport coefficients based on the reduced electric field (electric field divided by the number density of charged species). Finally, these coefficients are used in conjunction with known reaction coefficients to find the electron temperature. A typical EEDF for an APLTP is shown in Fig. 1.2.

The transfer of energy from plasma to other states of matter can be termed as the transfer of "reactivity". Here, reactivity is the ability to undergo chemical reactions. Plasma can "transfer" its "reactivity" by kinetic methods. Electric potential first imparts kinetic energy to electrons, which then collide with background gases. Total energy is conserved, and the resultant reactive species can undergo chemical reactions with other molecules. Reactivity is therefore used henceforth to mean "the ability to enable chemical reactions". Such a transfer can be done to all three of the other forms of matter: gases, solids and liquids. This unique ability makes atmospheric pressure plasma a crucial component to the rapidly-evolving worlds of pollutant control, medicine, energy storage and agriculture. In the following sub-sections, lower-level details regarding interactions with each state of above-mentioned states of matter will be discussed.

1.2 Reactivity Transfer to Gases: Packed Bed Reactors

Plasma discharges at atmospheric pressures allow efficient transfer of electrons' kinetic energy to chemical potential. In the process of breaking of bonds of molecular gases, plasmas produce high densities of reactive species. These species can then be utilized to treat flue gases and waste water [25–27]. However, currently deployed systems suffer from poor energy

efficiencies and throughputs, largely due to the lack of understanding of the underlying physics and chemistries.

Plasma Packed Bed Reactors (PPBRs) typically consist of two electrodes being separated by dielectric media in the form of small spheres [16]. Depending on the orientation of the applied electric field and spatial distribution of the beads, the dielectric media can become polarized, resulting in a local enhancement in the electric field. An example of this phenomenon can be seen in Fig. 1.3. Dielectric polarization driven electric field enhancement then results in formation of plasmas at lower applied voltages than would otherwise be required for breakdown [28,29].

A gas flowed through the PBR is then exposed to the plasma, allowing it to be modified (ex. removal of Volatile Organic Compounds, CO_2 reprocessing, and production of value-added compounds such as ammonia) [30–32]. In particular, PPBRs are advantageous because they can be operated at atmospheric pressures and temperatures, requiring lower initial investment costs and simplified system design [33]. Typically, PPBRs operate in the pulse repetition frequencies between 100s of Hz and 10s of kHz. Both DC and AC power supplies have been utilized.

Nominally, the operation of PPBRs is theoretically simple. It involves formation of microdischarges similar to those observed in other Dielectric Barrier Reactors and generally follow a modified Paschen Law [34]. Paschen Law is the relation between the breakdown voltage in a given gas as a function of pressure and distance between two electrodes, as given in Eq. 1.6.

$$V_B = \frac{Bpd}{\ln(Apd) - \ln\left(ln\left(1+\frac{1}{\gamma_{se}}\right)\right)} \tag{1.6}$$

Where V_B is the breakdown voltage, B and A are gas-specific constants determined experimentally, p is pressure, d is the gap distance between electrodes, and γ_{se} is the electrodes' secondary electron emission coefficient. Example Paschen curves are shown in Fig. 1.4.

These reactors have shown the ability to produce a wide variety of chemical species. However, due to the complex topology existing between the packing materials, their material properties (dielectric constant, surface emission coefficients, surface roughness, surface reaction rates), complex kinetics taking place and thermal/fluid dynamics within the reactor, they are still too poorly understood to be competitive in most commercial applications [3].

There exists a critical need for modeling efforts of Plasma Packed Bed Reactors due to the difficulties of detailed observation of plasma formation in experimental set-ups [35]. Modeling allows for the investigation of principal plasma properties (such as field strength, electron temperature, electron density, and reaction rates) within reactor regions with no optical access. Modeling studies done to date include work by Kang et al. who developed 1.5 and 2-dimensional (2-d) models of PBR-like DBDs and found that discharges evolve in three phases: avalanche, streamer and decay [23]. They also found that streamer discharges tend to be stabilized by the presence of dielectric materials. Zhang et al. computationally investigated DBD-PBR discharges in air at atmospheric pressure using a 2-d particle-in-cell/Monte Carlo technique [36]. They predicted the formation of positive streamers following surface charging of the dielectric surface as well as the occurrence of limited surface discharges.

Van Laer et al. modeled a pulsed atmospheric-pressure plasma discharge sustained in helium in a PBR using a 2-d multi-fluid simulation [28,29]. They found that the greatest electric field enhancement occurred near bead contact points which then resulted in the formation of discharges near the surfaces of the beads. When no contact points were included in the model, the largest electron densities occurred at the vertical axis of beads perpendicularly aligned with respect to the applied electric field. The group also collaborated with experimentalist T. Butterworth who earlier investigated the effects of dielectric constant on plasma discharges. [37,38] Through both

modeling and experimentation they showed the importance of capacitance of the packing media with regards to the discharges formation. They identified four types of plasmas – Polar Townsend, Polar Streamer, Unstable Streamer and Stable Streamer. These can occur with any medium, but as the permittivity increases, the applied voltage required to reach subsequent stages also increases. This can be seen in Figs. 1.5 a) and b).

The reactivity transfer to gases is crucial, particularly at the long-term time scales (beyond single pulse time-scales of nano- to micro-seconds). However, computational limitations do not allow for the simulation of large-scale reactors typically observed in the industrial or experimental set-ups. For this reason, a periodic boundary condition was developed in *nonPDPSIM*. This module relies on Navier-Stokes equations within *nonPDPSIM* to solve the fluid flow within a reactor. Once a gas exits the computational domain via a "pump" (a designated set of surface nodes), the species exiting are recorded and re-injected via a different set of surface nodes, known as the "nozzle". The treated gas can therefore circulate through the small computational domain, allowing for the tracking of the evolution of gas chemistry. This option allowed for the modeling of kinetics evolution in a plasma PBR tens of centimeters in length, therefore giving a clearer picture regarding important PPBR parameters.

1.3 Reactivity Transfer to Solids: Plasma Catalysis

Plasma packed bed reactors can be thought of as a sub-genre of plasma catalysis. Catalysis is the process of using a material, substance or additional chemical compound to enable favorable reaction pathways by decreasing the activation energy. Industrial catalysis is a highly mature field, however, it is continuously improved upon, and Plasma Catalysis is a relatively new means of achieving it. While the dielectric materials described in the previous section could be thought of

as a catalysts, generally, Plasma Catalysis focuses on the addition of metallic particles to further increase rates of surface reactions [39–41]. In that context, the dielectric acts as a support material for the metallic catalysts. Fig. 1.6 a) shows a schematic of a catalyst supported on Zeolite while plasma formed in a catalytic PBR is presented in Fig. 1.6 b).

Plasmas interact with metallic catalysts in a synergistic manner [42]. There are a multitude of possible explanations for the presence of this synergy. High energy electrons ($\approx$5-10 eV) are present within plasma microdischarges and surface ionization waves. These electrons then interact with background gases, leading to formation of vibrationally and electronically excited species [43]. These species, then, do not require as high catalyst surface temperatures to achieve high surface reaction rates because the added energy allows for overcoming of the reaction activation energy [31]. Furthermore, polarization of the metallic particles can lead to the formation of increased (local) electric fields near the catalysts. As a result, higher energy electrons and ions form and impact the catalysts. These charged species can then sputter off other molecules present on the surfaces, freeing surface sites and allowing for additional surface reactions – a process called "self-cleaning" [44]. Presence of localized, higher density plasmas in the proximity of the catalysts can also preferentially increase fluxes of reactive species to the surface sites, leading to higher reaction rates [25]. Lastly, the presence of these increased fluxes can also lead to localized heating of the catalysts.

The presence of high energy electrons in the microdischarges and surface ionization waves that occur in PBRs initiates reaction pathways producing high radical and ion densities. Similarly, presence of metallic catalysts can increase chemical reaction rates at lower temperatures and improve selectivity and efficiency. Combining plasmas with catalysts in PBRs has demonstrated these increases in energy efficiency and selectivity [32,42,45].

Plasma interactions with catalysts and their underlying support structures need better metrics to be able to evaluate the goodness of plasma catalysis systems and to make comparisons between systems [26,46,47]. As mentioned earlier, recent experimental results indicate that coupling between plasma kinetic processes and thermo-catalytic reactions leads to synergetic increases in reaction rates [41,48–52]. For example, Kim et al has shown a substantial increase in the production of ammonia from methane over Ru-Mg/γ-Al2O3 catalyst when plasma is present [53]. This increase was greater than the sum of ammonia production when separately using plasma or thermal catalysts. Kim and colleagues also found that additional plasma formed in a DBD having dielectrics with imbedded metallic particles compared to a reactor not having metallic particles [54]. Mehta et al. investigated plasma/catalyst synergy in ammonia synthesis using microkinetics global modeling [26,31]. They postulated that the fluxes of vibrational excited nitrogen produced by the plasma could lead to a decrease in the nitrogen dissociation barrier on the surface of the catalyst and increased rates of ammonia production.

Other modeling investigations have primarily focused on interactions between dielectrics and plasmas. In particular, Bogaerts et al have modeled several systems addressing plasma interactions in PBRs and with pores [35,55,56]. In particular, their work showed that plasmas can develop within micron-scale pores and indicated that even in these small structures, transport is predominantly electric field driven drift as opposed to diffusion dominated. Due to polarization of the pore materials and subsequent electric field enhancement, large electron densities were produced in the pores. Variation in pore sizes also was impactful on ionization rates and potential distribution, as can be seen in Fig. 1.6. While higher plasma densities near surfaces were observed, surface ionization waves were not observed suggesting that the higher plasma densities were due

to secondary electron emission. Photoionization was not found to be impactful, especially when the pore topology obstructs electron movement.

The interactions between plasma and metallic catalysts present modeling challenges due to their simultaneous and mutual impacts. The plasma produces high energy electrons, ions, excited and radical species, and UV/VUV photons [57]. The fluxes of these species can introduce additional surface kinetics (e.g., adsorption of intermediates, UV/VUV activation), change surface morphology (e.g., sputtering, melting, self-cleaning) and increase local catalyst temperature. The electrical triple point is the intersection of a dielectric, metal and gas. Electric field enhancement occurs at triple points due to the geometry and discontinuity in permittivity, and as a response to charge-redistribution upon application of an electric field. If of sufficient magnitude, the electric field enhancement at the triple points of metallic catalyst sites can produce electric field emission of electrons, a process that is accelerated by heating of the catalyst. Electric field emission is particularly sensitive to the geometry of the metallic particles, polarization of the underlying dielectric and local plasma conditions, all of which can intensify the electric field at the surface of the catalyst. These phenomena have been studied in other areas, primarily high-voltage electrical systems [58–60]. The electric field emission in turn affects the local plasma conditions and can impact the rates of surface reactions [61]. To resolve these interactions, plasma dynamics and surface interactions must be simultaneously modeled in a self-consistent fashion.

As part of this effort, modifications and additions were made to *nonPDPSIM* – in particular to surface heating module to show the impact of plasma fluxes on local catalyst temperatures. This was done by integrating the kinetic and ionization energy deposition due to fluxes of electrons and ions, change in enthalpy due to surface reactions, and heating due to UV fluxes incident on the surfaces, as shown in Eqs. 1.7-1.11.

$$J\left(\frac{W}{cm^2}\right) = S_{ion} + S_e + S_{neut} + S_{UV} \tag{1.7}$$

$$S_{ion} = \Gamma_{ion}\left(\phi_{drop} + \Sigma(H_{ion} - H_i)\right) \tag{1.8}$$

$$S_e = \Gamma_e T_e - (4\ eV)(\Sigma\Gamma_{\mathrm{ion,i}}\gamma_i + \Gamma_{\mathrm{FE}}) \tag{1.9}$$

$$S_{neut} = \Gamma_{\mathrm{neut}}\big(\Sigma(H_{neut} - H_i)\big) \tag{1.10}$$

$$S_{UV} = \Sigma\big(\Gamma_i \epsilon_i (1 - R_i)\big) \tag{1.11}$$

where J is the power deposited per area of the material. S_{ion}, S_e, S_{neut} and S_{UV} are the source terms due to ions, electrons, neutrals and UV, respectively. In equation 1.8, Φ_{drop} is the difference in electric potential between the surface node and its nearest gas-phase neighbor (representing the kinetic energy of ions), H_{ion} is the enthalpy of formation of incident ion and H_i is the enthalpy of formation of the species returning to the gas-phase following ion reaction on the surface. In equation 1.9. Γ_e is the flux of electrons to the surface, T_e is the temperature of those electrons. This is the heating term. The second term is a cooling terms due fluxes of secondary emission electron away from the surfaces. Here, γ_i is the secondary electron emission coefficient for given ions and Γ_{FE} is the flux due to electric field electron emission. For all these electrons, we assume 4 eV of energy is being carried away, which is the typical work function of a metal. In equation 1.9, Γ_{neut} is the flux of neutral reactive species to the surface, H_{neut} is that species' enthalpy of formation and H_i is the enthalpy of formation. Lastly, in equation 1.11, Γ_i is the flux of UV photons with energy ϵ_i. The energy deposited then depends on the material's reflectivity, R_i.

1.4 Reactivity Transfer to Liquids: Aerosols

Plasmas can also be extended to interact with liquids, further enabling reactivity transfer. These interactions are being studied for a large scope of purposes: biomedical, agricultural, and

water treatment applications [2,16,62]. From a pollutant remediation perspective, plasma acts as an advanced oxidation method, enabling its use to address a variety of pollutants [2]. From a biomedical perspective, beneficial effects of plasma treated liquids are generally attributed to the production of reactive oxygen and nitrogen species (RONS) by the plasma which solvate in and further react in the liquid [63,64].

For example, plasmas produce high densities of ozone (O_3) in oxygen environments. This species is an oxidative agent that is stable in water. It is currently used in regional water treatment facilities as a non-toxic means of remediating biological infestations [65,66]. Another example is a hydroxyl radical, which is produced at high volumes in water-plasma systems. OH is the most oxidative agent in aqueous solutions with a reduction potential of $E^0 = 2.85$ V, which makes it highly reactive [16,67,68]. However, due to its propensity to recombine to form either H_2O or H_2O_2, OH does not have a long half-life. Because air plasmas can be produced in close proximity to liquid water, hydroxyl can be transferred directly to it, allowing for high degree of solvation and direct treatment of liquids.

The means of maximizing plasma/liquid reactivity transfer is a topic of active study. Whether treating high volumes of liquid (agriculture, pollutant removal) or requiring high densities of reactive species in small liquid volumes (medicine, sterilization), transfer of reactivity is transport-limited. The activating species must first transport from their site of creation in the plasma to the surface of liquid, the species must then transport into the liquid and finally transport from the surface of the liquid into the interior. Many of these transport limits can be addressed by plasma activation of small liquid droplets immersed in the plasma as they increase the interaction region. In this plasma activation scheme, radicals and ions are produced in the immediate vicinity of the droplet, thereby minimizing transport limits to the liquid surface.

Small (micron-scale) water droplets are able to be completely surrounded by the plasma, maximizing exposure. Further, at smaller radii, the surface-to-volume ratio of the liquid is increased, therefore maximizing the fluences reaching water. Lastly, the small volume maximizes the total densities of reactive aqueous species present within the liquid. Several experimental studies have addressed this type of plasma activation scheme. For example, plasma treatment of droplets by electrospray of water has been found to be effective for inactivation of biofilms, as found by the Mahala group [68,69]. In particular, they also found that both negative and positive discharges have a similar impact on bacteria survival. In fact, the most impactful experimental variable was exposure time (or total deposited energy). This makes sense, as most oxidants (OH, H_2O_2) are produced regardless of applied polarity. This result can be seen in Fig. 1.7. Plasma treated water mist has effectively sterilized E. coli and while influencing the production of RONS in the liquid [70]. Plasma treatment of water droplets has produced particularly high concentrations of aqueous hydrogen peroxide – H_2O_{2aq} [71].

Additionally, akin to solid catalysts, the liquid droplets affect the behavior of plasmas and vice-versa. De-ionized water (with conductivity of 5.5×10-8 S-cm^{-1} and permittivity of 7.1×10-12 F-cm^{-1}) has the dielectric relaxation time of

$$\tau_d = \frac{\varepsilon}{\sigma} = 0.13\ ms \tag{1.12}$$

This means that at plasma time-scales (nano- to micro-seconds), the droplets behave like a dielectric. In a fashion similar to that discussed in section 1.2 with dielectric beads, the droplets lead to local electric field enhancement and an increase of local ionization rates. Plasma, therefore, preferentially forms near the droplets, increasing rates of reactivity transfer. Additionally, processes such as surface ionization waves (SIWs) often occur on dielectric-like surfaces (as is low conductivity water). SIWs produce reactivity in immediate proximity of the liquid, even

further increasing reactivity transfer rates. The resultant high electron and ion fluxes then charge the surface of the droplet, further interacting with the electric field in accordance with the Poisson's equation. The high charge density solvated in the droplets can also lead to their breakup if the Rayleigh Limit is reached [72]:

$$q^2 = 64\,\pi^2 \varepsilon_0 \gamma a^3 \tag{1.13}$$

Where q is the amount of charge required for the Columbic repulsion forces to overcome the surface tension leading to breakup of the droplets, ε_0 is the permittivity of free space, γ is the surface tension of the droplet and a is the surface radius. Lastly, due to polarization of the droplet, the electrostatic forces can lead to changes in the topology of the aerosols – changing spherical droplets to more oblong shapes.

Furthermore, liquids can sustain species densities that are vastly different than those sustained in gases in accordance with the Henry's Law constant of solvation. For example, ozone has a Henry's Law (H_0) constant of 0.274. This means that, at equilibrium, for every 100 gas molecules present near liquid surface, water can sustain only 27. On the other end of the scale, hydrogen peroxide has $H_0 = 1.92\times10^6$ meaning that for every H_2O_2 molecule present in the surrounding gas, water can sustain nearly 2 million molecules at equilibrium [64,73]. This fact opens several avenues to chemical selectivity by varying plasma parameters which preferentially produce given species. Additionally, the droplet can therefore act as a sink of local reactive gas species, completely draining some species, while coming to an equilibrium with other nearly instantaneously. This phenomenon cannot be modeled in low-dimension simulations, as it is space- and time-dependent. But it is of crucial importance to chemical selectivity and reactivity transfer rates. It should also be noted that as the aerosol evaporates, the reactive species deposited to its surface is transported back to the gas-phase. As such, the activated media should be deposited

onto a surface it is meant to treat or mixed with other media (larger liquid volume with smaller surface-to-volume ratio) to prevent the decrease in aqueous reactive species.

1.5 Motivation

Due to their dynamic nature, atmospheric pressure plasmas a difficult to probe experimentally. Insertion of majority of probes can destabilize plasmas and change their behavior. Furthermore, elucidating step-by-step kinetic processes can easily disrupt chemical pathways due the need for the presence of scavengers change chemical reaction rates and absorb chemical species of interest. Simultaneously, plasmas have shown the potential to positively impact some of the most pressing issues currently faced by society through its reactivity transfer properties – medicine, food production, and pollution control. The primary drawbacks of these plasma applications are connected to the poor understanding of the underlying fundamental processes – which leads to poor economics.

Computational modeling can elucidate means by which these processes take place. Simulations – when properly validated – explain the cause for observed phenomena. They allow one to probe without interfering. They permit for observations at time-scales varying between nanoseconds and minutes, while studying special scales between microns and tens of centimeters. As such, computational simulations are perfectly situated to expand our knowledge in the highly realm complex realm of plasma reactivity transfer, hopefully allowing for the furtherment of mitigation of society's greatest issues.

Detailed analysis of the processes undergoing in a wide variety of Atmospheric Pressure Plasma application is presented in this work. Plasma electrodynamics, their influence on the surround media, and plasma-chemical reaction sets are taken into account wholistically, as it aims

to integrate fields of plasma physics, chemical engineering, thermodynamics, and aerosol physics. With the end result being the widening of the current body of knowledge and furtherment of practical plasma-based technologies.

1.6 Scope of this Dissertation

The work presented in this thesis aims to elucidate the basic plasma physics and kinetics present in complex systems which are not easily probed in experiments. Knowledge of the processes at the microscopic scale can then be used to advance plasma chemical technologies on the macroscopic scales. As roles of next-generation energy sources (renewables, nuclear) expand and energy costs decrease (both in economic and environmental senses), plasma can become an avenue to energy storage, agricultural fertilization, medicine and pollution mitigation. Here, we discuss the means by which chemical reactivity is transferred to all three phases of matter, which may impact all of the above-mentioned application.

In Chapter 2, the description of the model used, *nonPDPSIM* will be provided. This includes the fundamental equations of state, computational scheme regarding matrix solutions, time-stepping, and integration, important physical phenomena being taken into consideration and code performance. The contributions to the model by the author – including parallelization, surface heating, implementation of new meshing software, and fluid periodic boundary conditions – are also discussed in this chapter. Lastly, discussion regarding experimental validation pertinent to this work is also overviewed.

In Chapter 3, the transfer of reactivity to gases via packed bed reactors are discussed. Discharges within reactors with different geometries, background gases, applied voltages and gas pressures are all shown to follow the same step-by-step process. These results are validated by

experimental collaborators. The types of plasmas observed then had an impact on which reactive species formed – leading to an insight on selectivity.

In Chapters 4 and 5, respectively, the interaction between plasmas and metallic catalysts and propagation of plasmas into pores are explained. These discharges showcase the transfer of reactivity to solids. With respect to catalysts, the reasons for observable synergy are explored. Local surface heating, electric field enhancement and field emission are shown to contribute to prior-observed increases in conversion rates in plasma-catalytic systems. In Chapter 6, the impact of pore topology on uniformity of surface coverage by reactive species is addressed. In particular, the angle of the pore-chain with respect to applied electric field was found to be critical. The more tangential this angle, the lower the uniformity was found to be.

In Chapter 6, interactions between liquid water droplets and plasmas are discussed. The study showed the importance of Henry's Law constant and local effects on the efficacy of activation of water. Furthermore, droplets with higher surface-to-volume ratio (smaller radius) are shown to acquire higher densities of reactive, high-*h* species.

The summary and conclusions are presented in Chapter 7. Perspectives on future work are also discussed in this chapter.

1.7 Figures

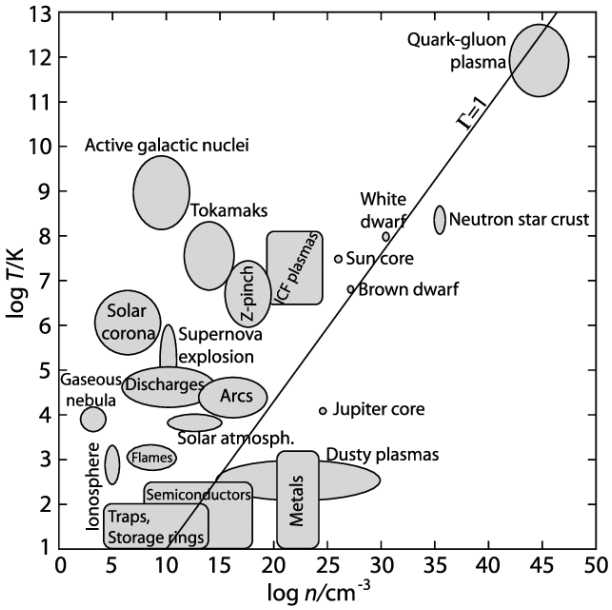

Fig. 1. 1 Types of plasmas and their electron densities and temperatures. Credit: Donko et. al. [74]

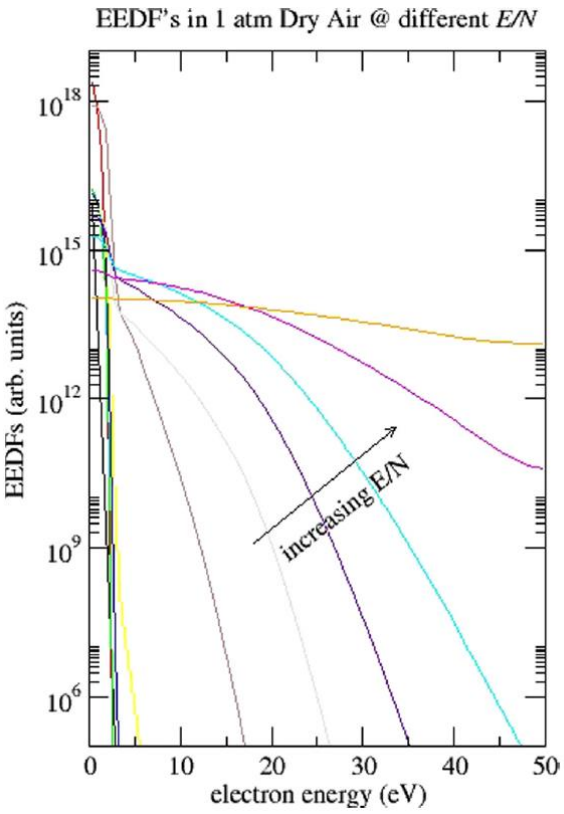

Fig. 1. 2 Electron energy distribution functions in air at varying reduced electric fields, E/N (electric field divided by number density). Credit: Laroussi et al. [75]

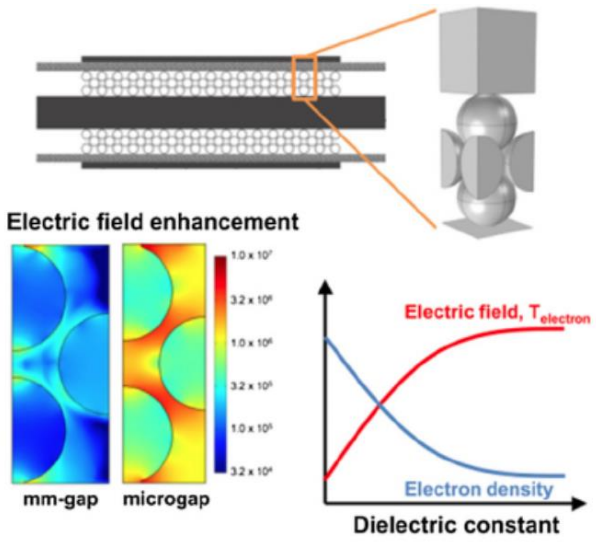

Fig. 1. 3 Extent of electric field enhancement in PPBRs due to dielectric polarization. Credit: Van Laer et al. [29]

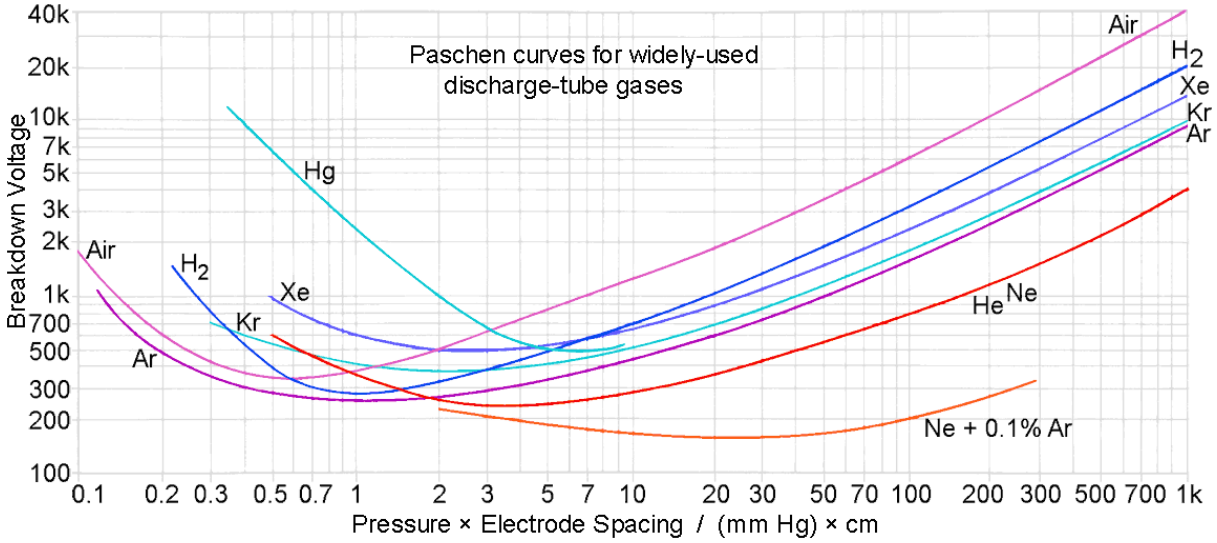

Fig. 1. 4 Paschen curves for different gases. Credit: H. H. Wittenberg [76]

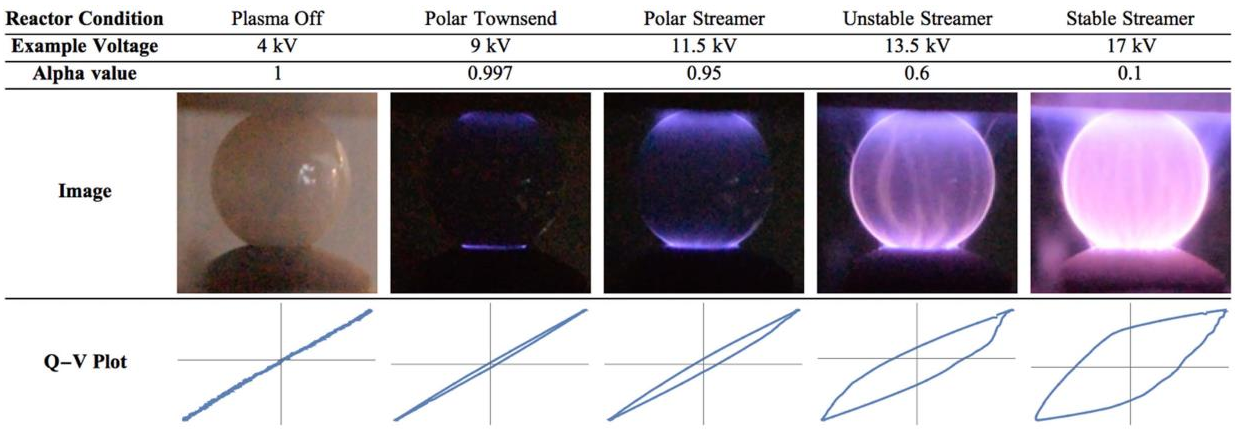

a)

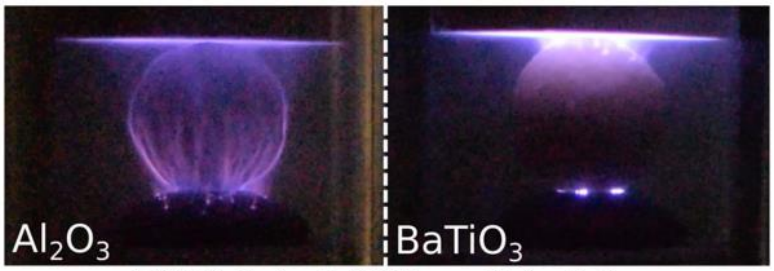

b)

Fig. 1. 5 Formation of various plasmas in a single-pellet packed bed reactor. Impact of applied voltage (a)) and permittivity (b)). Credit T. Butterworth and R. W. K. Allen [37]

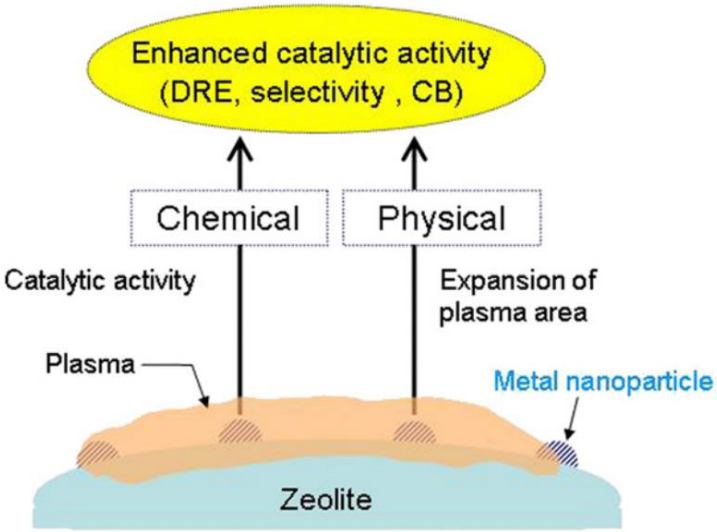

a)

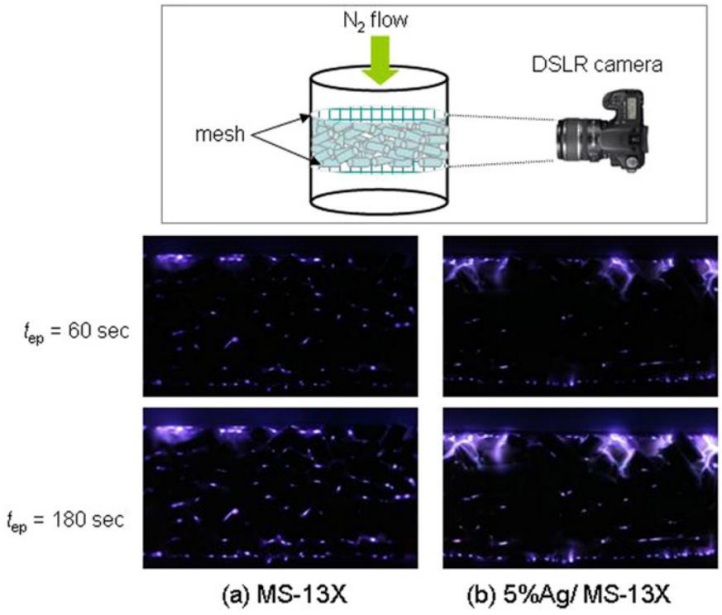

b)

Fig. 1. 6 Impact of metallic catalysts on plasma discharges in a PBR. a) Schematic of a plasma-catalytic packed bed reactor. b) plasma discharges in a zeolite/metal catalytic PBR. Credit H. H. Kim [77]

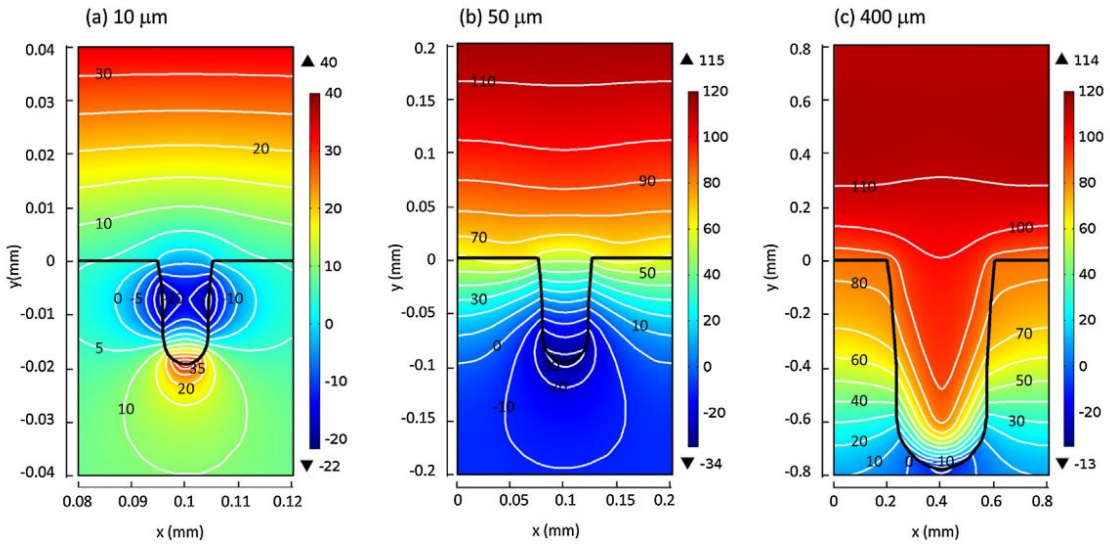

Fig. 1. 7 Impact of pore size on distribution of electric potential (kV). Credit: Yu-Ru Zhang et al. [56]

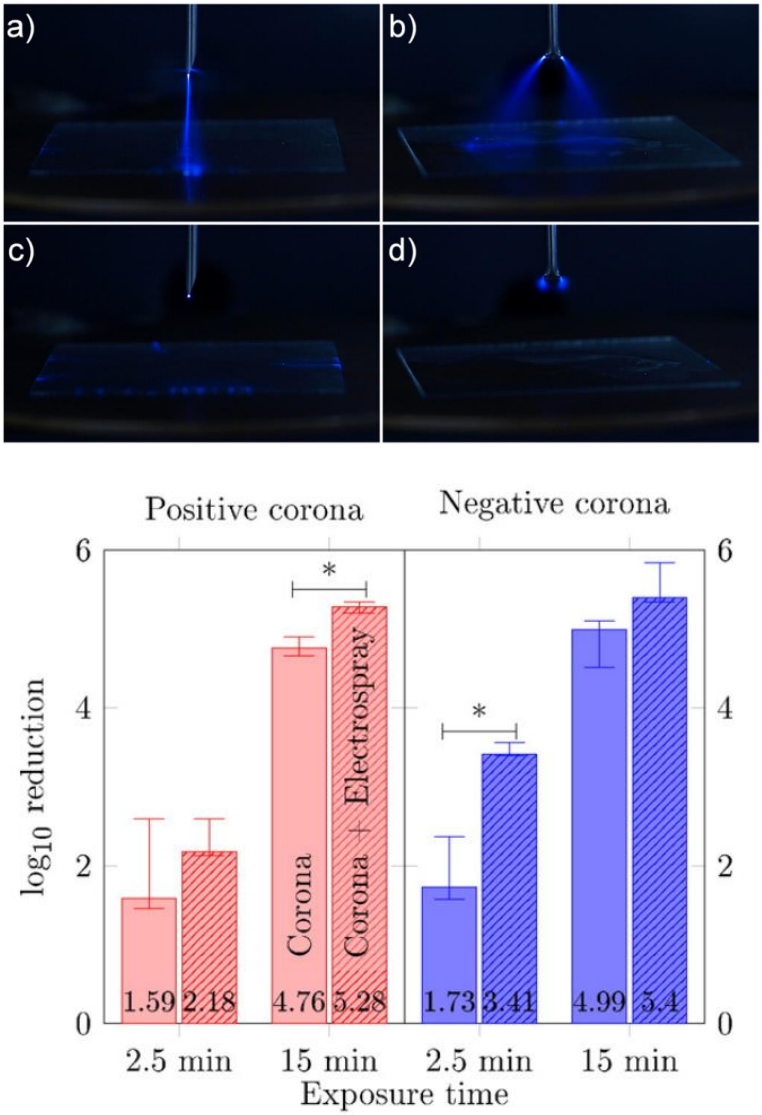

Fig. 1. 8 Corona discharges with an electrospray. Top: a) positive corona, b) positive corona with electrospray, c) negative corona, d) negative corona with an electrospray. Bottom: reduction in bacteria for positive and negative discharges at various times. Credit: Kovalova et al. [69]

1.8 References

[1] C. G. N. Lee, K. J. Kanarik and R. A. Gottscho, J. Phys. D. Appl. Phys. **47,** 273001 (2014).

[2] P. J. Bruggeman, M. J. Kushner, B. R. Locke, J. G. E. Gardeniers, W. G. Graham, D. B. Graves, R. C. H. M. Hofman-Caris, D. Maric, J. P. Reid, E. Ceriani, D. Fernandez Rivas, J. E. Foster, S. C. Garrick, Y. Gorbanev, S. Hamaguchi, F. Iza, H. Jablonowski, E. Klimova, J. Kolb, F. Krcma, P. Lukes, Z. Machala, I. Marinov, D. Mariotti, S. Mededovic Thagard, D. Minakata, E. C. Neyts, J. Pawlat, Z. Lj Petrovic, R. Pflieger, S. Reuter, D. C. Schram, S. Schröter, M. Shiraiwa, B. Tarabová, P. A. Tsai, J. R. R. Verlet, T. Von Woedtke, K. R. Wilson, K. Yasui and G. Zvereva, Plasma Sources Sci. Technol. **25,** 053002 (2016).

[3] H. L. Chen, H. M. Lee, S. H. Chen and M. B. Chang, Ind. Eng. Chem. Res. **47,** 2122 (2008).

[4] L. Di, J. Zhang and X. Zhang, Plasma Process Polym. **15,** 1700234 (2018).

[5] M. G. Kong, G. Kroesen, G. Morfill, T. Nosenko, T. Shimizu, J. van Dijk and J. L. Zimmermann, New J. Phys. **11,** 115012 (2009).

[6] X. Lu, G. V. Naidis, M. Laroussi and K. Ostrikov, Phys. Rep. **540,** 123 (2014).

[7] F. F. Chen, Introduction to Plasma Physics and Controlled Fusion, (Plenum Press, New York) (1984).

[8] R. K. Kirkwood, J. D. Moody, J. Kline, E. Dewald, S. Glenzer, L. Divol, P. Michel, D. Hinkel, R. Berger, E. Williams, J. Milovich, L. Yin, H. Rose, B. Macgowan, O. Landen, M. Rosen and J. Lindl, Plasma Phys. Control. Fusion **55,** 103001 (2013).

[9] N. J. Fisch, Physi. Rev. Let. **41,** 13 (1978).

[10] M. Kikuchi, K. Lackner and M. Quang, 'Fusion Physics', (IAEA, Vienna, Austria) (2012).

[11] R. P. Drake, 'High-energy-density physics', (Springer International Publishing, New York, NY) (2010).

[12] P. M. Bellan, 'Fundamentals of Plasma Physics', (Cambridge University Press, Cambridge, UK) (2006).

[13] H. F. Calcote and R. N. Pease, Ind. Eng. Chem. **43,** 12 (1951).

[14] A. R. Choudhuri, Astrophysics for Physicists (Cambridge University Press, Cambride, UK) (2010).

[15] M. A. Lieberman and A. J. Lichtenberg, Principles of Plasma Discharges and Materials Processing (Wiley-Interscience, Hoboken, New Jersey) (2005).

[16] V. I. Parvulescu, M. Magureanu and P. Lukes, (Wiley-VCH, 2012).

[17] A. Bogaerts, X. Tu, J. C. Whitehead, G. Centi, L. Lefferts, O. Guaitella, F. Azzolina-Jury, H. Kim, A. B. Murphy, W. F. Schneider, T. Nozaki, J. C. Hicks, A. Rousseau, F. Thevenet, A. Khacef and M. Carreon, J. Phys. D Appl. Phys. **53,** (2020).

[18] M. Gherardi, R. Tonini and V. Colombo, Trends Biotechnol. **36,** 583 (2018).

[19] G. J. M. Hagelaar and L. C. Pitchford, Plasma Sources Sci. Technol. **14,** 722 (2005).

[20] Q. Z. Zhang and A. Bogaerts, Plasma Sources Sci. Technol. **27,** 035009 (2018).

[21] H. Wang, W. Jiang and Y. Wang, Plasma Sources Sci. Technol. **19,** 045023 (2010).

[22] J. Teunissen and U. Ebert, Plasma Sources Sci. Technol. **25,** 044005 (2016).

[23] K. Woo Seok, P. Jin Myung, K. Yongho and H. Sang Hee, IEEE Trans. Plasma Sci. **31,** 504 (2003).

[24] S. A. Norberg, E. Johnsen and M. J. Kushner, Plasma Sources Sci. Technol. **24,** 035026 (2015).

[25] H. Puliyalil, D. Lašič Jurković, V. D. B. C. Dasireddy and B. Likozar, RSC Adv **8,** 27481 (2018).

[26] P. Mehta, P. Barboun, D. B. Go, J. C. Hicks and W. F. Schneider, ACS Energy Lett. **4,** 1115 (2019).

[27] H. Kim, Y. Teramoto, A. Ogata, H. Takagi and T. Nanba, Plasma Process. Polym. **36,** 45 (2016).

[28] K. Van Laer and A. Bogaerts, Plasma Sources Sci. Technol. **25,** 015002 (2016).

[29] K. Van Laer and A. Bogaerts, Plasma Sources Sci. Technol. **26,** 085007 (2017).

[30] A. Bogaerts, T. Kozák, K. van Laer and R. Snoeckx, Faraday Discuss. 217 (2015).

[31] P. Mehta, P. Barboun, F. A. Herrera, J. Kim, P. Rumbach, D. B. Go, J. C. Hicks and W. F. Schneider, Nat. Catal. **1,** 269 (2018).

[32] Y. X. Zeng, L. Wang, C. F. Wu, J. Q. Wang, B. X. Shen and X. Tu, Appl. Catal. B Environ. **224,** 469 (2018).

[33] S. Paulussen, B. Verheyde, X. Tu, C. De Bie, T. Martens, D. Petrovic, A. Bogaerts and B. Sels, Plasma Sources Sci. Technol. **19,** 034015 (2010).

[34] D. B. Go and D. A. Pohlman, J. Appl. Phys. **107,** 103303 (2010).

[35] A. Bogaerts, A. Berthelot, S. Heijkers, S. Kolev, R. Snoeckx, S. Sun, G. Trenchev, K. Van Laer and W. Wang, Plasma Sources Sci. Technol. **26,** 063001 (2017).

[36] Y. Zhang, H. Wang, W. Jiang and A. Bogaerts, New J. Phys. **17,** 083056 (2015).

[37] T. Butterworth and R. W. K. Allen, Plasma Sources Sci. Technol. **26,** 065008 (2017).

[38] W. Wang, T. Butterworth and A. Bogaerts, J. Phys. D Appl. Phys. **54,** 214004 (2021).

[39] H. H. Kim, Y. Teramoto, A. Ogata, H. Takagi and T. Nanba, Plasma Process. Polym. **14,** 1600157 (2016).

[40] K. H. R. Rouwenhorst, H.-H. Kim and L. Lefferts, ACS Sustain. Chem. Eng. **7,** 17515 (2019).

[41] H. Lee, D.-H. Lee, Y.-H. Song, W. C. Choi, Y.-K. Park and D. H. Kim, Chem. Eng. J. **259,** 761 (2015).

[42] E. C. Neyts, K. Ostrikov, M. K. Sunkara and A. Bogaerts, Chem. Rev. **115,** 13408 (2015).

[43] J. Hong, S. Pancheshnyi, E. Tam, J. J. Lowke, S. Prawer and A. B. Murphy, J. Phys. D Appl. Phys. **51,** 109501 (2018).

[44] M. Meyyappan, J. Phys. D. Appl. Phys. **42,** 213001 (2009).

[45] S. Liu, L. R. Winter and J. G. Chen, ACS Catal. **10,** 2855 (2020).

[46] J. C. Whitehead, J. Phys. D Appl. Phys. **49,** 243001 (2016).

[47] S. Tanaka, H. Uyama and O. Matsumoto, Plasma Chem Plasma Process **14,** 4 (1994).

[48] F. Holzer, F. D. Kopinke and U. Roland, Plasma Chemistry and Plasma Processing **25,** 595 (2005).

[49] E. C. Neyts, K. K. Ostrikov, M. K. Sunkara and A. Bogaerts, Chem. Rev. **115,** 13408 (2015).

[50] F. A. Herrera, G. H. Brown, P. Barboun, N. Turan, P. Mehta, W. F. Schneider, J. C. Hicks and D. B. Go, J. Phys. D Appl. Phys. **52,** 224002 (2019).

[51] L. F. Spencer and A. D. Gallimore, Plasma Sources Sci. Technol. **22,** 015019 (2013).

[52] L. Di, J. Zhang, M. Craven, Y. Wang, H. Wang, X. Zhang and X. Tu, Catal. Sci. Technol. **10,** 6151 (2020).

[53] H.-H. Kim, Y. Teramoto, A. Ogata, H. Takagi and T. Nanba, Plasma Chem Plasma Process Relat. **36,** 45 (2015).

[54] H. H. Kim and A. Ogata, Eur. Phys. J. Appl. Phys. **55,** 13806 (2011).

[55] K. Van Laer, S. Kolev and A. Bogaerts, Plasma Sources Sci. Technol. **25,** 015002 (2015).

[56] Y. R. Zhang, K. Van Laer, E. C. Neyts and A. Bogaerts, Appl. Catal. B Environ. **185,** 56

(2016).

[57] D. Mei, X. Zhu, C. Wu, B. Ashford, P. T. Williams and X. Tu, Appl. Catal. B Environ. **182,** 525 (2016).

[58] A. M. Darr, A. M. Loveless and A. L. Garner, Appl. Phys. Lett. **114,** 014103 (2019).

[59] F. Schertz, M. Schmelzeisen, M. Kreiter, H. Elmers and G. Schönhense, Physi. Rev. Let. **108,** 237602 (2012).

[60] R. G. Forbes, J. Vac. Sci. Technol. B **26,** 2 (2008).

[61] F. Che, J. T. Gray, S. Ha, N. Kruse, S. L. Scott and J. S. McEwen, ACS Catal. **8,** 5153 (2018).

[62] J. Foster, B. S. Sommers, S. N. Gucker, I. M. Blankson and G. Adamovsky, IEEE Trans. Plasma Sci. **40,** 1311 (2012).

[63] W. Tian, A. M. Lietz and M. J. Kushner, Plasma Sources Sci. Technol. **25,** 055020 (2016).

[64] A. M. Lietz and M. J. Kushner, J. Phys. D. Appl. Phys. **49,** 425204 (2016).

[65] S. Pekárek, Acta Polytech. **43,** 6 (2003).

[66] W. H. Glaze, J. W. Kang and D. H. Chapin, Ozone Sci. Eng. **9,** 335 (1987).

[67] D. B. Graves, IEEE Trans. Radiat. Plasma Med. Sci. **1,** 281 (2017).

[68] Z. Machala, L. Chládeková and M. Pelach, J. Phys. D Appl. Phys. **43,** 222001 (2010).

[69] Z. Kovalova, M. Leroy, M. J. Kirkpatrick, E. Odic and Z. Machala, Bioelectrochemistry **112,** 91 (2016).

[70] K. Patel, A. Mannsberger, A. Suarez, H. Patel, M. Kovalenko, A. Fridman, V. Miller and G. Fridman, Plasma Med. **6,** 447 (2016).

[71] R. J. Wandell and B. R. Locke, Ind. Eng. Chem. Res. **53,** 609 (2014).

[72] D. C. Taflin, T. L. Ward and E. J. Davis, Langmuir **5,** 376 (1989).

[73] R. Sander, Atmos. Chem. Phys. **15,** 4399 (2015).

[74] Z. Donko, P. Hartmann and G. J. Kalman, Eur. Phys. J. **arXiv:0710,** 1 (2007).

[75] M. Laroussi, X. Lu and M. Keidar, J. Appl. Phys. **122,** 020901 (2017).

[76] H. Wittenburg, Electron Tube Design (Lancaster, UK) (1962).

[77] H. H. Kim, J. H. Kim and A. Ogata, J. Phys. D Appl. Phys. **42,** 135210 (2009).

Chapter 2 Description of the Model

2.1 Description of *nonPDPSIM*

The computational model used in this work is *nonPDPSIM* – a fluid-based plasma simulator described in detail in Ref. [1]. *nonPDPSIM* uses an unstructured 2-dimensional mesh over a set geometry. An example of one is shown in Fig. 2.1 [2]. Each node within the plasma region (gas and liquid alike) includes densities of species defined by the user. These densities are then used in conjunction with the Boltzmann's equation to tabulate electron energy distribution and transport coefficients as functions of reduced electric field (E/N – the electric field divided by number density). Poisson's equation is then used to find the potential and electric field strength on each individual node. This is done implicitly, as well as simultaneously with charged-particle transport calculations. Furthermore, additional modules enable the simulation of phenomena related to radiation transport (via Green's function calculation), fluid flow (Navier-Stokes equations), gas and surface heating, RF and DC pulsing power cycles, and long-term plasma kinetics via the omission of electrostatic calculations. These phenomena vary widely in time-scales from seconds (fluid flow, gas heating) to nanoseconds (discharge propagation and radiation transport). This presents a difficulty regarding their solution within a single simulation. This is addressed in *nonPDPSIM* through the utilization of a time-splitting technique, wherein equations pertinent to individual phenomena are updated only in accordance to time-steps relevant to them.

nonPDPSIM is written in Fortran and is primarily run on Linux servers. The simulation times vary widely depending on cases being studied – from a few hours up to several weeks. The

code is primarily serial, but several regions of OpenMP parallelization were added by the author, allowing for increased performance. Primarily, these additions were made in the calculation of neutral species' transport coefficients. This was determined be the most time-consuming calculation by utilizing Allinea Forge profiling software by Arm Limited [3]. As a result of the implemented optimization, an approximately 50% reduction in simulation time was achieved on 4 cores, as can be seen in Fig. 2.2.

The typical plasma discharge time-scales vary between a few nanoseconds (streamer development) and microseconds (steady state RF discharges), while the plasma time-steps vary between fractions of picoseconds and nanoseconds.

The required input files which define a case are as follows:

- .nam – the primary definition input file (namelist), which defines material properties, pulse characteristics, and enabled modules (fluid, radiation, gas heating etc.), sets the time-steps and pertinent time-periods, and contains the table of E/N values of interest for the solution of Boltzmann's equation.
- .nlist – the mesh file (nodelist) defining each node (location, material number, and zone number, whether the node is at the border of the computational domain), each mesh cell (by providing the set of immediate neighbors for each node), and geometry lines.
- .dat – the chemistry file defining the species included in the kinetic mechanism (including their names, specific heats, charges, Leonard-Jones radii and energies, weights, surface interaction parameters, and enthalpies of formation), as well as the reactions between said species (including reactants, Arrhenius coefficients, if following the Arrhenius form and reference to cross-section tables otherwise,

temperature exponent, activation energy).

Beyond the three primary input files, several others can be added depending on the case. For instance, complex surface chemistries can be tracked using a surface.dat file, which would include specific surface species, site densities, and reaction rates. Fig. 2.3 provides a flow diagram of a typical *nonPDPSIM* case.

2.2 Geometry and Mesh

nonPDPSIM utilizes a formatted-read node list as explained in section above. Work presented herein utilized Skymesh2 by SkyBlue systems and Pointwise by Pointwise, Inc [4]. The latter was implemented by the Author due to its superior ease of use and expanded capabilities. For example, while Skymesh2 requires post-processing to transform its output files into an .nlist format, a plug-in was developed for Pointiwse that automatically produces *nonPDPSIM*-readable output. This was done through the implementation of a C++ plug-in through a Software Development Kit provided by Pointwise. In short, Pointwise inputs were adopted to allow for custom designations of materials, zones, and boundaries. They are then outputted in the .nlist format.

Beyond simply outputting the .nlist file, Pointwise provided several additional advantages. These include visual-based geometry design, copy-pasting of points and features, mirroring and shifting of features, and the ability to control the location of individual nodes (increasing mesh cell uniformity). Perhaps most importantly, Pointwise allows for the production of hybrid meshes, which combine triangular and rectangular mesh cells. This allows for the combination of the versatility of unstructured (triangular) meshes in terms of the variety of scales with the structured (rectangular) meshes' uniformity near surfaces.

In short, unstructured meshes allow some nodes to be further away from a flat surface than

others. As a result, the electric field at the nodes *nearest to the surfaces* (which is the physical resolution of the simulation) may vary. This is an unphysical solution and can lead to an accumulation of numerical errors. On the other hand, structured meshes do not possess the ability for variation in resolution, which may lead to an unnecessary increase in computational cost through an increase in the number of nodes. A hybrid mesh takes advantage of both – allowing for rectangular cells to exist in the proximity of surfaces and triangular cells further away. An example of this is shown in Fig. 2.4.

Once a mesh is set up, its properties can be set. Regions within the geometry are assigned values based on their material and zone. Materials can have various applied potentials, permittivities, conductivities, thermal properties, emission coefficients, and reaction rates. The zone parameter allows for different sets of equations to be applied to different regions – for example, when simulating a liquid/plasma system. If a node exists at the boundary of different materials, it is assigned to the metal first, dielectric second, and gas third.

Finite Volume Method is utilized to solve the partial differential equations discussed in latter sections. Each node is interconnected with its immediate neighbors, forming a cell. This cell is calculated based either on the intersections of the perpendicular bisectors of the two lines joining two neighbor nodes or on the chords between centroids of adjacent triangular sub-cells (formed from connections between the main node and two of its neighbor nodes). The latter can be utilized in both rectangular and triangular meshes, and it is therefore preferred. An example of a computational cell computation via both methods is shown in Fig. 2.5. In the case of a structured or hybrid mesh, only the perpendicular bisector method is used. The area of the cell is then calculated. Depending on the case set-up, the volume of the cell is found either by multiplying the area by the "depth" component of the geometry (if in Cartesian coordinates) or by integrating the

volume based on its radial position (if in cylindrical coordinates).

While there are no explicit limits on the number of nodes in *nonPDPSIM*, the computational time scales as N^2 with increased mesh size – particularly the number of nodes in the plasma regions where charged species transport calculations are performed. As a result, the typical *nonPDPSIM* case varies between 7,000 and 15,000 nodes. More complex geometries, particularly ones requiring the resolution of small features, necessitate careful mesh consideration. Ideally, the mesh would be composed of equilateral triangles with minimal variation is cell size. This is because sharp variations in mesh resolution lead to deviation from the ideal and strain the ability of the solvers within *nonPDPSIM*.

2.3 Boltzmann's and Electron Energy Equations

As was mentioned earlier, the Boltzmann's equation is solved at the beginning of each simulation for a given input chemistry and defines reduced electric field values. This solution is then updated frequently enough to account for changes in gas chemistry due to the presence of the plasma. The Boltzmann's equation is:

$$\frac{\partial f}{\partial t} + \vec{v} \cdot \nabla_{\vec{r}} f + \frac{\Sigma \vec{F_i}}{m} \cdot \nabla_{\vec{v}} f = \left(\frac{\partial f}{\partial t}\right)_{coll} \tag{2.1}$$

where f is the electron energy distribution function, t is the time, v is the velocity, ∇_r is the gradient in space, F_i is the ith force acting on electrons, m is the mass of the electrons, ∇_v is the gradient in velocity space, and $\left(\frac{\partial f}{\partial t}\right)_{coll}$ are the energy losses due to collisions with background gasses. The two-term spherical harmonic expansion is used to solve Eq. 2.1 in zero dimensions, accounting for isotropic and anisotropic components. This simplification allows for rapid solutions, while maintaining a high degree of accuracy [5,6].

The average energy – or temperature – of the electrons is solved using the Electron Energy

Equation. The solution is local at each node, which allows for the calculation of heterogenous plasma states, such as those which appear in ionization fronts. The Electron Energy Equation is:

$$\frac{\partial\left(\frac{3}{2}n_e k_b T_e\right)}{\partial t} = \vec{j}\cdot\vec{E} - \nabla\cdot\left(\frac{5}{2}\vec{\Gamma}k_B T_e - \kappa(T_e)\nabla T_e\right) - \sum_i \Delta\varepsilon_i R_i \qquad (2.2)$$

Where n_e is the electron number density, k_b is the Boltzmann's constant which relates kinetic energies of particles to the temperature of the substance, T_e is the electron temperature and t is the time. On the right-hand-side, j is the current density, E is the electron field and their dot product represents the energy deposited into the system. $\vec{\Gamma}$ is the flux of electrons into and out of the mesh cell, κ is the thermal conductivity, and $\Delta\varepsilon_i$ is the change in energy due to the i'th reaction with the reaction rate of R_i. The reaction rate coefficients are based on experimentally-determined reaction cross-sections, when available, and otherwise take the Arrhenius form (Eq. 2.3).

$$k = A * T_e * \exp\left(-\frac{\Delta\varepsilon}{T_e}\right) \qquad (2.3)$$

Where k is the reaction rate coefficient, A is the Arrhenius coefficient and $\Delta\varepsilon$ is the reaction activation energy.

2.4 Poisson's Equation and Charged Species Transport

Once the electron temperature and transport coefficients have been found for each of the user-defined E/N values, they are applied to individual mesh cells. On each node, the electric field is found using the Poisson's equation. This includes the simultaneous integration of applied voltage, cell-based potential (based on local permittivity and charges), charge densities, and surface charges as shown in Eq. 2.4:

$$\nabla\cdot(\varepsilon\nabla\Phi) = -(\sum_i n_i q_i + \rho_s) \qquad (2.4)$$

where ε is the local permittivity (based on local species in gasses and liquids, and material properties in the solids), Φ is the local potential, n_i is the local number density of the i'th species,

q_i is its charge, and ρ_s is the number density on the surface of a solid material.

Simultaneously, the transport equation for the charged species is solved. This is required in implicit solutions due to the charges' movement impacting the local potential and vice-versa. The charge transport is done using Eq. 2.5:

$$\frac{\partial n_i}{\partial t} = -\nabla \cdot \vec{\Gamma}_i + S_i + \left(\sum_j -\nabla \cdot \overrightarrow{\Gamma_j}\gamma_j + \sum_k -\nabla \cdot \overrightarrow{\phi_k}\gamma_k\right) \tag{2.5}$$

Where Γ_i is the flux of the i'th species into a node, S_i is its local source term due to reactions, Γ_j and ϕ_k are the fluxes of the j'th ion and k'th photon to the surface of a material, with secondary electron emission coefficient of γ_j and photoelectron emission coefficient of γ_k, respectively. S_i includes sources due to reactions, as well as due to radiation. To discretize the drift-diffusion of heavy charged species, the Scharfetter-Gummel scheme is utilized. [7]

Additionally, surfaces can emit electrons if the electric field in their proximity is sufficient to overcome their work function, W. This is calculated using the Fowler-Nordheim equation for thermionically enhanced emissions [8]:

$$j_E = AT^2 \exp\left(-\frac{\left(W-\sqrt{\frac{q^3\beta E}{\varepsilon_0}}\right)}{k_B T}\right) \tag{2.6}$$

where j_E is the resultant electron current, A is the Richardson-Dushman constant (120.13 A/cm^2-K^2), T is the temperature of the surface, W is the work function of the metal, k_B is Boltzmann's constant, q is the elementary charge, and E is the electric field at the surface of the metal. The variable β is a multiplicative factor allowing for the increase in emission rates due to topology (or other properties) of the material – for example, surface roughness too small to be resolved via meshing. It can be estimated using:

$$\beta = \frac{2\left(\frac{h}{r}\right)}{\ln\left(\frac{4h}{4}\right)-2d}\frac{1}{d} \tag{2.7}$$

where h is the height of the roughness, r is the radius of curvature of its tip, and d is the distance between roughness maxima.

Radiation in *nonPDPSIM* is solved using the Green's function approach. This means that particular photons are not tracked. Rather, the intensity of irradiation is tracked based on emitting species, absorbing species, and an r^{-2} dependency, where r is the distance from the emitting species. The Green's function is:

$$G_j(\overrightarrow{r_m}, \overrightarrow{r_l}) = \frac{\exp\left(-\frac{|\overrightarrow{r_m}-\overrightarrow{r_l}|}{\lambda_j}\right)}{4\pi|\overrightarrow{r_m}-\overrightarrow{r_l}|^2} \tag{2.8}$$

where r_m is the location of emitting species m, r_l is the location of absorbing species l, and λ_j is the mean free path of j'th photon along the r_l-r_m distance based on absorption cross-section (σ). As a result, the photon-based source term becomes:

$$S_{photo,i}(\overrightarrow{r_l}) = N_i(\overrightarrow{r_l}) \sum_j A_j \int \sigma_{ji} N_j(\overrightarrow{r_m})\, G_j(\overrightarrow{r_m}, \overrightarrow{r_l}) d^3\overrightarrow{r_m} \tag{2.9}$$

where N_i is the density i'th absorbing species, A_j is the Einstein coefficient, σ_{ji} is the absorption cross-section, N_j is the j'th density of emitting species, and r_m is the distance between the nodes containing the i'th and j'th species.

Radiation calculations are computationally expensive. Fluxes of photons from each emitting node to each absorbing node must be calculated, leading to matrices with the order of $n_{photons} \times N_{nodes}^2$. For this reason, the 'horizon' or distance limit within which the emitted photon can be absorbed can be set. This assumption is valid because the intensity of radiation decreases as $1/r^2$, meaning that the fluxes will be inconsequential far from the emission node. However, the computation is still time-consuming. For this reason, the author implemented OpenMP parallelization within the photo-reaction module, allowing for the simultaneous calculation of each photon's impact on a separate computational thread. With 4 photons being tracked and on 4 computer threads, this addition sped up the calculation by a factor of 3.

In *nonPDPSIM*, the $A \cdot x = B$ sparse matrix is solved in a fully implicit manner. Here, A is the Jacobian matrix, x is the unknown vector, and B contains the solution. To increase computational performance, the elements of the matrix (species densities, potential, surface charges, time-steps) are normalized. This is done by estimating the average expected values a-priori and inputting them into the namelist file. For instance, the species density normalization value may be 10^9 (a typical plasma density at atmospheric pressure) and time-step normalization value may be 10^{-12} (a typical time-step taken by the code). By normalizing these values, both become close to 1 – therefore decreasing the strain on the solver.

The Jacobian is either the result of a perturbation method variation, or an analytical solution. Typically, the latter is used. In general, the Jacobian elements can be described as the changes in one value due to another. For example, $\partial n_{ki}/\partial n_{mj}$ is the change in density of species k at node I due to change in density of species m at node j. For a given time-step Δt, the matrix A can be expressed as

$$A_{ij} = \frac{1}{\Delta t}\left(\delta_{ij} - \frac{\delta n_i}{\delta n_j}\right) \tag{2.10}$$

where n_i and n_j are the densities or potentials on nodes i and j, and δ_{ij} is 1 when i = j, and 0 otherwise. While some Jacobian elements can be solved once (ex. node-pair potential), other evolve with time (charge densities, surface charge). As an example, the change in density of species i will depend on its fluxes, reaction rates, and fluxes of other species from neighboring nodes. The analytical expression for time-change in density of species s on node i will then be:

$$\frac{\delta n_{si}}{\delta n_{si}} = \beta \sum_j \left[\frac{\alpha(D_{si}+D_{sj})}{1-\exp(\alpha \Delta x_{ij})}\right]\frac{A_{ij}}{V_i}\Delta t \tag{2.11}$$

where β is the implicitness factor, α is a Scharfetter and Gummel parameter as described in Ref. [9], D_{si} and D_{sj} are the diffusion coefficients, Δx is the distance between the nodes, A_{ij} is the area

of contact between computational cells, V_i is the volume of the computational cell i, and Δt is the current time-step. Similar expressions are then produced for reaction, photoionization and surface charging.

Various solver types are available, but the Generalized Minimum Residual Method with ILUT preconditioning is generally used [10]. The stacking order of the matrix is as follows: potential on nodes (length: number of nodes), surface charges (length: number of boundary nodes allowing surface charging), and charged species densities (length: number of charged species in the chemistry × number of plasma nodes). Typical matrix sizes have the order 10^5 – meaning 100,000 rows and 100,000 columns of values. As a result, careful consideration must be given to minimize the number of charged species and the number of nodes.

2.5 Neutral Transport

Neutral species are not influenced by electric fields. As a result, the primary influence on their transport is diffusion when gas flow is absent. This is represented by equation 2.12:

$$\frac{\partial n_i}{\partial t} = \nabla \cdot (-D_i \nabla n_i) + S_i \tag{2.12}$$

where n_i is the density of the neutral species, t is the time, D_i is the diffusion coefficient of the species, and S_i is the source term due to reaction – both gas-phase and surface-based. To solve this equation, both explicit and implicit options are available. The implicit solution involves a Successive Over-Relaxation method (SOR), which requires a user-determined time-step. Alternatively, the first through third-order Runge-Kutta (RK) method is available for an explicit solution. In the latter case, the Author has implemented an automatic time-stepping method. This is done by the comparing the relative error produced from the lower order solution to the RK method and the higher order solution. For example, the user may select to use the third order

solution, and the maximum error difference set to 10^{-6}. Should the variance between the second and third order solutions exceed 10^{-6}, the time-step taken will decrease by a set fraction (it should be noted that higher order solutions require lower-order solutions to also be performed). Similarly, if the relative error is very small (for example, 10^{-8}), the time-step may increase. This allows the user to simply designate an error range and not require them to explicitly determine the time-step prior to the simulation run.

It is important to note that the transport of neutral species is solved separately (but at the same time-step) from the charged species. This is due to the time-slicing algorithm which allows variation in solution times. The diffusion coefficients are estimated using Eq. 2.13:

$$D_{ij} = 0.001858\sqrt{\frac{M_i+M_j}{M_iM_j}}\frac{T_g^{\frac{3}{2}}}{P\sigma_{ij}\Omega_D} \tag{2.13}$$

where M_i and M_j are the masses of the species of interest and the background gas, respectively. T_g is the gas temperature, P is the gas pressure, σ_{ij} is the Leonard-Jones parameter given by Eq. 2.14, and Ω_D is a temperature-dependent collision integral [11]. It should also be noted that the pressure coefficient is crucial in the determination of transport rates within a liquid. Thanks to the zone parameter described earlier, different pressures can be assigned to different regions. As a result, a 1 atmosphere gas region and a directly neighboring 1,000 atmosphere liquid (based on number density) can both be resolved simultaneously.

$$\sigma_{ij} = \frac{1}{2}\left(\sigma_i + \sigma_j\right) \tag{2.14}$$

where individual diffusion coefficients are experimentally determined.

2.6 Fluid Flow

In *nonPDPSIM*, continuity, momentum, and energy forms of Navier-Stokes equations are solved on all gas-phase nodes. Nodes that represent the surfaces of solid materials assume a no-slip condition. Similarly, liquid surfaces are assumed to have a non-slip boundary condition and momentum transfer into the liquid is not considered. This is a good assumption under the small time-scales simulated in most atmospheric-pressure plasma cases. Furthermore, the algorithms used are mostly unsteady and compressible, with constant pressure boundary condition at the exit nozzles, though these can be adjusted based on the requirements of the case. The inlet boundary is determined by specifying fluxes (in SCCM) of species being injected perpendicularly into the computational domain.

Additionally, the author implemented a periodic boundary for fluid flow. Within that scheme, fluxes of species exiting the computational domain are being recorded on each of the exit nozzles. The ratios of each species' fluxes to the total are then calculated, and re-injected through the inlet nozzle nodes. A flowchart showing this, along with an example of results obtained, can be seen in Fig. 2.6. The injection velocities are maintained in accordance with the initial SCCM. This allows the user to track changes that multiple plasma pulses have on gases, when the simulated time exceeds the gas residence time within the reactor.

The densities, momenta and temperatures are calculated on the mesh nodes (as opposed to chords), as described by Norberg et al [1]. To find these, the continuity equations are first solved:

$$\frac{\partial N_t}{\partial t} = -\nabla \cdot \left(N_t \vec{v} + \sum_{i,j} \frac{f_{ij}}{A_i} \right) \tag{2.15}$$

and

$$\frac{\partial N_t M_t}{\partial t} = -\nabla \cdot \left(\sum_j m_j \Gamma_j N_j + \sum_{i,j} \frac{m_j f_{ij}}{A_i} \right) \tag{2.16}$$

where N_t is the total number density at a given node, v is the gas velocity, f_{ij} is the j'th species'

inlet flow velocity from the i'th inlet, and A_i is the i'th cell's area. In Equation 2.16, M_t is the mass of all species at a given node, m_j is the mass of the j'th species, and Γ_j is its flux.

Next, the momentum is calculated using Equation 2.17:

$$\frac{\partial N_t M_t \vec{v}}{\partial t} = -\nabla \mathrm{P} - \nabla \cdot (M_t N_t \vec{v}\vec{v}) - \vec{v} \cdot \vec{\tau} + \sum_i q_i N_i \vec{E} + N_t M_t g \frac{\vec{v} \cdot \hat{n}}{|\vec{v}|} \tag{2.17}$$

where P is the pressure, τ is the viscous stress, and E is the electric field. The latter accounts for the additional transport of charged heavy species due to presence of applied and self-induced electric fields. Lastly, the energy equation is:

$$\frac{\partial N_t c_v T}{\partial t} = -\nabla(-\kappa \nabla T + \rho \vec{v} c_v T) + P \nabla \cdot \vec{v} - \sum_m R_m \Delta H_m + \sum_i \vec{J_i} \cdot \vec{E} \tag{2.18}$$

where c_v is the specific heat of the gas, κ is the thermal conductivity, T is the gas temperature, R_m and ΔH_m are the m'th reaction's rate and change in enthalpy, respectively, and $j \cdot E$ is the Joule heating term. The heating term can then also be extended into materials through a thermal lumped capacitance model. Moreover, individual reactions on the surface of the material can also impact the material's surface. The author extended this algorithm to include heating through radiation, neutral reactions, electron fluxes, and electron emission. These are governed by Equations 2.19 through 2.23:

$$J\left(\frac{W}{cm^2}\right) = S_{ion} + S_e + S_{neut} + S_{UV} \tag{2.19}$$

$$S_{ion} = \Gamma_{ion}\left(\phi_{drop} + \Sigma(H_{ion} - H_i)\right) \tag{2.20}$$

$$S_e = \Gamma_{\mathrm{e}} T_e - (4\ eV)(\textstyle\sum_i \Gamma_{\mathrm{ion,i}} \gamma_i + \Gamma_{\mathrm{FE}}) \tag{2.21}$$

$$S_{neut} = \Gamma_{\mathrm{neut}}(\textstyle\sum_i (H_{neut} - H_i)) \tag{2.22}$$

$$S_{UV} = \Sigma\big(\Gamma_{\mathrm{i}} \epsilon_i (1 - R_i)\big) \tag{2.23}$$

where J is the power deposited per area of the material. S_{ion}, S_e, S_{neut}, and S_{UV} are the source terms due to ions, electrons, neutrals, and UV, respectively. In equation 2.20, Φ_{drop} is the difference in

electric potential between the surface node and its nearest gas-phase neighbor (representing the kinetic energy of ions), H_{ion} is the enthalpy of formation of incident ion, and H_i is the enthalpy of the formation of the species returning to the gas-phase following ion reaction on the surface. In equation 2.21, Γ_e is the flux of electrons to the surface, while T_e is the temperature of those electrons. This is the heating term. The second term is a colling terms due to the fluxes of secondary emission electron away from the surfaces. Here, γ_i is the secondary electron emission coefficient for given ions and Γ_{FE} is the flux due to the electric field electron emission. For all these electrons, we assume that 4 eV of energy is being carried away, which is the typical work function of a metal. In equation 2.22, Γ_{neut} is the flux of neutral reactive species to the surface, H_{neut} is that species' enthalpy of formation, and *Hi* is the enthalpy of formation. Lastly, in equation 2.23, Γ_i is the flux of UV photons with energy ϵ_i. The energy deposited then depends on the material's reflectivity, R_i.

The above equations are solved using the Successive Over Relaxation (SOR) method with a typical relative error of 10^{-6}. Depending on the settings, time slicing may be used to appropriately address kinetics or electrostatics and couple them with the fluid flow. This is done by performing chemistry and plasma calculations at time-steps that are smaller than those of the fluid-flow. The resulting number densities are then set as the initial values within the fluid solver. The typical time-steps for fluid flow varies between 10^{-8} and 10^{-6} s, depending on the complexity of the geometry and rates of neutral reactions.

2.7 Liquid Module

Plasmas possess the ability to 'activate' (or transfer reactivity to) liquids. However, liquids can behave quite differently compared to gases. Several phenomena not considered in gas-phase

modeling must be included when simulating plasma/liquid interactions. Generally, *nonPDPSIM* treats liquids as partially ionized fluids – the same way as the gases. All equations described in sections 2.4 and 2.5 are solved in the same fashion within a liquid. However, due to the high number densities occurring in liquids (approximately 3×10^{22} cm^{-3}, factor of 10^3 increase over gas number densities), regular diffusion equations cannot be applied at the boundaries of the two phases. Rather, the cross-phase transport is done via evaporation and solvation.

Solvation in *nonPDPSIM* is handled by restricting some species' ability to cross the inter-phase boundary. In general, assuming the liquid is water, all gas-phase charged species can enter the liquid region due to the assumption that their kinetic energy can overcome the surface energy of water. On the other hand, no charged solvated species can exit the liquid due to the high density and degree of polarization of the water molecules, which then 'trap' ions. Neutral species require further analysis, however. We utilize the Henry's Law equilibrium in the Noyes-Whitney formulation as the estimate for saturation density values. [12] Diffusion and drift diffusion fluxes are calculated for individual species based on the transport coefficient calculated within each phase. The transfer across the boundary for a given species is then determined by:

$$\Gamma_{gl} = \frac{D_g}{\Delta x}\left(1 - \frac{n_l}{n_g h}\right)\left(n_g - n_l\right), \quad n_g \leq h n_l \tag{2.24}$$

Where Γ_{gl} is the flux of a gas species into the liquid, D_g is the species' diffusion coefficient within the gas; Δx is the distance between the gas node and the gas/liquid boundary; n_g and n_l are its number densities within the gas and liquid phases, respectively; and h is its Henry's law constant. It should be noted that the values of n_g and n_l are those at nodes in direct contact with the boundary, allowing local variation in transfer rates. The flux goes to zero if the product of Henry's law constant and the liquid density surpasses the value of the density in the gas. The same restriction is done for the transfer of a liquid species into the gas:

$$\Gamma_{lg} = \frac{D_l}{\Delta x}\left(1 - \frac{h n_g}{n_l}\right)(n_l - n_g), \quad n_g \leq \frac{n_l}{h} \tag{2.25}$$

The result of Equations 2.24 and 2.25 is that species with a high Henry's law constant can have densities sustained within liquid that are many times greater than the densities present within the gas. For example, H_2O_2 has *h* value of 1.92×10^6. This means that, at equilibrium, nearly 2 million hydrogen peroxide molecules are present within the liquid for every gas-phase hydrogen peroxide molecule. Conversely, O_3 has *h* value of 0.274, leading to only one ozone molecule within the liquid for every three present within the gas. Once those values are reached, cross-boundary transport stops. Other species' *h* values are given in Table 2.1.

Evaporation for any given species depends on its saturated vapor pressure, temperature of the liquid and gas, and the density of the species directly above the liquid. In *nonPDPSIM*, this function is hard-coded for H_2O, but it can be expanded for any other species of interest. Currently, the vapor pressure approximation assumes a linear relationship between the number density and the temperature of the gas – which is valid in the temperature ranges of interest. Transfer of the liquid species is then performed by setting the number density of the gas-phase equivalent species on the surface of the liquid equal to the saturated vapor pressure number density.

Lastly, the liquid chemistry can be significantly different than its gas-phase counterpart. For example, gas-phase reactions between OH and NO_2 have a rate coefficient of 4×10^{-11} cm^3s^{-1}, while their liquid counterparts interact at a rate of 7.1×10^{-12} cm^3s^{-1} [13]. To address this situation, species present in the liquid-phase are given the subscript 'aq' and undergo their own set of reactions, independent of their gas-phase equivalent. The process of changing these species can be time-consuming, as it depends on a reaction between the 'solvating' (or 'de-solvating') species and its background. As an example, solvation of oxygen would require the following reaction:

$$O_{2,g} + H_2O_{aq} \rightarrow O_{2,aq} + H_2O_{aq} \quad (2.26)$$

This process, therefore, requires the inclusion of multiple additional reactions to address each species. To remedy this issue, the Author implemented an automatic solvation algorithm. First, species with a liquid phase equivalent are tabulated (ex. N_2, $N_{2,l}$). Second, all densities of the tabulated species' present within the opposite phase are zeroed out. Third, the densities are transferred to the correct-phase equivalent, therefore conserving mass. This is done at every update to species' densities.

2.8 Tables

Table 2. 1: Henry's Law Constants used in this work, primarily based on Ref. [14]

Species	h (unitless)	Note
H_2O_2	1.92×10^6	
HO_2	1.32×10^5	
OH, OH($A^2\Sigma$)	620	a
H, H*	6.00×10^3	a
H_2, H_2(r), H_2(v), H_2*	1.9×10^{-2}	a
H_2O(v)	1	a,b
O, O(^{1}D)	1	a,b
O_2, O_2(r), O_2(v), $O_2(^1\Delta_g)$, $O_2(^1\Sigma_u)$	3.24×10^{-2}	a
O_3, O_3*	0.274	
N_2, N_2(r), N_2(v), N_2*, N_2**, N, N(^{2}D)	1.6×10^{-2}	a
N_2O_3	600	
N_2O_4	37.0	
N_2O_5	48.5	
N_2O, N_2O(v)	0.599	a
HO_2NO_2	9.73×10^4	
NO	4.4×10^{-2}	
NO_2	0.28	
NO_3	41.5	
HNO_2, HNO	1.15×10^3	a
HNO_3, ONOOH	4.80×10^6	
CO, CO(v)	2.42×10^{-2}	a
CO_2, CO_2(v)	0.823	a
NH	1.47×10^3	c

a) Value corresponds to the first species in the list. Other species were assumed to have the same Henry's law constant.
b) Approximated. Species reacts quickly in water and will not reach Henry's law saturation.
c) Approximated by analogy to NH_3.

2.9 Figures

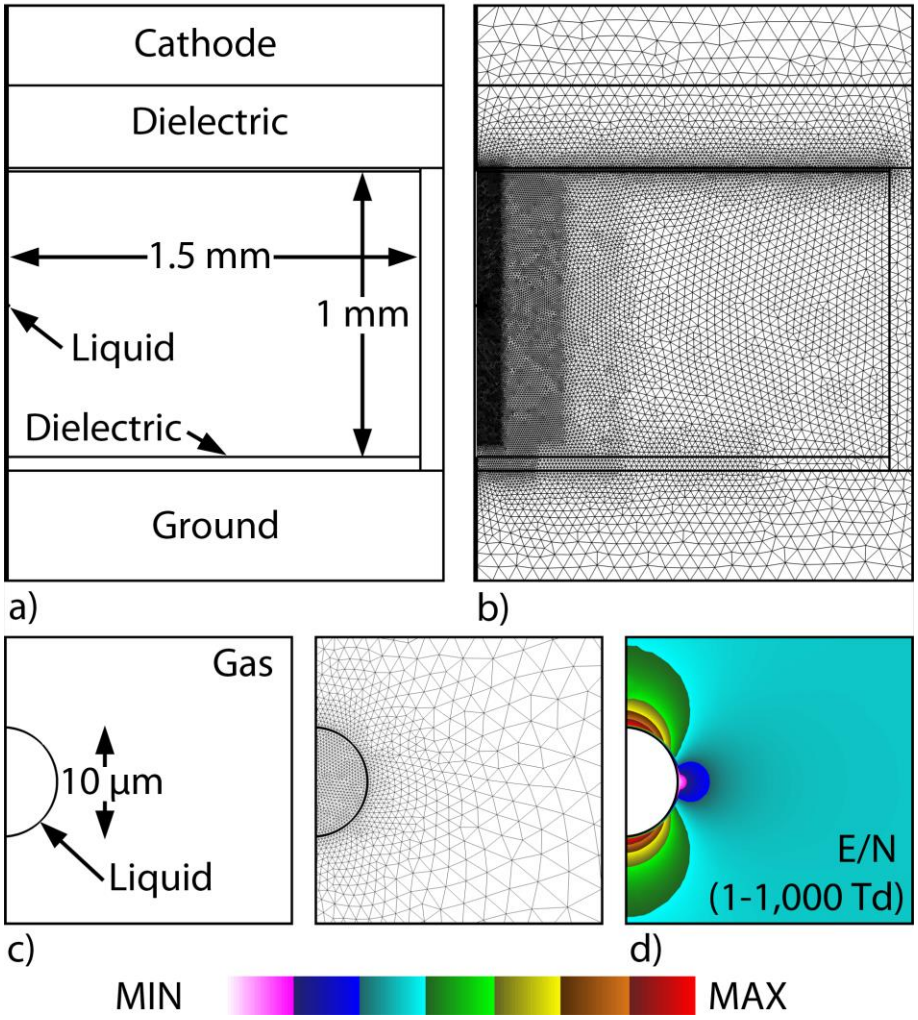

Fig. 2. 1 Example of geometry and mesh used in *nonPDPSIM*. [2]

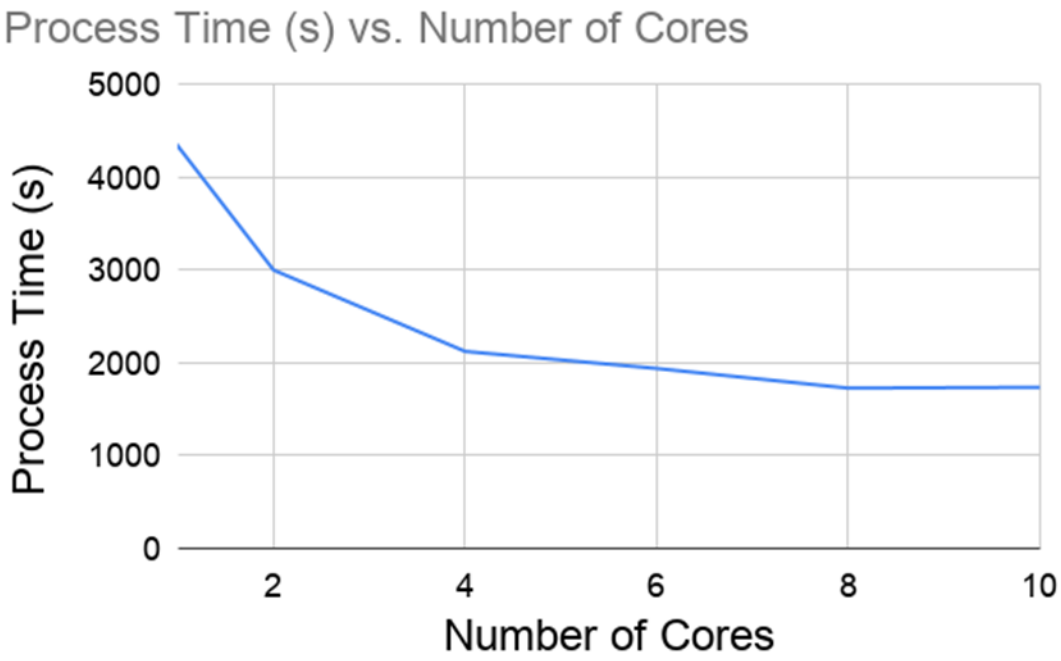

Fig. 2. 2 Impact of OpenMP parallelization on model performance.

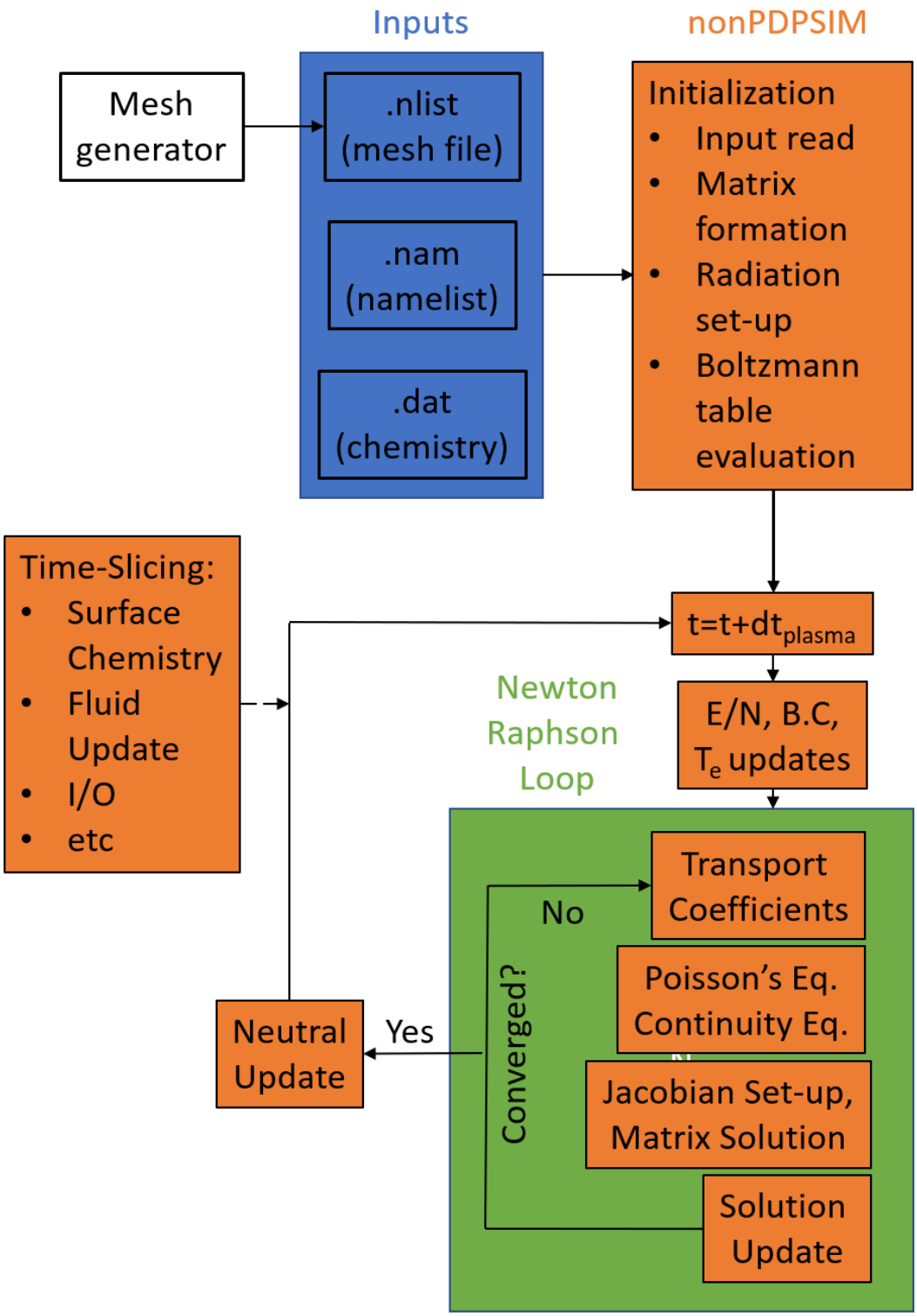

Fig. 2. 3 Flow-chart of *nonPDPSIM*.

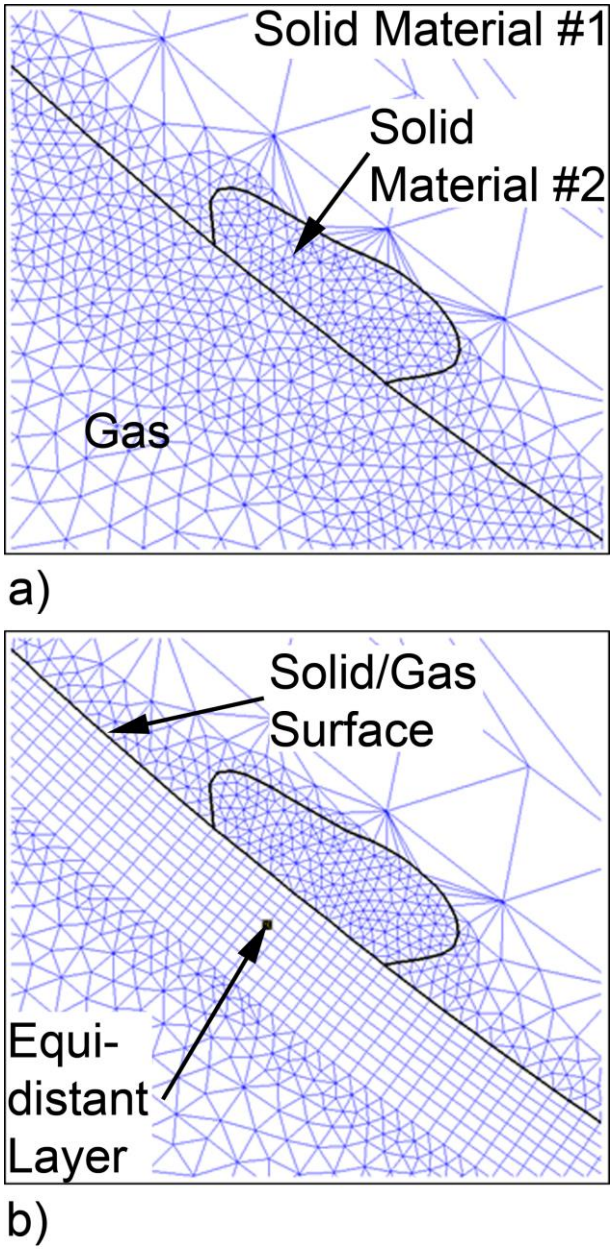

Fig. 2. 4 Examples of unstructured (top) and hybrid (bottom) meshes in the proximity of a solid surface. Hybrid mesh enables creation of equidistant mesh nodes.

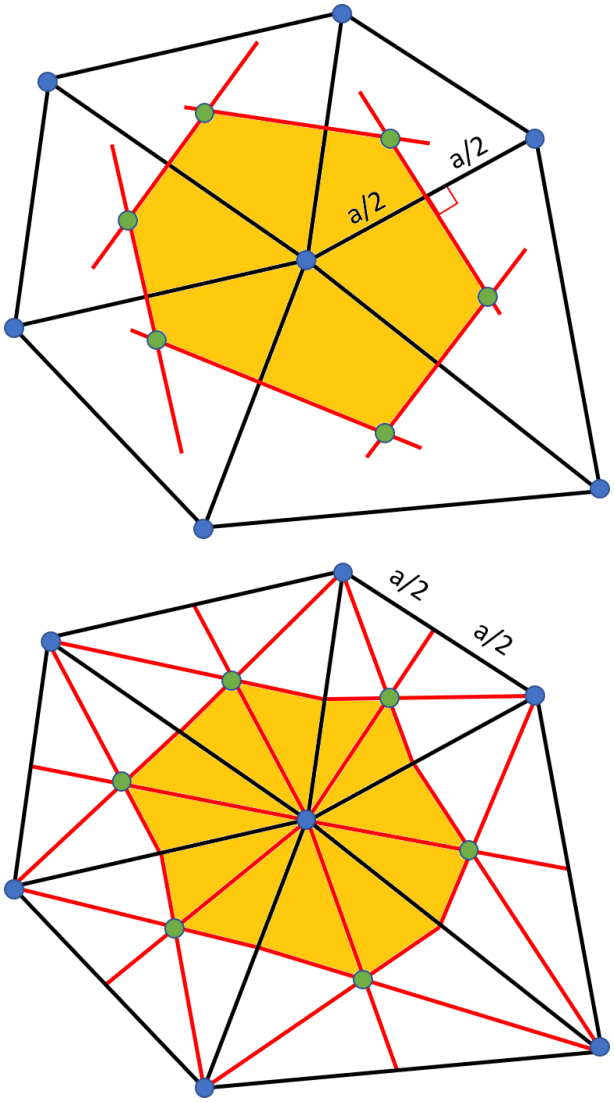

Fig. 2. 5 Calculation of control cell via perpendicular bisector method (top) and triangle centroid method (bottom). On top: Control cell (yellow) calculated between mesh nodes (blue). Perpendicular bisectors (red) are found for each chord (black). The intersections between the bisectors (green) then designate corners of the computational control volume. On bottom: bisector connectors (red) of each triangle cell chord (black) intersect at the centroid of the triangle (green). The interconnections between the centroids (green) form a control cell (yellow).

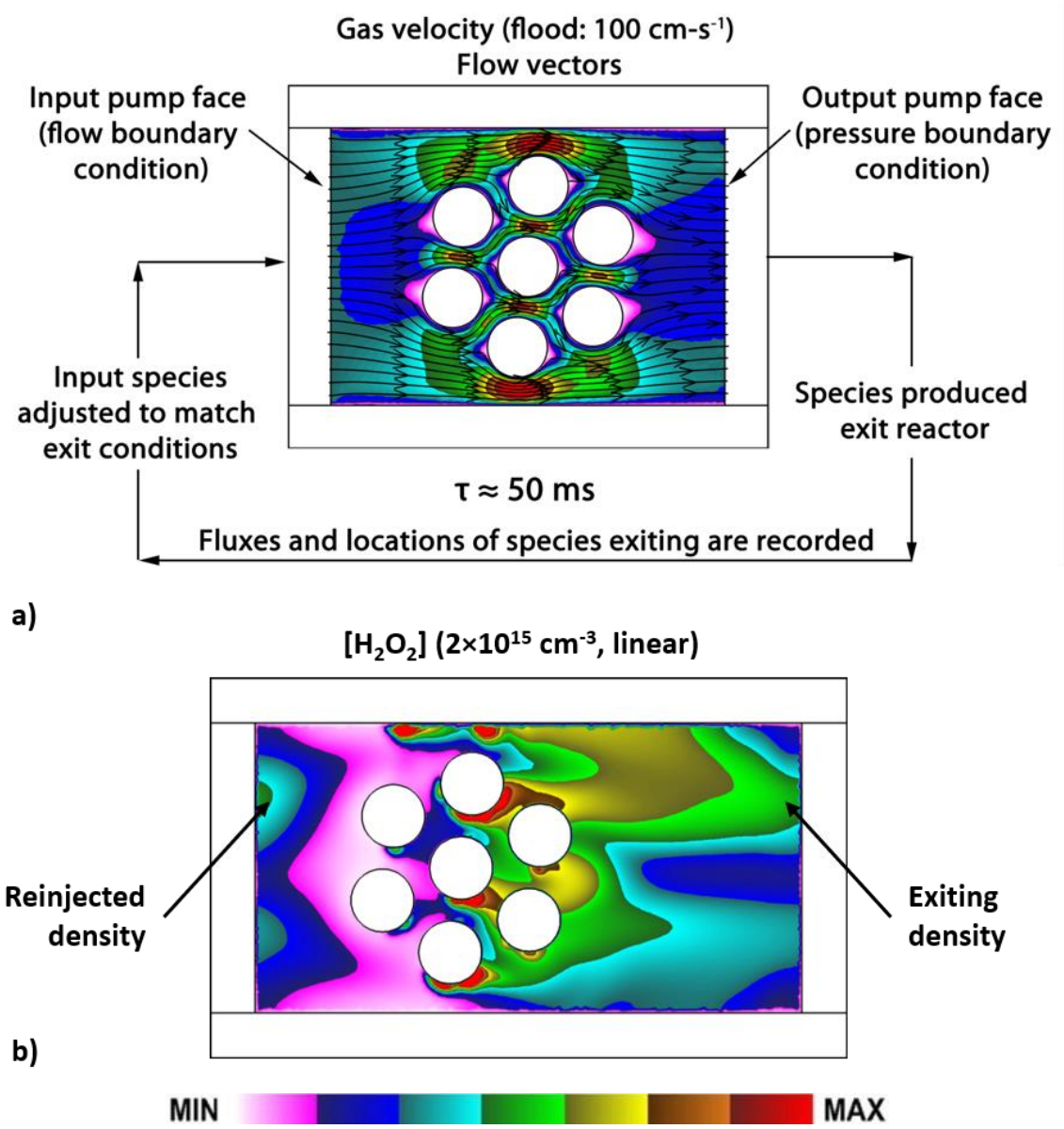

Fig. 2. 6 a) flow chart of fluid periodic boundary condition and b) example of re-injection of H_2O_2 densities.

2.10 References

[1] S. A. Norberg, E. Johnsen and M. J. Kushner, Plasma Sources Sci. Technol. **24,** 035026 (2015).

[2] J. Kruszelnicki, A. M. Lietz and M. J. Kushner, J. Phys. D Appl. Phys. **52,** 35 (2019).

[3] Allinea Software Ltd., (2017).

[4] Pointwise Inc., (2021).

[5] S. Yachi, Y. Kitamura, K. Kitamori and H. Tagashira, J. Phys. D. Appl. Phys. **21,** 914 (1988).

[6] G. J. M. Hagelaar and L. C. Pitchford, Plasma Sources Sci. Technol. **14,** 722 (2005).

[7] D. L. Scharfetter and H. K. Gummel, IEEE Trans. Plasma Sci. **16,** 64 (1969).

[8] R. G. Forbes, J. Vac. Sci. Technol. B **26,** 2 (2008).

[9] D. L. Scharfetter and H. K. Gummel, IEEE Trans. Electron Devices **16,** 64 (1969).

[10] 'SPARSKIT: A basic tool-kit for sparse matrix computations' Saad Y, (2005).

[11] J. O. Hirschfelder, C. F. Curtiss and R. B. Bird, *Molecular Theory of Gases and Liquids*, Wiley (1954).

[12] R. E. Skyner, J. L. McDonagh, C. R. Groom, T. Van Mourik and J. B. O. Mitchell, Phys. Chem. Chem. Phys. **17,** 6174 (2015).

[13] J. A. Manion, R. E. Huie, R. D. Levin, D. R. B. Jr., V. L. Orkin, W. Tsang, W. S. McGivern, J. W. Hudgens, V. D. Knyazev, D. B. Atkinson, E. Chai, A. M. Tereza, C.-Y. Lin, T. C. Allison, W. G. Mallard, F. Westley, J. T. Herron, R. F. Hampson and D. H. Frizzell, National Institute of Standards and Technology, Gaithersburg, Maryland (2015).

[14] R. Sander, Atmos. Chem. Phys. **15,** 4399 (2015).

Chapter 3 Reactivity Transfer to Gases: Packed Bed Reactors[1]

Plasma-based pollutant remediation and value-added gas production have recently gained increased attention as possible alternatives to currently-deployed chemical reactor systems. Electrical discharges in packed bed reactors (PBRs) are of interest due to their ability to synergistically combine catalytic and plasma chemical processes. In principle, these systems could be tuned to produce specific products based on their application by combinations of power format, materials, geometries, and working gases. Negative voltage, atmospheric-pressure plasma discharges sustained in humid air in a PBR-like geometry are experimentally characterized using ICCD (Intensified Charge-Coupled Device) imaging and simulated in 2-dimensions to provide insights to possible routes to this tunability. Positive discharges were also examined but are not discussed here. Surface ionization waves (SIWs) and positive restrikes through the lattice of dielectric rods are shown to be the principal means of producing reactive species. The number and intensity of SIWs and restrikes are sensitive functions of the alignment of the lattice of dielectric beads (or rods in 2-d) with respect to the applied electric field. Decreased spacing between dielectric elements leads to increased electric field enhancement in the gas and, therefore, locally higher plasma densities, but does not necessarily impact the types of discharges that occur through the lattice.

[1] The results discussed and a portion of the text in this chapter have been previously published in J. Kruszelnicki, K. W. Engeling, J. E Foster and M. J. Kushner, "Propagation of negative electrical discharges through 2-dimensional packed bed reactors", J. Phys. D.: Appl. Phys. **50,** 025203 (2017); K. W. Engeling, J. Kruszelnicki, J. E Foster and M. J. Kushner, "Time-resolved evolution of micro-discharges, surface ionization waves and plasma propagation in a two-dimensional packed bed reactor", Plasma Sources Sci. Technol. **27** 085002 (2018); and Z. Mujahid, J. Kruszelnicki, A. Hala and M. J. Kushner, "Formation of surface ionization waves in a plasma enhanced packed bed reactor for catalysis applications", Chemical Engineering Journal, **382** 123038 (2020).

3.1 Introduction

Dielectric barrier discharges (DBDs) in packed bed reactors (PBRs) at atmospheric pressures are of interest for the removal of toxic gases, CO_2 reprocessing, and gas conversion [1–6]. A PBR typically consists of dielectric material (usually spherical beads or pellets) distributed between two electrodes. Depending on the orientation of the applied electric field and spatial distribution of the beads, the electric field in the gas phase between the beads can be enhanced. This enhancement, in turn, leads to higher rates of ionization and greater production of reactive species [7]. The degree of electric field enhancement, in turn, depends on the shape of the dielectric beads, their alignment with respect to the applied electric field, and their dielectric constant, ε.

The manner in which an electric discharge avalanches through a PBR is still poorly understood. Generally, the breakdown is governed by a surface-modified Paschen's law [8]. However, subtleties pertaining to tuning plasma properties depend on many other variables. These variables include the material properties of the beads (secondary electron emission coefficient, microscopic electric field enhancement, surface charging, and dielectric constant); gas properties (electron transport coefficients, temperature, thermal conductivity, and UV opacity); and the physical arrangement of the beads (alignment with respect to the applied electric field, shape, and spacing between beads). Understanding the relationship among these variables is critical to maximizing the selectivity and energy efficiency of processing gases in a PBR.

This section discusses the results from a computational investigation of the propagation of negative ionization waves (IWs) through a 2-d PBR with validation by a companion experiment. The evolution of discharges through the lattice of dielectric rods of the PBR, including types of

discharges, plasma properties, and production of reactant species, are described. The primary modes of discharge are positive streamers (restrikes), filamentary microdischarges (FMs), and surface ionization waves (SIWs). Positive restrikes form following breakdown in regions of high electric fields. In cases where restrikes are confined between two dielectric rods, the discharges develop into standing filamentary microdischarges. FMs more easily form in geometries where the spacing between the rods is small. Surface ionization waves form following the surface charging of the rods by the FMs. SIWs are the most intense types of discharges and produce the highest electron densities. They generally form in regions where the applied electric field has components tangential to the surface of the dielectric rods. Production of radical species is primarily a result of restrikes and surface discharges. These results indicate that production of reactants in PBRs is not a continuous process, but rather results from the accumulation of individual, transient events.

In the following sections, results from two studies will be presented: a 7-rod packed bed reactor and a "patterned" PBR with 12 domes. Both studies include experimental validation. The experiments and conditions for this investigation are discussed in Secs. 3.2.1 and 3.2.2, respectively. The model used is described in Chapter 2. The modeling results along with experimental validation for the hexagonal-lattice Packed Bed Reactor (PBR) are discussed in Sec. 3.3. In Sec. 3.4, plasma properties in patterned Dielectric Barrier Discharge (DBD) reactor are discussed. Lastly, the conclusions are presented in Sec. 3.5.

3.2 Experimental Conditions

3.2.1 Hexagonal Lattice PBR

A schematic of the first experimental apparatus is shown in 3.1. This system was set up by K. Engelling and J. E. Foster at the University of Michigan. The plasma is sustained between two quartz plates of 6.35 mm in thickness. One plate contains a recessed area to accommodate the dielectric disks and the electrodes. Seven dielectric disks of quartz (5 mm in diameter and 3 mm thick) and zirconia (6.2 mm in diameter and 3.5 mm thick) are sandwiched into this quartz plate assembly. The hexagonal array of dielectric material, whose span is 20 mm, is located between two metal electrodes configured in a pin-to-plane configuration. The pin electrode with a 2-mm diameter is molybdenum, and the planar electrode (25 mm wide x 4 mm depth) is copper. A short voltage pulse utilized for operation at 1 atm has a peak amplitude of 20 kV DC and a pulse-width of 120 ns. The spacing, thickness, and orientation of the dielectric disks are chosen so that the discharge propagates through, rather than over, the array of dielectric disks. In this manner, the discharge is limited to a single plane. The quartz disks have a dielectric constant of ε_r=3.8. For this study, the dielectric properties of the zirconia disks are characterized by the resonant post technique described elsewhere [15,16]. The measured dielectric constant for the zirconia disks is ε_r=26.6±0.24 at 6.2 GHz.

In this study, the working gas is humid air ($N_2/O_2/H_2O$ = 78/21/1) at atmospheric pressure and with an initial temperature of 300 K. The model included a subset of the reaction mechanism described by Dorai et al. [9]. For the ease of computation, the mechanism is reduced to include 33 species and 143 reactions. Radiation transport includes VUV photons produced by highly excited states of N_2 [($N_2(b^1\Pi)$ and $N_2(b^1\Sigma)$] and the ionization of O_2. We use a line-of-sight approach and a Green's function method for radiation transport. VUV photons are consumed by

both ionizing and non-ionizing absorption. The non-ionizing absorption cross sections are 1×10^{-18} cm^2 for O_2 and N_2, and 3×10^{-17} cm^2 for H_2O. The ionization cross section for O_2 is 1×10^{-19} cm^2. In this study, focus is on the propagation of ionization waves through the dielectric lattice, which occurs on timescales of < 30 ns. Given these short timescales, advection is not included – transport for neutral species is only by diffusion.

The dielectric rods are embedded within the plasma with a specified conductivity and permittivity. As described below, the dielectric in this study is quartz with negligible conductivity and permittivity $\varepsilon/\varepsilon_0$=4.0. Charged particle fluxes intersecting with the surface of the rods are calculated assuming that all positive and negative ions are neutralized and return to the plasma as their neutral counterparts, and electrons are collected with a zero-secondary electron emission coefficient. This occurs instantaneously, and depending on the species, recombination reactions may also simultaneously occur. These conditions result in charging of the surface of the rod, which is then included in the calculation of electric potential, which extends into the interior of the rods. Since the rods have essentially zero conductivity, there is no conduction of surface charge into the interior of the rods. The thermal conduction for electrons to the surface of the rods uses a thermal conductivity, accounting for the diminished electron density in the sheath, which produces a small electron thermal conduction to the surface.

A static, unstructured, triangular mesh, is used to discretize the transport equations. The mesh includes 12746 nodes, 9787 of which belong to the plasma. Refinement of mesh cells vary from 0.14 cm in regions of the mesh where the plasma does not propagate to 30 μm near the surfaces of the dielectric rods, where the highest electron densities are observed. Reflective boundary conditions are implemented on the left and right sides of the computational domain. On the top and bottom sides, voltage is specified. The depth of the device – necessary for volumetric

calculations – is assumed to be 1 cm. The geometry can be seen in Fig. 3.2.

3.2.2 Patterned DBD Reactor

The second experimental set-up (created by Z. Mujahid and A. Hala at Jazan University) utilizes a patterned dielectric barrier reactor (p-DBDs) and helium gas. The p-DBD is contained in a 100-mm diameter, 10-mm high quartz ring (dielectric constant ε_r = 3.75 -3.8) with two tubes for the gas inlet and outlet. The quartz ring is covered on the top and bottom with two 1-mm thick glass plates. The bottom borosilicate glass plate includes twelve semi-spherical dome structures having ε_r =4.6, as shown in Fig. 3.3 a), set on a grounded electrode. The dome structures are also made of borosilicate glass and have radii of curvature of 15 mm, spacing of 24 mm, and height of 6 mm. The top glass plate is made of soda lime glass (ε_r = 7-7.6) coated with ≈ 220 nm of indium tin oxide (ITO), a transparent conductor, on its outside surface, which serves as the powered electrode while enabling optical access to the plasma. The packing material takes up 22.5% of the total volume.

A second p-DBD system, shown in Fig. 3.3 b), consists of a rectangular quartz (dielectric constant ε_r = 3.75 -3.8) 100-mm tube with 1.5-mm thick walls having internal dimensions of 25 mm width, 90 mm length, and a 10-mm gap where the plasma is generated. The rectangular quartz tube is terminated on both ends with quartz rectangular plugs containing fittings for gas source inlet and exhaust. The bottom plate (borosilicate glass, ε_r =4.6) includes three dome structures, having the same dimensions as in the first apparatus, set on a ground plane consisting of copper tape. The structures accounts for 19.6% of the total reactor volume. The top powered electrode is also copper tape. This geometry is sufficiently similar to first that the plasma discharge formation mechanisms are essentially the same, while also allowing for optical observations from

the side. Combining the results from both systems then enables quasi-3-dimensional perspectives of discharge formation within a p-DBD.

In this study, the initial background gas is pure helium at one atmosphere and 300 K. The reaction mechanism includes 11 species (e^-, He^+, He_2^+, He, and seven excited states of atomic and molecular helium), which result in 135 reactions. The computational geometry is shown in Fig. 3.4 and mirrors the experimental geometry. Three 24 mm wide domes extend 6 mm into a 10-mm gas gap between two dielectric plates. The radius of curvature of the domes is 15 mm, separated at the apex by 24 mm. All dielectric materials have a permittivity of $\varepsilon_r = 4.0$ (quartz). The powered electrode is located at the top, while the bottom electrode is grounded. The width of the reactor is 76 mm, with dielectric covering both of its sides. Given the 2-D geometry, the domes are functionally infinite rods perpendicular to the image in Fig. 3.3. These rods intrinsically have less electric field enhancement at their apexes than do the 3-D semi-spheres used in the experiments. For all calculations of volumetric energy deposition, we assume a reactor depth of 0.5 cm. The computational mesh includes 9241 nodes, with 6834 nodes located in the plasma region. The size of mesh cells varies between 0.2 mm near the surfaces of the dielectric to 1.8 mm at the center of the domes.

3.3 Plasma Propagation in Hexagonal PBR

3.3.1 Base Case: Hexagonal PBR

The base case geometry for the computations is shown in Fig. 3.2 a). The 2-D PBR consists of two parallel electrodes, 0.8 cm wide, separated by 1 cm. The top electrode has a small protrusion to enable the discharge to be consistently started from the same point. An initial seed of plasma (0.1 cm diameter, 10^{12} cm^{-3} peak density) is placed at the tip of the protrusion, but otherwise there

is no pre-ionization. A step voltage of -30 kV is applied to the top electrode, while the bottom electrode is grounded. Both voltages are held constant. Seven dielectric rods, 1.8 mm in diameter, are distributed in a symmetric hexagonal pattern with the closest separation of 700 μm in the base case. The dielectric constant of the rods is that of quartz – $\varepsilon/\varepsilon_0$=4.0 with a secondary electron emission coefficient for ion impact of 0.15. Charges incident onto the dielectric surfaces are deposited with unity probability and the surface becomes charged. Two variations to this geometry are also investigated – a layout with a smaller separation between the rods, 430 μm, and a configuration in which the lattice is rotated counterclockwise by 22.5 degrees relative to the direction of the applied field. These geometries are shown in Fig. 3.2(c) and 3.2(d), respectively.

When an external electric field is applied to a solid dielectric immersed in a gas, polarization of the material results in a reduction of the electric field inside the dielectric relative to the electric field in the gas. When the dielectric material is spherical or circular, its polarization produces an additional enhancement in the electric field in the gas at the poles of the solid (where the vector-applied electric field is parallel to the surface normal) [10]. Simultaneously, electric field minima form in the gas at the equator of the dielectric (where the vector applied electric field is perpendicular to the surface normal). In our geometries, the vertical poles of the top row of rods are approximately aligned with the applied electric field. This configuration then produces regions of electric field enhancement near the vertical poles of the rods and electric field minima near their equatorial planes, as shown in Figs. 3.2 (b-d). These enhancements and minima occur to some degree for all three investigated geometries.

The electron density and electron impact ionization rate for the base case are shown in Figs. 3.5 and 3.6. The images of ionization rates are provided with the goal of showing the causality of discharge development and, therefore, the times for images of the ionization rates may be different

than those for the electron densities. Upon application of voltage, separation of charge in the initial plasma seed occurs – ions are accelerated towards and neutralize on the cathode, while electrons accelerate downward. The electrons then undergo a Townsend-like avalanche process by electron impact ionization (rate $S_{EI} \approx 5\times10^{20}$ $cm^{-3}s^{-1}$) of the background gases, particularly O_2, resulting in a high production rate of positive oxygen ions ($[O_2^+] \approx 5\times10^{13}$ cm^{-3}). At ≈5 ns, the discharge begins to resemble a negative streamer, characterized by negative space-charge in the head of the streamer ($[-q] \approx 5\times10^{11}$ cm^{-3}) and a trailing quasi-neutral column. The streamer propagation is sustained by electron impact ionization at the head of the streamer ($S_{EI} \approx 5\times10^{20}$ $cm^{-3}s^{-1}$), as shown in Fig. 3.6 (a), which in turn is supported by a relatively high electron temperature ($T_e \approx 3.6$ eV). In the plasma column behind the head of the streamer, the electron temperature decreases to $T_e \approx$ 2.5 eV. As the streamer approaches the symmetrically arrayed lattice of dielectric rods (t = 6 ns), the electron density, $n_e \approx 6\times10^{11}$ cm^{-3}, is diverted towards the poles of the top two rods, shown in Fig. 3.5 (a). Electric field enhancement at the poles of the two rods produces regions of high ionization [Fig. 3.6 (b)], which produces momentary positive restrikes. However, charging of the top surface of the rods and reduction in the adjacent electric field reduces the rate of ionization to small values [Fig. 3.6 (c)] and leads to a reduction in electron density [Fig. 3.5 (b)] as attachment begins to dominate – similar to the operation of a DBD. By t = 11 ns, there is comparatively little net ionization at the top poles of the rods ($S_{EI} < 5\times10^{17}$ $cm^{-3}s^{-1}$). The plasma between the cathode and top row of rods then slowly decays. Meanwhile, the plasma charges the surface of the rods, producing tangential components of the electric field, important to later producing SIWs.

As a result of minima in the electric fields near the equator of the rods, the electric field between the top two rods is ≈25 kV cm^{-1} (or, in terms of electric field/gas number density, E/N = 100 Td, where 1 Td = 10^{-17} V-cm^2). This magnitude of electric field is below the breakdown

electric field of air (≈30 kV cm^{-1} or 130 Td for 1 atm dry air). Dissociative attachment reactions of O_2 into O and O^- (peak [O] ≈ 8×10^{13} cm^{-3}, peak [O^-] ≈ 1×10^{12} cm^{-3}) begin to dominate in the equatorial gap between the top two rods, and the electron density peaks at only $n_e \approx 8\times10^{10}$ cm^{-3} [Fig. 3.5 (b)]. At this time, charging of the top row of rods has already reduced the electric field and T_e in the gap between the cathode and top row of rods to below self-sustaining. The speed of the streamer propagation before reaching the top of the rods is ≈5×10^7 cm-s^{-1}; whereas, after reaching top rods and before reaching the central rod, the speed is ≈2.3×10^7 cm-s^{-1}. These speeds are comparable to those experimentally measured. For example, Briels at al. measured speeds of positive and negative streamers in air [11]. For an applied voltage of -30 kV in 4-cm separation gap, they report speeds of 5×10^7 cm-s^{-1}. Overall, for voltages varying between 10 kV and 100 kV, the streamer speeds are between 2×10^7 cm-s^{-1} and 4×10^8 cm-s^{-1}.

The conductive plasma in the upper region of the lattice redistributes the applied potential, resulting in a larger voltage drop across the lower section. The already intensified E/N near the top pole of the central rod reaches 300 Td. When the plasma drifts downward into the vicinity of the central rod, rapid avalanching occurs in the high E/N region at its pole, as shown in Fig. 3.6 (c). An anode-seeking restrike is then launched from the surface of the central rod, as shown in Fig. 3.5 (c). Here, we define a restrike as a streamer propagating in the direction opposite to that of the initiating negative ionization wave. The restrike has the characteristics of a positive streamer with large positive space-charge ([+q] ≈ 5×10^{12} cm^{-3}) at its head, followed by a quasi-neutral column. The electron temperature at the head of the streamer is ≈4.1 eV, decreasing to a 0.7 eV in the conductive, trailing column. The space charge separation and electric field enhancement in the head of the restrike produces an electron impact ionization rate of ≈ 5×10^{21} $cm^{-3}s^{-1}$, as is shown in Fig. 3.6 (c).

Simultaneously, regions of high electric field between the pairs of outer rods result in electron heating, as well as the increased electron impact ionization rates shown in Fig. 3.6 (d). The initial electrons in these regions are seeded by photoionization produced by photons emitted from the plasma near the central rod. The lack of initial seeding through photoionization is also the reason that avalanches between the bottom rods and the center rod do not occur – this region is shadowed from the photo-ionizing radiation from higher in the lattice by the rods above it.

Depending on the degree of electric field enhancement, partial or full positive restrikes then develop. These restrikes are indicated by a column-like discharge with a high electron density (1×10^{13} cm^{-3}) and high rate of ionization (1×10^{21} cm^{-3}s^{-1}) near the heads of the streamers, shown in Figs. 3.5 (d)(e) and 3.6 (d)(e). We define a full restrike (as opposed to partial restrike) as one that is able to bridge a gap between two solid surfaces. Whether a full restrike takes place depends on the presence of pre-ionization, gap distance, and the magnitude of the electric field at the time the restrike is launched. For example, the peak E/N between the outer rods in the center row and the top-most rods is ≈280 Td. Full restrikes do not occur at those locations, even though there is significant pre-ionization due to photoionization ($n_e \approx 1\times10^{9}$ cm^{-3}). At t = 21 ns, the E/N between the central and the bottom rods peaks at 370 Td (92.5 kV/cm). As a result, rapid avalanching and formation of full restrikes take place, as shown in Fig. 3.5 (d)(e) and Fig. 3.6 (d)(e). The pre-ionization at the time of breakdown reaches $n_e \approx 1\times10^{7}$ cm^{-3} in this region. These examples indicate that the minimum E/N required to generate full restrikes (and later microdischarges) falls between 280 and 370 Td for our geometry.

Once positive restrikes form between the bottom and center rods, electron impact ionization dominates [Fig. 3.6 (e)] over photoionization from other regions of the lattice. These local avalanches, sustained by electron impact ionization in the streamer head, have large, positive

space charge ([+q] ≈ 5.7×10^{12} cm^{-3}) and cross the inter-rod gap in < 1 ns, implying streamer speeds of at least 8×10^{7} cm-s^{-1}. Standing filamentary microdischarges (FMs) – shown in Fig. 3.6 (e) – then form between the rods. The structure of the FMs is typical of DBD microdischarges – a relatively narrow column of plasma (≈250 μm) between two dielectric materials, on the surfaces of which form wider "feet" of plasma. The initial head of the streamer has a width of approximately 300 μm, and the final width of the column of the FM is ≈190 μm.

Tu et al. reported formation of such FMs between beads in their $BaTiO_3$-filled PBR, where the separation between the beads exceeded 200 μm [12,13]. When the separation distance was decreased below 200 μm, they reported a transition to a surface discharge-like regime. Based on the results from this work, the transition could be due to the inability of the initiating positive streamers to fully develop in the small gap-size structures. The streamers do not fully develop because sufficient charge separation cannot be established when the column height limit is comparable to the width of the head of the streamer.

Qualitative validation of the predicted trends in development of discharges in PBRs comes from experimental observations of light emission. The time-integrated densities of the light-emitting species included in the model are compared to experimental measurements by fast-camera imaging in a similar geometry in Fig. 3.7. The latter was captured using an ICCD camera with a microscope lens and an observation gate width of 0.5 μs. The location of the image is between the central and the bottom-left rods. In both cases, the cathode is located towards the top of the images. The formation of a cathode seeking FM between the rods with similar structure and widths is indicated both in the simulated and experimental results. Lack of plasma near the bottom pole of the top rod is, in part, due to the direction of the applied electric field which points upwards, toward the cathode. Since the microdischarges between the rods result from positive restrikes, the

propagation of the plasma is directed upward, leaving the region near the bottom of the central rod relatively plasma-free.

Another validation is shown in Fig. 3.8 [14]. The top row of frames is experimental ICCD images of optical emission between zirconia disks with an exposure time of 5 ns. The exposures of the images are digitally enhanced to show the features of interest, so intensity cannot be directly compared frame-to-frame. The bottom row of frames is produced from the results of the model. The computed results are the densities of the main photo-emissive species in the model ([($N_2(b^1\Pi)$ and $N_2(b^1\Sigma)$]). The choice of frames is made to show correlating phenomena. Intense filamentary microdischarge structures initially form between disks 6 and 3, and disks 6 and 4, as shown in Figs. 3.8 a) and b) (experiment and model). The electrons incident onto disks 3 and 4 charge the surfaces of the dielectrics and SIWs begin forming in Figs. 3.8 c) and d). As the potential between the disks drops due surface charging, the intensity of the FMs decreases, and the propagating SIWs become the brightest regions in the images, as shown in Figs. 3.8 e) through 3.8 h). The surface ionization waves are cathode-seeking discharges – regardless of the polarity of the applied voltage, as demonstrated in our previous work [20]. This is because electrons impact the dielectric surfaces, leaving behind a region of positive space charge in the gas-phase. Through a process similar to that of the propagation of positive streamers, the positive SIWs then propagate down the potential gradient.

In addition to the FM, surface discharges also occur, as shown in the model and experimental results in Figs. 3.7 and 3.8. Ions produced in the positive polarity FMs are accelerated toward the surface of the central rod, positively charging its surface. Due to the orientation of the surface, this charge produces a component of the electric field parallel to the surface, which eventually leads to the development of an SIW. This process takes approximately

4 ns in the model. SIWs form on both the left- and right-bottom sides of the central rod, as shown in Fig. 3.5 (f) and 3.6 (f). The SIWs are indicated by ionization fronts on the two sides of the central rod. Enlarged images of the reduced electric field and electron temperature during the propagation of an SIW around the central rod are shown in Fig. 3.9. The space charge in the ionization front supports an E/N of ≈600 Td (150 kV/cm) producing $T_e \approx 9$ eV with a propagation speed of $\approx 3.5 \times 10^7$ cm-s^{-1}. These high values of E/N and T_e, result in surface-hugging electron and ion densities of $\approx 3 \times 10^{15}$ cm^{-3}. The volumes of these discharges are small – only protruding tens of microns from the surface of the dielectric and, thus, the density is difficult to see in Fig. 3.5.

Once the SIWs are initiated in the PBR, the predicted E/N, propagation speeds, and electron temperatures are similar to those found in literature. Having said that, SIW properties are sensitive to voltage, orientation of the electric field, and surface properties [15]. For example, Petrishchev et al. investigated the formation of SIWs on a quartz plate produced by high voltage, nanosecond pulses in nitrogen at low pressure, and measured propagation speeds of $\approx 5 \times 10^7$ cm-s^{-1} [16]. Goldberg et al. studied these phenomena on a planar dielectric plate in hydrogen and found average SIW speeds of $\approx 10^8$ cm-s^{-1} with a peak E/N of only 100 Td [17]. Starikovskiy investigated SIWs in air at atmospheric pressure, finding that, in a point-to-plane geometry, the discharge propagation speed is $\approx 10^9$ cm-s^{-1} while the E/N is 530 Td [18]. The SIWs produced along the surfaces of rods in PBRs resemble conventional and intentionally produced SIWs.

SIW propagation also coincides with increased production of reactive species – a result also indicated by Petrishchev et al. [16]. For example, the highest density of OH produced in the middle of the lattice after propagation of the positive restrike is $\approx 6 \times 10^{11}$ cm^{-3}. OH densities due to the SIWs routinely exceed 1×10^{13} cm^{-3}. SIW phenomena, therefore, likely play an important

role in plasma chemical PBR systems.

Overall, plasma discharges in 2-D PBRs can be classified into three modalities – positive restrikes, filamentary microdischarges, and surface ionization waves. Restrikes between dielectrics result in formation of microdischarges. Surface charging creates electric field components parallel to the dielectric's surface, and it leads to the formation of surface discharges. Production of reactive species primarily takes place near the surfaces, as a result of restrikes and SIWs.

3.3.2 Separation of the Rods

As the separation between the rods decreases, the regions between rods, where the electric field is enhanced by polarization of the rods, have more overlap. As a result, the electric field near the poles between rods increases, and the minima near the equators decrease. To evaluate the influence that the packing factor may have on discharge properties, base case simulations are repeated with the separation between the rods decreased to 430 μm from 700 μm. The geometry and the resultant applied reduced electric field are shown in Fig 3.2 (c). The time evolutions of the electron density and electron impact ionization rate during avalanche through the PBR with this more compact lattice are shown in Figs. 3.10 and 3.11. During the initial 6 ns, the discharge propagates in the same fashion as in the base case. Being driven by electron impact ionization [Fig. 3.11 (a)], the initial Townsend avalanche develops into a negative streamer and intersects with the top two rods [Fig. 3.10 (a)]. The electric field at the equator between the top two rods is lower than that in the base case, ≈55 Td as compared to ≈76 Td. This lowering of E/N decreases the electron temperatures in the gap and prevents significant electron impact ionization near the equator of the rods, as shown in Fig. 3.11 (b). As a result, electron collisions in this region are

dominated by attachment.

Similar to the base case, upon reaching the central rod, the discharge negatively charges its surface. In the base case, this charging results in the development of a single positive streamer propagating upwards between the top two rods. This positive restrike does not occur in the more compact lattice. With the decrease in distance between the rods in the compact lattice, the overlap of electric field enhancement from the top and central rods (near their poles) produces an E/N approaching 340 Td. This large E/N then drives development of two, smaller positive streamers that connect with the top two rods, as shown in Figs. 3.10 (c). The propagation of the streamers is facilitated by large values of electron impact ionization in the streamer head [Fig. 3.11 (c)]. The positive streamers then evolve into standing filamentary microdischarges [Fig. 3.10 (d)]. These results suggest that the threshold in E/N for the formation of microdischarges between the rods for these conditions lies between 280 Td (base case) and 340 Td (more compact lattice). These FMs have peak electron densities of $n_e \approx 1 \times 10^{14}$ cm^{-3}, with electron temperatures of a few tenths of eV in the conductive plasma behind the ionization fronts. The width of the FMs in the compact lattice, 150 μm, is smaller than those produced in the base case due to locally higher values of E/N. The time required for SIWs to form is approximately 10 ns.

The discharge continues propagating downward due to electron transport and sideways due to the photoionization that seeded electrons in regions of high E/N. Partial restrikes driven by electron impact ionization at the top of most of the rods eventually form non-self-sustained discharges, as shown in Figs. 3.10 (d) and 3.11 (d). At t = 21 ns [Figs. 3.10 (e) and 3.11 (e)], positive restrikes also develop between the central and the bottom-most rods. At the time of breakdown, the E/N in these regions reaches 420 Td – about 50 Td higher than in the base case. As a result, the electron densities in the FMs reach 4×10^{13} cm^{-3} – almost two times larger than

those in the base case. T_e does not significantly change. FMs then form as a result of the initiating restrikes. Their characteristics are similar to those in the base case. Again, akin to the base case, SIWs then form due to FMs charging the surface of the dielectric. The surface ionization waves are difficult to discern in Fig. 3.10 (f), but are indicated by the ionization fronts shown in Fig. 3.11 (f). Ionization does occur between each row of dielectric rods [Fig. 3.11 (f)], however, this ionization does not develop into either restrikes or FMs.

Overall, decreasing the separation between the rods changes neither the plasma modalities, nor the breakdown mechanisms. However, the increased overlap of regions having electric field enhancement due to polarization of the rods promotes the formation of microdischarges, while delaying the onset of SIWs. It appears that a threshold E/N of near 300 Td is required for the establishment of FMs between the rods for these conditions.

3.3.3 Rotation of the Lattice

Electric field enhancement is maximum at the poles of the rods when the applied electric field is perpendicular to the surface of the rod. The orientation of the applied electric field with respect to the lattice may, therefore, impact the types of discharges that are produced. To investigate these geometrical effects, the lattice from the base case is rotated about the central rod by 22.5 degrees. This angle is chosen because, in our geometry, a symmetric alignment with the electric field occurs with every 15 degrees of rotation – 22.5 degrees is halfway between two such symmetric alignments. The geometry, along with the resulting initial reduced electric field, is shown in Fig. 3.2 (d). Even for this moderate rotation, there is a significant change in the orientation magnitude of the electric fields in the lattice.

The evolutions of the electron density and electron impact ionization rate are shown in

Figs. 3.12 and 3.13. In the rotated lattice, the initiating streamer first strikes the top-right rod, which is physically closer but, more importantly, has a surface normal more closely aligned with the vacuum electric field. This better alignment results in an intense avalanche at the top surface of the rod shown in Fig. 3.12 (a). The discharge is sustained by electron impact ionization, which peaks at $\approx 1\times10^{21}$ $cm^{-3}s^{-1}$ near the surface of the rod [Fig. 3.13 (a)]. Secondary electron emission and photoionization rates are both approximately two orders of magnitude lower than those of electron impact ionization. The resulting conductive plasma column, with its low voltage drop, then intensifies the electric field in the vicinity of the top-left rod. Heated electrons near the pole then lead to breakdown, and the discharge subsequently propagates in that direction, as shown in Figs. 3.12 (b) and 13 (b).

In the base case, the top two rods are horizontally aligned, which results in alignment of the minima of electric field at their equators. This symmetry results in the vertical component of the electric field between the top two rods at the equator, $E_y \approx 25$ kV, greatly exceeding the horizontal component, $E_x \approx 100$ V cm^{-1}. In the rotated lattice, the electric field located horizontally between the top two rods is minimized, but to a lesser degree than in the base case due the equators of the two rods not exactly aligning. There is now a significant horizontal component to the electric field ($E_y \approx 29$ kV V cm^{-1}, $E_x \approx 19$ kV cm^{-1}). This electric field results in the plasma propagating towards the right via electron impact ionization [Fig. 3.13 (c)] between the central and top-right rods, as shown in Fig. 3.12 (c). The highest ionization rate occurs near the vertical pole of the central rod. Charge separation occurs in the plasma in this region, and a positive restrike forms between the central and the top-right rods [Fig. 3.12 (c)]. The positive restrike is sustained by pre-ionization in its path and high electron impact ionization rates near the streamer head, peaking at $\approx 1\times10^{21}$ $cm^{-3}s^{-1}$ [Fig. 3.12 (d)].

Due to the combined effects of surface charging and the orientation of the lattice with respect to the applied electric field, an electric field parallel to the surface of the top-right rod is generated (E ≈ 57 kV/cm, E/N ≈ 240 Td). A surface ionization wave quickly forms, as indicated by the ionization front on the surface of the top-most rod [Fig. 3.13 (e)]. The electron density resulting from the SIW is shown in Figs. 3.12 (c-f). The SIW has a high E/N (≈660 Td) in the ionization front, which then leads to T_e ≈7.6 eV and n_e ≈5×10^{15} as the SIW propagates at ≈7×10^7 cm-s^{-1} around the contour of the rod. The SIW is cathode-directed, with a positive space charge at the ionization front ([+q] ≈ 4×10^{13} cm^{-3}). The SIW ionization front gains in intensity as it propagates around the rod, reaching its peak electron density at t = 22 before initiating a positive streamer directed towards the cathode at t = 25 ns.

As the plasma spreads around the central rod, the gaps between the center and bottom two rods are no longer in shadow from the photons emitted from plasma higher in the lattice. These gaps are then illuminated by the ionizing radiation producing a photoionization rate of $S_{Ph} \approx 5 \times 10^{14}$ $cm^{-3}s^{-1}$. An avalanche is initiated in the gaps and, once the electron density reaches a threshold value of approximately $n_e \approx 1 \times 10^7$ cm^{-3}, electron impact ionization surpasses photoionization as the dominant ionization mechanism and a restrike develops. This threshold value of electron density to surpass the seeding photoionization is nearly the same in all geometries investigated in this work.

This sequence of seeding electrons in a region of high electric field, development of a positive streamer, and FM, which then develops into an SIW, is then repeated between the lowest rod and the center rod. This process is shown in Figs. 3.11 (e)(f) and 3.12 (e)(f). Whenever a conductive plasma column is produced, the electric field is then shorted out or reduced at that height to some extent across the entire device. This reduction in electric fields extends to portions

of the lattice at the same height in which there is not already plasma. Due to the combined effects of the initial electric field enhancement produced by the orientation of the lattice, shadowing of ionizing radiation from regions of high E/N by intervening rods, and shorting of the electric field by plasma columns elsewhere in the lattice, plasma does not form in portions of the lattice. For this particular orientation of the lattice, breakdown does not occur in the gaps between the three left-most rods.

To summarize, regardless of the orientation of the dielectric rods with respect to the electric field, three main types of discharges occur in the PBR: positive restrikes, filamentary microdischarges, and surface ionization waves. Which type of discharge is dominant, however, strongly depends on the topology of the dielectric rods. Several factors – including local electric field strength, distance between rods, alignment of the electric field with respect to the surface of the dielectric, and pre-ionization – play important roles in determining the type of discharges that dominate. Partial restrikes occur in regions of electric field enhancement. However, a threshold E/N of approximately 300 Td is required for the formation of full restrikes and microdischarges for our conditions. If the electric field has a component that is parallel to the surface of the dielectric, where a filamentary microdischarge has occurred, surface ionization waves may form. The SIWs then propagate along the curvature of the dielectric, enabled by electric field enhancement at the ionization front. These processes allow for an increased production of reactive species near the dielectric surfaces.

These results are sensitive to many parameters, including the secondary electron emission coefficient and the dielectric constant of the rods. Photoionization also plays an important role in discharge propagation through the lattice, as it seeds initial charge in regions of high electric field,

regions that are difficult to access for electrons from the main streamer, and so can initiate avalanches at remote locations. These dependencies will be discussed in a future publication.

3.3.4 Consequences on Production of Reactive Species

Four types of discharges occur in the investigated negative discharge PBRs– initial subcritical or Townsend-like discharges that may develop into negative streamers, positive streamer restrikes, filamentary microdischarges, and surface ionization waves. The topography and layout of the dielectric rods determine the electric field enhancement (magnitude and direction). The electric field enhancement, in turn, controls the types of discharges that are produced. While FMs and subcritical discharges and negative streamers are stable and occupy relatively large volumes, they do not necessarily dominantly contribute to plasma-chemical processes. Their lesser role is due to their lower electron densities and electron temperatures. The higher electron densities and temperatures in restrikes and SIWs often produce significantly larger inventories of reactive species, in spite of these discharges' smaller volumes and lifespans.

The contributions of the different types of discharge to the production of reactant species during their initial propagation through the lattice are summarized in Fig. 3.14. The total inventories of reactive species in the three geometries discussed above are shown as a function of time. (The total inventory of species is the volume integral of the density of that species.) Discontinuous increases in inventories occur in all three configurations of the lattice, which can be attributed to either restrikes or SIWs. For example, a spike in reactant inventory occurs in the base case – shown in Fig. 3.14 (a) – which corresponds to the formation and propagation of the restrikes between bottom-most and central rod at approximately 21 ns. Inventories for the lattice having a smaller separation between the rods are shown in Fig. 3.14 (b). The rapid increases in

electron density and reactive species inventories at 14.5 ns and 20 ns coincide with development of positive streamers between the central and outer rods. Following these events, the densities continue to steadily increase at a lower rate.

The lack of symmetry in the rotated lattice results in the formation of SIWs. The time evolution of the total inventory of reactive species for the rotated lattice, shown in Fig. 3.14 (c), has discontinuities at approximately 14 ns and 22 ns, which coincides with the developments of restrikes. However, unlike inventories for the symmetric lattices, the increases in densities between the restrikes are significant. These continuous increases result from SIWs, which more slowly propagate around the contour of the rods. In this particular case, the SIW making the largest contribution to the inventories propagates on the surface of the top-most rod.

The neutral reactant species experiencing the greatest increases during the discontinuous *spikes* in production are those species whose precursor reactions directly depend on the density of high energy electrons. Those species here are N, O, and OH. For example, N atom production dominantly results from the dissociative excitation of N_2, which has a threshold energy of 12 eV. Similarly, the threshold energy for production of O atoms is as low as 5 eV for dissociative attachment. Both species experience discontinuous increases in inventories, but the production of O atoms is less sensitive to the increase in T_e produced by the restrikes or SIWs due to lower threshold energy. The production of OH also occurs through a single electron impact reaction with H_2O. The production of species such as O_3 and NO_x, requires three-body reactions or a sequence of two-body reactions, which take place on microsecond time-scales or longer. For this reason, increases in densities of N, O, and OH shown in Figs. 3.14 (a)(b) are more impulsive and more closely correlated with restrikes or SIWs on nanosecond timescales than with increases of NO_x or O_3. However, since NO_x and O_3, alike, depend on the presence of O and N, increases in

the production of all NO_x and O_3 can ultimately be traced to restrikes in these geometries.

The densities of N and O atoms between the bottom-right and central rods of the base case are shown in Fig. 3.14 as the discharge transitions from restrike and microdischarge to surface ionization wave. These species are generated as direct electron impact dissociation products, and so their production is a qualitative measure of the electron density and rate of collisions for high threshold processes. The sequence shown in Fig. 3.14 is responsible for the spike in inventory indicated in Fig. 3.14 a) after 20 ns. At t = 21.5 ns, the densities of both species begin to rise as the restrikes starts forming, producing a column of N and O atoms between the two rods. The densities peak at 2×10^{13} cm^{-3} for N atoms and 3×10^{13} cm^{-3} for O atoms. Between t = 22.5 and t = 27.5 ns, a surface ionization wave sweeps around the surface of the rod, producing densities of [N] = 5×10^{14} cm^{-3} and [O] = 6×10^{16} cm^{-3}. During this time, the densities in the column of the microdischarge do not significantly change, indicating that FMs play only a small role in the production of reactants. Rather, the large spikes in inventory shown in Fig. 3.14 result from the positive restrike that seeded their formation. Even though the peak densities produced by the SIW are higher than those produced by the restrike, the total inventory atoms produced in the SIW is smaller due to the small total volume of the SIW. However, these trends are species-specific. For example, at t = 22.5 ns, N atoms are produced at a greater rate relative to their previous inventory than are O atoms. This trend results from the electron-impact dissociation of nitrogen having a higher threshold energy (12 eV) than oxygen (5 eV). As a result, production of N atoms is more sensitive to the formation of discharges with energetic electrons – such as restrikes and SIWs.

These results indicate that the production of reactant species in negative plasma PBRs may not be due to enduring, stable discharges such as standing FMs or to the initial subcritical discharges or negative streamers. Rather, the production of reactant species is likely due to

transient, short-term events producing transient bursts of energetic electrons. Since geometry can impact which types of discharges are favored, the orientation and packing of the dielectrics in PBRs can have a significant effect on the magnitude and reproducibility of reactant production.

3.3.5 Variations in Pressures

Discharge formation in the PBRs at 1 atm is typically highly localized, propagating through the medium essentially as a sequence of ionization waves within gaps (FM) or along surfaces (SIW). The geometry used for the simulations is a good-faith reproduction of the experiment and is shown in Fig. 3.2. The numerical mesh uses 12746 nodes, with a resolution varying from 0.14 cm to 30 μm. Seven dielectric disks with diameters of 1.8 mm and separation distance of 700 μm are placed between the electrodes in a symmetric pattern. The geometry is given a depth of 0.5 cm to allow for volumetric calculations. The gas is humid air ($N_2/O_2/H_2O$ = 78/21/1) at the initial temperature of 300 K. Pressures of 760, 200, 100, and 50 Torr are simulated with potential applied to the top electrode, while the bottom electrode is grounded. The applied voltages are +40 kV for the 760 Torr cases, and +24 kV for the low-pressures. These values are double of the experimental voltages to account for the 3-dimensional effects of electric field enhancement at sharp edges of electrodes not captured in the 2-dimensional model. The gas is uniformly pre-ionized to an electron density of 1×10^6 cm^3 (balanced by O_2^+ and N_2^+) at 760 Torr. The magnitude of the pre-ionization is then scaled down for the low-pressure cases to maintain a constant pre-ionization fraction. A plasma seed with the diameter of 0.05 cm and peak density of 10^{12} cm^{-3} is also placed at the tip of the top electrode to provide a consistent starting location of the positive streamers.

The base case is a discharge at atmospheric pressure with dielectric disks having the relative permittivity of quartz ($\varepsilon_r = \varepsilon/\varepsilon_0 = 4.0$). The resulting discharge evolution is shown in Fig.

3.15. Upon the application of the potential to the top electrode, the plasma seed avalanches. The discharge initiated at the tip propagates similarly to a positive streamer, with its propagation depending on photoionization seeding electrons in front of the streamer head. The electrons are then accelerated towards the positive space charge in the head of the streamer, leaving behind positive ions which then become the new streamer head. The electron density in the initial streamer (Fig. 3.15 a)) peaks at $\approx 6 \times 10^{14}$ cm^{-3}, while the photoionization source term near the head of the streamer has a value of 1.2×10^{16} cm^{-3}-s^{-1}. At this time, the streamer continues to propagate downwards towards the ground.

Owing to its high conductivity, as the plasma expands through the assembly, the size of the spatial region over which the applied voltage drops decreases with time. This results in an increase in the peak reduced electric field (E/N, or the electric field per particle) between the disks. The E/N between the bottom-most disks and the grounded electrode then increases from ≈ 350 Td to ≈500 Td in Fig. 3.15 b). In the gap between disks (disks 1 and 5; 7 and 2), there is an increase from ≈290 Td to ≈470 Td. These electric fields are strong enough to allow for the formation of discharges in between the disks themselves (Figs. 3.15 b)-d)). A similar process then occurs between the middle and bottom row of disks (Figs. 3.15 c)-d)). The discharges initially take the form of positive streamers propagating through the gaps. Once the gaps are bridged, stable microdischarges form. This mechanism of plasma formation is the same as that seen in negative discharges described in our previous work [19]. In both cases, the electric field enhancement due to the presence of the dielectric disks produces the formation of positive, cathode-directed streamers (or restrikes), which are the seed for the formation of microdischarges.

The electron densities in the microdischarges are maximum near the surfaces, and they have peak values approaching $\approx 6 \times 10^{15}$ cm^{-3}. The discharge column of the microdischarges is

relatively neutral, with space-charge values of $\approx +3.5 \times 10^{-9}$ C-cm^{-3}. Simultaneously, the plasma continues to charge the surfaces of the disks, eventually reaching value of $\approx +4 \times 10^{-6}$ C-cm^{-2}. This charge deposition causes the formation of electric field vectors parallel to the surfaces of the dielectric, which then results in the formation of the surface ionization waves. For example, the electron density, electron temperature, surface charge, and electric field are shown in Fig. 3.16 on the surface of disk 1. The magnitude of the electric field is shown by the contours, while the arrows show the direction of the electric field. As the surface charges and a surface-parallel electric field vectors form, electrons accelerate along the dielectric. The surface charge shields the potential at the surface of the dielectric, while the volume charge in the gas-phase produces a peak in the electric field of 200 kV-cm^{-1} or E/N = 1,000 Td. This local maximum results in electron densities of up to 4×10^{16} cm^{-3}. At the head of the SIW propagating in both directions, electric fields in excess of 850 Td produce a local maximum electron temperature of $T_e \approx 9.0$ eV.

The electron density in the 2-D-PBR for the permittivity of the disks of $\varepsilon/\varepsilon_0=27.0$ corresponding to zirconia is shown in Fig. 3.17. The asymmetry in the electron density is due to the high sensitivity of the model to small differences in the distribution of mesh nodes. Since the mesh between individual disks is not exactly alike, a small degree of asymmetry is expected. Similar to the experimental results, the computed trends for zirconia are similar to those for quartz. The initial streamer starts at the tip of the electrode and connects with the top-most dielectric disks. Breakdown between the dielectric disks then follows, resulting in the formation of FM. The time required for breakdown between all disks decreases from ≈8 ns for quartz disks to ≈ 6 ns due to the increased field enhancement provided by zirconia. The plasma between the bottom-most disks and the grounded electrode forms at an earlier time than does quartz. This behavior mirrors the

experimental results, and it is due to the additional field enhancement resulting from the higher dielectric constant.

The initial (t=0 s) E/N in the regions of field enhancement between disks increases from ≈290 Td to ≈350 Td with the higher dielectric constant, which produces nearly simultaneous breakdown and formation of FM throughout the lattice. The propagation of the initial ionization wave is therefore obstructed, which may explain the change in the mode of propagation experimentally observed. The experimental imaging shows that, with quartz disks, a sequential breakdown progresses from the anode to the ground (Fig. 3.18). When the packing material is changed to zirconia (Fig. 3.19), a more stochastic behavior takes place, with plasma forming randomly between disks.

The higher electric field between the individual disks with zirconia leads to the formation of higher-density FM. For example, the electron density in the center of the plasma column between disks 6 and 7 increases from $n_e \approx 3.9\times10^{14}$ cm^{-3} with quartz disks to $n_e \approx 2.2\times10^{15}$ cm^{-3} with zirconia disks. With the capacitance of disk being directly proportional to permittivity, a larger amount of charge can be stored on the surfaces of the zirconia disks before the SIWs, which then occurs at a later time, as compared to quartz, allowing for a longer time for the FM to develop. For example, with quartz disks, the surface of disk 7 charged to 1.6×10^{-5} C-cm^{-2} before a SIW begins propagating. This value increases to 2.9×10^{-5} C-cm^{-2} with zirconia disks. With the capacitance of the quartz disks smaller than that of zirconia, the time required to fully charge the quartz surfaces is shorter, which then enables the SIWs to propagate at a higher speed, in addition to starting at an earlier time. Since the experimental imaging integrates emission (even over the 5-ns observation window), the surface discharges and then appears less intense with quartz disks.

3.3.6 Impact of Packing Material: Quartz and Zirconia

Discharges through air at pressures of 50 Torr, 100 Torr, and 200 Torr are simulated for quartz and zirconia disks. To approximate the ICCD imaging, two decades of the densities of $N_2(b^1\Pi)$, the primary emitter of low-energy photons in the simulation, are shown in Fig. 3.20 for each pressure. The times for frames are chosen to show the approximate moment when breakdown occurs between all dielectric disks. The simulated emission indicates that a mode transition occurs from emission dominated by distinct FM at high pressures to emission dominated by volumetric and surface discharges at low pressures. In both the experiment and simulations, this transition occurs at approximately 200 Torr. With low dielectric constant – and, particularly, at lower pressures – the microdischarges do not necessarily follow the vector electric field having the largest intensity. For example, with zirconia disks at 200 Torr (bottom frame in Fig. 3.20 b)), the emission from the microdischarges is nearly normal to the surface of the disks, where the electric field enhancement is largest. With quartz disks at 50 Torr (top frame in Fig. 3.20 a)), optical emission is diffuse and volumetric, or produced by SIWs.

At low pressures and low dielectric constants, optical emission is eventually observed in regions of relatively low field-enhancement – such as the void between disks 1, 7, and 6. As the pressure decreases and the mean free path of ionizing radiation increases, seed electrons are produced in regions of low electric field enhancement. Since the radiation transport is isotropic, intense SIWs can produce seed electrons behind the ionization front, as well as ahead of the ionization front, thereby providing an external source of ionization in the low electric field regions. The discharges then appear more diffuse. These longer mean free paths for both radiation and charge transport result in the thickness of SIWs increasing with decreasing pressure, as shown in Fig. 3.20.

Although the optical emission undergoes a mode transition, closer examination indicates that the discharges develop in the same way, regardless of pressure. For example, in Fig. 3.21, the electron density and electron impact ionization source term are shown for three times during a discharge between zirconia disks at 50 Torr. As the voltage is applied, plasma is first produced in the electric field enhanced regions between the disks – just as is the case at atmospheric pressure. However, due to the high E/N throughout the lattice and long mean free paths for electrons and ionizing photons, the ionization is not restricted to only between the gaps. Planar-like ionization waves propagate downwards throughout the lattice, similar to the initial streamers that form FM at higher pressures, but less localized. The modeling results predict that the diffuse microdischarges above the surfaces of the dielectrics have electron densities of 1.1×10^{13} cm^{-3} and similar spatial distributions as the masked experimental images shown in Fig. 3.22. The experimental observation is that the surface discharges are far more intense at 50 Torr (see Fig. 3.22), which is corroborated by the large density of excited states shown in Fig. 3.20. When propagation of the ionization front becomes restricted to the surfaces of the zirconia disks (t = 3.9 ns in Fig. 3.21 b)), the electron densities exceed 5×10^{15} cm^{-3} (t = 3.9 ns in Fig. 3.21 a)). These surface regions then dominate the experimental optical images due to the ICCD programmed contrast.

3.3.7 Summary – Hexagonal PBR

The propagation of negative discharges in humid air through an idealized 2-dimensional PBR have been computationally and experimentally investigated. The primary means of discharge propagation through the dielectric lattice is breakdown between the dielectric rods driven by electric field enhancement. Surface charging and subsequent electric field enhancement results in

the formation of positive streamers between dielectric surfaces. These streamers then evolve into standing filamentary microdischarges that bridge the gaps between the dielectric rods. Eventually, surface charging near the feet of the microdischarges results in the formation of surface ionization waves. Decreasing the distance between the rods resulted in an increase in peak and average electric fields throughout the lattice. While this leads to an increase in the number of and intensity of the filamentary discharges, it does not change the breakdown mechanisms. Rotating the lattice results in the development of intense surface ionization waves due to the asymmetry of electric field with respect to the lattice. Most production of reactive species takes place near the surfaces of the rods, particularly in the proximity of either the filaments or surface ionization waves. The total inventory of reactive species increased during short, transient events, correlated with the propagation of positive streamers (restrikes) or development of an SIW. These waves are characterized by high densities of energetic electrons, leading to increased production of reactants in spite of their small volumes.

3.4 Plasma Properties in Patterned Dielectric Barrier Discharge Reactors

3.4.1 Base Case: Patterned DBD

The base case for the 2-D modeling uses a 200-ns voltage pulse of +6 kV, with a 5-ns rise time and a 5-ns fall time, followed by 600 ns of a voltage-off period. With the simulations being performed in 2-dimensions, higher voltages are required to reproduce the same phenomena as in the experiments. This disparity in voltage is due to the larger electric enhancement that occurs at the apexes of the 3-dimensional semi-spherical domes and hemispherical ionization fronts in the experiment, as compared to the 2-dimensional representation of these structures as cylinders or rods in the model. Although the majority of the experimental phenomena are reproduced and

explained by the model, the applied voltages at which these phenomena occur are larger in the model, which then reduces their timescale.

The electron impact ionization source term and electron density during the base case discharge are shown in Fig. 3.23. As a positive potential is applied to the top electrode, electrons quickly respond to the electric field, drift upwards, and deposit charge on the top dielectric. Heavy ions are left behind in the gas-gap, resulting in the formation of positive space-charge with a peak positive space-charge density of 3.7 nC-cm^{-3}. The production of positive charge enables the formation of positive streamers between each of the domes and the top dielectric, shown at t = 35 ns in Fig. 10a and t = 37 ns in Fig. 3.23 b). The electrons in the streamer head have temperatures of $T_e \approx 6.0$ eV, resulting in electron impact ionization peaking at $S_{e\text{-}impact} \approx 1\times10^{20}$ cm^{-3}-s^{-1}. Once the streamers breach the gas-gap, microdischarges form (Fig. 3.23 b), t = 62 ns). Filamentary microdischarges between the domes and the top dielectric are the initiating discharges seen in the experimental results in Fig. 3.24 and identified as 1. Once plasma forms in these regions, the high conductivity reduces the E/N (electric field/gas number density), which produces lower electron temperatures (0.1 eV $\leq T_e \leq$ 4.3 eV). The electron-impact ionization in the region largely ceases (-1.6×10^{20} cm^{-3}-s^{-1} $\leq S_{e\text{-}impact} \leq +1.8 \times 10^{17}$ cm^{-3}-s^{-1}), and only remnant plasma remains, as shown in Fig. 3.23 a), t = 60 ns.

As plasma charges the dielectric domes, electric fields parallel to the surface form, leading to the development of surface ionization waves (SIWs), shown at t = 60 ns and t = 62 ns in Fig. 3.23. The electrons in the ionization fronts of the SIWs have electron temperatures peaking at 7.3 eV, which lead to high rates of ionization (6×10^{22} cm^{-3}-s^{-1}), as well as high densities of excited and light-emitting species (2×10^{16} cm^{-3}). This stage of the discharge corresponds to that identified as 2 in Fig. 3.24 (from the side) at 5 μs. While light emitting species are still present in the bulk

plasma, their densities are 3 orders of magnitude lower than those in the SIW fronts near the surfaces, and so emission from the SIWs dominates. As the SIWs spread, ionization in the bulk gas ceases (Fig. 3.23 a) at t = 189 ns) as the high conductivity plasma in the bulk plasma lowers the local E/N. As in the experiments, the SIWs across the domes merge at the contact points where the highest electron density occurs, 6×10^{15} cm^{-3}. The thinness of the dielectric in these regions produces high capacitance, which supports a high surface charge density (peaking at 20.4 nC-cm^{-2}). These computed results correspond well with the experimental results shown in Fig. 3.24, where the brightest optical emission occurs from contact points between domes when SIWs merge. With the voltage pulse ending at t = 205 ns, the charge deposited on the dielectric leads to restrikes, as shown in Fig. 3.23 a) at t = 209 ns, and an increase in the electron density in the microdischarges shown in Fig. 3.23 b) at t = 211 ns. While not shown in Fig. 3.24, this process also occurs in the experiments when the polarity of the voltage is reversed.

3.4.2 Positive Polarity Voltage Amplitude

The base case is repeated with the positive voltage varied between +4 kV and +8 kV. No breakdown occurs at +4kV. At V = +5 kV, only microdischarges develop at the apex of the domes, as shown in Fig. 3.25 a). These structures are similar to the experimental trends observed. While SIWs begin to form, the plasma densities in the F-MDs are relatively low (peak $n_e \approx 5 \times 10^{13}$ cm^{-3}), leading to a low rate of charging of the dielectric domes (peaking at 5.9 nC-cm^{-2} at the end of the pulse – approximately 5 times lower than in the +6 kV base case). This low rate of surface charging does not produce a large enough parallel component of the electric field (peaking at 13.2 kV/cm) to support the propagation of SIWs while the voltage is on.

Discharges at higher voltages (V_p = +7 kV and +8 kV) generally follow the same discharge

sequence as the base case, and so only the results for V_p = + 8 kV will be discussed in detail. (See Fig. 3.26.) The discharge is initiated by a positive streamer beginning on the axis above the apex of each dome, which evolves into a F-MD. However, due to higher applied voltage, the electron temperatures in the streamer head are larger ($T_e \approx 6.8$ eV compared to 6.0 eV for the base case) and the resulting electron densities double from (base case) 8.0×10^{11} cm^{-3} to 1.6×10^{12} cm^{-3}. The time required for the plasma to breach the gas gap decreases from approximately 41 ns to 18 ns. Similar behavior is observed in experimentally measured discharge current (Fig. 3.27) and space resolved emission (Fig. 3.28), where, with an increase in applied voltage from 1.9 to 3.8 kV, the F-MD (1) initiates ≈ 10 μs earlier. The increases in energies and densities enable the SIWs to develop and propagate more quickly.

With an applied voltage of +8 kV, plasma nearly fully covers the domes by t = 50 ns, as shown in Fig. 3.26. As the surface of the dome charges, the potential lines are bent (Fig. 3.26 b)), leading to electric field enhancement and larger E/N, which supports an electron temperature $T_e \approx$ 8.5 eV, and electron impact ionization source peaking at $S_{e\text{-impact}} \approx 1 \times 10^{25}$ cm^{-3}-s^{-1} in the head of the SIW. Due to the resulting high electron densities (peaking at 1×10^{16} cm^{-3}, Fig. 3.26 c)), when the SIWs reach the contact points between the domes, the capacitance of the surface is quickly charged and the discharge extinguishes. This sequence is not observed experimentally, likely due to the applied voltage being lower. In the model, once the capacitance of the contact points is fully charged, plasma acts as a conductive sheet on top of the domes. At this time, the potential at the top of the domes becomes nearly equal to the potential at the contact points. This equality leads to an increase in electric field and ionization rate in the bulk plasma, as shown in Figs. 3.26 b) and 3.26 e), where electron impact ionization sources are shown directly before and after the SIWs merge. As a result, a short-lived burst in bulk ionization takes place (Fig. 3.26 e)).

3.4.3 Negative Polarity Voltage Amplitude

A voltage sweep is also performed for negative polarity (-4 kV to -8 kV). No discharge occurs at -4 kV, as this voltage is lower than the breakdown field of helium. At -5 kV, only the F-MD forms, as shown in Fig. 3.25 b). The discharge evolution for -6 kV is shown in Fig. 3.29 in the same format as the positive base case. In a similar fashion to positive polarity, the discharge begins with electrons moving away from the cathode and charging the dielectric domes. A positive streamer develops as positive space-charge is left behind in the gas-gap (shown in Fig. 3.29 at t = 35 and 37 ns). The resulting microdischarges is more diffuse than those at +6kV, which is typical of negative discharges [11]. As the microdischarges charge the top dielectric, surface ionizations form (Fig. 3.29 at t = 83 and 85 ns). The structure is similar to the experimental results from the side in Fig. 3.24 at 4, 9, and 10 μs. The SIWs over the top dielectric are less intense ($S_{e\text{-}impact}$ =1.6 × 10^{19} cm^{-3}-s^{-1}) than those on the surfaces of the domes (8.3×10^{21} cm^{-3}-s^{-1}) due to the topology. The top dielectric surface is perpendicular to the applied electric field, requiring parallel electric fields to sustain SIWs to be produced dominantly by surface charging. The electric field at the surfaces of the domes has a component parallel to the surface, which enhances initiation and propagation of SIWs.

In the negative voltage base case, electrons spread across the surfaces of the domes, but their density is relatively low, peaking at $n_e \approx 5\times10^{12}$ cm^{-3} (Fig. 3.29 at t = 149 ns and 150 ns). The electrons along the surface are not self-propagating ionization fronts. Rather, they are due to electron transport along the electric field lines. The surfaces of the domes charge to -9 nC-cm^{-2}, while the top dielectric reaches +34 nC-cm^{-2}. Once the applied voltage is turned off, this surface charge results in a peak electric field of ≈16 kV-cm^{-1}, which is sufficient for breakdown and the

formation of a restrike, as shown in Fig. 3.29 at t = 205 ns and 210 ns. These trends are similar to the experimental results in Fig. 3.24 (negative half) at 14 and 18 μs. The difference in location of the restrikes between the model and experiment could be explained by the fact that, in the experiment, the SIWs over the flat dielectric merge at a location above the contact point. The F-MD or re-strike occurs at the same location. However, in the simulation during this time, the SIWs from the two sides do not merge together and, therefore, the restrike is near the center of the dielectric structures.

In general, increasing the magnitude of the voltage results in similar trends, regardless of polarity. The evolution of E/N, electron impact ionization source term with equipotential lines and electron density, is shown for -8 kV in Fig. 3.30. Following the initial upward-directed positive streamer, plasma spreads across the domes, while an intense SIW propagates along the top dielectric (Fig. 3.30 b) and c)). Since the electrons near the domes follow the electric field lines, a region of low electron density ($\approx 10^{11}$ cm^{-3}) forms at the top of the domes, (Fig. 3.30 f)). The plasma here is, therefore, less conductive than with the positive polarity pulse. As a result, the potential does not redistribute, and the burst of ionization that occurs with +8 kV does not form. This sequence is shown in Fig. 3.30 e).

The sums of the densities of species that emit in the visible spectrum at t = 800 ns are shown in Fig. 3.31 for each of the applied voltages. These states include He(3P), He(3S), and He(2^1P). At ±5 kV, only a microdischarge between the domes and the top dielectric form. Surface ionization waves form, but the pulse length is too short to allow for their propagation along the entirety of the dielectric. At higher voltage magnitudes, plasma covers the entirety of the domes, and the highest densities of light-emitting species are found at the top dielectric layer during negative pulses [Fig. 3.31 a)-d)] and at contact points between the domes when the applied voltage

is positive [Fig. 3.31 e)-h)]. The highest densities of excited He species occurs at +8 kV, with peak value of 6.9×10^{14} cm^{-3} at t = 55 ns, which then decreases to 3.7×10^{12} cm^{-3} at t = 800 ns. Of the light-emitting species, He(2^1P) and He(3P) have the highest densities, peaking at 2.7×10^{14} cm^{-3} and 3.7×10^{14} cm^{-3}, respectively, at t = 55 ns. Their densities decrease to 3.6×10^{12} cm^{-3} and 6.0×10^{12} cm^{-3} at t = 800 ns, indicating that the He(3P) state is the main source of visible light.

The structure of the plasma also varies as the polarity reverses at a given voltage amplitude. When the applied voltage is negative, the plasma is largely diffuse and fills a greater fraction of the volume of the reactor. However, the peak densities of light-emitting species are greater during a positive-polarity pulse. These trends are due to the topology of the dielectric with respect to the applied electric field. The curvature of the domes enables the applied electric field to have components parallel to the surface. When the applied voltage is negative, the direction of the vector electric field enables electrons to drift downward and along the curvature of the domes, diffusing into regions further away from the initiating microdischarge. Conversely, during a positive polarity pulse, the electrons move towards the flat dielectric layer at the top of the reactor and the plasma remains more compact.

3.4.4 Summary – Patterned DBD

In summary, the simulation produces qualitatively similar phenomena to the experiment. Experiments and simulations indicate that the discharge is sustained first by F-MDs, followed by the SIWs and S-MDs at the contact points and F-MD after the first two mechanisms. With these experimental and computational results as a background, the discharge dynamics during positive and negative voltage are summarized in Fig. 3.32. Discharges with both negative and positive polarities begin with a positive streamer directed towards the cathode. This is the precursor to the

formation of filamentary microdischarges (F-MDs) across the gap at the apex of the domes, which is the minimum gap between the two dielectrics. While similar combinations of positive streamer and filamentary microdischarges generate plasma in conventional parallel plate DBDs, in the case of the packed DBD, the generation of the streamer and F-MDs are always at the location of the minimum gap and only happens once during each half cycle. This phase is followed by the SIW travelling over the dielectric surface from the center of the dome (or the location on the flat dielectric facing the dome) towards the side. With a positive polarity, the SIW propagates over the curved dielectric and, in the negative cycle, the SIW propagates over the plane dielectric. There is a weaker SIW on the opposite dielectric for both polarities, on the flat and curved dielectrics during the positive and negative polarity, respectively. SIWs on adjacent domes may merge before reaching the contact point. For both polarities, the SIW from the sides result in S-MD either at the contact point or at the location on the flat dielectric axially opposite the contact point. The second current pulse starts as SIWs propagate across the dielectric, and current peaks when the opposing SIWs merge at the contact point. For sufficiently high voltage, multiple current pulses may be generated with the number of current pulses increasing with voltage. Each current pulse results from microdischarges either as S-MDs or a combination of S-MDs and F-MDs. These S-MDs and or F-MDs could be more intense at the edges or in the center depending on conditions.

The sensitivity of plasma structures and discharge types on applied voltage shown here can have important broader implications. For example, formation of SIWs leads to higher electron temperatures and, therefore, higher rates of ionization and dissociation of strongly-bonded molecules such as N_2. Controlling the formation of SIWs is thus an additional pathway to selectivity. The proximity of SIWs to catalysts enables plasma-produced reactive species with short diffusion lengths and lifetimes to interact with surface sites at a greater rate. Careful packing

design is also shown to be of importance. The topology of the packing material can determine the direction, morphology, and intensity of plasma discharges. These factors, then, impact energy efficiency, selectivity, and throughput of commercial plasma packed bed reactors.

3.5 Concluding Remarks

Modeling of dielectric barrier reactors has been qualitatively validated through experiments for different gases, geometries, pressures, voltages, and materials – lending credence to *nonPDPSIM* as a modeling platform. Furthermore, in all investigated cases, we find the same plasma formation phenomena. The discharge initiates as a positive streamer between the apex of dielectric structure and opposite dielectric plate (at the location of minimum distance), which transforms into a filamentary microdischarge in the gap. The surface charging of the dielectric generates surface-parallel electric fields, which propagates surface ionization waves (SIWs) from the apex of the dielectric structure towards the contact points (for the positive polarity). The SIWs across the domes merge at the contact points, where the highest electron density is produced, as the lower dielectric thickness at the contact point produces a high capacitance that supports a high surface charge density. The SIW is followed by a restrike or F-MD due to high surface charge resulting in an electric field sufficient for breakdown. The types of plasmas developing then impact the reactive species being transferred into the gas, and therefore the extent of plasma-gas activation. It is especially interesting to note that these formation modalities were observed in both: complex gas mixtures (humid air) and in a pure noble gas case (helium). Noble gases lack metastable states which act as energy sinks. As a result, at a given set of system parameters (voltage, pressure, system critical dimension), discharges in noble gases tend to be more diffuse and glow-like. Yet the restrike-FM-SIW steps were observed in DBDs of both kinds.

3.6 Figures

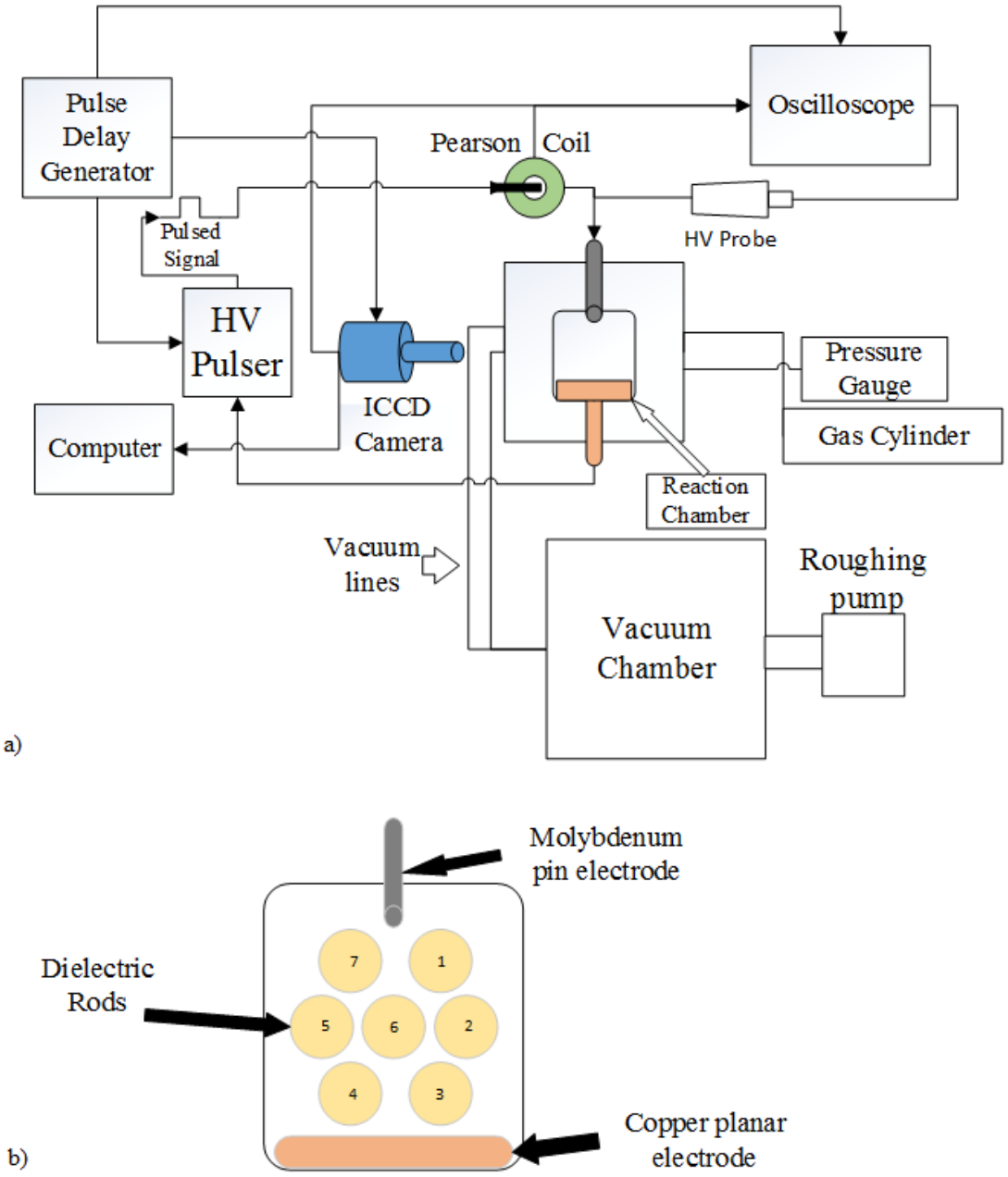

Fig. 3. 1 (a) Experimental setup for the time-resolved microdischarge imaging. (a) Schematic of apparatus. (b) Top-view of reaction chamber with media

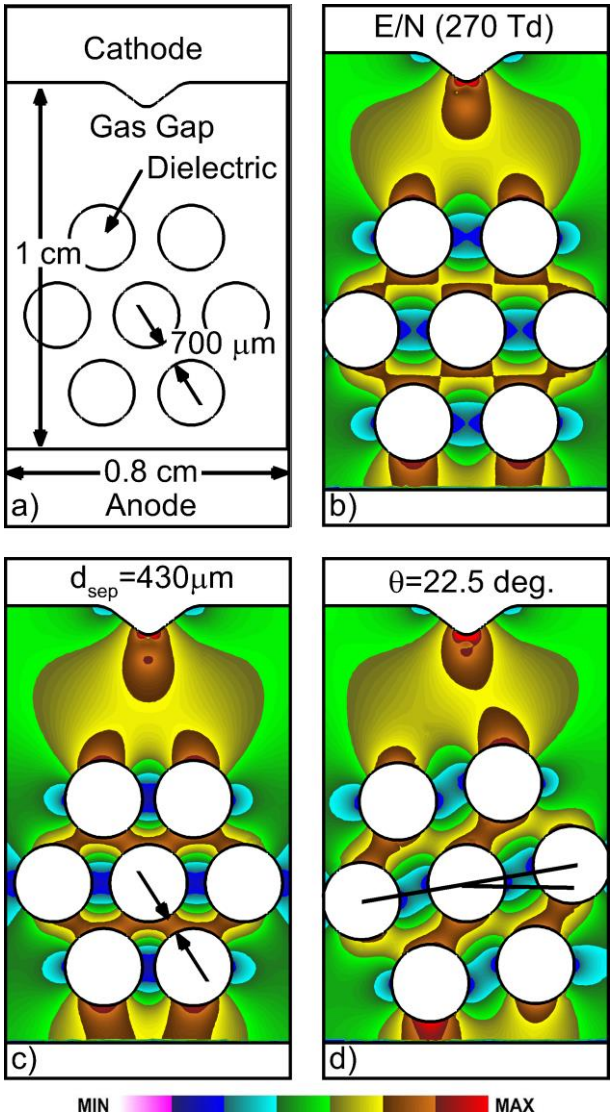

Fig. 3. 2 Initial conditions for simulations: (a) base case geometry and (b) base case initial reduced electric field, E/N. (c) Initial E/N for smaller separation between the rods and for (d) rotated lattice. E/N is plotted on a linear scale, 2.7–270 Td for total voltage drop of −30kV in humid air.

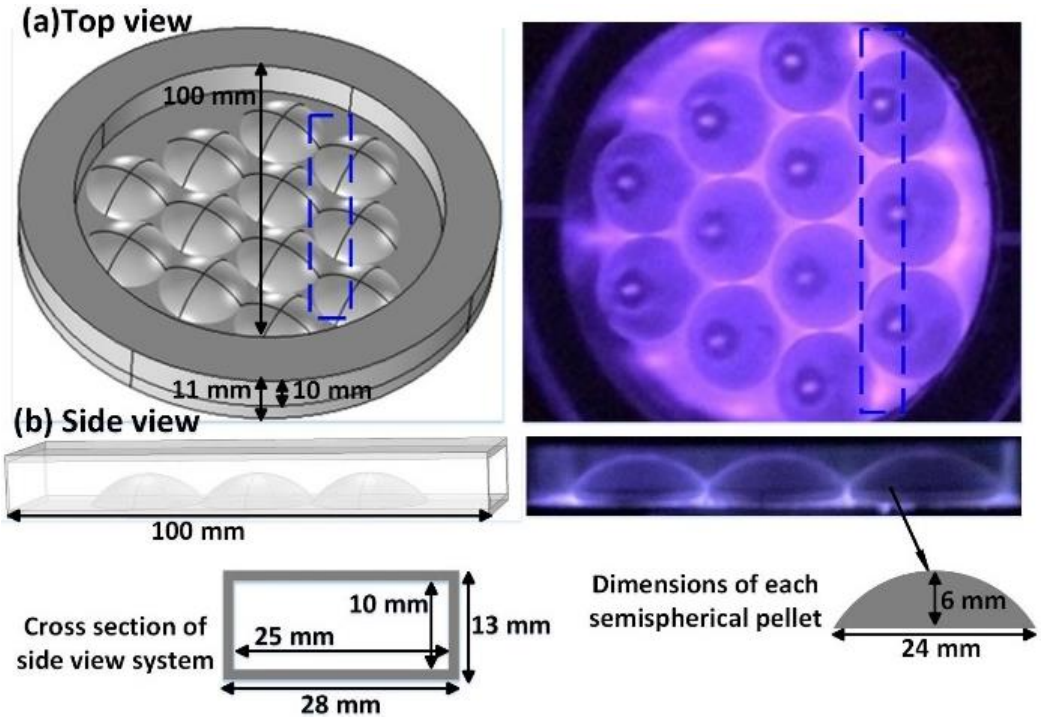

Fig. 3. 3 Experimental setup with a patterned DBD. (left) Schematic and (right) CCD camera image of the (a) top view and (b) side view.

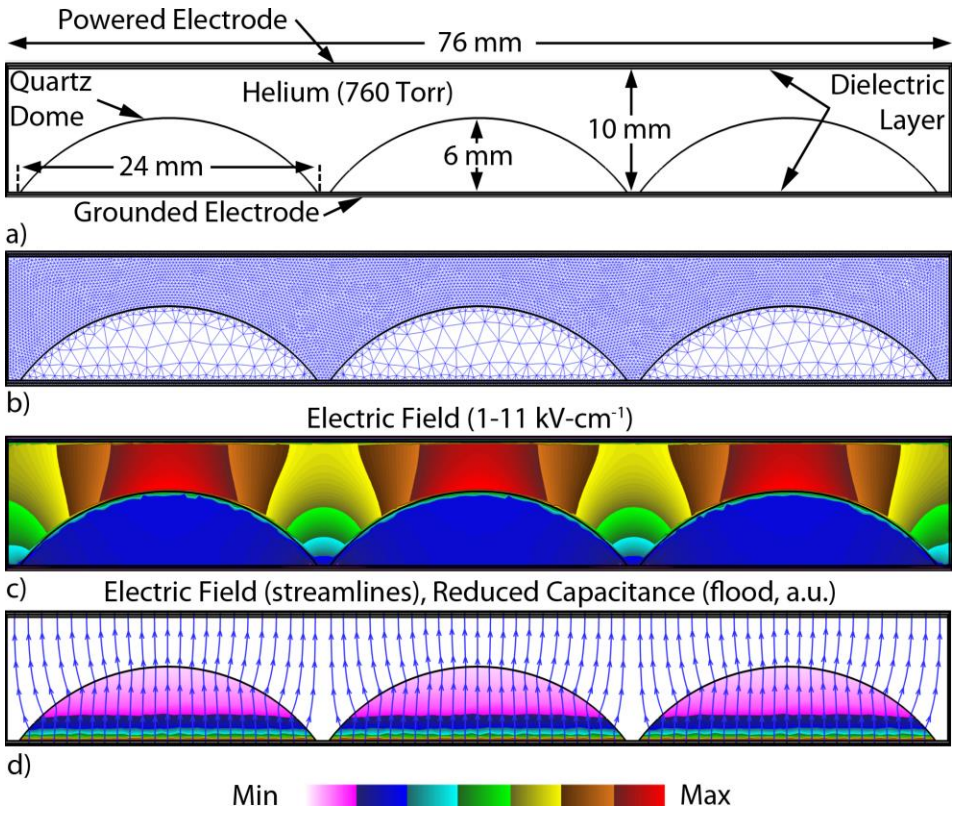

Fig. 3. 4 Computational geometry. a) Schematic of the reactor having a height of 10 mm, width of 76 mm and a depth of 5 mm. Both electrodes are covered by a layer of dielectric 0.2 mm thick. b) Computational mesh. c) Electric field contours resulting from an applied voltage of 6 kV. The peak electric fields occur between the top dielectric layer and the apexes of the dielectric domes. d) Electric field streamlines along the surface of the dome and relative reduced capacitance. Angle between applied electric field vectors and surface of the dome decreases towards the con-tact points. Capacitance is lowest near the top of the domes.

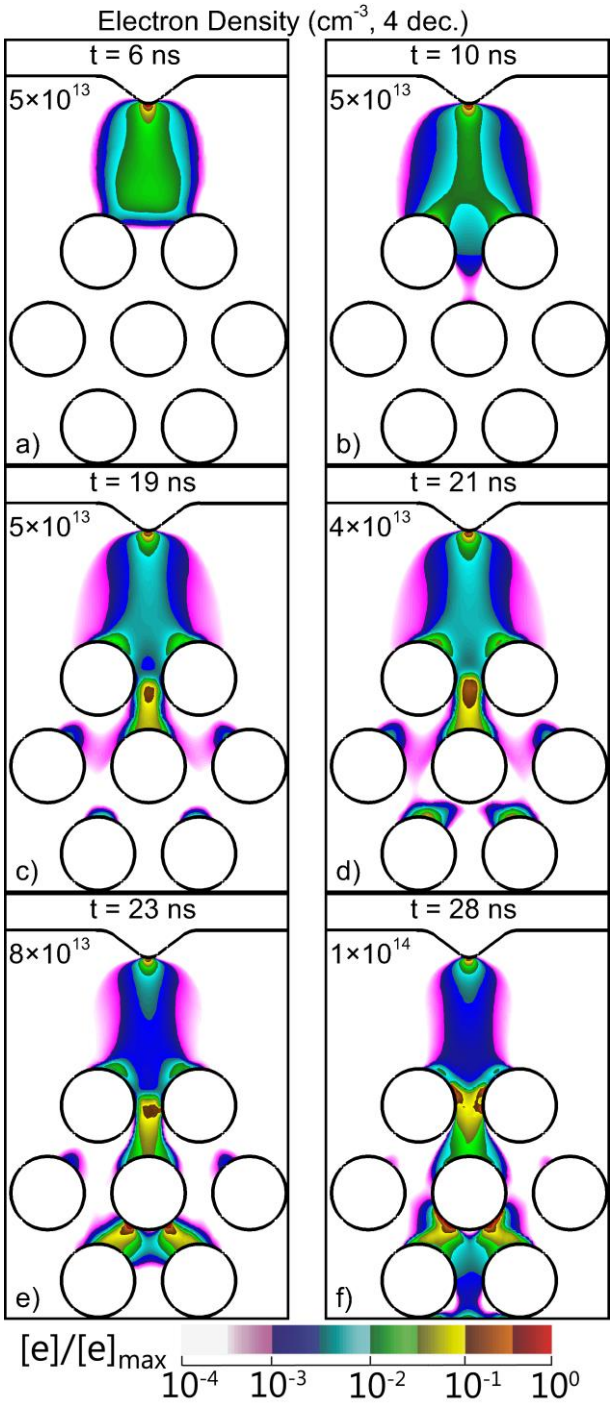

Fig. 3. 5 Electron density at different times during propagation of the discharge through the PBR for the base case (−30kV, humid air, 700 µm rod separation). Densities are plotted on a 4-decade log scale with maximum value (cm^{-3}) indicated in each frame.

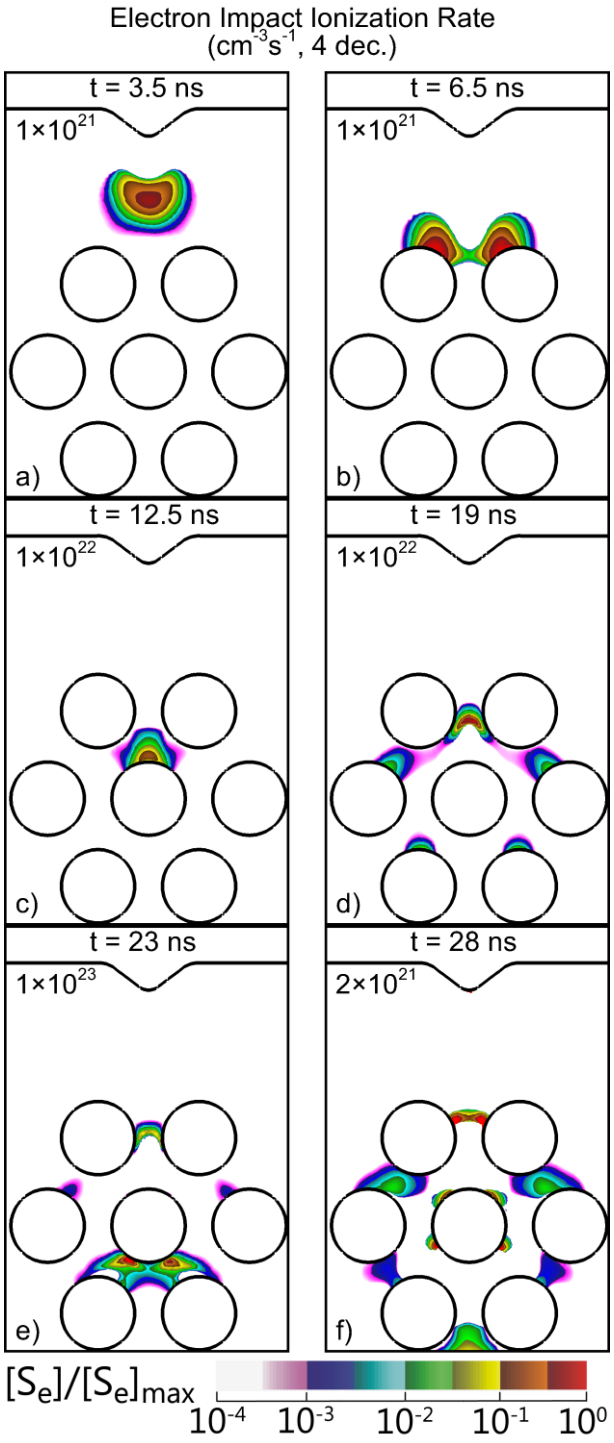

Fig. 3. 6 Electron impact ionization rate at different times during propagation of the discharge through the PBR for the base case (−30 kV, humid air, 700 µm rod separation). Rates are plotted on a 4-decade log scale with the maximum value (cm^{-3} s^{-1}) indicated in each frame.

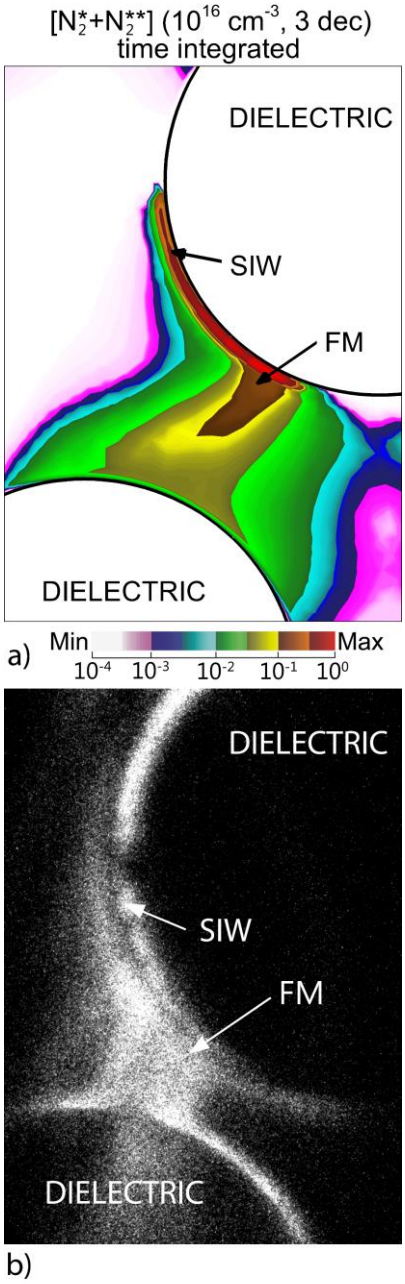

Fig. 3. 7 Comparison of modeling and experimental imaging of a microdischarge and SIW in a 2D PBR. The computed values are for the base case conditions (−30kV, humid air, 700 μm bead separation). (a) Time integrated computed densities of excited nitrogen species [$N_2(b^1\,\Pi)$ and $N_2(b'^{\,1}\,\Sigma)$]. Densities are plotted on a 4-decade log scale. (b) Experimental fast camera imaging of visible emission using a 0.5 μs gate.

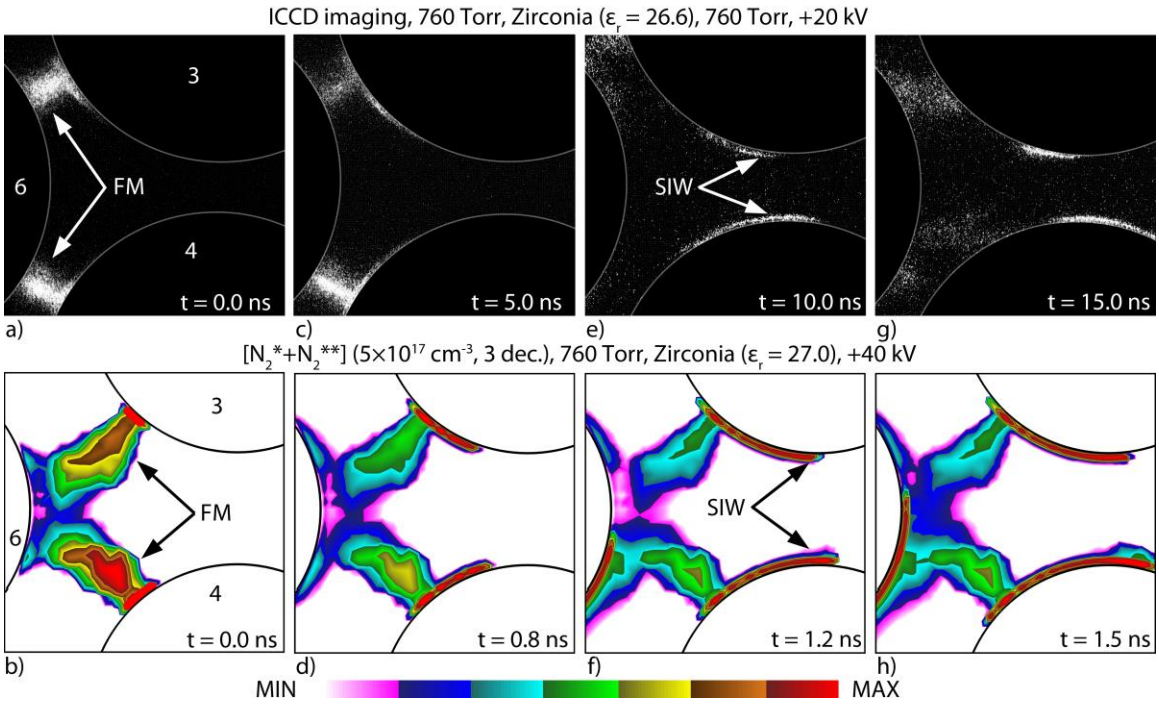

Fig. 3. 8 Transition from microdischarges to surface ionization waves between disks 3, 4, and 6 and at sequential times. (top) Experimental ICCD imaging and (bottom) computed densities of light-emitting species from the model (bottom). The disparity in time between the model and the experiment arises from the different voltages being applied.

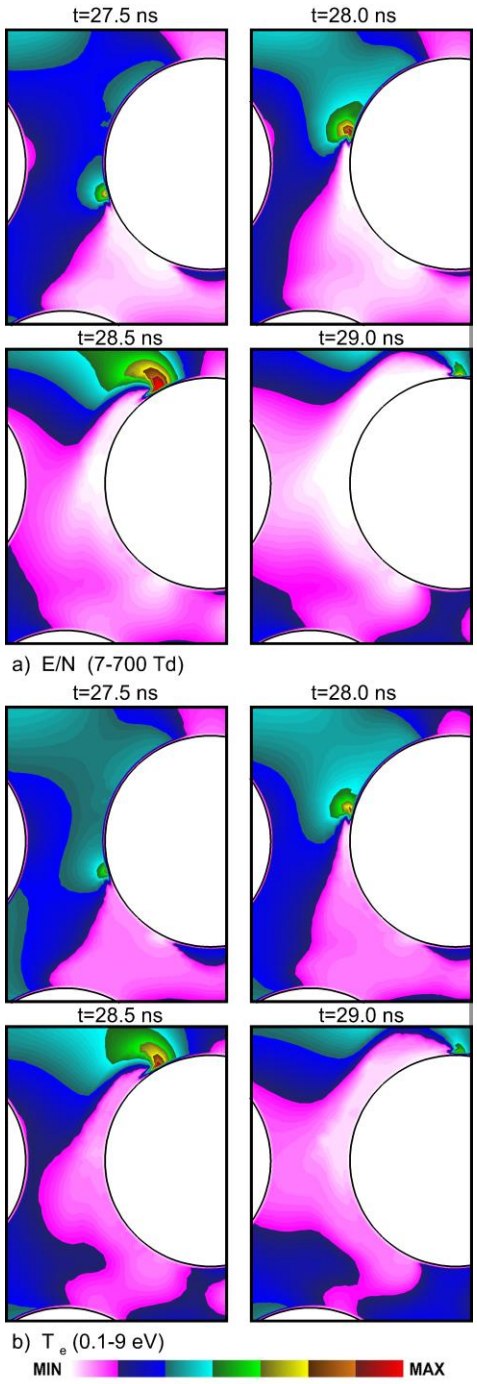

Fig. 3. 9 Time evolution of (a) reduced electric field and (b) electron temperature during propagation of an SIW propagation for the base case conditions. E/N is plotted on a linear scale, 7–700 Td. T_e is plotted on a linear scale, 0.1–9 eV. The location is between the center rod and the lower-left rod.

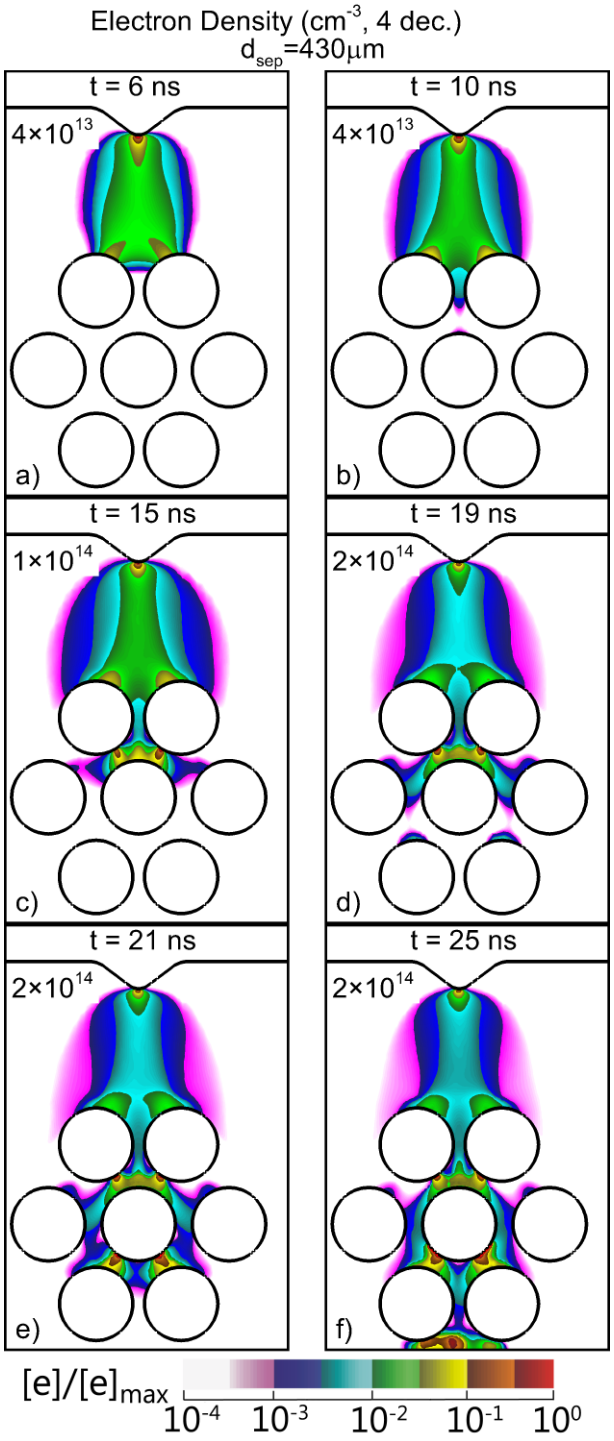

Fig. 3. 10 Electron density at different times during propagation of the discharge through the PBR for smaller separation between the rods (−30kV, humid air, 430 μm rod separation). Densities are plotted on a 4-decade log scale with maximum value (cm^{-3}) indicated in each frame.

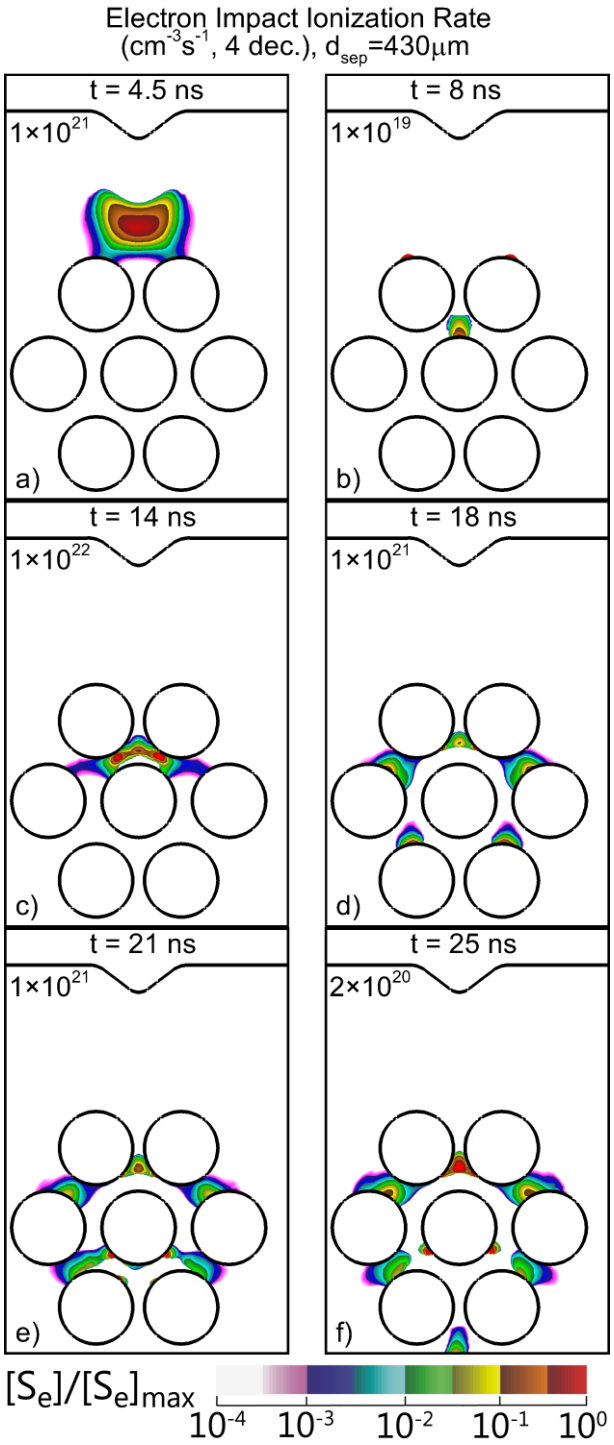

Fig. 3. 11 Electron impact ionization rate at different times during propagation of the discharge through the PBR for smaller separation between the rods (−30kV, humid air, 700 μm rod separation). Rates are plotted on a 4-decade log scale with the maximum value (cm^{-3} s^{-1}) indicated in each frame.

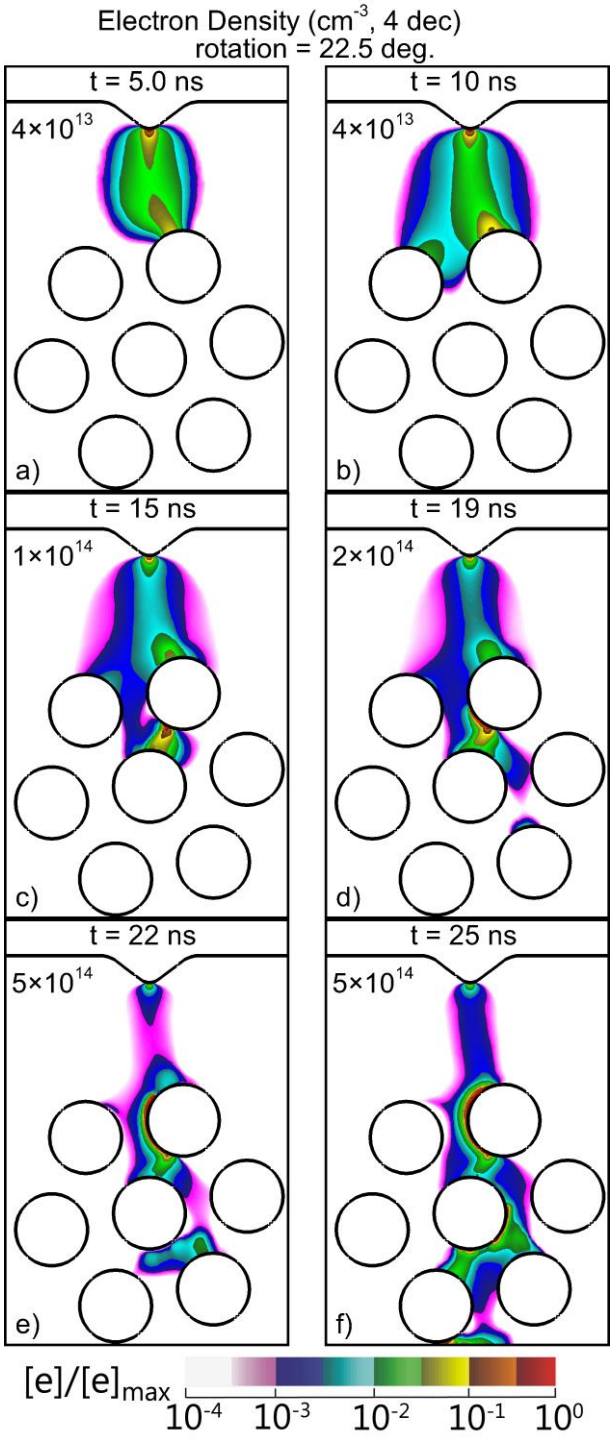

Fig. 3. 12 Electron density at different times during propagation of the discharge through the PBR for the rotated lattice (−30kV, humid air, 700 μm rod separation, 22.5° rotation). Densities are plotted on a 4-decade log scale with maximum value (cm^{-3} s^{-1}) indicated in each frame.

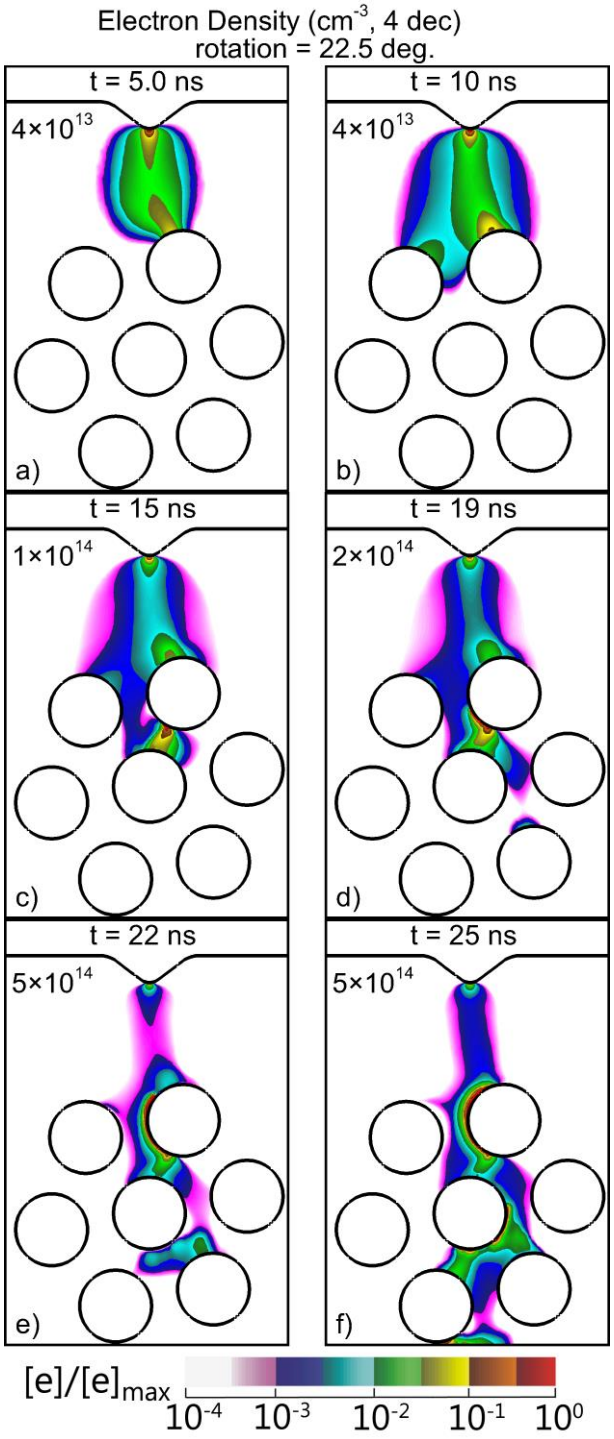

Fig. 3. 13 Electron impact ionization rate at different times during propagation of the discharge through the PBR for the rotated lattice. (−30kV, humid air, 700 μm rod separation, 22.5° rotation). Rates are plotted on a 4-decade log scale with the maximum value (cm^{-3} s^{-1}) indicated in each frame.

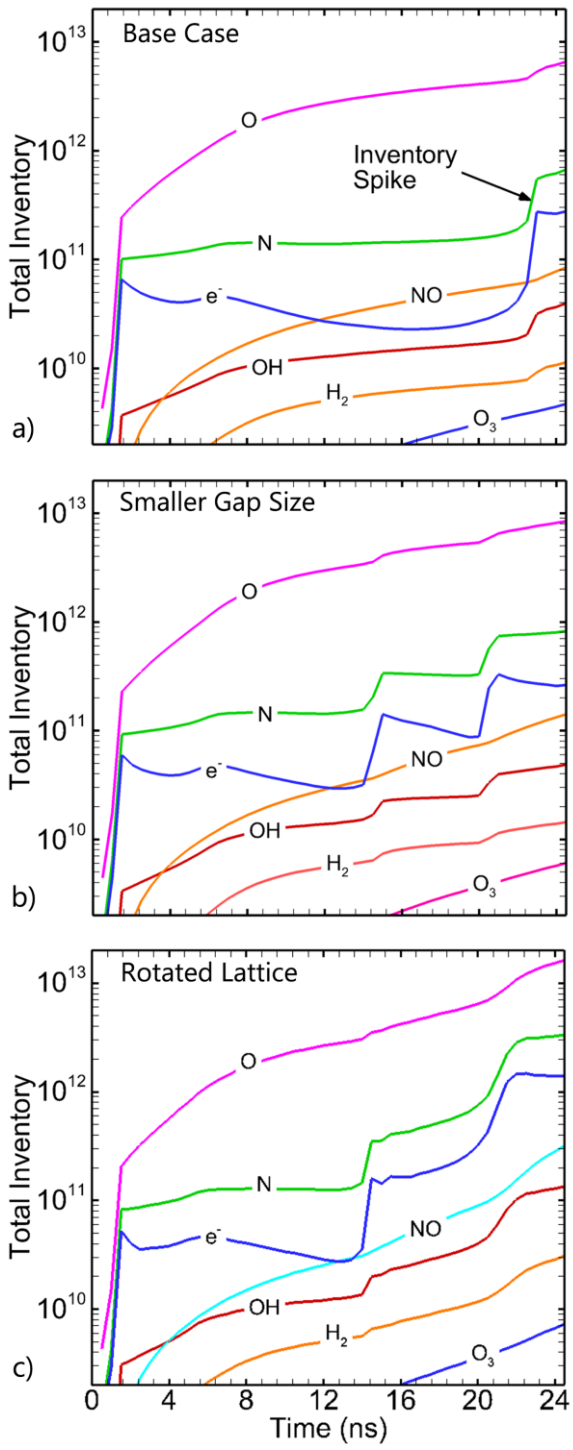

Fig. 3. 14 Time evolution of the total inventories of reactive species: (a) base case, (b) smaller separation between rods, and (c) rotated lattice. Total inventory is the unitless total number of atoms or molecules representing the volume-integrated density of the species throughout the reactor.

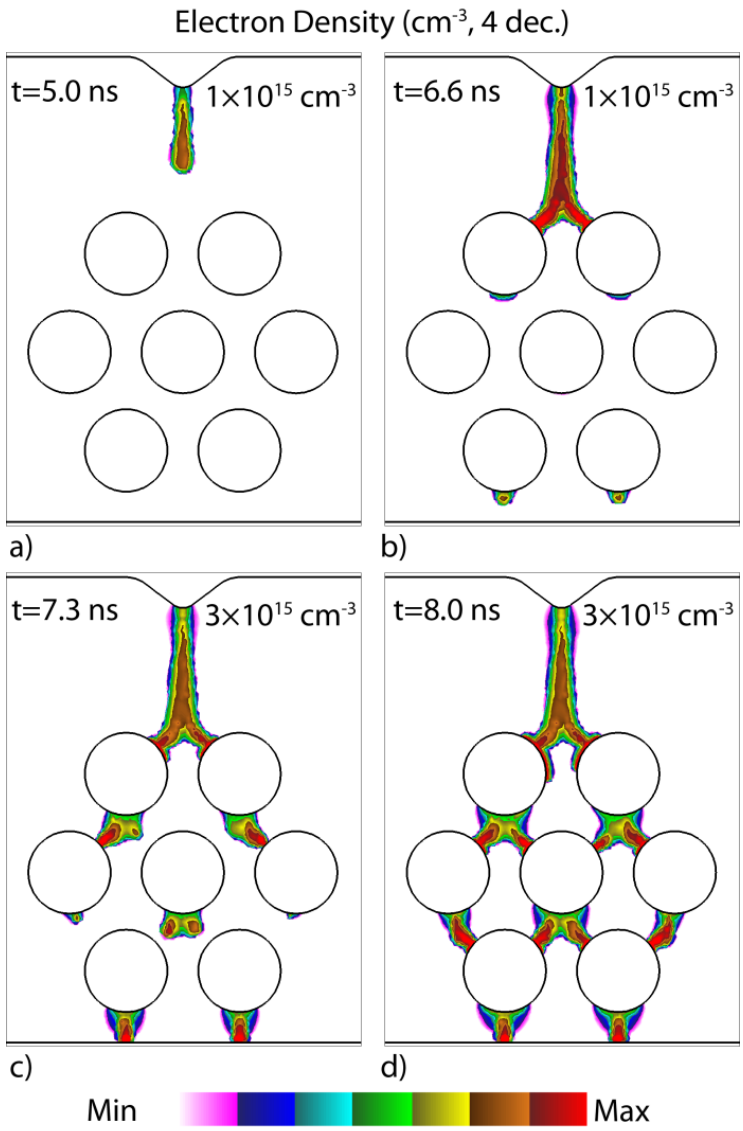

Fig. 3. 15 Time evolution of electron density in quartz lattice at 760 Torr with a +40 kV pulse. (a) 5 ns, (b), 6.6 ns, (c), 7.3 ns and (d) 8.0 ns. Log scale over 4 decades, with maximum value noted in each frame.

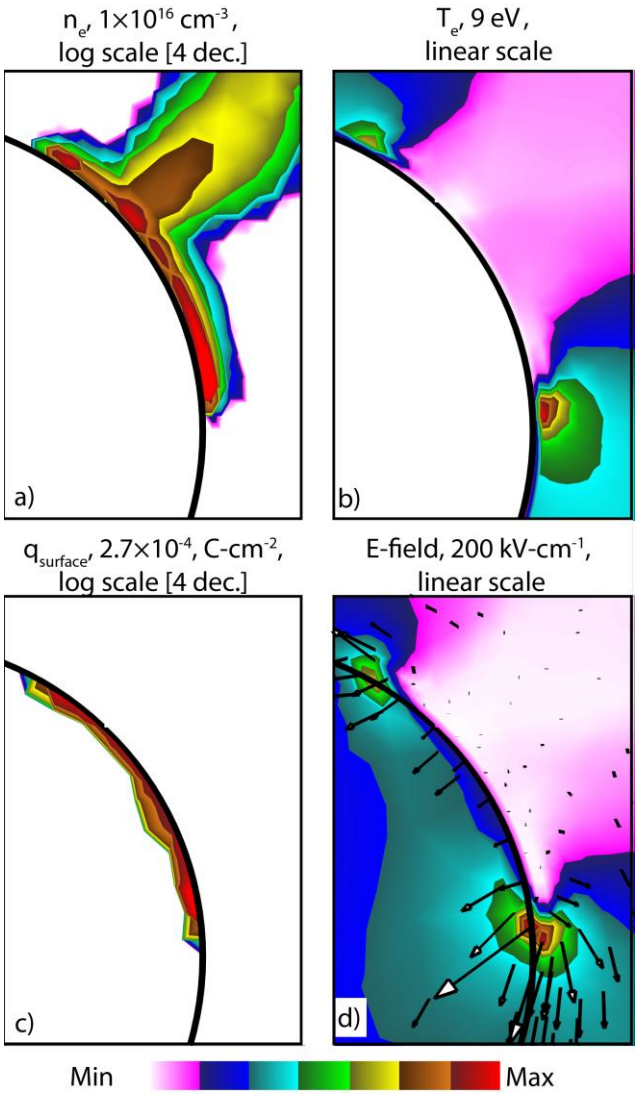

Fig. 3. 16 Plasma properties in the vicinity of disk 7 during the propagation of a surface ionization wave (t= 8 ns). a) Electron density (log scale, 4 decades, 1×10^{16} cm^{-3} maximum), b) electron temperature (0 to 9 eV), c) surface charge (log scale, 4 decades, 2.7×10^{-4} C-cm^{-2} maximum) and d) electric field amplitude (contours, 0 to 200 kV-cm^{-1}) and the electric field vectors.

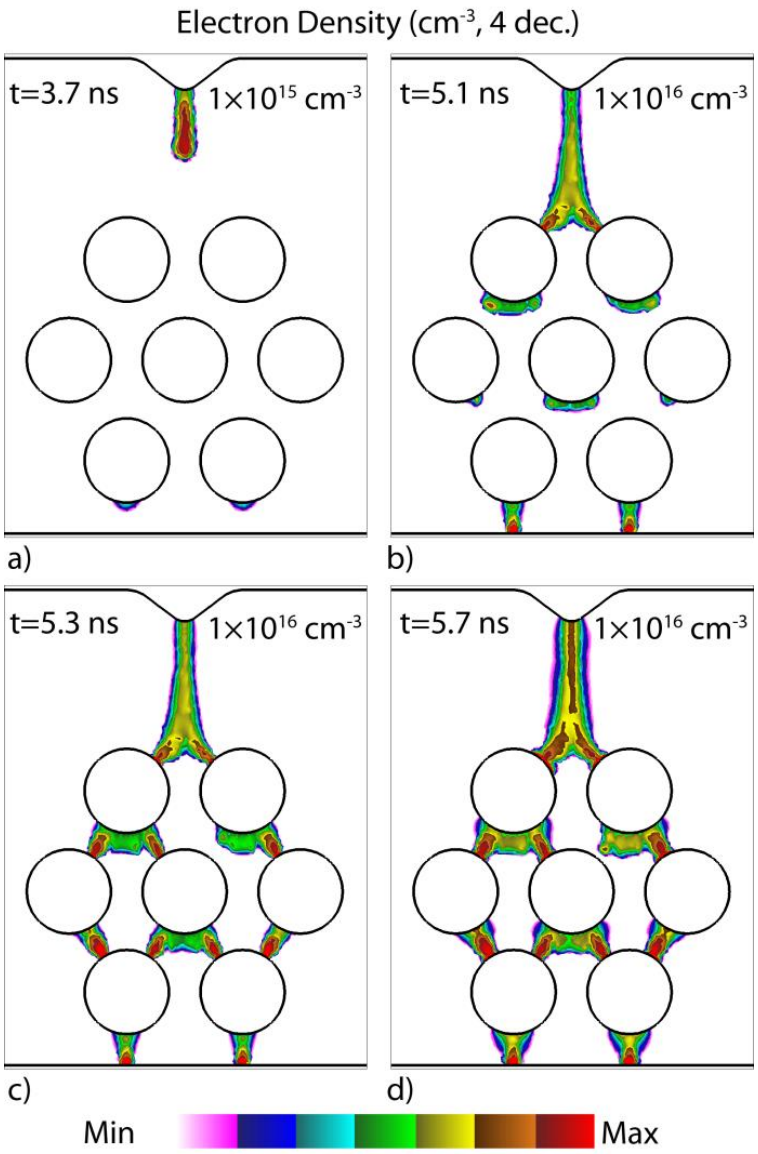

Fig. 3. 17 Time evolution of electron density in zirconia lattice at 760 Torr with a +40 kV pulse. (a) 3.7 ns, (b), 5.1 ns, (c), 5.3 ns and (d) 5.7 ns. Log scale over 4 decades, with maximum value noted in each frame.

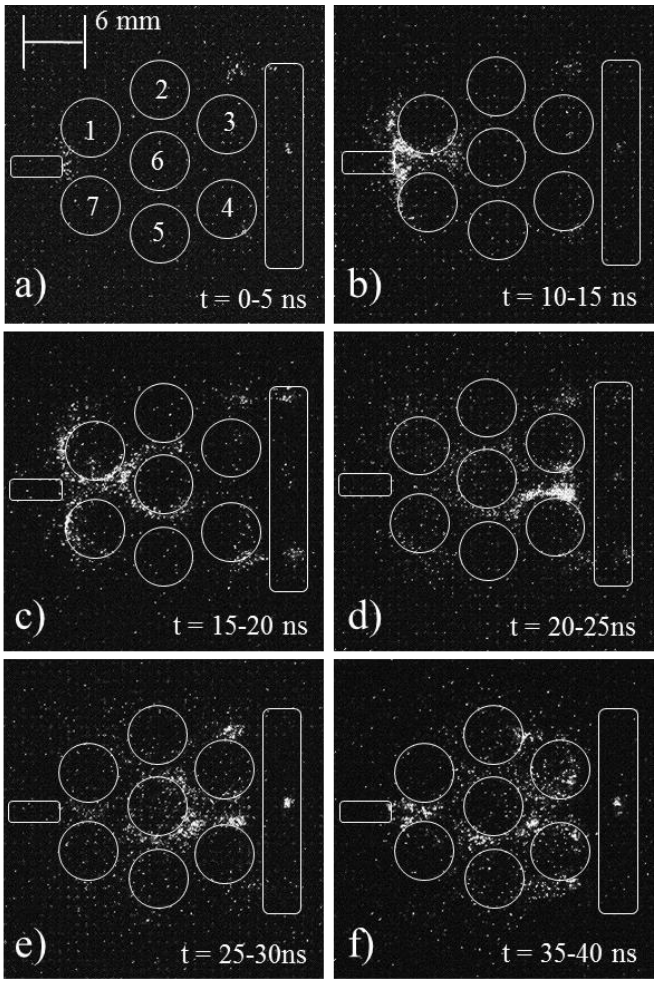

Fig. 3. 18 Time-resolved imaging of the 2D-PBR discharge through quartz disks at 1 atm integrated over 5 ns. (a) 0-5 ns, (b), 10-15 ns, (c) 15-20 ns, (d), 20-25 ns. (e) 25-30 ns and (f) 35-40 ns

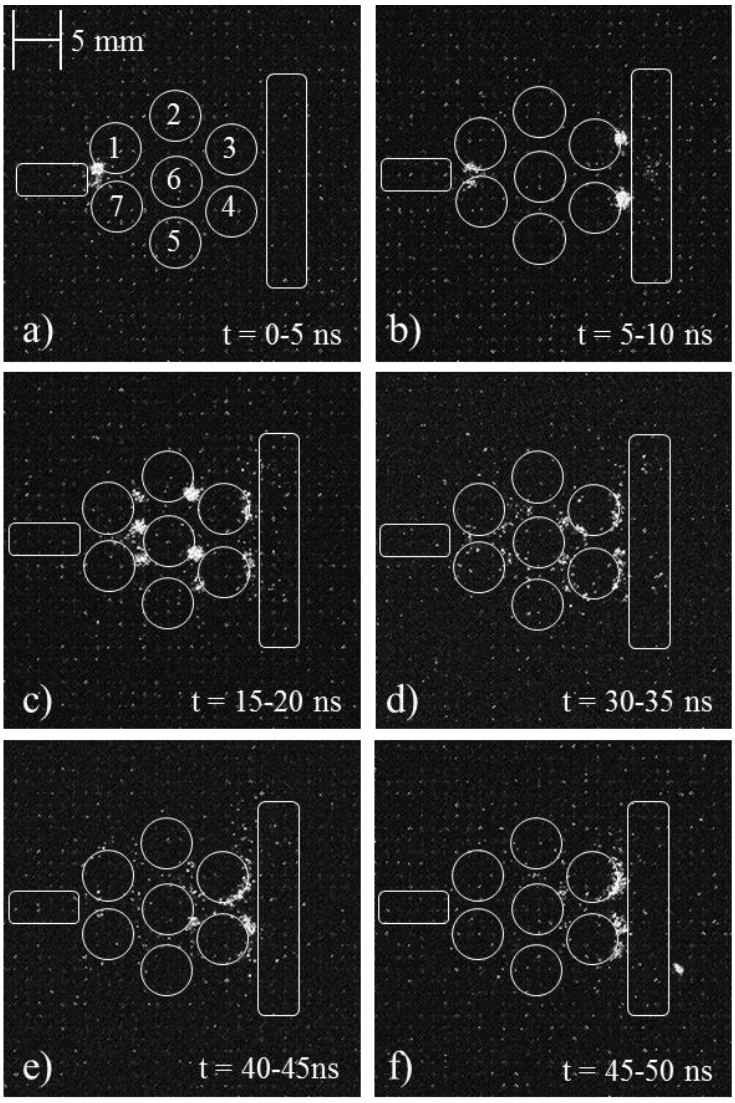

Fig. 3. 19 Time-resolved imaging of the 2D-PBR discharge through zirconia disks at 1 atm integrated over 5 ns. (a) 0-5 ns, (b), 10-15 ns, (c) 15-20 ns, (d), 30-35 ns. (e) 40-45 ns and (f) 45-50 ns.

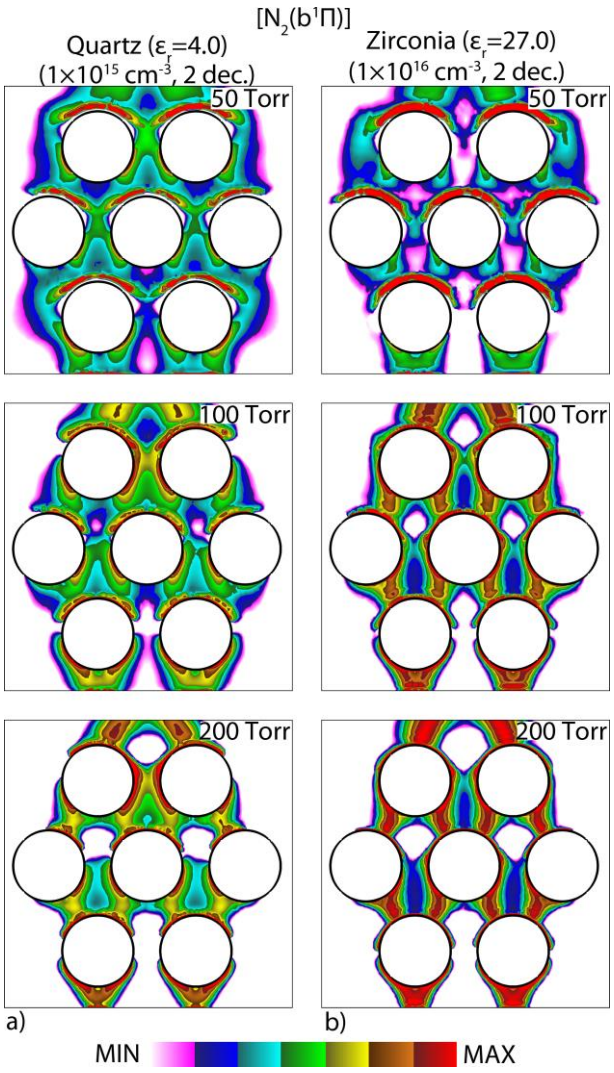

Fig. 3. 20 Densities of light-emitting species for different pressures and a 24 kV pulse with a) quartz and b) zirconia dielectric disks. Log scale over 4 decades with maximum value indicated in figure.

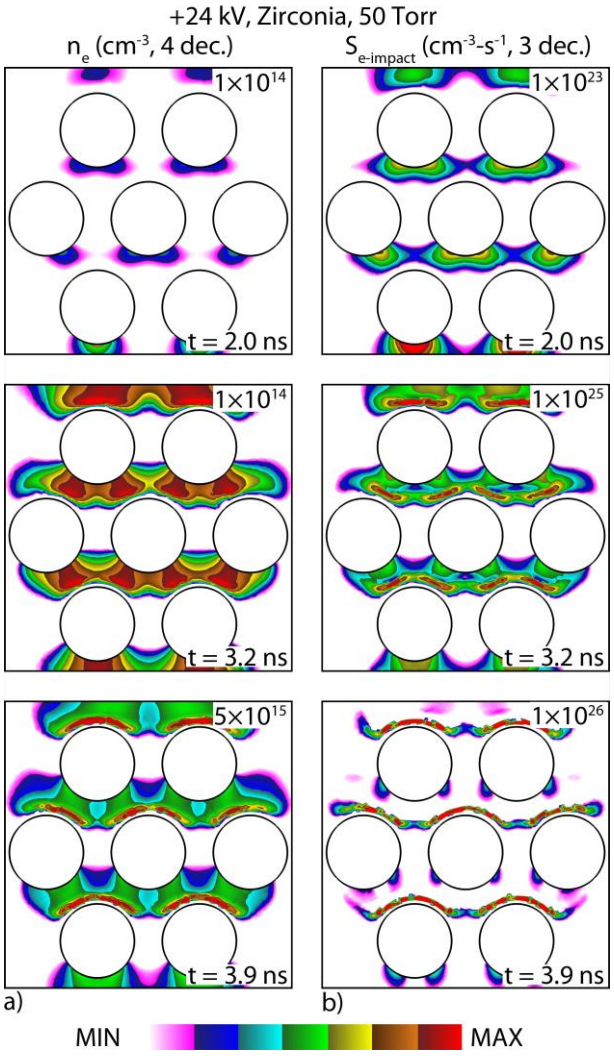

Fig. 3. 21 Densities of light-emitting species for different pressures and a 24 kV pulse with a) quartz and b) zirconia dielectric disks. Log scale over 4 decades with maximum value indicated in figure.

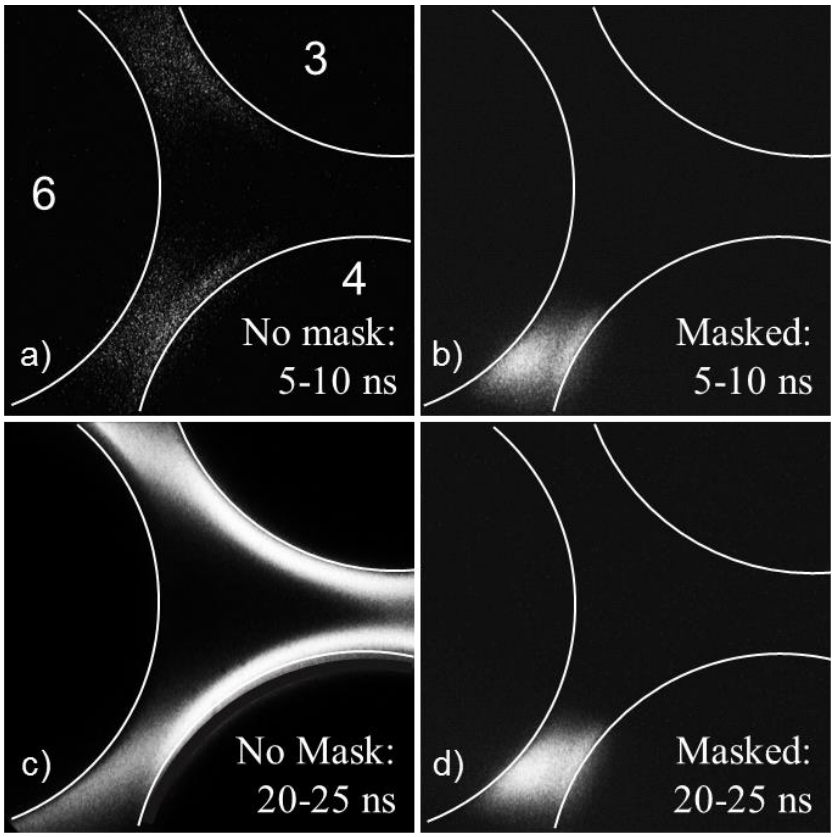

Fig. 3. 22 Imaging of discharges through zirconia disks at 50 Torr (5 ns exposure) with and without masking. The masking blocked emission from the surface ionization waves. (a) Without mas, 5-10 ns, (b) with mask, 5-10 ns, (c) without mask, 20-25 ns and (d) with mask 20-25 ns.

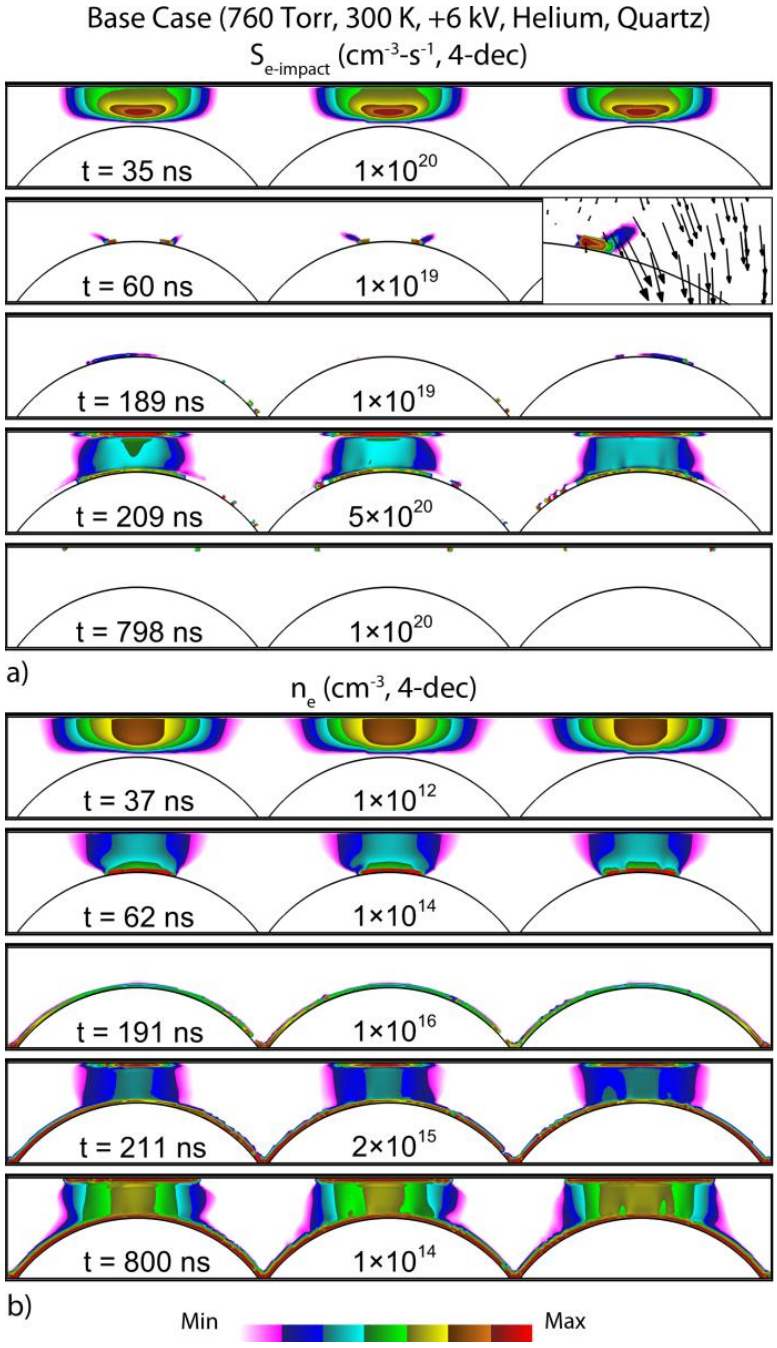

Fig. 3. 23 Evolution of a) electron impact ionization source and b) electron density during the discharge in the base case (+6 kV) displayed using log scales. Times and peak plotted values are noted in the figures

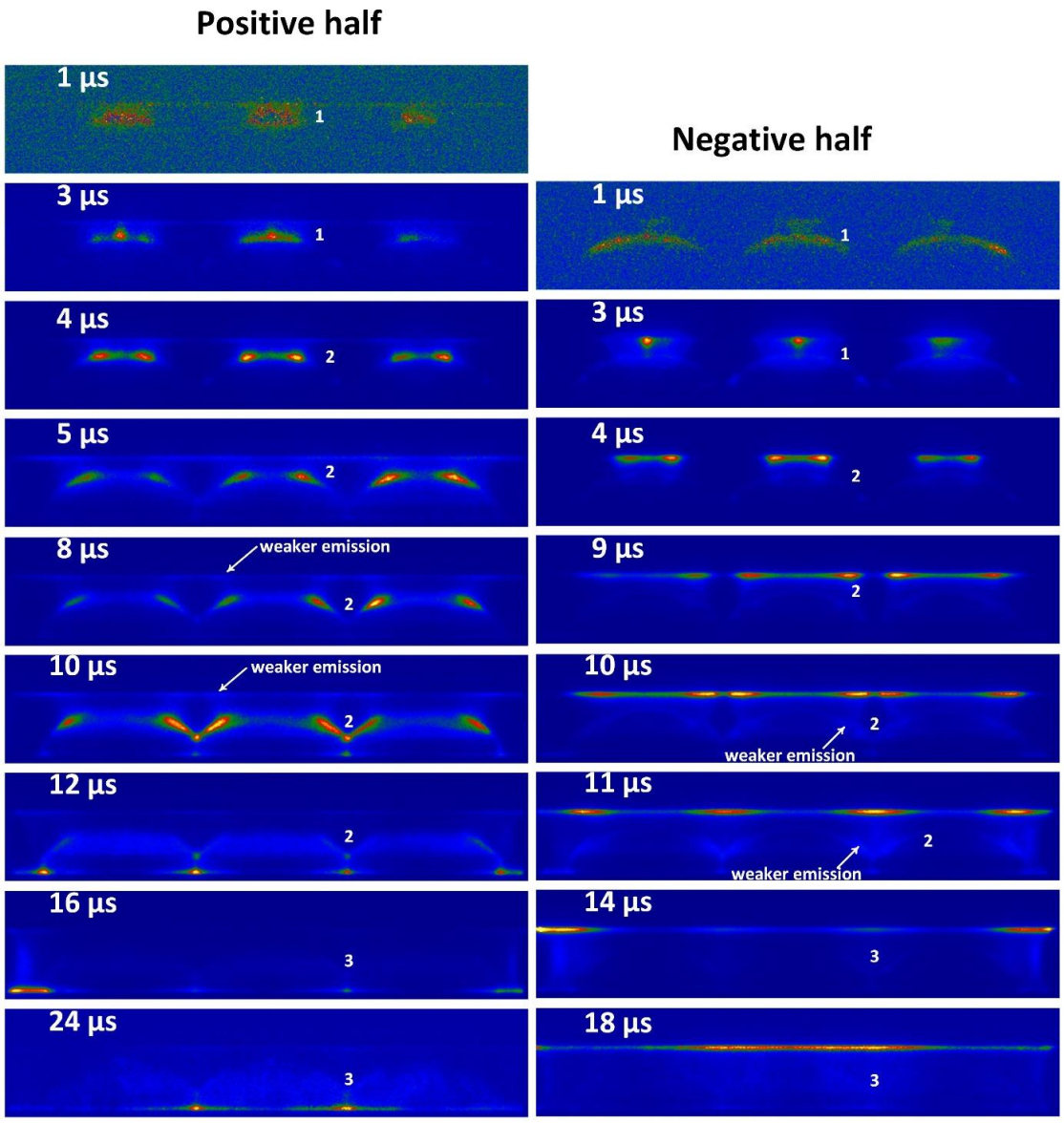

Fig. 3. 24 Time-resolved images of the He (3^3S_1) emission for the positive (left) and negative (right) half cycle, for an applied voltage amplitude of 3 kV. The images are recorded with an integration time and time shift of 1 µs.

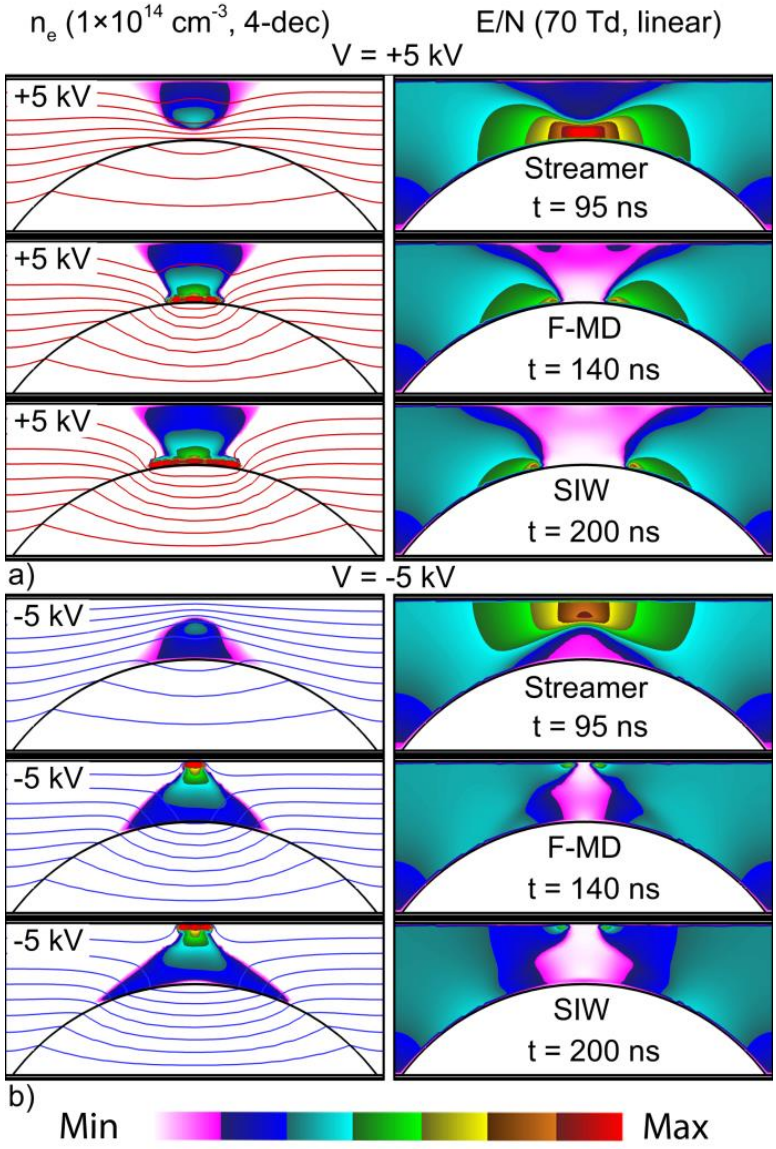

Fig. 3. 25 Evolution of electron density, equipotential lines (left) and reduced electric field (right) for a) +5 kV and b) –5 kV voltage pulses. Formation of positive streamers, filamentary micro-discharges and surface ionization waves are shown at times noted in the figure. Each equipotential line represents a potential change of 500 V. Electron densities are plotted on a log-scale.

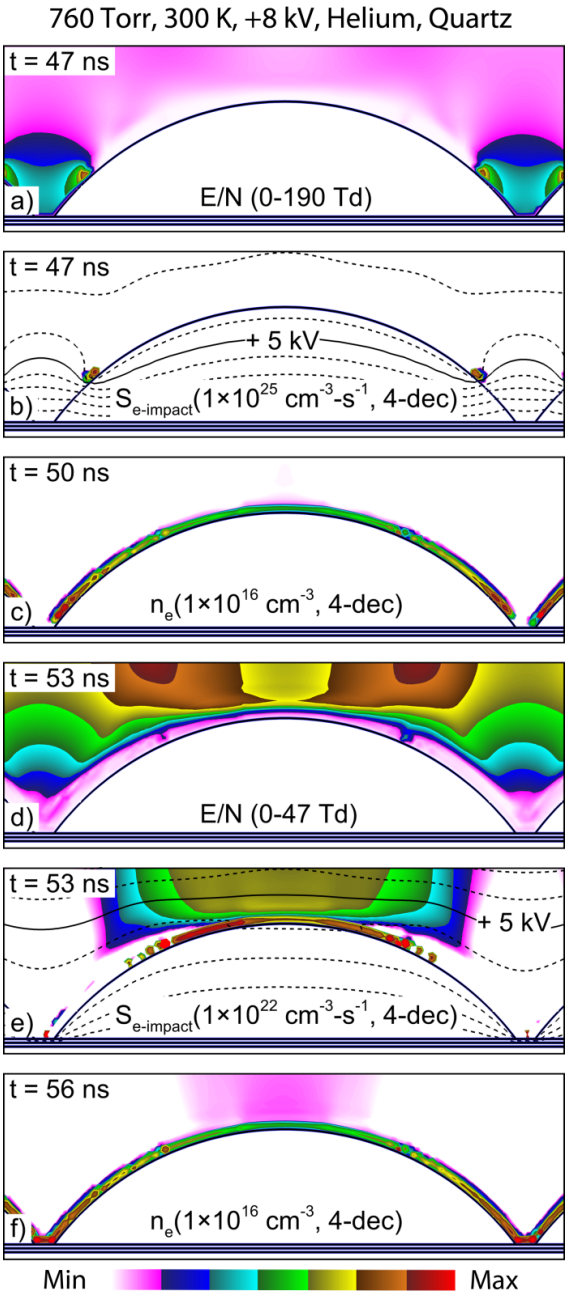

Fig. 3. 26 Reduced electric field (E/N), electron impact ionization source term, electron density for +8 kV applied voltage. Electric potential lines are overlaid on electron impact ionization source term contour plots, with each line representing a 1 kV change. Times and peak plotted values are noted in the figures.

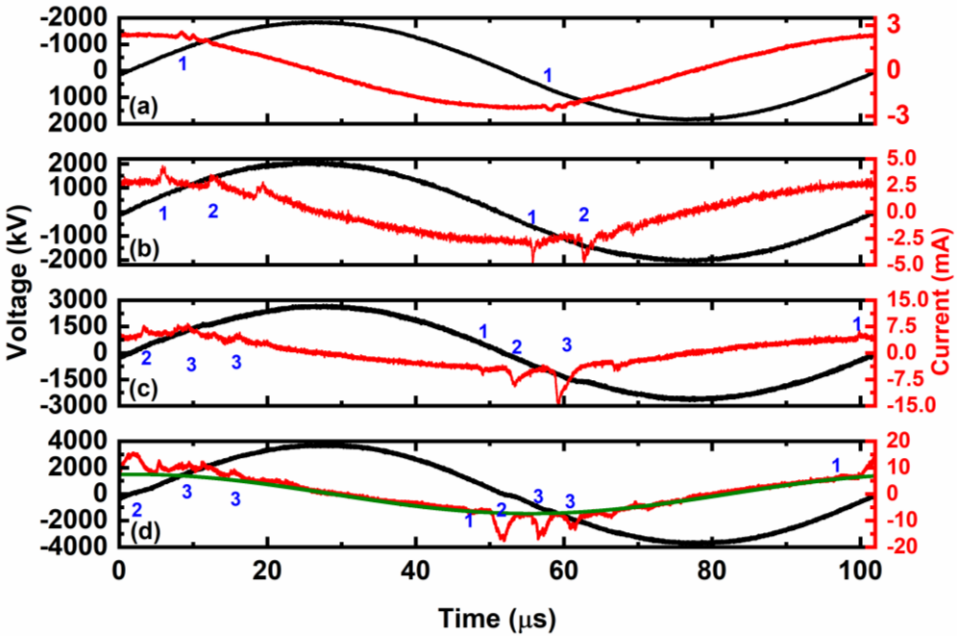

Fig. 3. 27 Voltage and current waveforms of a p-DBD operated in helium, at a peak-to-peak applied voltage of (top-to-bottom) 1.9, 2.25, 2.7 and 3.8 kV. Sinusoidal waveform with no discharge current profile is shown in green in d).

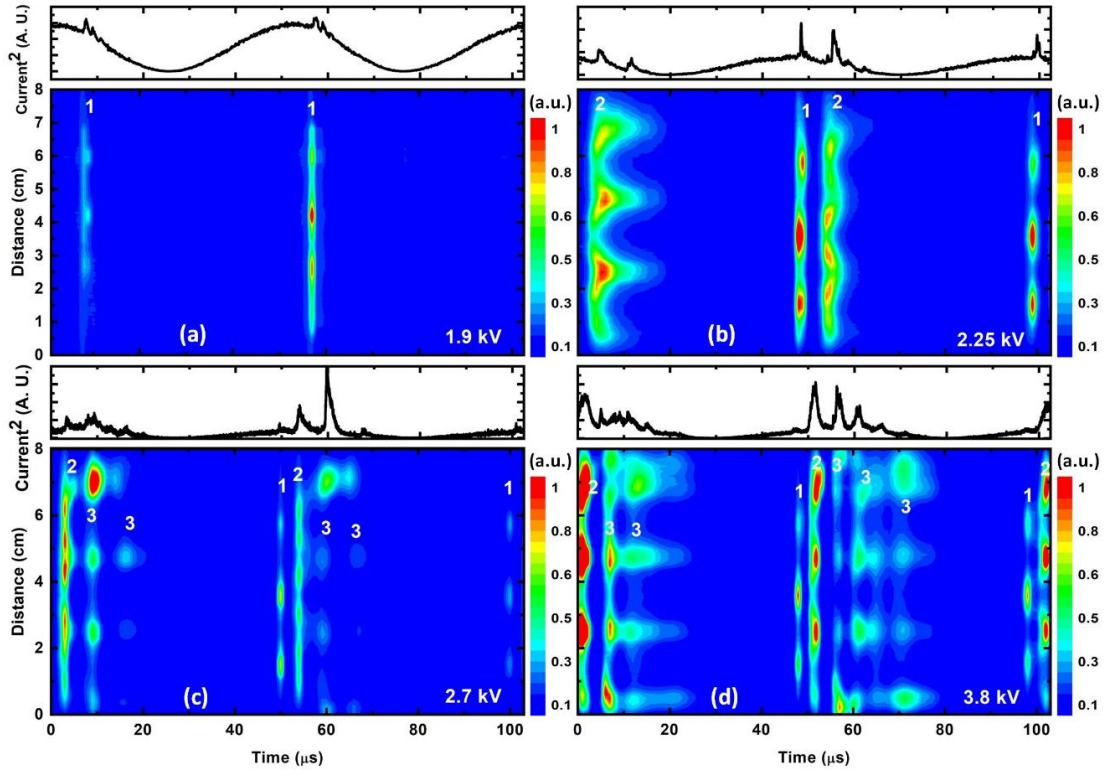

Fig. 3. 28 Time resolved variation of the (top) square of the current and (bottom) axial emission from the He (3^3S_1) state for voltage amplitudes of (a) 1.9 kV, (b) 2.25 kV, (c) 2.7 kV and (d) 3.8 kV.

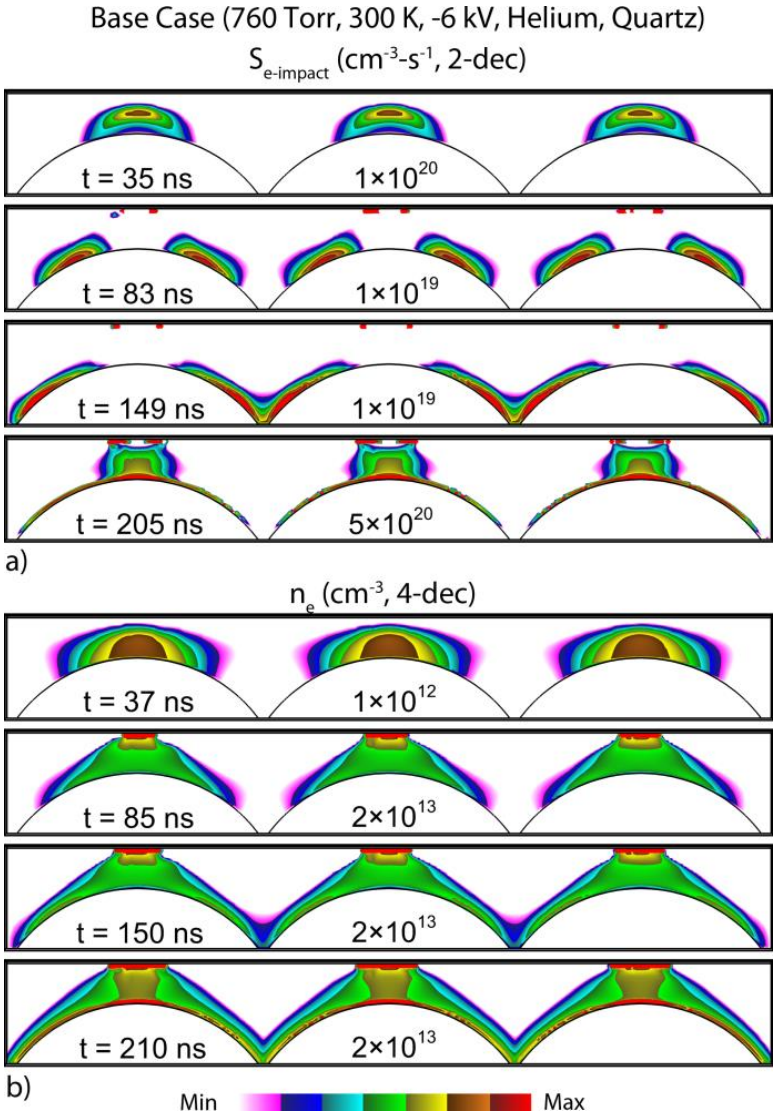

Fig. 3. 29 Evolution of a) electron impact ionization source term and b) electron density during the discharge in the negative base case (-6 kV). Times and peak plotted values are noted in the figures. Log scales.

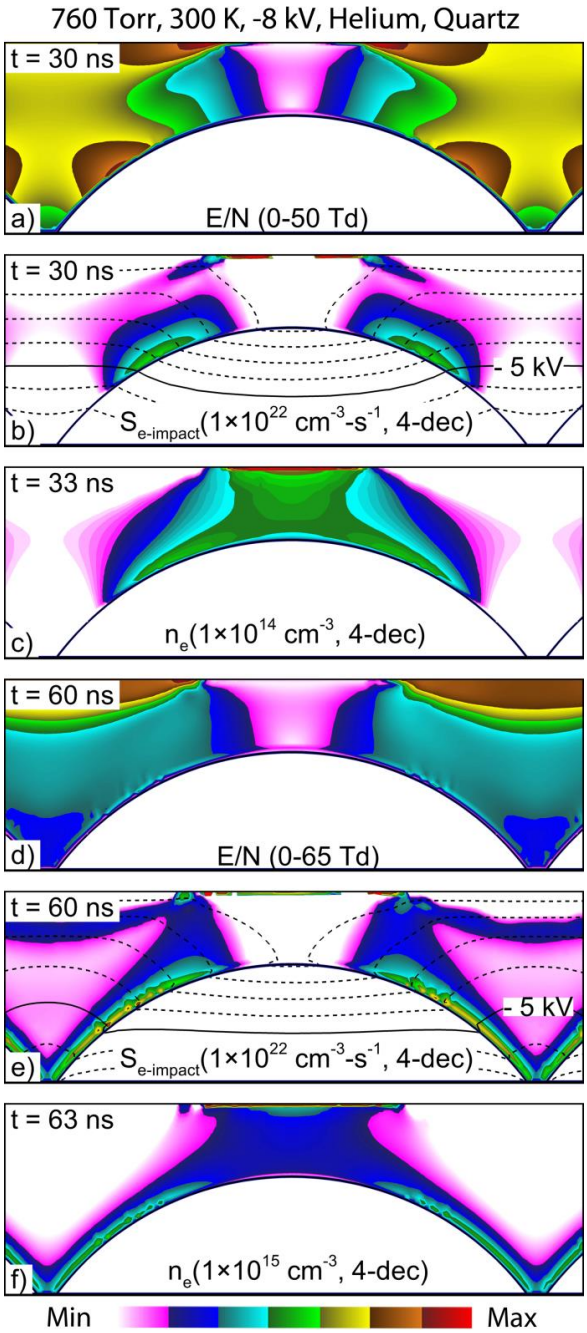

Fig. 3. 30 Reduced electric field, electron impact ionization source term, electron density for -8 kV applied potential. Electric potential lines are overlaid over electron impact ionization source term contour plots, with each line representing a 1 kV change. Times and peak plotted values are noted in the figures.

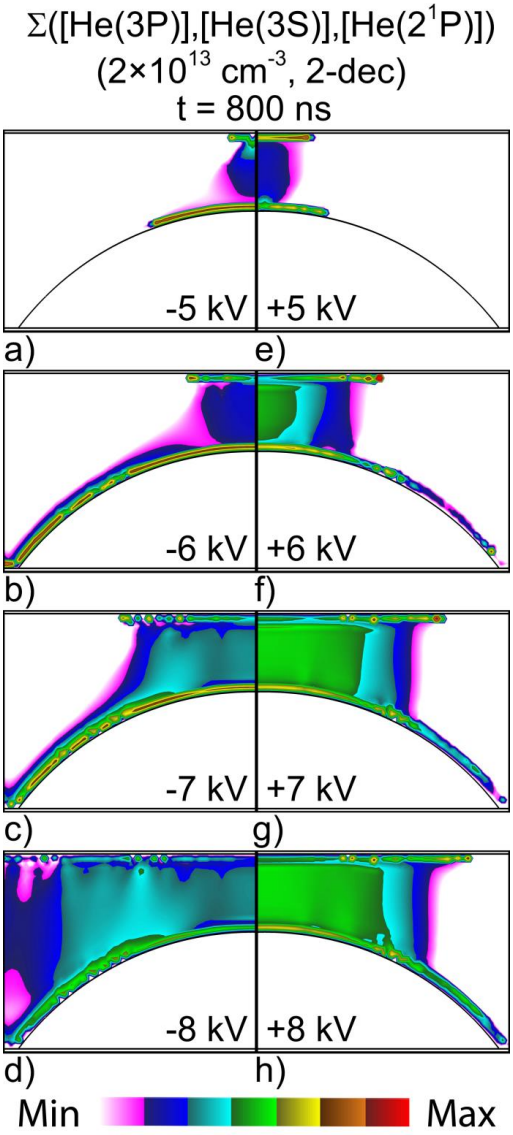

Fig. 3. 31 Sums of the densities of excited species of Helium emitting in the visible spectrum at 800 ns, and at different applied voltages.

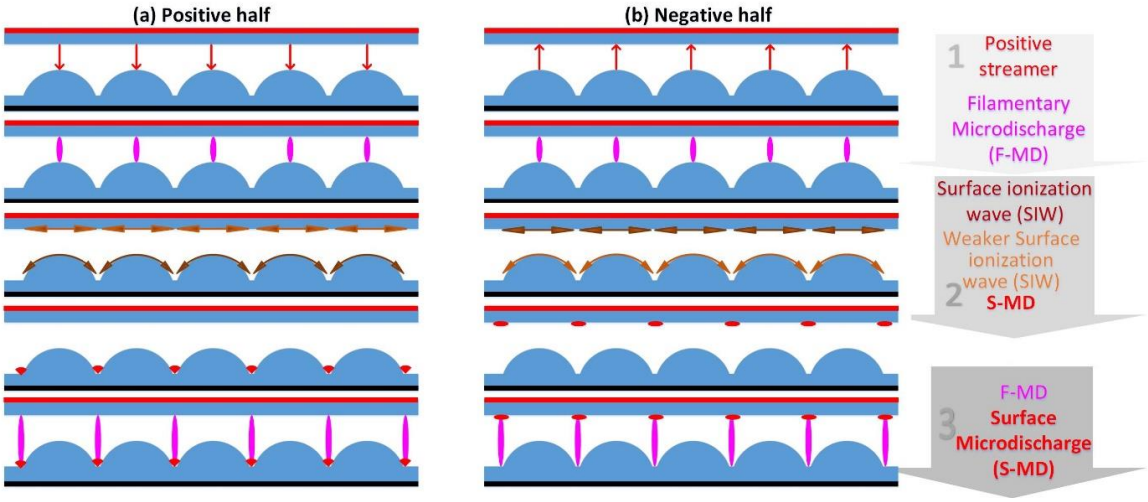

Fig. 3. 32 Schematic representing operation of the discharge for (a) positive and (b) negative polarities of the voltage.

3.7 References

[1] K. Schmidt-Szatowski and A. Borucka, Plasma Chem. Plasma Process. **9,** 235 (1989).

[2] S. Jodzis, Ozone Sci. Eng. **25,** 63 (2003).

[3] C. Chang and T. Lin, Plasma Chem. Plasma Process. **25,** 227 (2005).

[4] H.-X. Ding, A.M. Zhu, X.-F. Yang, C.H. Li and Y. Xu, J. Phys. D. Appl. Phys. **38,** 4160 (2005).

[5] Q. Yu, M. Kong, T. Liu, J. Fei and X. Zheng, Plasma Chem Plasma Process **32,** 153 (2012).

[6] H. Liang Chen, H. Ming Lee and M. Been Chang, Ozone Sci. Eng. **28,** 111 (2006).

[7] K. Takaki, J. S. Chang and K. G. Kostov, IEEE Trans. Dielectr. Electr. Insul. **11,** 481 (2004).

[8] D. B. Go and D. A. Pohlman, J. Appl. Phys. **107,** 103303 (2010).

[9] R. Dorai and M. J. Kushner, J. Phys. D. Appl. Phys. **36,** 666 (2003).

[10] D. K. Cheng, F. Wave Electromagn. 2nd Ed. 95 (1989).

[11] T. M. P. Briels, J. Kos, G. J. J. Winands, E. M. van Veldhuizen and U. Ebert, J. Phys. D. Appl. Phys. **41,** 234004 (2008).

[12] X. Tu, H. J. Gallon and J. C. Whitehead, IEEE Trans. Plasma Sci. **39,** 2172 (2011).

[13] X. Tu, H. J. Gallon, M. V Twigg, P. a Gorry and J. C. Whitehead, J. Phys. D. Appl. Phys. **44,** 274007 (2011).

[14] K. W. Engeling, J. Kruszelnicki, M. J. Kushner and J. E. Foster, Plasma Sources Sci. Technol. **27,** 085002 (2018).

[15] L. M. Vasilyak, S. V Kostyuchenko, N. N. Kudryavtsev and I. V. Filyugin, Phys. Uspekhi **37,** 247 (1994).

[16] V. Petrishchev, S. Leonov and I. V. Adamovich, Plasma Sources Sci. Technol. **23,** 065022 (2014).

[17] B. M. Goldberg, P. S. Böhm, U. Czarnetzki, I. V. Adamovich and W. R. Lempert, Plasma Sources Sci. Technol. **24,** 055017 (2015).

[18] A. Starikovskiy, IEEE Trans. Plasma Sci. **39,** 2602 (2011).

[19] J. Kruszelnicki, K. W. Engeling, J. E. Foster, Z. Xiong and M. J. Kushner, J. Phys. D Appl. Phys. **50,** 025203 (2017).

Chapter 4 Atmospheric Pressure Plasma Activation of Water Droplets[2]

Low temperature plasma treatment of water is being investigated due to its use in pollution abatement, wound treatment, and agriculture. Plasma-produced reactive oxygen and nitrogen species (RONS) are formed in the gas phase and solvate into the liquid phase. Activation of the liquid is often limited by transport of these RONS species to the liquid surface. Micrometer-scale droplets immersed in the plasma have a large surface-to-volume ratio (SVR), which increases the interaction area for a given volume of water and can increase the rates of transport from the gas to liquid phase. The solvation dynamics are sensitive to the Henry's law constant (h) of each species, which describes its hydrophobicity (low h) or hydrophilicity (high h). Constants used in this work are listed in Table 4.1. The liquid densities of stable species with high h values (e.g., H_2O_2 and HNO_x) are sensitive to droplet diameter. For large droplets, hydrophilic species may deplete the gas-phase inventory of RONS before liquid-phase saturation is reached, limiting the total density for species with high h. For smaller droplets, higher average in-droplet densities of these species can be produced. Liquid concentrations of stable species with low h (e.g., O_3, N_2O, and H_2) have a weak dependence on droplet size, as droplets are quickly saturated and solvation does not deplete the gas phase. Spatial non-uniformity of the plasma also has an impact on solvation rates and kinetics. Gas phase depletion of high h species leads to a decrease in solvation rates. Low h species that saturate the surface of the droplets during plasma-on periods can quickly de-solvate in the afterglow.

[2] The results discussed and a portion of the text in this chapter have been previously published in J. Kruszelnicki, A. M. Lietz, and M. J. Kushner, "Atmospheric pressure plasma activation of water droplets", J. Phys. D.: Appl. Phys. **52**, 355207 (2019).

4.1 Introduction

Plasma/liquid interactions have the ability to impact growth of seeds, sterilize surfaces, and treat diseases and are therefore an active area of investigation [1]. From a pollutant remediation perspective, plasma acts as an advanced oxidation method, enabling its use to address a variety of pollutants [2–4]. From a biomedical perspective, the beneficial effects of plasma-treated liquids are generally attributed to the production of reactive oxygen and nitrogen species (RONS) by the plasma, which solvate in and further react in the liquid [5–12].

For example, H_2O_{2aq} can act as either an oxidant (reduction potential $E^0 = 1.77$ V) or a reductant ($E^0 = -0.70$ V) [13]. (The "aq" subscript denotes a solvated or in-liquid aqueous species.) The oxidation probability of a species is measured by its reduction potential, E^0, which describes the propensity to acquire electrons in a solution. E^0 is analogous to pH as means of determining proton transfer. H_2O_{2aq} may produce DNA damage and oxidize lipids and proteins, thereby affecting the viability of human cells [14]. H_2O_{2aq} reacts with nitrite ($NO_2^-{}_{aq}$) to form peroxinitrite ($ONOO^-{}_{aq}$), which can affect the physiology of living cells and participate in catalytic processes that affect the abatement of water pollutants [15–17].

Ozone, an oxidative product of discharges in air with $E^0 = 2.07$ V, is relatively stable in water with a half-life of thousands of seconds in the absence of impurities such as organics [13,18]. Ozone is effective in abating a wide range of micro-pollutants, pharmaceutical compounds, pesticides, and endocrine disruptors from water [19]. The direct reactions between ozone and organic compounds in water are often pH-dependent [20]. Since plasma treatment may reduce the pH of liquids, regulating the pH of the liquid by plasma exposure may enable additional control over liquid kinetics and selectivity [21].

APPs in humid mixtures produce hydroxyl radicals, which are the strongest oxidant in

aqueous solutions, with $E^0 = 2.85$ V [13]. This large reduction potential enables OH_{aq} to degrade a variety of chemical compounds, including phenol and aromatic hydrocarbons, organic dyes, and aliphatic compounds [13]. OH_{aq} attacks the outer cell membranes enabling microbial decontamination of water and surfaces [13,22]. The reactivity of OH_{aq} results in the formation of numerous secondary species [6].

Many types of low temperature plasma sources have been experimentally investigated for water treatment [23–29]. Modeling efforts have addressed the kinetics and dynamics of plasma-liquid interactions [26,30–32]. The majority of plasma sources for treating liquids are designed to keep the temperatures of both the gas and liquid low, as the liquid being treated (or, in the case of biomedical applications, the tissue lying under the liquid) is often heat sensitive. When the liquid (or contacting surface) is not heat sensitive, higher specific power can be used. Low temperature plasma sources investigated for sterilization or water treatment include a plasma jet impinging onto a water surface, a pin-to-pin discharge in liquid water, discharges sustained in bubbles, two-phase gliding arc discharges, and treatment of films of water flowing through a dielectric barrier discharge [33–37].

Many water treatment applications require processing large volumes of water, while in other applications, treatment is more focused on producing high concentrations of RONS. In either case, activation of the liquid is typically transport limited. The activating species must first transport from their site of creation in the plasma to the surface of liquid. The species must then transport into the liquid and finally transport from the surface of the liquid into the interior. Many of these transport limits can be addressed by plasma activation of small liquid droplets immersed in the plasma. In this plasma activation scheme, radicals and ions are produced in the immediate vicinity of the droplet, thereby minimizing transport limits to the liquid surface. The large surface-to-

volume ratio of small droplets then minimizes transport limits from the surface of the liquid into the bulk of the liquid. Several experimental studies have shown efficient plasma activation of droplets, as compared to the treatment of bulk liquids. For example, plasma treatment of droplets by electrospray of water has been found to be effective for the inactivation of biofilms [22,37]. Plasma-treated water mist has effectively sterilized *E. coli* and influenced the production of RONS in the liquid [38]. Plasmas also produced high densities of species with high oxidation potential – H_2O_{2aq}, OH_{aq}, and $O3_{aq}$ [39].

In this chapter, results are discussed from a computational investigation of plasma treatment of water droplets. Fundamental scaling laws and plasma chemistry of the air plasma-water droplet system are investigated using global models and analytical analysis. Results from 2-dimensional modeling that incorporate the consequences of electrodynamics, anisotropy, and local transport are also discussed. Droplets were exposed to a series of hundreds of pulses, followed by an afterglow period. We found that the primary neutral reactive species produced in the droplets are acids, HO_{2aq}, H_2O_{2aq}, and O_{3aq}. Hydroxyl radicals are also formed at high rates during the plasma-on periods. However, radicals there are generally confined to the surface of the droplets due to their high reactivity and short lifespans. The primary terminal species are $NO_3^-{}_{aq}$, and $H_3O^+_{aq}$, the high densities of which leads to a significant decrease in the pH of the water droplets to as low as pH $\approx$ 1 at droplet diameters of 5 μm. The surface-to-volume-ratio (SVR) significantly impacts the final average densities of species possessing a high Henry's law constant, *h*. Conversely, densities of aqueous hydrophobic species with low *h* show little dependence on the diameter of the droplets. This selectivity based on *h* could provide additional avenues to selectively control liquid kinetics. The spatially-resolved 2-d modeling further shows that aqueous species, which reach their saturation densities at the surface of the droplet during plasma pulsing,

may de-solvate at high rates in the afterglow in order to maintain gas-liquid equilibrium. Control over the size and distribution of droplets is, therefore, critical for the efficient transfer of the desired reactive plasma species to and from the liquid.

The models are described in Sec. II. The reaction mechanisms and initial conditions are discussed in Sec. III. Discussed in Sec. IV are the results from global modeling, including the dynamics of the base case, the effect of droplet diameter, the role of depletion of species from the gas phase, and the number of droplets. Results from the 2-dimensional modeling investigation of reactive species transport are discussed in Sec. V. Concluding remarks are in Sec. VI.

4.2 Description of the Model

Transport of neutrals is calculated using a species-specific, local diffusion coefficient everywhere, except for the liquid-gas boundary region. In this study, convection by bulk gas flow is not considered. The specific calculation performed at the gas-liquid boundary is described below. Radiation transport is performed using a Green's function formulation to provide fluxes from each node to a set of neighbors within its line-of-sight. Photoionization of O_2 by photons emitted by excited nitrogen species ($N_2(C^3\Pi)$ and $N_2(E^3\Sigma)$) is included. The non-ionizing absorption cross sections in the base case are 1×10^{-18} cm^2 for O_2 and N_2, and 3×10^{-17} cm^2 for H_2O, while the ionization cross section is assumed to be 1×10^{-19} cm^2 [40]. No photoionization of the liquid species is included in these cases. Transport of gas and liquid phase species within their respective phases is given by their diffusion (or drift-diffusion) fluxes using transport coefficients for that phase. The flux of a gas phase species into the liquid, Γ_{gl}, is limited by Henry's law equilibrium at the surface of the liquid. Further details regarding *nonPDPSIMs* can be found in Chapter 2.

The use of Henry's law in this system has certain short-comings, even if applied only at the surface. First, using this method assumes that the system is at kinetic equilibrium, which may not necessarily be the case for our conditions. Assuming kinetic equilibrium could lead to underestimating the flux of species entering the liquid [41]. However, because Henry's law is applied only at the surface, the assumed equilibrium is only local and not global. For species and droplet sizes of interest, this time is between microseconds and 10s of seconds – all vastly exceeding the femtosecond-level time-steps taken in the simulations. The limits on transport into and out of the liquid reflect the evolution of the species' densities in time. At these time and length scales, the assumptions of local kinetic equilibrium hold, and Henry's law allows for first-order approximation of evolutions of densities.

The use of Henry's law also assumes thermodynamic equilibrium where it is applied, in this case, only at the surface of the liquid [42]. The variations in Henry's constants with gas temperatures can be large – changing by as much a factor of two for a 10 K change in temperature [41]. Although gas and liquid temperatures are computed, the temperature dependence of Henry's law constants is not currently accounted for in the model, which could lead to quantitative errors in saturation densities. However, the scope of this work is to show the differences in the behavior of species with vastly different h values. This qualitative comparison should not be impacted by temperature because Henry's law constants for all species generally follow similar trends – increasing with temperature [43].

Rates of solvation may also vary with the radius of the droplet, particularly as the droplet evaporates. In this work, the background gas is highly humid at 1% H_2O. As a result, the impact of evaporation is decreased. However, the evaporation of the microscopic droplets, particularly at low pressures and high temperatures, is a complex process [44]. Evaporation initiates additional

phenomena – for example, Stefan flow, wherein spatial gradients in vapor densities near the droplet cause convective movement of the fluid [45]. Proper resolution of Stefan flow should be addressed by dedicated models, adding a level of complexity beyond the scope of this study [46]. Here, evaporation from the liquid water into the gas is addressed by maintaining a surface density of water vapor equal to the vapor pressure of liquid water. This surface density of gas phase water then acts as a source for the diffusion of water vapor into the gas. Due to limitations in the numerical mesh (the mesh is not adaptive), the volume of water is held constant.

Numerous studies have been performed in the area of atmospheric aerosols and their ability to scavenge compounds. For example, Djikaev and Tabazadeh modeled a droplet's ability to adsorb and solvate organic species as a function of the droplet diameter [47]. Their theory predicts large increases in the effective Henry's law constant for small droplets. The model requires an affinity parameter, b, that is related to the probabilities of adsorption and desorption, which can be calculated from molecular dynamics simulations [48]. Based on these results, $b = 1.01$ for O_3 and $b = 11.1$ for H_2O_2. Using the theoretical formulation of Djikaev and Tabazadeh for the conditions in this chapter, the effective h increases by no more than 50% for O_3 and 5% for H_2O_2 for the smallest droplet diameter included in this study (0.1 μm). These enhancements in h are small compared to the variation in Henry's law constants between species, which span 7 orders of magnitude.

To address reaction kinetics over long interpulse and afterglow periods, a neutral plasma option is developed for *nonPDPSIM*. Using this option, Poisson's equation is not solved and charge neutrality is enforced. The neutral-plasma option is typically invoked sufficiently after the discharge pulse that ion densities have decreased to the point that reactivity is dominated by neutral species. Any space charge that may remain at that time is removed not only by scaling the local

densities of positive ions to match the densities of the negative ions in the regions of negative space-charge, but also by increasing electron density into the regions of positive space-charge. The diffusion coefficients of all ions are then averaged to prevent charge separation and the electron density is set equal to the positive ion minus the negative ion densities. The shortest time-scales are then dictated by the reaction mechanism, which then enables time-steps up to microseconds. The integration of the continuity equations in the neutral-plasma period is performed implicitly, with gradual, dynamic increases in the time-steps from 10^{-9} s at the end of the discharge pulse to 10^{-6} s towards the end of the subsequent afterglow.

Multiple discharge pulses are addressed in the same manner as described in Ref. [49]. Following simulation of the first discharge pulse during which Poisson's equation is solved, the source functions for radicals and ions are recorded. On the timescales of the interpulse period, the discharge pulses appear to be instantaneous. Assuming this delta-function-like production of reactive species is the same on each pulse following the first, the recorded source functions are added to the rate equations at the specified pulse repetition frequency (PRF). This integration with impulsive additions is performed using the neutral-plasma option. This technique does not capture the change in source functions that may result from changes in gas phase densities, which would require that each discharge pulse be individually resolved solving Poisson's equation. It does, however, allow for approximation of source functions that enable simulation of tens to thousands of pulses, which would otherwise be prohibitive.

4.2.1 Reaction Mechanism

The mechanism includes 88 gas phase species, 93 liquid species, 1855 gas phase reactions, and 176 liquid reactions simulating humid-air plasma interactions with liquid water droplets.

In the gas phase, during the discharge pulse, the generation of electrons is driven by the electron impact ionization of N_2, O_2, and H_2O, including the reactions

$$e + N_2 \rightarrow N_2^+ + e + e, \quad (4.1)$$

$$e + N_2 \rightarrow N^+ + N + e + e, \quad (4.2)$$

$$e + O_2 \rightarrow O_2^+ + e + e, \quad (4.3)$$

$$e + O_2 \rightarrow O^+ + O + e + e, \quad (4.4)$$

$$e + H_2O \rightarrow H_2O^+ + e + e. \quad (4.5)$$

The dominant mode of electron energy loss is inelastic collisions producing electronic, vibrational, or rotational excitation. In this reaction mechanism, the rotational and vibrational states of O_2 and N_2 are each approximated as a single state [$O_2(r)$, $O_2(v)$, $N_2(r)$, and $N_2(v)$], and only a single vibrational excited state of H_2O [$H_2O(v)$] is included.

The dissociation of O_2, N_2, and H_2O is critical for generating the RONS that activate water. Electron impact dissociation generates reactive products, while the electron temperature is elevated during the voltage pulse, including

$$e + N_2 \rightarrow N + N + e, \quad (4.6)$$

$$e + O_2 \rightarrow O + O + e, \quad (4.7)$$

$$e + H_2O \rightarrow OH + H + e, \quad (4.8)$$

$$e + H_2O \rightarrow O + H + H + e, \quad (4.9)$$

$$e + H_2O \rightarrow O + H_2 + e, \quad (4.10)$$

Attachment to O_2 and H_2O result in electron losses during and immediately after the plasma pulse, with the dissociative processes producing additional radicals,

$$e + O_2 \rightarrow O^- + O, \quad (4.11)$$

$$e + O_2 + M \rightarrow O_2^- + M, \quad (4.12)$$

$$e + H_2O \rightarrow O^- + H_2, \quad (4.13)$$

$$e + H_2O \rightarrow OH + H^-, \quad (4.14)$$

$$e + H_2O \rightarrow OH^- + H, \quad (4.15)$$

where M is a third body. After initial dissociation produces reactive neutrals, reactions among these species generate more complex species such as O_3, H_2O_2, NO_x, and HNO_x.

The gas-phase reaction set is a modified version of the mechanism developed by Van Gaens *et al* [50]. A schematic of the liquid water reaction mechanism is in Fig. 4.1. The mechanism has been previously discussed in detail and so will only be summarized here [51]. The plasma-produced species that come in contact with the liquid include electrons, positive and negative ions, excited neutrals, and ground state neutrals. The electrons that enter the liquid are rapidly solvated, and then undergo dissociative attachment with water, forming H_{aq} and OH^-_{aq}. Most of the positive ions (with the exception of H_3O^+) solvate charge exchange with H_2O_{aq}, forming $H_2O^+_{aq}$, followed by

$$H_2O^+_{aq} + H_2O_{aq} \rightarrow H_3O^+_{aq} + OH_{aq}, \quad (4.16)$$

producing hydronium and a hydroxyl radical. Electronically excited gas phase species entering the liquid that have enough energy to dissociate a water molecule are assumed to undergo dissociative excitation transfer reaction with H_2O_{aq} producing H_{aq} and OH_{aq}. Excited states with less energy than this threshold energy, such as vibrationally excited molecules, simply collisionally de-excite.

The mechanism includes forward and reverse reactions for acids in the liquid, HA_{aq}, which enable them to dissociate and recombine according to their equilibrium pKa ($HA_{aq} + H_2O_{aq} \leftrightarrow A^-_{aq} + H_3O^+_{aq}$). These acids include HNO_{3aq}, HNO_{2aq}, $ONOOH_{aq}$, HO_2NO_{2aq}, H_2O_{2aq}, and HO_{2aq}. HNO_{3aq} is the only strong acid that completely dissociates into $NO_3^-{}_{aq}$ and $H_3O^+_{aq}$. During the

afterglow following repetitive discharge pulses, the other weak acids stay predominately in the form of HA_{aq} rather than in the form of their conjugate bases, A^-_{aq}.

The reactive neutrals in the liquid are primarily produced by solvation of their gas phase counterparts. Important reactions occurring in the liquid, which convert solvated species from the plasma into more stable compounds, include the reactive oxygen species (ROS) reactions,

$$OH_{aq} + OH_{aq} \rightarrow H_2O_{2aq}, \quad (4.17)$$

$$H_{aq} + H_{aq} \rightarrow H_{2aq}, \quad (4.18)$$

$$O_{aq} + H_2O_{aq} \rightarrow OH_{aq} + OH_{aq}, \quad (4.19)$$

$$O_{aq} + O_{2aq} \rightarrow O_{3aq}, \quad (4.20)$$

and the reactive nitrogen species (RNS) reactions,

$$N_{aq} + N_{aq} \rightarrow N_{2aq}, \quad (4.21)$$

$$N_2O_{5aq} \rightarrow NO_{2aq} + NO_{3aq}, \quad (4.22)$$

$$N_2O_{5aq} + H_2O_{aq} \rightarrow HNO_{3aq} + HNO_{3aq}, \quad (4.23)$$

$$N_2O_{5aq} + H_2O_{aq} \rightarrow ONOOH_{aq} + ONOOH_{aq}, \quad (4.24)$$

$$NO_{2aq} + OH_{aq} \rightarrow HNO_{3aq}, \quad (4.25)$$

$$NO_{3aq} + H_2O_{aq} \rightarrow HNO_{3aq} + OH_{aq}. \quad (4.26)$$

The mechanism includes slow-decay processes. Several species – including O_3, H_2O_2, ONOOH, and HO_2NO_2 – are relatively stable and often survive for several minutes after the plasma treatment. However, as slow reactions or thermal decay occur at long timescales, these relatively stable species can produce more reactive products, such as OH_{aq}, NO_{aq}, HO_{2aq}, O_{aq}, and NO_{2aq}. These chain reactions enable plasma-activated liquids to deliver reactivity long after the plasma treatment has ended. Several important slow-decay reactions include

$$H_2O_{2aq} + OH_{aq} \rightarrow HO_{2aq}, \quad (4.27)$$

$$O_3^-{}_{aq} + H_3O^+{}_{aq} \rightarrow OH_{aq} + O_{2aq} + H_2O_{aq}, \quad (4.28)$$

$$O_{3aq} \rightarrow O_{aq} + O_{2aq}, \quad (4.29)$$

$$H_2O_{2aq} + H_{2aq} \rightarrow H_{aq} + OH_{aq} + H_2O_{aq}, \quad (4.30)$$

$$ONOOH_{aq} + H_2O_{aq} \rightarrow OH_{aq} + NO_{2aq} + H_2O_{aq}, \quad (4.31)$$

$$HO_2NO_{2aq} \rightarrow HO_{2aq} + NO_{2aq}. \quad (4.32)$$

In the discussion that follows, particular attention will be paid to ozone and hydrogen peroxide due to the large difference in their Henry's law constants (≈ 0.274 and $\approx 1.92 \times 10^6$, respectively), their stability in aqueous form, and their use in biological processes and abatement of pollutants. Note will also be made of the pH of the droplets. The pH of the droplets is calculated based on the molarity of hydronium, $H_3O^+{}_{aq}$,

$$pH = -\log_{10}\left([H_3O^+_{aq}]\right), \quad (4.33)$$

where the density of $H_3O^+{}_{aq}$ is in moles/liter.

In the *nonPDPSIM*, a species is a gas phase or solvated species depending on its location in the mesh – gas phase or liquid. In cases where different reactions occur in the gas and liquid phases for the same gas phase and solvated analogues, the same radical is treated as a different species in the gas and liquid. In doing so, an artificial reaction is added to the mechanism to quickly convert a gas species to its solvated analogue (or vice versa) when crossing the gas-liquid interface. With prior knowledge of the importance or lifetimes of a species, the gas-to-liquid conversion can be used to economize on the number of species and reactions. For example, knowing that $N_2(v)$ quickly collisionally relaxes as it solvates into the water, a single reaction is used to represent both processes, $N_2(v) + H_2O_{aq} \rightarrow N_{2aq} + H_2O_{aq}$. Using this method, the number of liquid species in the 2-d model is reduced from 93 to 36 without significantly changing the reaction mechanism.

4.2.2 Model Parameters

Two types of 2-dimensional simulations are performed to distinguish the effects of the non-uniformity of the plasma from the spatial dependence of solvation of reactive species. The first simulation, called *reactive diffusion*, addresses a single water droplet surrounded by humid air containing a uniform density of RONS. The simulation tracks the resulting transport and chemistry as these species react in the gas phase, solvate, and react in the water. The second type of simulation is of a DBD in which an ionization wave (IW) produces a non-uniform distribution of RONS. In both cases, no fluid flow is simulated.

A schematic of the reactive diffusion geometry is in Fig. 4.2. The numerical mesh is cylindrically symmetric about the left boundary with a single droplet at the center. The initial densities of gas-phase species are taken from global modeling after 500 pulses with no liquid present in the reactor, but otherwise with parameters the same as those of the base case. These initial densities are in Table 4.2. The liquid is initialized with a pH = 7 (1.85 ppb $H_3O^+_{aq}$ and OH^-_{aq}), and with the Henry's law equilibrium density of N_{2aq} (8.75 ppm) and O_{2aq} (4.69 ppm). Electrodynamic equations are not solved in this geometry with the intent of investigating space-resolved droplet chemistry in a reactor following many discharge pulses, but without direct plasma interaction with the liquid.

The second geometry shown in Fig. 4.3 is that of a DBD reactor with a 1 mm gas gap and, for the base case, a d = 10 μm diameter liquid droplet at its center. The mesh is cylindrically symmetric about the left boundary. The resolution of the mesh varies from 90 μm in the solids to 1 μm near the surface of the droplet. The mesh nodes neighboring the surface of the liquid are equidistant from the surface in order to prevent the artificial enhancement of electric fields and

solvation rates. The top electrode is the cathode, while the bottom electrode is grounded. Both electrodes are covered by a dielectric with $\varepsilon/\varepsilon_0 = 4.0$. A small cloud of neutral plasma (electrons and oxygen (O_2^+) nitrogen (N_2^+) ions) is initialized at the intersection of the axis and the top dielectric. The peak density is 10^{11} cm^{-3}, with a Gaussian distribution to 10^6 cm^{-3}, resulting in a radius of approximately 50 μm. No other pre-ionization is included. The gas is humid air having a relative humidity of 29% ($N_2/O_2/H_2O$ = 78/21/1). As in the reactive diffusion simulations, the water is initialized as being at equilibrium with air with N_{2aq} and O_{2aq} at their Henry's law equilibrium densities, and a pH ≈ 7.

4.3 Spatial Effects in Plasma Activated Droplets

4.3.1 Reaction-Diffusion: Uniform Initial Gas-Phase Densities

Simulating a droplet interacting with uniformly distributed gas-phase species emulates a diffuse plasma reactor or a droplet entering a reactor directly after the plasma has been turned off. This approach is conceptually similar to global modeling, while accounting for local gradients both in the gas phase and in the droplet. The base case has a 10 μm droplet at the center of a cylindrically symmetrical reactor with a height of 0.46 mm and radius of 0.23 mm. The densities of liquid and gas-phase of OH, H_2O_2, and O_3, are shown in Fig. 4.4 after 1.0 ms. The mean lifetime of OH_{aq} in the liquid is approximately 200 μs, which is reflected in its short penetration distance into the droplet, as shown in Fig. 4.4 a). The OH_{aq} densities are highest at the surface of the droplet, with OH_{aq} combining to form H_2O_{2aq} before diffusing into the interior of the droplet. However, the main source of H_2O_{2aq} is not hydroxyl reactions in the droplet, but rather solvation of H_2O_2 from the gas-phase. A depletion region of H_2O_2 forms near the surface of the droplet as H_2O_2 rapidly solvates at the surface (Fig. 4.4 b)). The Henry's law constant for H_2O_2 is high ($h = 1.92 \times 10^6$),

so the droplet can support liquid-phase densities that are six orders of magnitude greater than those in the gas-phase before saturating. The opposite is true for ozone (h = 0.274). The droplet quickly saturates with O_{3aq} and solvation from the gas phase ceases – no local gas phase depletion occurs (Fig. 4.4 c)).

The average aqueous densities of selected species after 80 ms as a function of droplet diameter are shown in Fig. 4.5. These results mirror those from the global simulations. The high-h, stable species are sensitive to droplet diameter. The densities of H_2O_{2aq} decrease from 1.5×10^{16} cm^{-3} (2.5×10^{-5} M) for a droplet diameter of d = 5 μm to 1.0×10^{14} cm^{-3} (2.0×10^{-6} M) for d = 1 mm. Similarly, the average density of hydronium decreases from 2.0×10^{18} cm^{-3} (3.3×10^{-3} M) to 1.0×10^{16} cm^{-3} (1.7×10^{-5} M) resulting in an increase of average pH (2.5 at d = 5μm to 4.8 at d = 1 mm). Low-h and long-lived aqueous species have densities that are nearly independent of droplet diameter. The change in O_{3aq} density, for example, is less than 10% when the droplet diameter increases from 5 μm and to 1 mm. As discussed for the global modeling, when high-h gas phase species solvate and fail to saturate the droplet, their local gas densities are depleted around the droplets, leading to lower rates of solvation in the afterglow. The effect is more dramatic when accounting for local depletion and gradients around the droplets, which then increase the effect distance from the droplet from which the solvating species originate.

4.3.2 Droplet in a DBD

The geometry in Fig. 4.3 is used to simulate a DBD sustained in humid air interacting with a single droplet, enabling analysis of the discharge dynamics, as well as of the effect of non-isotropic distribution of reactive species. A step pulse of -13 kV is applied to the cathode and held constant for approximately 2 ns – sufficient for the development of a microdischarge in this 1-mm

gap. The applied electric field is ≈ 500 Td or 120 kV-cm^{-1}. Assuming typical values for conductivity and permittivity of ultra-pure water (5.5×10^{-8} S-cm^{-1} and 7.1×10^{-12} F-cm^{-1}), the dielectric relaxation time of the droplet is approximately 0.13 ms [52,53]. As a result, the liquid behaves like a dielectric over the timescale of the discharge. When the external electric field is applied, dielectric polarization of the droplet leads to regions of electric field enhancement at the vertical poles of the droplet, with a peak of ≈ 1200 Td or 310 kV-cm^{-1}, as shown in Fig. 4.3 d). This electric field enhancement increases the likelihood of discharge formation in the vicinity of the droplet.

The electron density (n_e) and electron impact ionization source term (S_e) are shown as a function time in Figs. 4.6 and 4.7. Following application of the negative voltage, separation of charges occurs in the initial plasma cloud, with electrons accelerating downward towards the ground. This initial breakdown resembles a Townsend avalanche, with a local peak electron density ≈ 3×10^{13} cm^{-3} and peak electron-impact ionization rate of 5.5×10^{23} cm^{-3}-s^{-1} (Figs. 4.6 a), 4.7 a)). As the avalanche reaches the droplet, the discharge enters the region of electric field enhancement produced by the dielectric polarization. The high electric field produces an increase in T_e (maximum ≈ 10.6 eV) and in S_e (maximum ≈ 4.5×10^{24} cm^{-3}-s^{-1}) near the droplet surface (Fig. 4.7 b)). The electron density then increases to ≈ 1.5×10^{14} cm^{-3} in the same region (Fig.4.6 b)).

Following this initial interaction between the plasma and droplet, a cathode-seeking restrike propagates from the surface of the droplet. Simultaneously, the primary (negative) ionization wave propagates downwards around the droplet towards the ground. The region directly beneath the droplet is temporarily shielded from the plasma by charging of the surface, leading to anisotropy in the charge distribution (Fig. 4.6 c)). By t = 1.15 ns, a microdischarge bridges the entire gas gap and envelops the droplet in plasma. Simultaneously, surface ionization waves

develop along the dielectric covering both electrodes, with electron density reaching its maximum value of 8.5×10^{15} cm^{-3} near the cathode. The electron density near the droplet is maximum at 1.95×10^{14} cm^{-3} at its top vertical pole. In spite of the locally high electric field, the region near the bottom pole of the droplet does not undergo breakdown due to the droplet shielding it from the initial negative streamer. This then leads to a change in polarity of surface charging between the top and bottom poles of the droplet.

Primary gas-phase species produced during the pulse are ions (O_2^+, N_2^+, and N^+), products of electron impact dissociation of primary background gases (N, O, and OH), and vibrationally excited nitrogen and oxygen molecules. The highest densities of these species occur in the upper foot of the microdischarge along the dielectric due to the high intensity of the surface ionization wave. The distributions of species around the droplet are due the anisotropy of the electron avalanche around the droplet.

With the conductivity of the droplet low, the charges solvating into the outer layers of the droplet do not dissipate on short timescales, leading to what would appears to be surface charging of a solid. Charging of the droplets can lead to electrostatic interactions. For example, Grashchenkov and Grigoryev found that closely spaced charged evaporating droplets can coalesce due to attractive polarization forces. When like-charged droplets have larger separations, Coulomb repulsion dominates [54]. Maguire et al. investigated radio frequency plasma-water droplet interactions and found that the plasma affects the movement and evaporation rates of the droplets, indicating charging and surface chemistry effects [55]. Electro-hydrodynamic effects due to convective flow of ions as a response of local charging could be included in this study through the utilization of a fluid-flow module. However, since only single droplet is investigated and few dielectric surfaces exist, impact of such flow should be minimal. Interactions between several

droplets would also be if interest, but it is outside of the current capabilities of the model. Such electro-hydrodynamic effects are, therefore, outside the scope of this study.

With the exception of the top vertical pole (where the initial negative discharge first intersects with the droplet), the outer layer of the droplet is positively charged. The total densities of positive and negative species and the density of gaseous and solvated electrons are shown in Fig. 4.8 at t = 1.6 ns. The maximum charge density in the positive region is 1.9 μC-cm^{-3}, primarily due to solvation of gas-phase cations to form $H_2O^+_{aq}$ (1.9×10^{12} cm^{-3}), $O_2{}^+_{aq}$ (1.4×10^{12} cm^{-3}), and $N_4{}^+_{aq}$ (1.3×10^{12} cm^{-3}). (On these short timescales, charge exchange to the water and formation of hydronium have not yet occurred.) The liquid-phase densities closely follow the distribution of their gas-phase precursors. In the negatively-charged region, the peak charge density is approximately two orders of magnitude greater, -240 μC-cm^{-3}, due primarily to solvating electrons. Once solvated, the low mobilities of charged species in the droplet impede their drift and diffusion into the interior of the droplet, giving the appearance of surface charging.

As electrons enter the liquid, they quickly solvate and their mobility further decreases. The nature of electron solvation from plasmas is an active area of research [56]. In our model, an electron entering into the droplet reacts with a water molecule to form what appears to be a water negative ion, $H_2O\text{-}e^-_{aq}$. The rate coefficient for this reaction is set based on work of Rumbach et. al. who estimated the penetration depth of solvated electrons into water to be 2.5 nm [57]. We set the rate coefficient for the solvation reaction, so that the electrons would solvate only within this depth during the full plasma calculation. As a result, there is a large accumulation of solvated electrons at the upper pole of the droplet having a peak density (1.3×10^{15} cm^{-3}) at t = 1.8 ns. The solvated electrons then charge exchange to liquid-phase anions, including O^-_{aq} ($\approx 2.1\times10^{11}$ cm^{-3}, 3.5×10^{-8} M), OH^-_{aq} ($\approx 3.5\times10^{10}$ cm^{-3}, 5.8×10^{-11} M), and $O_2{}^-_{aq}$ ($\approx 1.5\times10^{10}$ cm^{-3}, 2.5×10^{-11} M),

the latter due to attachment to dissolved O_2. These reactions take place on the microsecond time-scales. With time, gas-phase positive ions drift into to the negative regions of the droplet, thereby reducing the net charge.

The maximum amount of charge that can be stored by a liquid droplet can be estimated using the Rayleigh Limit [58]:

$$q^2 = 64\pi^2\varepsilon_0\gamma a^3, \tag{4.34}$$

where q is the stored charge, ε_0 is the permittivity of free space, γ is the surface tension of the droplet, and a is its radius. As the electrostatic force overcomes the surface tension of the liquid, a droplet becomes unstable. Assuming surface tension of a pure water droplet with radius of 5 μm in air at 1 atm, the charge limit is approximately 0.25 pC or 1.4×10^6 elementary charges. In these simulations, the charge in the droplet at the end of the discharge pulse is below the Rayleigh limit, with an average charge density -72.1 μC-cm^{-3}, which, when volume-integrated, yields a total charge of -37.8 fC.

At the timescale of the discharge pulse, the primary anions produced in the droplet are O_{2aq}^-, O_{aq}^-, and OH_{aq}^-. Cations solvate and produce $H_2O^+_{aq}$ on nanosecond timescales. On longer timescales, terminal liquid-phase ions are $H_3O^+_{aq}$ and $NO_3^-{}_{aq}$. They are primarily produced by dissociation of solvated acids. In our simulations, the lowest pH (≈ 6.90) at the end of the first pulse is near the top of the droplet, where the initial ionization wave interacts with the liquid.

4.3.2.1 Base Case: Interpulse Chemistry and Local Depletion

For the base-case, the pulse described in the previous section is repeated at a frequency of 100 kHz – corresponding to a 10 μs interpulse period for 100 pulses (elapsed time of 1 ms). This

high repetition rate is deliberately chosen so that large densities of discharge products are produced in a small volume, before diffusion significantly reduces their local densities. The goal is to demonstrate how spatial gradients in gas phase precursors can affect liquid phase chemistry.

The aqueous densities of ROS and RNS in the droplet are shown in Fig. 4.9 as a function of time. At the end of pulsing the discharge (t = 1 ms), the systematic behavior of aqueous densities is largely determined by Henry's Law constants. The trends of the densities of hydrogen peroxide and ozone are compared due to both being relatively stable and having similar diffusion coefficients, while having vastly different Henry's law coefficients (H_2O_2, $h \approx 1.92 \times 10^6$ and O_3, $h \approx 0.274$). Their densities can, therefore, show the effect of the equilibrium densities on long-term chemistry. As in the reaction-diffusion simulations, H_2O_2 is depleted near the droplet, as shown in Fig. 4.10, at the end of pulsing (1 ms). Since the droplet is not saturated, H_2O_2 continues to solvate into the droplet, increasing the depletion around the droplet and requiring that the gas phase H_2O_2 be replenished with H_2O_2 originating further from the droplet. Such depletion of gas phase O_3, also shown in Fig. 4.10, occurs as the droplet is saturated due to ozone's low Henry's Law constant. With saturation densities in the droplet, solvation ceases.

This trend determines which species has the highest aqueous densities at the end of pulsing. We predict that increasing pulse repetition frequencies (PRF) will increase local densities of gas phase precursors, which will disproportionately favor increases in the densities of high-h species. The local depletion around the droplets of gas phase high-h species occurring between pulses will be replenished by the following discharge pulse. Since depletion regions do not form for low-h species, higher PRF will not influence the densities of their liquid-phase counterparts to the same degree other than by increasing the aqueous equilibrium density corresponding to any increase in the gas phase density.

The diameter of the droplet is an important influencing factor for solvation rates. The transport of solvated species through the liquid bulk is driven by diffusion. Solvation into the droplet is determined by equilibrium at the surface. Solvation can continue into the droplet if the surface densities decrease by reactions or by transport into the volume. The time period between pulses may then have consequences. For example, consider high PRF with a short interpulse period. If the droplet surface layer is still saturated due to lack of time to diffuse into the interior by the time of the next pulse, then solvation does not occur. At low PRF (long interpulse period), there may be sufficient time for the saturated species at the surface to diffuse into the droplet, thereby enabling solvation during the next pulse.

When computing aqueous densities to 50 ms after the discharge pulses end, the densities of most liquid-phase species decrease, as shown in Fig. 4.9. In the after-glow (t > 1 ms), the density of O_{3aq} also decays, a trend not seen with 0-dimensional modeling. The cause of these trends is shown in Fig. 4.11, where the local densities of H_2O_2 and O_3 directly inside and outside the droplet surface are plotted as a function of time. There are 100 discharge pulses up to 1 ms, followed by afterglow. During the plasma-on period, the local densities of both O_3 and H_2O_2 begin to saturate at about 0.3 ms. This results in O_{3aq} saturating, while the density of H_2O_{2aq} continues to increase. Once the plasma is turned off, the gas-phase species cease to be repopulated and begin to rapidly diffuse away from the center of the reactor, in addition to gas phase reactants that may deplete densities. With the local gas phase densities depleting due to diffusion away from the axis, O_{3aq} de-solvates from the surface to maintain equilibrium. Since H_2O_{2aq} density is not saturated at the surface of the droplet (high *h*), the degree of de-solvation is much less than that of O_{3aq}. In this case, high SVR negatively impacts the ability of the liquid to retain species, and it may be another means of controlling reactivity in aerosol plasmas.

These rates of de-solvation are the worst-case scenario. The droplet is on the axis of a single discharge filament that repeats in the same location. This produces the maximum density of gas phase precursors in the immediate vicinity of the droplet, and most rapidly diffuse away from the droplet. In fact, DBDs usually have arrays of many micro-discharges that produce, on average, a more uniform distribution of gas phase precursors solvating into randomly occurring droplets. The gas phase environment around a given droplet is likely more stable. Having said that, de-solvation of species from the droplet will occur if the density of its gas phase precursors decrease adjacent to the droplet. It is merely a matter of degree.

The densities of most aqueous RNS decrease in the afterglow, as they undergo reactions and, in some cases, de-solvate, as shown in Fig. 4.9 b). The terminal RNS is $NO_3^-{}_{aq}$, which forms from the solvation of gas-phase nitrogen species and the dissociation of acids. Of the several weak and strong acids, HNO_{2aq} dominates for the first 4 ms, with densities reaching 5×10^{17} cm^{-3} (8×10^{-6} M) at the end of pulsing at 1 ms. The densities of N_xO_{yaq} species also decrease following pulsing. The density of $NO_{2aq,}$ for example, reaches a maximum of 2×10^{15} cm^{-3} (3×10^{-6} M) at t = 1 ms. Its density at t = 50 ms, 2×10^{14} cm^{-3} (3×10^{-7} M), is higher than, but comparable to, the global modeling results of 4.0×10^{13} cm^{-3} at 50 ms.

The densities of these and other charged species during pulsing are shown in Fig. 4.12 a). The spatial distributions of hydronium inside the droplet after 10, 50, and 100 pulses are shown in Fig. 22b. The charged particle densities are dominated by $NO_3^-{}_{aq}$ and $H_3O^+{}_{aq}$, with average densities approaching 1×10^{19} cm^{-3}. $ONOO^-{}_{aq}$ – the species with the next highest density – has a density that is nearly two orders of magnitude lower. Lastly, $O_2^-{}_{aq}$ is more reactive than the other ions, as its density is depleted and replenished with each pulse. $O_2^-{}_{aq}$ is primarily produced by a charge exchange between solvated electrons and dissolved oxygen, which leads to an increase in

its density on a pulse-to-pulse basis. The depletion between pulses occurs through reactions with $H_3O^+_{aq}$ converting $O_2^-{}_{aq}$ to its acid form, HO_{2aq}; reactions with NO_{aq}, leading to the formation of $NO_3^-{}_{aq}$ and $ONOO^-_{aq}$; and charge exchanges with OH.

The distribution of $H_3O^+_{aq}$ in the droplet and the local pH are shown in Fig. 4.12 b). These distributions are approximately isotropic, even though the distribution of the initial gas-phase species is not. This uniform distribution is a consequence of hydronium being primarily formed by a multi-step process culminating in the hydrolysis of the $(H)N_xO_y$ species. The long time required for these species to form, as well as intra-particle diffusion, smooths initially non-uniform sources. The pH is lowest at the surface of the droplet, where the density of $H_3O^+_{aq}$ is highest, decreasing to 1.9 at the end of 100 pulses.

4.3.2.2 Droplet Diameter

The base case is repeated with droplets having diameters of d = 5 μm and d = 20 μm in order to further investigate the influence of the SVR on liquid kinetics. The volume-averaged densities during pulsing and afterglow of selected ROS and RNS are presented in Fig. 4.13. The smaller droplets have higher average aqueous densities due to increased rates of solvation relative to their volume (larger SVR). For example, the density of OH_{aq} has a strong dependence on droplet diameter. At the end of the plasma-on period, the density of OH_{aq} scales inversely with droplet diameter, 2×10^{16} cm^{-3} (3×10^{-5} M) for d = 5 μm and 6×10^{15} cm^{-3} (1×10^{-5} M) for d = 20 μm. This scaling is not explained by changes in the discharge, as the average density of OH oscillates between 3×10^{12} cm^{-3} and 5×10^{12} cm^{-3} for all droplet sizes. In all cases, hydroxyl density is highest at the surface ($\approx 10^{17}$ cm^{-3}, 2×10^{-4} M) and decreases towards the center of the droplet. The density of OH_{aq} at the center of the droplet is two orders of magnitude smaller for the 20 μm droplet, and

one order of magnitude smaller for the 5 μm droplet when compared to the surface. In addition to longer transport times to reach the center of the droplet, OH_{aq} is depleted by the formation of H_2O_{2aq}.

At the end of the pulse-on period (t = 1 ms), the density of H_2O_{2aq} also has a strong dependence on droplet diameter, higher for smaller droplets, due to the increased relative rates of solvation as the SVR increases. However, once the plasma is turned off, the average droplet densities become nearly the same. Since none of the droplets is large enough to produce a global depletion of H_2O_2 within the simulated time, the inventories of gas phase H_2O_2 after pulsing are essentially the same independent of droplets. During the 50 ms of afterglow, there is sufficient time for diffusion to replenish local depletion around the droplet, resulting in the droplets equilibrating to the same H_2O_{2aq} densities in the afterglow. Interestingly, ozone undergoes the opposite process. The O_{3aq} density does reach saturation during pulsing, resulting in similar densities of O_{3aq} at 1 ms, regardless of droplet diameter. However, once the pulsing ends and the gas diffuses throughout the reactor, the local O_3 density decreases. The density of O_{3aq} within larger droplets is concentrated near the surfaces, which causes a higher initial rate of desolvation. With time, however, the average densities of solvated ozone trend to similar values. One possible means of mitigating this would be through the collection of the droplets within a bulk liquid directly following the plasma treatment, therefore decreasing the surface-to-volume ratio.

The local distributions of hydrogen peroxide, hydronium, and the local pH at the end of the pulsing period (1 ms) are shown for droplet sizes of 5, 10, and 20 μm in Fig. 4.14. While the surface densities of H_2O_{2aq} are similar, they vary appreciably within the liquid bulk. The diffusion speed through the liquid is approximately three orders of magnitude slower than in the gas at 1 atm, so the liquid species, whose production depends primarily on solvation, requires longer time

to equilibrate inside large droplets. The densities of $H_3O^+_{aq}$ at the surface and inside the bulk vary appreciably less as a function of droplet diameter. This is because its production depends on several reactions, including between relatively stable species such as acids. These species are able to penetrate deeper into the liquid region before undergoing a reaction, which homogenizes initially non-uniform densities of hydronium. With the timescales required for equilibration being longer with larger droplet diameters, the average pH at the center of the 5-μm droplet, pH = 0.82, is nearly five times lower than that of the 20-μm droplet, pH=4.0.

4.4 Concluding Remarks

The chemical activation of water droplets by atmospheric pressure plasma is sensitive to the droplet diameter and, for individual species, Henry's law constants. Results have been discussed from 2-dimensional modeling of water droplets activated by repetitively pulsed humid air plasmas. Results have shown how the non-uniformities produced by localized microdischarges or the localized depletion of species affect this scaling. By varying the radius of the droplet, the influence of the surface-to-volume ratio (SVR) is shown to be a critical parameter for the transfer of reactivity from the gas phase into the liquid bulk. Smaller droplets come to equilibrium with the surrounding reactive species in the gas phase within shorter times. This, in turn, enables high Henry's law constant (*h*) species to solvate into the droplet producing higher densities and lower pH. Scaling of aqueous densities of high *h* species as a function of droplet diameter and density of water droplets is sensitive to depletion of gas phase precursors. Low-*h* aqueous species come into equilibrium with the gas phase more rapidly, without depleting local gas-phase densities, and therefore show a lower degree of dependence on droplet diameter.

Results also emphasize the importance of the local plasma environment around the droplet

on final aqueous densities. In non-uniform discharges that might occur in filamentary DBDs, the gas-phase densities adjacent to the droplets may change due to diffusion between pulses (or after the discharge terminates). A droplet saturated with an aqueous species during the discharge may become super-saturated after the discharge terminates, leading to rapid de-solvation, and more so for droplets with large SVR. Rates of solvation (and de-solvation) also depend on the aqueous densities on the surface of the droplet, which may be very different from the interior of the droplet. Following termination of the discharge, saturated aqueous densities at the surface of the droplet may decrease because of transport both out of the droplet (de-solvation) and diffusion into the interior.

These dependencies of aqueous densities on droplet size and Henry's law constant provide guidance on how to activate mists of droplets, where the diameter and density of droplets are variables. Total inventories of aqueous species can be separately optimized, providing a control mechanism for the chemical activation of liquids.

4.5 Tables

Table 4. 1 Henry's Law Constants (Ref. [51])

Species	h (unitless)	Note
H_2O_2	1.92×10^6	
HO_2	1.32×10^5	
OH, $OH(A^2\Sigma)$	620	a
H, H*	6.00×10^3	a
H_2, H_2(r), H_2(v), H_2*	1.9×10^{-2}	a
H_2O(v)	1	b
O, $O(^1D)$	1	a,b
O_2, O_2(r), O_2(v), $O_2(^1\Delta_g)$, $O_2(^1\Sigma_u)$	3.24×10^{-2}	a
O_3, O_3*	0.274	
N_2, N_2(r), N_2(v), N_2*, N_2**, N, $N(^2D)$,	1.6×10^{-2}	a
N_2O_3	600	
N_2O_4	37.0	
N_2O_5	48.5	
N_2O, N_2O(v)	0.599	a
HO_2NO_2	9.73×10^4	
NO	4.4×10^{-2}	
NO_2	0.28	
NO_3	41.5	
HNO_2, HNO	1.15×10^3	a
HNO_3, ONOOH	4.80×10^6	
CO, CO(v)	2.42×10^{-2}	a
CO_2, CO_2(v)	0.823	a
NH	1.47×10^3	c

a) Value corresponds to the first species in the list. Other species are assumed to have the same Henry's law constant.
b) Approximated. Species reacts quickly in water and does not reach Henry's law saturation.
c) Approximated by analogy to NH_3.

Table 4. 2 Initial Gas-Phase Densities for 2-d Reaction Diffusion

Species[a]	Density (cm^{-3})	Species	Density (cm^{-3})
N_2	1.87×10^{19}	HO_2NO_2	5.95×10^{12}
O_2	4.92×10^{18}	NO_3	4.35×10^{11}
H_2O	8.58×10^{17}	H	1.65×10^{10}
O_3	2.07×10^{16}	$O_2(^1\Sigma_u)$	3.95×10^{9}
$O_2(^1\Delta_g)$	5.09×10^{14}	N_2O_4	1.422×10^{8}
HNO_3	2.54×10^{14}	HNO	1.02×10^{8}
N_2O	1.52×10^{14}	$H_3O^+(H_2O)_6$	1.95×10^{7}
HNO_2	5.14×10^{13}	NH	1.06×10^{7}
O	1.98×10^{13}	$O_2^-(H_2O)_2$	9.44×10^{6}
H_2	3.67×10^{13}	$OH^-(H_2O)_2$	7.22×10^{6}
NO_2	2.46×10^{13}	e^-	1.05×10^{6}
N_2O_5	1.49×10^{13}	O_2^-	2.85×10^{5}
NO	1.39×10^{13}	NO_2^+	1.53×10^{5}
OH	1.37×10^{13}	O_3^-	1.55×10^{5}
N	8.91×10^{12}	NO_2^-	1.53×10^{5}
HO_2	6.90×10^{12}	OH^-	4.48×10^{4}

a) Species are sorted in order of decreasing density.

4.6 Figures

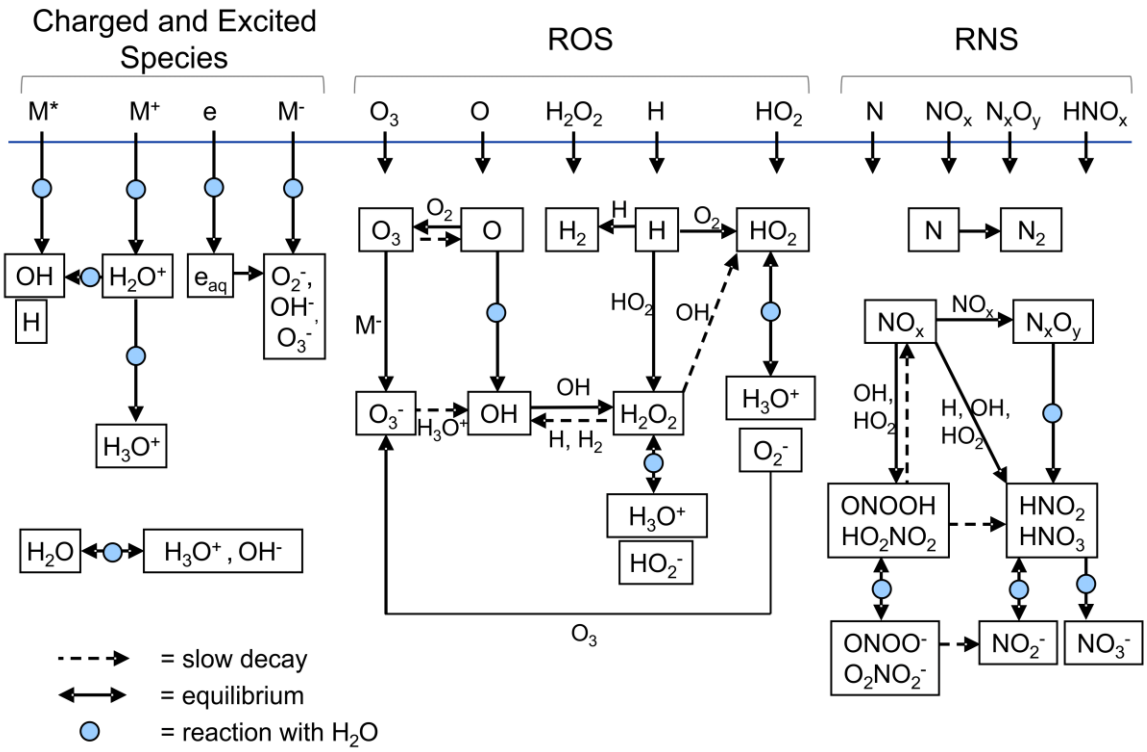

Fig. 4. 1 Schematic of the liquid reaction mechanism used in this investigation highlighting the most important reactions.

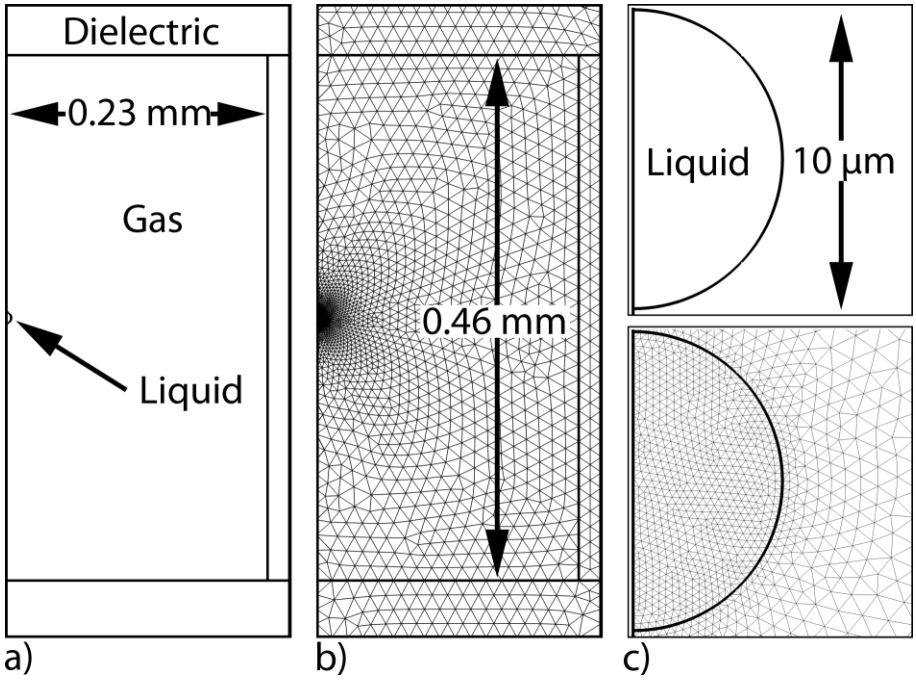

Fig. 4. 2 Numerical parameters for the base case of a droplet initially exposed to a uniform density of plasma activated species. The sizes of the droplet and reactor were varied to maintain a constant liquid/gas ratio. (a) Geometry, (b) numerical mesh and (c) close-up of droplet.

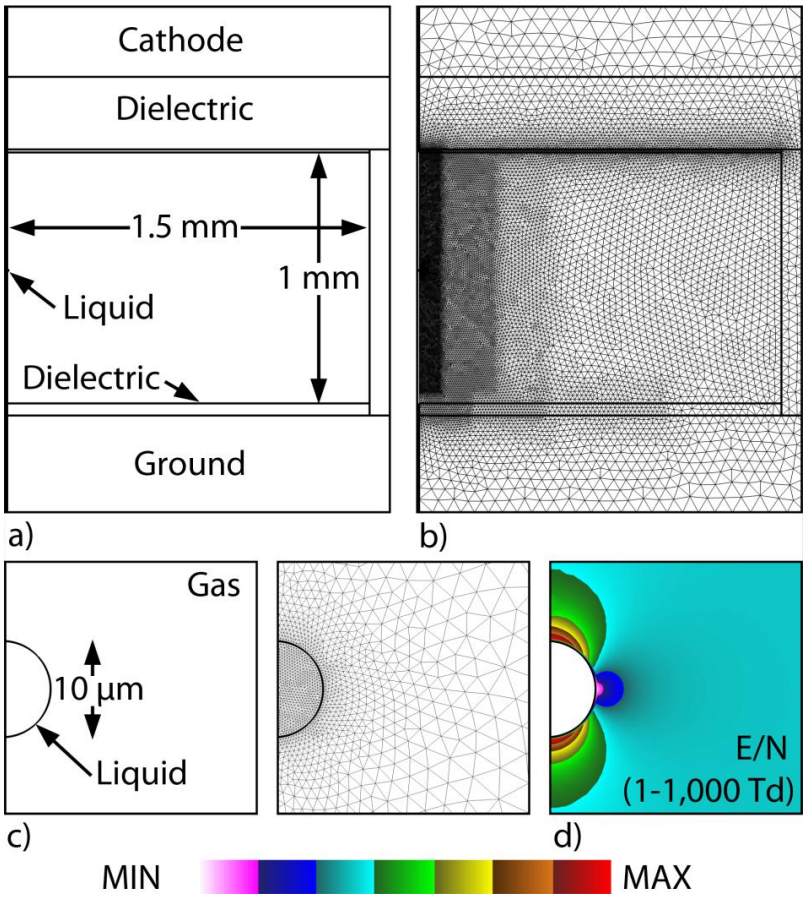

Fig. 4. 3 Gas phase reactive neutral species generated in a humid air discharge containing a single 10 µm droplet. (a) Reactive oxygen species (ROS) and (b) reactive nitrogen species (RNS) during the first 10 discharge pulses. (c) Accumulation of selected species during 500 pulses and an afterglow period.

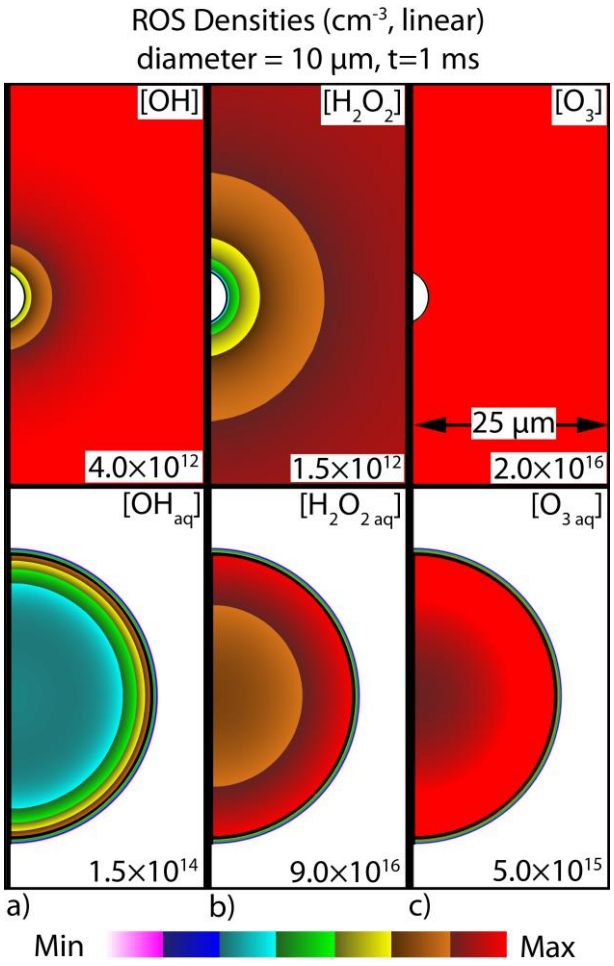

Fig. 4. 4 Local densities of gas-phase (top) and solvated (bottom) species after 1 ms in the reactive diffusion base case with (droplet diameter = 10 µm). Peak plotted values are noted in each frame. a) OH, b) H_2O_2, c) O_3. OH_{aq} is confined to the surface region of the droplet. Local depletion of H_2O_2 near the droplet is due to its high *h* while there is little gas depletion of O_3.

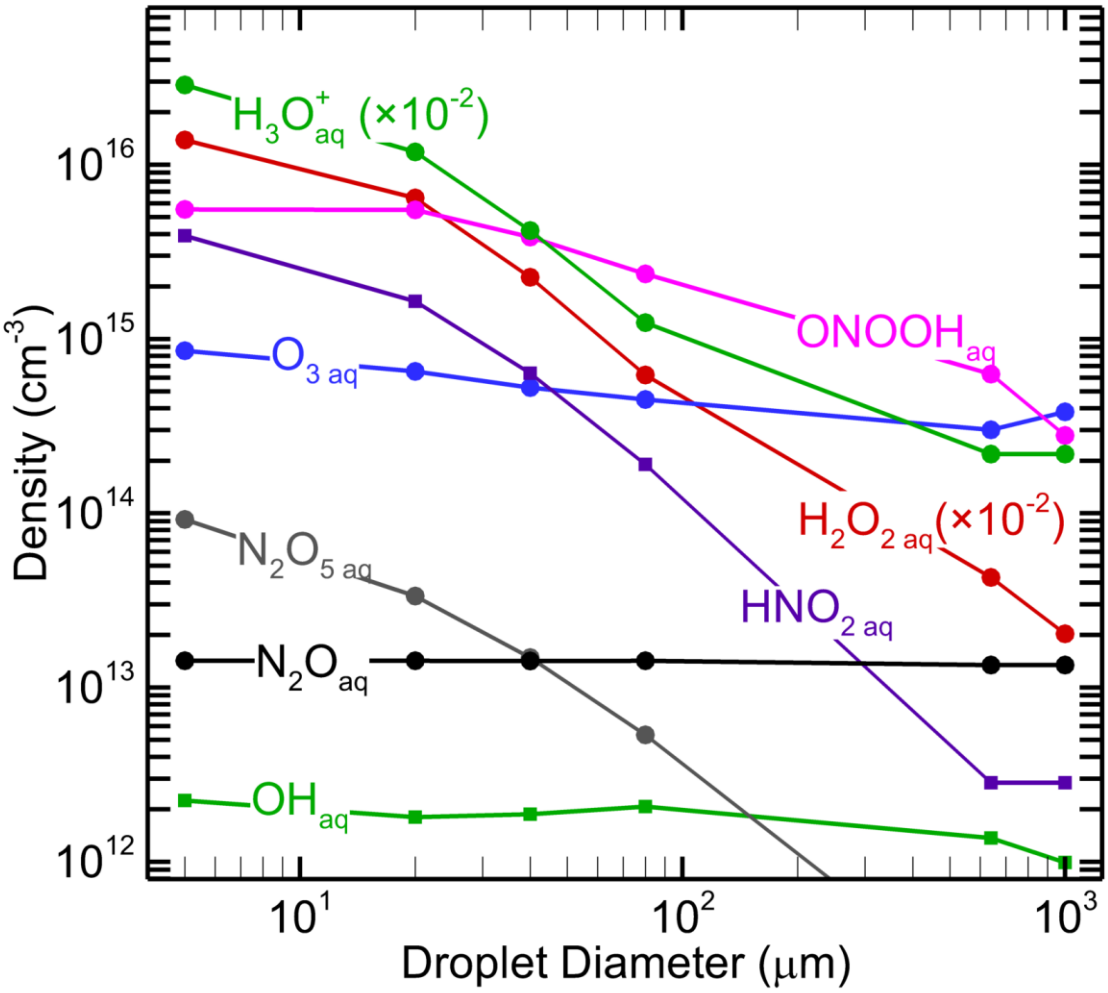

Fig. 4. 5 Final average densities of liquid-phase RONS as a function of droplet diameter. Stable, high-*h* species show strong dependence on droplet radius. Stable, low-*h* species have average densities less sensitive to droplet diameter.

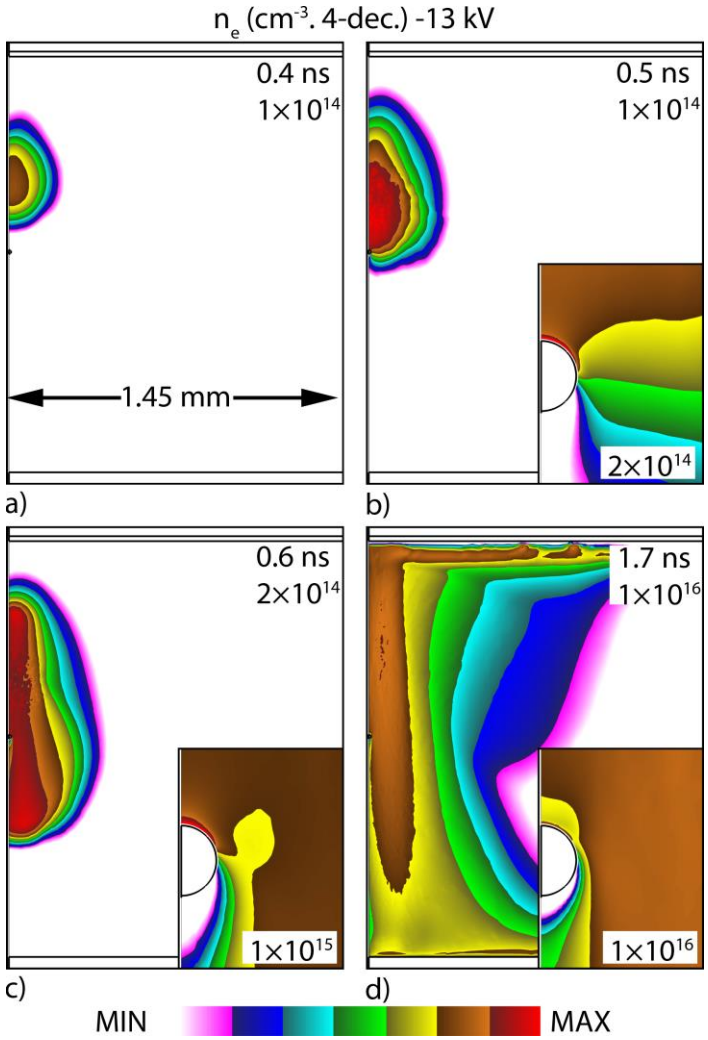

Fig. 4. 6 Evolution of electron density in the DBD for the base-case (10 μm droplet). The embedded figures are close-ups of the volume near the droplet. The microdischarge envelops the droplet. Anisotropies in distribution of electron densities develop. Images are plotted on a 4-decade log scale with peak values noted in the figures.

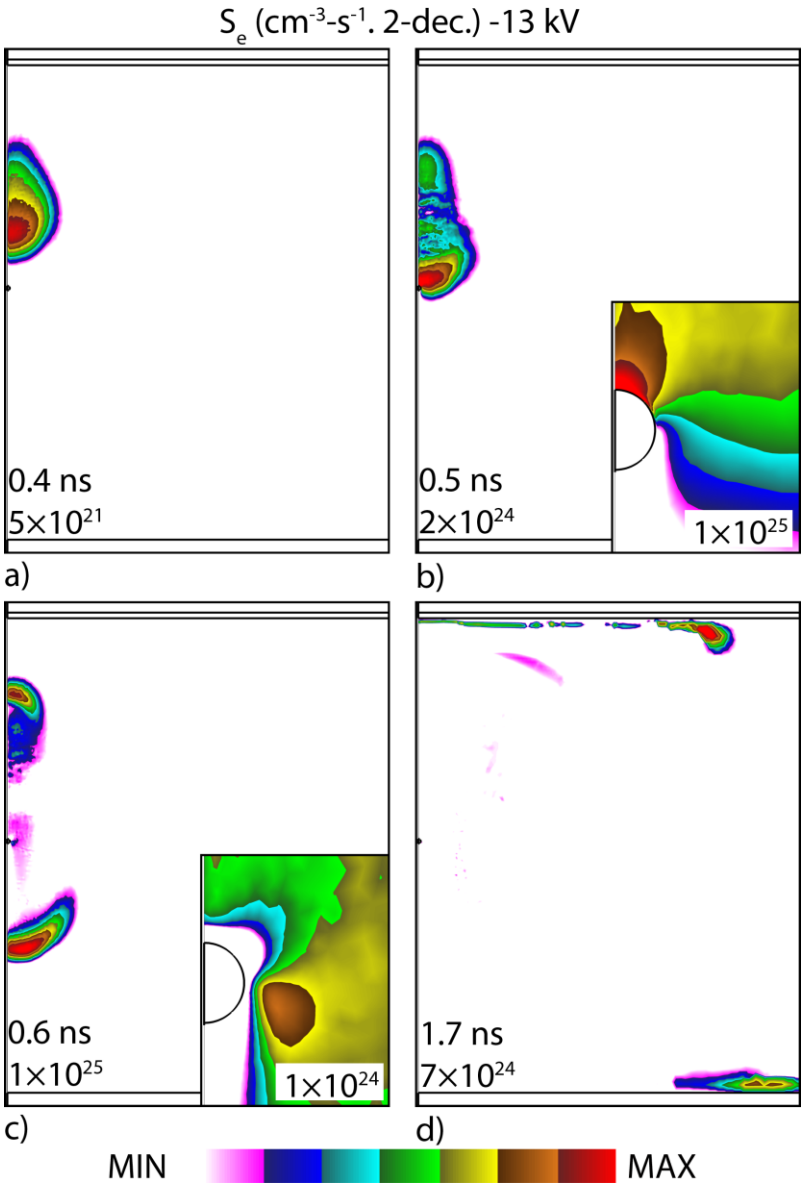

Fig. 4. 7 Evolution of the electron impact ionization source term in the DBD for the base-case (10 μm droplet). The embedded figures are close-ups of the region near the droplets Images are plot-ted on a 2-decade log scale with peak values noted in the figures.

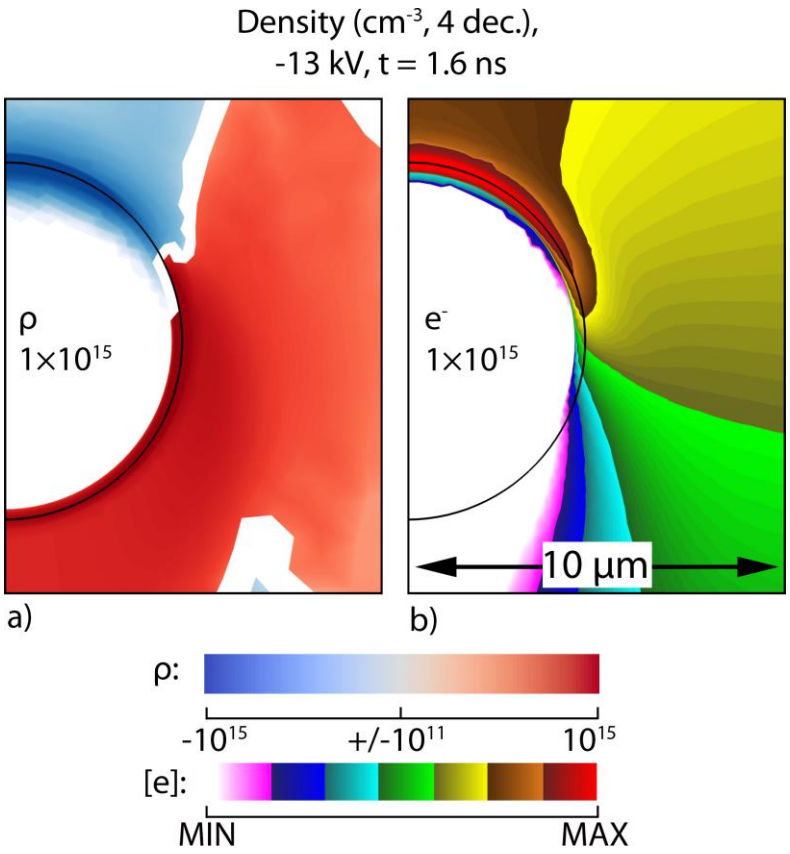

Fig. 4. 8 Electrical properties of the droplet. (a) Charge density (sum of densities of all charged species) and (b) sum of the solvated and gas-phase electrons in the 10 µm droplet at the end of a single pulse. In (a), blue indicates net negative density and red shows net positive density. The top vertical pole of the droplet becomes negatively charged as electrons in the negative downward directed discharge solvate. Other regions of the droplet become positively charged.

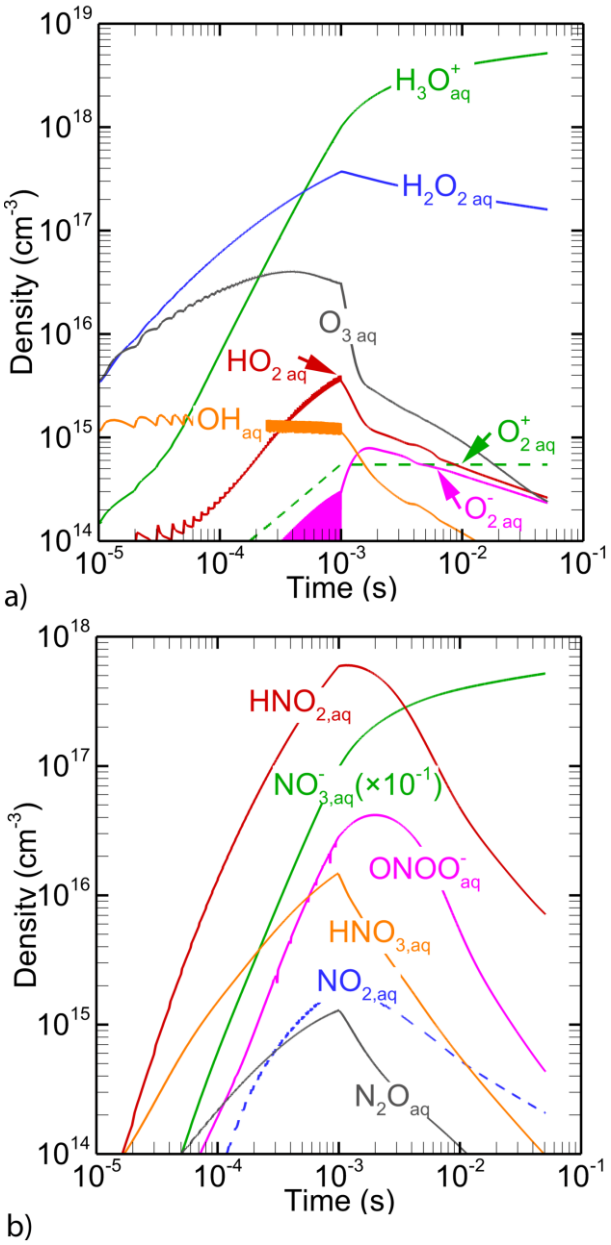

Fig. 4. 9 Time evolution of the average densities of (a) ROS and (b) RNS in the base case over 100 pulses lasting to 1 ms and afterglow to 50 ms. Note the density of O_{3aq} peaking at t = 1 ms, then sharply decreasing due to de-solvation following the cessation of pulsing.

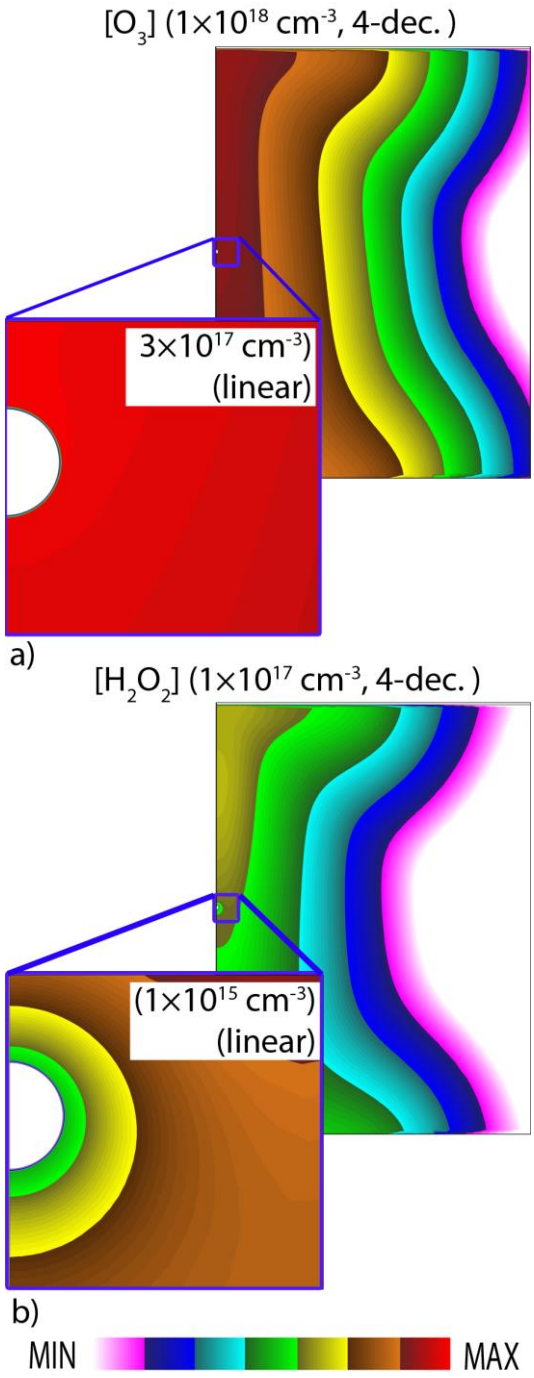

Fig. 4. 10 Densities of (a) gas-phase O_3 and (b) H_2O_2 near the droplet at the end of pulsing at 1 ms, showing the formation of local depletion region in the densities of high-*h* species.

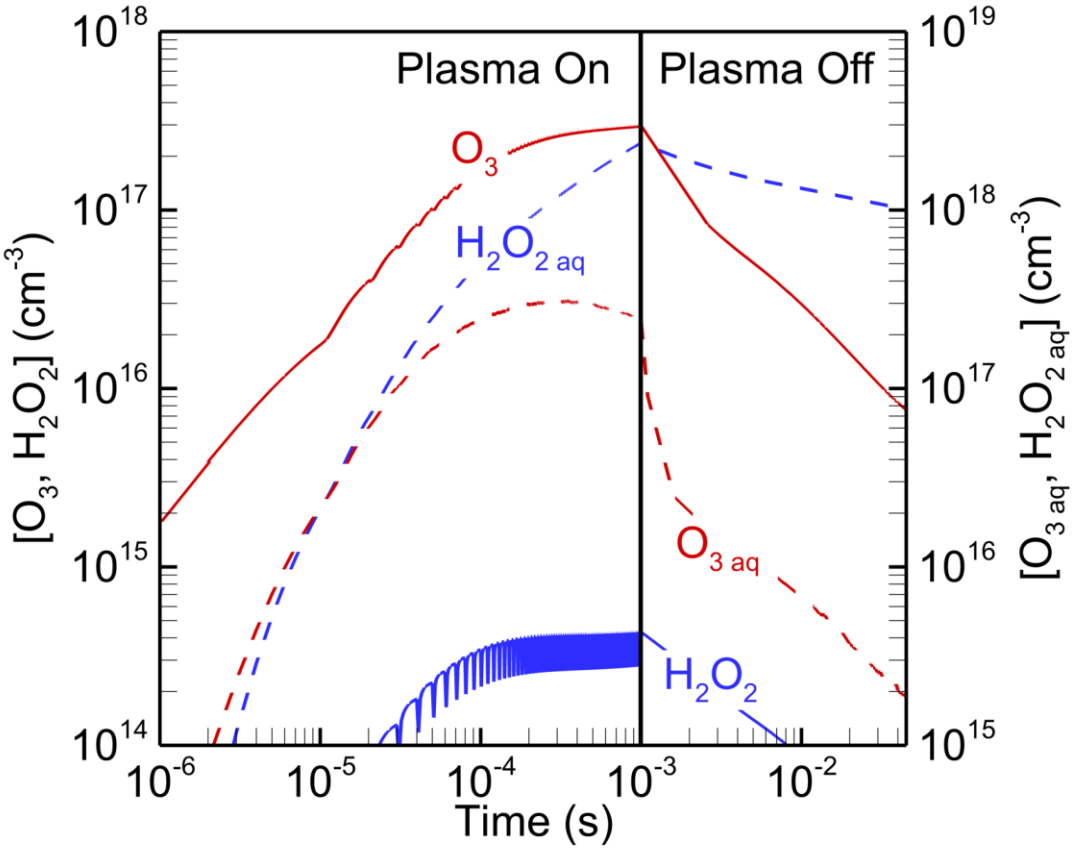

Fig. 4. 11 Time evolution of the densities of liquid and gas phase O_3 and H_2O_2 directly inside and outside of the droplet. The H_2O_{2aq} density remains stable as it has not yet saturated whereas the density of O_{3aq} as it de-solvates to maintain equilibrium.

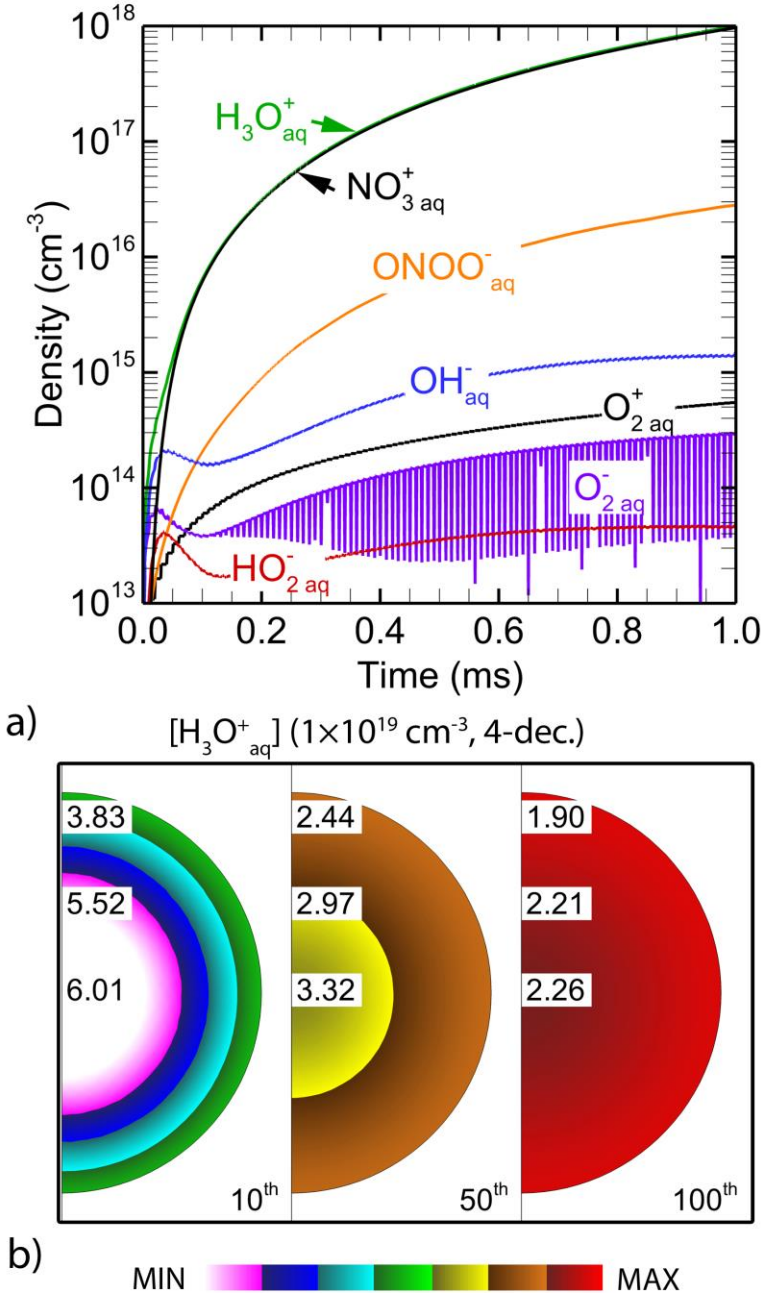

Fig. 4. 12 Properties of aqueous species. (a) Densities of liquid-phase ions as a function of time during pulsing and (b) local densities of $H_3O^+_{aq}$ and local pH after 10, 50 and 100 pulses.

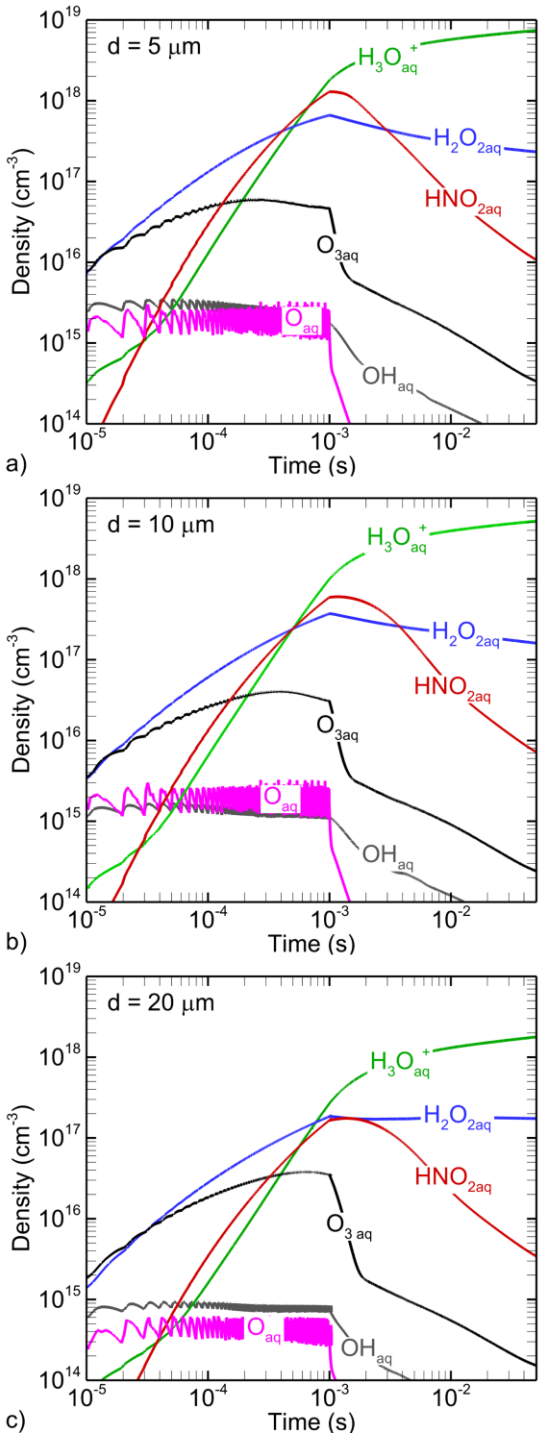

Fig. 4. 13 Time evolution of selected RONS during pulsing with droplet diameters of 5, 10 and 20 μm.

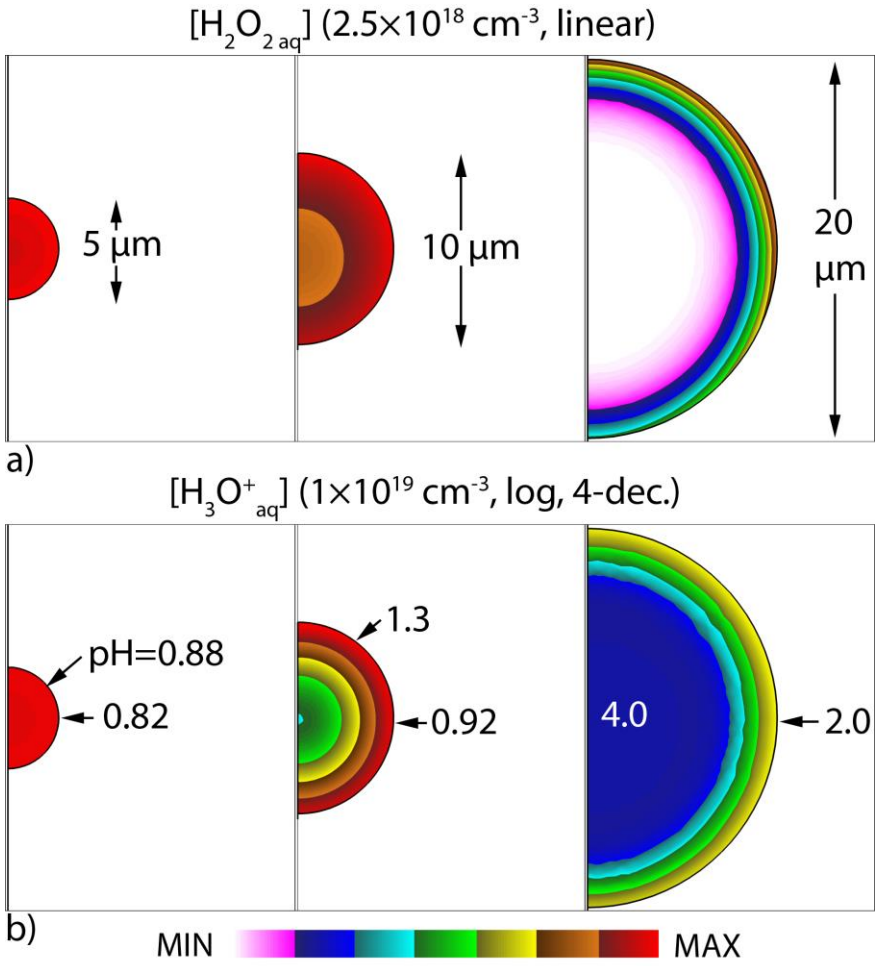

Fig. 4. 14 Distributions of the densities of (a) H_2O_{2aq} and (b) $H_3O^+_{aq}$ at the end of pulsing period for droplet diameters of 5, 10 and 20 µm.

4.7 References

[1] J. E. Foster, G. Adamovsky, S. Nowak Gucker and I. M. Blankson, IEEE Trans. Plasma Sci. **41,** 503 (2013).

[2] P. J. Bruggeman, M. J. Kushner, B. R. Locke, J. G. E. Gardeniers, W. G. Graham, D. B. Graves, R. C. H. M. Hofman-Caris, D. Maric, J. P. Reid, E. Ceriani, D. Fernandez Rivas, J. E. Foster, S. C. Garrick, Y. Gorbanev, S. Hamaguchi, F. Iza, H. Jablonowski, E. Klimova, J. Kolb, F. Krcma, P. Lukes, Z. Machala, I. Marinov, D. Mariotti, S. Mededovic Thagard, D. Minakata, E. C. Neyts, J. Pawlat, Z. Lj Petrovic, R. Pflieger, S. Reuter, D. C. Schram, S. Schröter, M. Shiraiwa, B. Tarabová, P. A. Tsai, J. R. R. Verlet, T. Von Woedtke, K. R. Wilson, K. Yasui and G. Zvereva, Plasma Sources Sci. Technol. **25,** 053002 (2016).

[3] T. H. Dang, A. Denat, O. Lesaint and G. Teissedre, Eur. Phys. J. Appl. Phys. **47,** 2 (2009).

[4] J. E. Foster, S. Mujovic, J. Groele and I. M. Blankson, J. Phys. D Appl. Phys. **51,** 293001 (2018).

[5] Z. Ke, P. Thopan, G. Fridman, V. Miller, L. Yu, A. Fridman and Q. Huang, Clin. Plasma Med. **7–8,** 1 (2017).

[6] D. B. Graves, IEEE Trans. Radiat. Plasma Med. Sci. **1,** 281 (2017).

[7] G. B. McCombs and M. L. Darby, Int. J. Dent. Hyg. **8,** 10 (2010).

[8] F. Rossi, O. Kylián, H. Rauscher, M. Hasiwa and D. Gilliland, New J. Phys. **11,** 115017 (2009).

[9] T. Nosenko, T. Shimizu and G. E. Morfill, New J. Phys. **11,** 115013 (2009).

[10] L. I. Partecke, K. Evert, J. Haugk, F. Doering, L. Normann, S. Diedrich, F.-U. Weiss, M. Evert, N. O. Huebner, C. Guenther, C. D. Heidecke, A. Kramer, R. Bussiahn, K.-D. Weltmann, O. Pati, C. Bender and W. von Bernstorff, BMC Cancer **12,** 473 (2012).

[11] M. G. Kong, G. Kroesen, G. Morfill, T. Nosenko, T. Shimizu, J. van Dijk and J. L. Zimmermann, New J. Phys. **11,** 115012 (2009).

[12] H. Xu, C. Chen, D. Liu, D. Xu, Z. Liu, X. Wang and M. G. Kong, J. Phys. D Appl. Phys. **50,** 245201 (2017).

[13] V. I. Parvulescu, M. Magureanu and P. Lukes, (Wiley-VCH, 2012).

[14] J. Winter, H. Tresp, M. U. Hammer, S. Iseni, S. Kupsch, A. Schmidt-Bleker, K. Wende, M. Dünnbier, K. Masur, K. D. Weltmann and S. Reuter, J. Phys. D. Appl. Phys. **47,** 285401 (2014).

[15] T. D. Oury, L. Tatro, A. J. Ghio and C. A. Piantadosi, Free. Rad. Res. **23,** 537 (1995).

[16] J. S. Beckman and W. H. Koppenol, Am. J. Physiol. **271,** C1424 (1996).

[17] J. S. Beckman, T. W. Beckman, J. Chen, P. A. Marshall and B. A. Freeman, Proc. Natl. Acad. Sci. **87,** 1620 (1990).

[18] W. H. Glaze, J. W. Kang and D. H. Chapin, Ozone Sci. Eng. **9,** 335 (1987).

[19] R. Broséus, S. Vincent, K. Aboulfadl, A. Daneshvar, S. Sauvé, B. Barbeau and M. Prévost, Water Res. **43,** 4707 (2009).

[20] P. Lukes and B. R. Locke, J. Phys. D Appl. Phys. **38,** 4074 (2005).

[21] K. Oehmigen, M. Hähnel, R. Brandenburg, C. Wilke, K. D. Weltmann and T. von Woedtke, Plasma Process. Polym. **7,** 250 (2010).

[22] Z. Machala, L. Chládeková and M. Pelach, J. Phys. D Appl. Phys. **43,** 222001 (2010).

[23] M. A. Malik, Plasma Chem. Plasma Process. **30,** 21 (2010).

[24] P. Bruggeman and C. Leys, J. Phys. D. Appl. Phys. **42,** 053001 (2009).

[25] B. S. Sommers and J. E. Foster, Plasma Sources Sci. Technol. **23,** 015020 (2014).

[26] L. Schaper, W. G. Graham and K. R. Stalder, Plasma Sources Sci. Technol. **20,** 034003 (2011).

[27] H. Aoki, K. Kitano and S. Hamaguchi, Plasma Sources Sci. Technol. **17,** 025006 (2008).

[28] J. E. Foster, B. Weatherford, E. Gillman and B. Yee, Plasma Sources Sci. Technol. **19,** 025001 (2010).

[29] J. Lai, V. Petrov and J. E. Foster, IEEE Trans. Plasma Sci. **46,** 875 (2018).

[30] E. C. Neyts, M. Yusupov, C. C. Verlackt and A. Bogaerts, J. Phys. D. Appl. Phys. **47,** 293001 (2014).

[31] M. Yusupov, E. C. Neyts, P. Simon, G. Berdiyorov, R. Snoeckx, A. C. T. Van Duin and A. Bogaerts, J. Phys. D. Appl. Phys. **47,** 025205 (2014).

[32] R. Gopalakrishnan, E. Kawamura, A. J. Lichtenberg, M. A. Lieberman and D. B. Graves, J. Phys. D Appl. Phys. **49,** 295205 (2016).

[33] V. I. Grinevich, E. Y. Kvitkova, N. A. Plastinina and V. V. Rybkin, Plasma Chem. Plasma Process. **31,** 573 (2011).

[34] X. Jin, H. Bai, F. Wang, X. Wang, X. Wang and H. Ren, IEEE Trans. Plasma Sci. **39,** 1099 (2011).

[35] B. R. Locke, M. Sato, P. Sunka, M. R. Hoffmann and J. S. Chang, Ind. Eng. Chem. Res. **45,** 882 (2006).

[36] V. V. Kovačević, B. P. Dojčinović, M. Jović, G. M. Roglić, B. M. Obradović and M. M. Kuraica, J. Phys. D. Appl. Phys. **50,** 155205 (2017).

[37] Z. Kovalova, M. Leroy, M. J. Kirkpatrick, E. Odic and Z. Machala, Bioelectrochemistry **112,** 91 (2016).

[38] K. Patel, A. Mannsberger, A. Suarez, H. Patel, M. Kovalenko, A. Fridman, V. Miller and G. Fridman, Plasma Med. **6,** 447 (2016).

[39] R. J. Wandell and B. R. Locke, Ind. Eng. Chem. Res. **53,** 609 (2014).

[40] J. W. Gallagher, C. E. Brion, J. A. R. Samson and P. W. Langhoff, J. Phys. Chem. Ref. Data **17,** 9 (1988).

[41] F. L. Smith and A. H. Harvey, Chem. Eng. Prog. **103,** 33 (2007).

[42] R. Fernández-Prini, J. L. Alvarez and A. H. Harvey, J. Phys. Chem. Ref. Data **32,** 903 (2003).

[43] D. W. O'Sullivan, M. Lee, B. C. Noone and B. G. Heikes, J. Phys. Chem. **100,** 3241 (1996).

[44] S. Tonini and G. E. Cossali, Int. J. Heat Mass Transf. **92,** 184 (2016).

[45] A. E. Kuchma, A. K. Shchekin and D. S. Martyukova, J. Aerosol Sci. **102,** 72 (2016).

[46] F. Gibou and R. Fedkiw, J. Comput. Phys. **202,** 577 (2005).

[47] Y. S. Djikaev and A. Tabazadeh, J. Geophys. Res. **108,** 4689 (2003).

[48] R. Vácha, P. Slavíček, M. Mucha, B. J. Finlayson-Pitts and P. Jungwirth, J. Phys. Chem. A **108,** 11573 (2004).

[49] S. A. Norberg, E. Johnsen and M. J. Kushner, Plasma Sources Sci. Technol. **24,** 035026 (2015).

[50] W. Van Gaens and A. Bogaerts, Plasma Sources Sci. Technol. **23,** 035015 (2014).

[51] A. M. Lietz and M. J. Kushner, J. Phys. D. Appl. Phys. **49,** 425204 (2016).

[52] T. S. Light, S. Licht, A. C. Bevilacqua and K. R. Morash, Electrochem. Solid-State Lett. **8,** E16 (2005).

[53] C. G. Malmberg and A. A. Maryott, J. Res. Natl. Bur. Stand. **56,** 2641 (1956).

[54] S. I. Grashchenkov and A. I. Grigoryev, Fluid Dyn. **46,** 437 (2011).

[55] P. D. Maguire, C. M. O. Mahony, C. P. Kelsey, A. J. Bingham, E. P. Montgomery, E. D. Bennet, H. E. Potts, D. C. E. Rutherford, D. A. McDowell, D. A. Diver and D. Mariotti, Appl. Phys. Lett. **106,** 224101 (2015).

[56] R. M. Young and D. M. Neumark, Chem. Rev. **112,** 5553 (2012).

[57] P. Rumbach, D. M. Bartels, R. M. Sankaran and D. B. Go, Nat. Commun. **6,** 7248 (2015).

[58] D. C. Taflin, T. L. Ward and E. J. Davis, Langmuir **5,** 376 (1989).

Chapter 5 Interactions Between Atmospheric Pressure Plasmas and Metallic Catalyst Particles in Packed Bed Reactors [3]

Reactivity transfer to liquids was reviewed in Chapter 2, while plasma reactivity transfer to gases was discussed in Chapter 3. In the proceeding chapters, reactivity transfer to solids will be discussed. This includes plasma interactions with metallic catalysts (this chapter), as well as its propagation into catalytic pores (Chapter 6).

Catalysis is the process of using a material, substance, or additional chemical compound to enable favorable reaction pathways by decreasing the activation energy. In spite of its industrial maturity, thermal catalysis is continually being improved. New catalysts with improved efficiencies, selectivity and turnover are being investigated experimentally and computationally [1–10]. Similarly, research is being pursued to investigate the plasma dynamics and kinetics in non-equilibrium plasma reactors in contact with catalysts, including dielectric barrier discharges (DBDs), gliding arcs, and PBRs [11–18], with support from modeling studies [19–25].

This chapter discusses results from a computational investigation of plasma surface interactions between micron-scale metallic catalysts and humid-air plasmas in PBRs. We found that higher-density plasma regions form in the proximity of the metallic catalysts. These regions were confirmed experimentally using ICCD imaging. The intense plasmas result from geometrical electric field enhancement and redistribution of charges within the conductive particles, leading to further enhancement. The high electric field at the triple points of the catalysts can produce field

[3] The results discussed and a portion of the text in this chapter have been previously published in J. Kruszelnicki, K. W. Engeling, J. E Foster and M. J. Kushner, "Interactions Between Atmospheric Pressure Plasmas and Metallic Catalyst Particles in Packed Bed Reactors," J. Phys. D.: Appl. Phys. **54,** 104001 (2021).

emission of electrons, which provides a pre-ionization source or additional source of electrons. These regions of high electric fields and sources of electrons guide discharges towards the catalysts and increases fluxes of excited species, ions, electrons, and photons to their surfaces. These fluxes are focused primarily at the triple points between the metal, dielectric, and gas. As a result, the catalyst is locally heated, which could further lead to increased rates of thermocatalytic reactions on the surface. The surface roughness of the metal inclusions can lead to additional electric field enhancement, which changes the character of the discharges in the vicinity of the catalysts, while reducing breakdown voltage.

5.1 Introduction

Atmospheric pressure plasmas sustained in packed bed reactors (PBRs), particularly using catalysts, are being investigated for pollutant abatement and chemical conversion for the production of value-added products [26]. These efforts include removal of volatile organic compounds (VOCs), NO_x abatement, CO_2 and CO chemical conversion, energy storage, and the production of hydrogen, syngas, ammonia, and ozone [12,13,27–37]. There is a large variety of plasma catalytic reactors. The common feature of these reactors is a non-equilibrium plasma being generated in near proximity of dielectric beads or granules, as in PBRs. These dielectrics are often impregnated with micro- to nano-meter-scale metallic catalyst particles.

The coupling between plasmas and thermal catalysts is still poorly understood. As such, plasma interactions with catalysts and their underlying support structures need better metrics to be able not only to evaluate the plasma catalysis systems, but also to make comparisons between systems [38–40]. The interactions between plasma and metallic catalysts present modeling challenges due to their simultaneous and mutual impacts. The plasma produces high-energy

electrons, ions, excited and radical species, and UV/VUV photons [41]. The fluxes of these species can introduce additional surface kinetics (e.g., adsorption of intermediaries, UV/VUV activation); change surface morphology (e.g., sputtering, melting, and self-cleaning); and increase local catalyst temperature. The electrical triple point is the intersection of a dielectric, metal, and gas. Electric field enhancement occurs at triple points due to the geometry and discontinuity in permittivity, as well as a response to charge-redistribution upon application of an electric field. If of sufficient magnitude, the electric field enhancement at the triple points of metallic catalyst sites can produce electric field emission of electrons, a process that is accelerated by heating of the catalyst. Electric field emission is particularly sensitive to the geometry of the metallic particles, polarization of the underlying dielectric, and local plasma conditions - all of which can intensity the electric field at the surface of the catalyst. These phenomena have been studied in other areas, primarily high-voltage electrical systems [42–44]. The electric field emission, in turn, affects the local plasma conditions and can impact the rates of surface reactions [25]. In order to resolve these interactions, plasma dynamics and surface interactions must be simultaneously modeled in a self-consistent fashion.

The models, including Author's contributions, were described in Chapter 2. The reaction mechanisms and initial conditions are discussed in Sec. 5.2. The description of the discharge dynamics in the base case is presented in Sec. 5.3. Sections 5.4 and 5.5 describe the influence of electric field emission and plasma-based heating of the catalysts. Concluding remarks are in Section 5.6.

5.2 Initial Conditions and Reaction Mechanism

The base case has initial conditions of 300 K and 760 Torr (or 1 atm). The gas is humid air ($N_2/O_2/H_2O$=78/21/1) with a background ionization of 10^5 cm^{-3}. The reaction mechanism

contains 88 species and 1855 reactions. The reaction mechanism is a modified version of that discussed in Ref. [45], taking into account only gas-phase species.

Two geometries were used in this investigation, as shown in Figs. 1 and 2. The first geometry, Fig. 5.1, is nominally full scale, and it includes 7 dielectric rods or disks (diameter 1.8 mm) distributed in a reactor with a width of 0.8 cm and a height of 1 cm. (In these 2-dimensional simulations, the circular dielectric disks are computationally equivalent to long rods.) The secondary electron emission coefficient for the dielectric is 0.15. The second geometry, Fig. 5.2, contains 2 dielectric rods with radii of 0.9 mm inserted into a gas region with a width 0.25 cm and a height of 0.29 cm. The latter geometry is used to investigate the impact of several system parameters with greater resolution of surface fluxes and of the metallic particles, while decreasing the computational cost. In both geometries, metallic catalysts are embedded into the surface of the dielectric rods. These catalysts are nominally electrically floating metals, which are modeled as high-conductivity dielectrics. The conductivity of the dielectric representing the catalyst particle is chosen to be high enough so that there is essentially no voltage drop across the interior of the catalyst and the interior electric field is negligible. The catalyst particles have the nominal properties of silver (work function = 5 eV, thermal conductivity = 4.06 W-cm^{-1}-K^{-1}, and thermal capacity = 0.023 J-cm^{-3}-K^{-1}). The relative dielectric constant (ε_r = 10) and conductivity (σ=100 Ω^{-1}-cm^{-1}) are selected so that the dielectric relaxation time, $\tau = \varepsilon_0 \varepsilon_r / \sigma \approx 1$ fs is smaller than the smallest time-steps taken by the model ($\approx 10^{-14}$ s).

5.3 Plasma Propagation in PBRs with Embedded Metallic Catalyst Particles

To investigate the consequences of embedded metallic catalysts, five metallic particles were inserted flush with the surface of the top-most rod in the full-scale geometry. The sizes of the catalysts varied between 15 and 50 μm. A -30 kV, 25-ns pulse was applied to the top electrode, while the bottom electrode was grounded. Based on our previous work, the location of catalysts and the voltage polarity were selected to ensure plasma formation near the metallic particles [46,47].

Polarization of a dielectric in an external electric field can produce electric field enhancement. A cylindrical dielectric rod placed in a uniform electric field will produce electric field enhancement at the poles of the rod aligned with the electric field, and it will also produce a reduction in the electric field at the equator [46,48]. In this geometry, the vacuum electric field is not strictly vertical. However, the electric field is enhanced near the vertical poles of the rods, and minimized near their equators, as shown in Fig. 5.3 a). With the catalysts being metal, they are equipotential and the electric field is zero inside the catalysts. This produces electric field enhancement near the triple points between the metal, dielectric, and gas, as shown in Fig. 5.3 b). At the onset of voltage, the peak E/N (electric field divided by number density) due to dielectric polarization is 245 Td (1 Td = 10^{-17} V-cm$_2$), which occurs near the top of the top-most rod. Near the catalytic particles, the E/N peaks at 295 Td. There are several locations at which the E/N is a minimum with values of approximately 65 Td, and they occur on the lateral axis between each rod pair.

The evolution of electron density, n_e, in the base case as a negative streamer develops and propagates through the lattice of dielectric rods is shown in Fig. 5.4. The electron impact ionization sources, S_e, are shown in Fig. 5.5. First, a negative streamer propagates downward from

the cathode (Fig. 5.4 a) and Fig. 5.5 a)). The streamer is directed towards the right by the polarization of the top dielectric rod, which increases the electric field at the top pole of the rod. The streamer strikes and quickly charges the top surface of the rod (Fig. 5.5 b)), forming a conductive channel from the cathode to the rod (Fig. 5.4 b)). This channel shorts the potential drop between the cathode and rod, which increases the polarization electric field of the adjacent rod, enabling the negative streamer to propagate in that direction. Photoionization and diffusion seed electrons in the polarized electric field at the top of middle rod, which then enables a positive streamer to propagate upwards as a restrike (Fig. 5.4 c) and Fig. 5.5 c)). The heads of the restrike streamer are characterized by large positive charge separation ($\rho/q \approx +5 \times 10^{12}$ cm^{-3}) and electron density ($n_e=5 \times 10^{14}$ cm^{-3}), as well as modest electron temperatures ($T_e \approx 4$ eV). Trailing the head of the ionization wave (IW) is a largely quasi-neutral plasma column, with low electron temperature $T_e \approx 1$ eV (Figs. 5.4 c), d); and Figs. 55.5 c), d)). The propagation of the restrike streamers is dependent on the presence of pre-ionization ahead of the streamer head – characteristic of positive streamers [49].

When the restrike streamers connect two dielectric rods, microdischarges form (Figs. 5.4 e), f); and Figs. 5.5 e), f)). These microdischarges have electron densities of $n_e \approx 1\times 10^{13}$ cm^{-3}. They positively charge the surfaces of the dielectric rods, prompting development of surface ionization waves (SIWs), as shown in Fig. 5c. SIWs propagate towards the cathode, along the surface of the rods, being led by an ionization front in which E/N $\approx$ 600 Td and $T_e \approx 7$ eV. These conditions produce a high electron impact ionization source of 5×10^{23} cm^{-3}s^{-1}, leading to electron and ion densities of up to $\approx 3 \times 10^{15}$ cm^{-3} along the surface of the rods.

The impact of the metallic particles on plasma formation and propagation are shown by the enlarged insets in Figs. 5.4 c), d); Figs. 5.5 c), d); and Fig. 5.6. As the external electric field is

applied, the metal catalyst particles polarize, with charge being driven to the boundaries of the particles, increasing the geometrical electric field enhancement that occurs near the metal/dielectric/gas triple points. A small density of electrons is produced by photoionization adjacent to the catalysts, which then begin to avalanche in the electric field enhanced regions. As the positive streamer propagates upwards towards the catalysts, the vacuum electric field enhancement is further increased by the compression of electric potential due to not only the conductive streamer, but also the gradient in charge density between the triple points ($\rho/q = -4\times10^{15}$ cm^{-3}) and the streamer head ($\rho/q = +5\times10^{13}$ cm^{-3}), as shown in Figs. 6b. Directly before the streamer impacts the surface, the electric field peaks at 150 kV-cm^{-1} (610 Td) at the edge of the catalyst. This electric field is sufficient to produce electron emission (Fig. 5.6 c)). The additional electrons then serve as seed ionization for the further propagation of the streamer, and the plasma is "directed" toward the catalysts (Fig. 5.4 c), d); Fig. 5.6 c)). The electric field emission appears to be an external source of negative charge, which produces a negative space charge region adjacent to the triple points.

Similar to non-catalytic regions, standing micro-discharges also form in the vicinity of the catalytic particles (Figs. 5.6 c), d)). With increasing conductivity adjacent to the catalysts, the electric field decreases which, in turn, decreases the rate of ionization (Fig. 5.6 d)). The end result is standing microdischarges adjacent to the active catalysts – those catalysts with a high enough electric field to produce electron emission. However, these microdischarges are also in regions with now low electric fields due to the high conductivity enabled by the electric field emission.

The propagation of surface ionization waves (SIWs) along the dielectric rods is also impacted by the catalytic particles. Due to the high conductivity of the catalysts, the electric field does not extend across the face of the particles. There is electric field enhancement at their edges.

However, there is no horizontal component of the electric field parallel to the face of the catalyst. As a result, the propagation of SIWs stalls at the edges of each of the catalytic particles. For there is insufficient horizontal component of the electric field to sustain the SIW across the metal particle.

The stalling effect is exaggerated in these simulations, as compared to the smaller metal particles that are used in conventional catalysts. In this 2D simulation, the metal particles appear to be infinite stripes that go into the plane of the image. In real systems, the particles have finite width (about a unity aspect ratio). Thus, the SIW would likely be able to propagate around the particles, while being slowed or stalled in crossing the particles. With the particles in some experimental systems approaching both the nanoscale and the mean free path of electrons in the SIW, electrons might have the ability to scatter over the particle.

This stalling of SIW by catalytic particles is further investigated by re-locating the catalysts to the left equator of the dielectric rod. The electron density in the entire reactor at the end of the discharge pulse for this configuration is shown in Fig. 5.7 a). Propagation of the SIW across the catalysts is shown in Fig. 5.7 b). The propagation of the SIW in the absence of catalysts is shown in Fig. 5.7 c). In the absence of the particles, a SIW smoothly propagates upwards along the surface of the rod with a maximum electron density of nearly 10^{16} cm^{-3}. As the SIW propagates along the surface of the rod having catalyst particles and the ionization front comes in contact with the edge of a particle, the SIW stalls. The SIW is then re-initiated at the opposite edge of the particle. The re-ignition occurs due to the availability of seed electrons from photoionization resulting from VUV photons emission on the stalled side of the catalyst and from the simple diffusion of electrons across the catalyst particles. These seed electrons arrive into the high electric field region at the triple point at the opposite side of the particle, where E/N reaches up to $\approx$ 1,000

Td. Avalanche quickly occurs, which restarts the SIW.

Formation of additional or higher density plasma regions near metallic catalysts has been experimentally observed by Kim et al. [50]. The authors find that the addition of silver catalysts to a zeolite packed bed reactor increased the light emission near the surfaces of the support dielectric in spots associated with the catalysts. We obtain similar results by modifying a 2-dimensional PBR previously used in experimental studies described in Refs. [46] and [47], as well as shown in Fig. 5.8 a). Here, seven dielectric disks (or rods) are inserted between electrodes in a pin-to-plane configuration. Two glass plates enclose the top and bottom sides of the reactor, while ambient air flows through the sides. A fast ICCD camera is employed to image the plasma dynamics. Silver film is applied to three locations on one of the zirconia dielectric rods, as shown in Fig. 5.8 a), in order to emulate catalysts. All other experimental parameters are the same as those in discussed in Ref. [47].

A pulsed high voltage power supply is used to generate 120 ns, 20 kV pulses applied to the anode in an ambient air atmosphere. Plasma propagates from the needle electrode and through the dielectric lattice. The ICCD imaging then reveals regions of intense light emission adjacent to the silver films, as shown in Fig. 5.8 b). These brighter regions do not occur in absence of the silver films. Results from the simulation for similar conditions, as shown in Fig. 5.8 c), have high densities of light emitting excited states of N_2 adjacent to the catalysts, concurring with the experimental imaging.

5.4 Influence of Electric Field Emission

The reduced geometry (Fig. 2) was utilized to further investigate the impact of electric field enhancement and electric field emission due to the metallic catalytic particles. Electric field

emission from surfaces in the model is given by the Fowler-Nordheim expression for thermionically enhanced emission [55],

$$j_E = AT^2 \exp\left(-\left(\Phi_W - \sqrt{q^3 E/\varepsilon_0}\right)/\left(k_B T\right)\right) \tag{5.1}$$

where A is the Richardson-Dushman constant (120.13 A/cm^2-K^2), T is the temperature of the surface, Φ_W is the work function of the metal, k_B is Boltzmann's constant, q is the elementary charge, and E is the electric field at the surface of the metal.

Two electric field enhancement mechanisms are investigated – geometry and surface roughness. The former naturally occurs as part of the simulation. The latter is included to account for surface structures that are too small to be resolved by the numerical mesh. Surface roughness is accounted for by including a multiplicative factor to increase the electric field at the surface of the metal in Eq. 5.1. The electric field enhancement factor, β, has been widely used for similar purposes in other studies, particularly in the field of high voltage pulsed power [61,62]. For roughness on a metal surface, β can be estimated by

$$\beta = \frac{2\left(h/r\right)}{\ln\left(4h/r\right) - 2d}\frac{1}{d} \tag{5.2}$$

where h is the height of the roughness, r is the radius of curvature of its tip, and d is the distance between roughness maxima. This electric field enhancement does not penetrate into the plasma far beyond a distance equal to a few radii of curvature of the tip. As a result, β has little effect on the rates of ionization in the bulk plasma further than a few microns off the surface. Electric field enhancement due to macroscopic roughness (having dimensions of hundreds of microns) would be proportionately smaller, but it would also penetrate further into the plasma and likely affect rates of ionization. The value of β in this investigation is varied between 1 (no enhancement) and

150, and it is applied to only the metal surfaces.

First, to investigate the impact of the geometric field enhancement, the catalysts are made to protrude from the dielectric rod, as shown in Fig. 5.9. The electric field, ionization source and electron density are shown as the positive ionization wave approaches the catalysts. Here, a -10 kV, 5 ns pulse is applied to the top electrode. The change in geometry (flat to protruding particles) has two primary impacts. The first is to increase the initial local electric field from 120 kV-cm^{-1} to 170 kV-cm^{-1}. The second is an apparent decrease in the importance of the metal/dielectric/gas triple point. The latter is due to the location of surface charge accumulation. Charge redistribution at the surface of the metal results from the applied field magnitude and direction. The topology of the surface, therefore, will impact the location of regions with highest surface charge density corresponding to the largest normal component of the electric field.

The overall evolution of the microdischarges is largely unchanged by the protrusion of the catalysts. As the positive ionization wave approaches the dielectric rod with the catalysts, a high conductivity plasma column is formed. The electric field in the plasma column decreases, compressing electric potential ahead of the IW. This results in additional electric field enhancement at the tip of the protrusions. When the IW wave enters into this region of high electric field, the IW focuses onto the protrusion, increasing the plasma density and ultimately reducing the electric field. The reduction in electric field adjacent to the protrusion increases the electric field along the neighboring surface, which enables the spread of the plasma by a SIW. The SIW then stalls at the next catalyst. The positive streamer propagation is focused toward the regions of negative surface charge, as is the case with flat catalysts. Photoionization and electron drift are responsible for seeding electrons ahead of the protruding catalysts and restarting the SIWs. The final product is a microdischarge between the rods, with an intense region of plasma at the tip of

the protrusion.

Surface electric field enhancement factors, β, is then used to investigate the impact of enhancement produced by a roughness that cannot be resolved in the numerical mesh. The geometry used is the same as that shown in Fig. 5.2. Electron densities for β values between 25 and 150 are shown in Fig. 5.10. For β < 10-20, there are no significant departures from the previously described discharge dynamics. For example, for β=25, electric field emission is induced from the triple-point of the middle catalyst particle. (The location of the middle catalyst particle is where the vacuum electric field is the largest due to polarization of the rods.) This catalyst becomes electric field-emission active as the positive IW approaches the catalysts and increases the electric field in front of the IW. When the IW approaches within approximately 25 μm of the surface, the electric field at the triple point increases to ≈530 kV/cm, which triggers electric field emission. As shown in Fig. 5.10 a), this produces a filament of electron density that bridges the gap between the IW and the catalyst.

With larger values of β, the plasma becomes more strongly supported by surface processes. For progressively larger values of β (50 < β < 75), the electric fields adjacent to the catalysts required to overcome the work function of the metal are produced earlier. The catalysts become active when the IW is further from the catalysts. Electric field emission transitions from being only from the triple points of the center catalyst particle to covering the surface of the catalyst. For β > 75, electric field emission begins to occur at the triple points of the neighboring catalysts. Due to seed electrons from field emission at earlier stages of the discharge, the streamers become more directed toward the catalysts and the streamer propagation velocity increases (1×10^{7} cm-s^{-1} to 3×10^{8} cm-s^{-1}).

At high values of β (>100), the discharge is initially fully sustained by surface electric field

emission, as in Fig. 5.10 d). The emitted electrons initially follow the electric field lines, producing a negative, Townsend-like discharge propagating downwards. The direction of plasma propagation depends upon the type of discharge formed. With low values of β, positive streamers propagate upwards between the dielectric rods. Upon approach of the positive streamer to the metal catalyst particles, which intensifies the electric field, electron emission occurs. At this point, a negative streamer may be launched, but it will be weak compared to the incoming positive streamer. With high values of β, electrons emission occurs at lower electric field, which seeds a negative streamer propagating downwards. The three negative streamers are all focused towards the maximum in electric field at the pole of the lower rod where they converge.

Electric field emission requires that the metal emitting the electrons be cathodic (electrically negative) with respect to the local plasma potential. Given this requirement, the placement of the metal inclusions in this investigation is based on the particles being cathodic during the initial avalanche when electric fields are expected to be the highest. To demonstrate these principles, the reduced geometry (Fig. 5.2) is used to compare otherwise identical discharges but with opposite polarities. The surface roughness factor is $\beta = 10$. The electron density and charge density are shown in Fig. 5.11 a), with +10 kV applied to the bottom electrode and the top electrode being grounded. The metal inclusions are on the bottom of the top dielectric rod. The relative direction and magnitude of the electric field is the same as those in the -10 kV base case. In this configuration, the metal inclusions have a cathodic role. As the positive streamer approaches the metal particles, the electric field intensifies, leading to electric field emission of electrons.

When placing +10 kV on the top electrode, the orientation of the field is reversed and the initial streamer travels in the opposite direction – as shown in Fig. 5.11 b). (Microdischarges in

these systems tend to be initiated by positive streamers.) The metal inclusions in this configuration have an anodic role with respect to the local plasma potential, polarizing charge to be positive along the surface of the particle. As plasma forms, the high current of electrons to those surfaces neutralizes and then charges them negatively. As the streamer approaches the lower dielectric rod, compression of the potential intensifies the electric field at the surface, directly analogous to the opposite polarity near the metal inclusions. Had metal inclusions instead been placed on the plasma facing surface of the bottom rod, electric field emission would have occurred in the same manner as the opposite polarity on the top dielectric rod.

The outcome of these studies is that electric field emission occurs in PBRs independent of the applied polarity, so long as the metal inclusions have a geometrical orientation that places them in a cathodic role when the local electric field intensifies to sufficient magnitude. Metal inclusions on the bottom side of a dielectric rod serving in an anodic role do not produce electric emission. Inclusions on the opposite side of the rod, which are geometrically positioned in a cathodic role, may produce electric field emission even if the applied polarity is positive.

The practical implications of these phenomena are several. Polarization of metallic particles results in the guiding of streamers towards the catalysts, leading to preferential rates of interaction between catalysts and plasma products. The resulting electric-field emission of electrons can lead to increased plasma volumes and plasma/catalyst interactions, and it potentially explains the additional plasma formation observed in experiments. Simultaneously, the increases in electric field emission can serve to decrease local, transient charge gradients, therefore reducing instantaneous electric fields and cooling electrons near the catalyst surfaces. Variation in electron temperature can, then, affect the local gas kinetics, and provide an additional pathway to catalytic selectivity.

The electric field at the surface of the catalyst determines the onset of the field emission. Sustaining that field emission depends on being able to sustain this critical electric field, which becomes progressively more difficult as conductive plasma forms in front of the catalyst particle. Even if this electric field could be sustained, the total amount of electric field emission would ultimately be limited by the capacitance of the particle. In electric field emission from, for example, an electrode connected to a power supply, there is a nearly unlimited amount of current that can be emitted. Electrons emitted from the surface of the metal are replaced by electrons from the power supply. The power supply may itself have a finite capacitance but, in principle, the electron source is not limited. In a PBR, where the catalyst particles are electrically floating bodies whose ability to deliver charge is limited by their capacitance, the catalyst stops emitting when its capacitance has been charged to the degree that the electric field at its surface decreases. This charging process is influenced by the displacement current that can be delivered to the back side of the catalyst through the dielectric in which the catalyst is embedded, the size of the particle, and the conductivity of the plasma by the particle. Lastly, during a pulse, charges are deposited on the dielectric surrounding the metallic particles. This can result in different-polarity charges coexisting in near proximity – one polarity net charge on the dielectric (resulting from a previous pulse) and opposite net charge (resulting from external, applied electric field). This, in turn, should result in high local electric fields and perhaps additional charge re-alignment within the metallic particles.

5.5 Fluences of Reactive Species and Impact on Catalyst Temperature

While catalysts can have a large impact on the dynamics of the discharge, the reverse is also true. The plasma can heat the catalysts, increasing the rates of some thermostatic reactions. Fluxes of energetic UV photons, electrons, and ions can clean contaminants from surface sites; and high

applied electric fields can decrease the potential energy barriers of surface reactions. Only a subset of these phenomena could be investigated in this work – fluences of reactive species and heating rates.

The fluences of selected plasma-produced species and photons to the surfaces of the catalysts in the reduced geometry, as a function of β, are shown in Fig. 5.12. These fluxes are integrated over the surface of the center catalytic particle. As β increases, the fluences of all ions, radical, photons, and electrons decreases. This result, while counter-intuitive, is explained by the shorting of the electric field in the gas gap by the conductive plasma enabled by high β. In the instant that electric emission begins, there is an increase in the production of all ions, radicals, photons, and electrons. The electric field is large and so electron impact rate coefficients are also large. However, as the number of electric field emitted electrons near surfaces increases, the electric field in the plasma decreases and the local electron temperature decreases, causing the rates of electron-impact reactions to also decrease. The relative rates of reactions with higher threshold energies decreases more quickly with increasing β. For example, the electron impact dissociation of N_2 has a higher threshold energy ($\approx$ 12 eV) than that of O_2 ($\approx$ 5 eV). As a result, the fluence of atomic nitrogen onto the catalysts decreases more rapidly than does the fluence of atomic oxygen. This effect could be used to tune the species that adsorb onto and react with catalysts.

Power deposition onto the surface of the catalyst results from the reactions of neutral species, UV fluxes, kinetic energy of charged species, and the ionization potential of incident ions, as described in Chapter 2. The power deposition onto the surface of the catalyst and the fractional contribution to heating the catalyst due to electrons, ions, and neutrals are shown in Fig. 5.13 for β = 10. The contribution from UV photons is small. At the beginning of the discharge (t < 1.5

ns), the majority of heating is by electrons, though the absolute magnitude of that heating is small. Once a streamer forms and makes contact with the surface, the total energy deposition increases by two orders of magnitude due to power deposition by ions, which carry with them their ionization potential, as well as kinetic energy due to the local electric field. With increasing dissociation of the gas adjacent to the particle, neutral reactions on the surface of the particles also begin to heat the particles. The heating of the particles, up to 60 kW/cm^2, occurs over about 1 ns, dominated by ion impact. In the post-pulse period ($t > 3$ ns), the heating by ions decreases as the plasma dissipates, while power deposition continues due to surface reactions of the neutral species. Heating of the particles by surface reactions continues as long as there are radicals diffusing to the particle.

The total amount of energy deposited onto the surface of the catalyst per pulse is not large; however, the particles are small. The energy deposition per pulse is about 10 $\mu J/cm^2$. The heating of the particle is then determined by the repetition rate of the discharge and the thermal conductivity of the dielectric in which the particle is embedded. To model the heating of the catalyst, the temperature equation is integrated while providing impulsive increments of surface energy (as would be delivered by the discharge). The energy source terms as a function of position on the catalyst from the first pulse are recorded and inserted as a delta function at a frequency of 10 kHz. Heat conduction and convection equations are solved throughout the reduced computational domain while having a constant temperature (300 K) boundary condition on the walls of the reactor. Over the equivalent of 150,000 pulses (15 seconds at 10 kHz), the temperature of the catalyst increases to $\approx$500 K before reaching a quasi-equilibrium. This increase of 200 K is high enough to impact the rates of thermocatalytic reactions. Since the streamers are focused on the triple points, energy deposition and temperature increases are not uniform. Rather, the

temperatures first increase at these locations. Thermal conduction then spreads the higher temperature throughout the rest of the solid – metal and dielectric alike.

5.6 Concluding Remarks

Interactions between atmospheric-pressure plasmas and metallic catalysts in a packed-bed reactor were computationally investigated. In addition to geometrical electric field enhancement, the metallic particles produce further local electric field enhancement due to the redistribution of charges in the particles. As a result, discharges are guided towards the metallic particles, and higher density plasma forms in the proximity of their surfaces. Formation of additional plasma near the catalysts therefore leads to higher fluxes of reactive species to their surfaces which could, in part, produce an increase in the efficiency of atmospheric pressure plasma-based catalysis. The geometrical electric field enhancement is intensified by the space-charge gradient between the streamer heads and the particles, leading to electric-field emission of electrons. These effects then lead to a decrease in the voltage required to reach breakdown, when compared to the same reactor without metallic particles.

An electric field enhancement factor, β, is used as a proxy for enhancement that occurs due to surface roughness that cannot be resolved in the numerical mesh. Increasing β and increasing the local electric field produces rapid increase in electric field emission. This field emission enables the formation of plasma in regions where discharges would not otherwise occur, leading to a larger total plasma volume. However, higher β also results in a decrease in local electric fields, once plasma formed due to the additional source of electrons nears the surface. This transformation in the electric field in the plasma changes the selectivity of the plasma-produced reactive species formed near the catalysts. Plasma-produced species are preferentially focused onto the surface in the vicinity of the catalyst, resulting in preferential heating of the particles that

would directly affect thermally sensitive chemical processes.

During review of this paper, a referee asked about the electric field emission that might occur from the dielectric support due to surface roughness represented by a β factor. Dielectrics do emit electrons following ion bombardment with secondary emission coefficients, γ, as large as 0.15 [63]. Dielectrics undergo photo-electron emission [64], though the emission may be transient due to the resulting positive charging of the surface. Dielectrics have work functions. As a result, there exists some form of electric field emission, which is very sensitive to the resulting positive charging of the surface [65]. In metals, this positive charging is neutralized by the electron current from within the metal. Thin films of dielectrics over metals are able to continuously emit electrons as the metal injects electrons into the dielectric, which then traverse the thin insulator. Thick dielectrics only transiently emit due to this surface charging. Simulations of our PBR reactor were performed for the base case, while applying the expression for metal electric field emission (Eq. 5.1) to the surface of the dielectric rods (β = 100). This expression likely greatly over-estimates the emitted current. In these simulations, electric field emission occurs from the dielectric only near the metal inclusions already possessing physical electric field enhancement, while surface charging eventually diminishes the emission. Due to the thickness dependence of electron emission from dielectrics, the fact that dielectrics in these systems are typically not in electrical contact with metals, except at isolated points, as well as the fact that unrealistically large values β would likely be required, we do not expect that electric field emission from dielectrics of the type found in PBRs to be important. As a result, the field emission of electrons from dielectric surfaces should not significantly compete with emission from metallic particles, and addition of metallic catalysts in a PPBR should result in an increase of total plasma volume.

Different metal catalysts produce significant differences in chemical processing. However,

the electrical processes discussed here apply to all types of metal particles. For example, the tendency for metal inclusions to block propagation of surface ionization waves depends only weakly on the type of metal as the conductivity of all metals is large enough to produce the blockage. The greatest sensitivity to the type of metal is through the work function of the metal. Larger work functions require larger electric fields to produce significant electric field emission. The work functions of most metals are between 4-5 eV [66]. Inclusions with component metals with lower work functions – for example, Ce [2.9 eV], Ba [2.52 eV], or Mg [3.66 eV] – are more sensitive to electric emission due to the onset of their emission occurring at lower electric fields. Inclusions with component metals having exposed crystallographic planes with higher work functions – for example Co [5.0 eV], W [5.22 eV], or Pt [5.2-5.9 eV] – are less sensitive to electric field emission.

To summarize – inclusion of low work-function metals with higher surface roughness should increase the rates of plasma formation. Particles which protrude from the support increase the local electric further field enhancement. The plasma itself would focus energy deposition onto those particles, increasing efficiency. Furthermore, an increase in overall temperature of the system could not only lead to higher rates of thermo-catalytic reaction rates, but also in the rates of electric field electron emission due to a decrease in the potential energy barriers. Plasmas interact with the materials in a synergistic manner, and inclusion of the above-stated properties should lead to an increase in energy efficiency, throughput and selectivity.

5.7 Figures

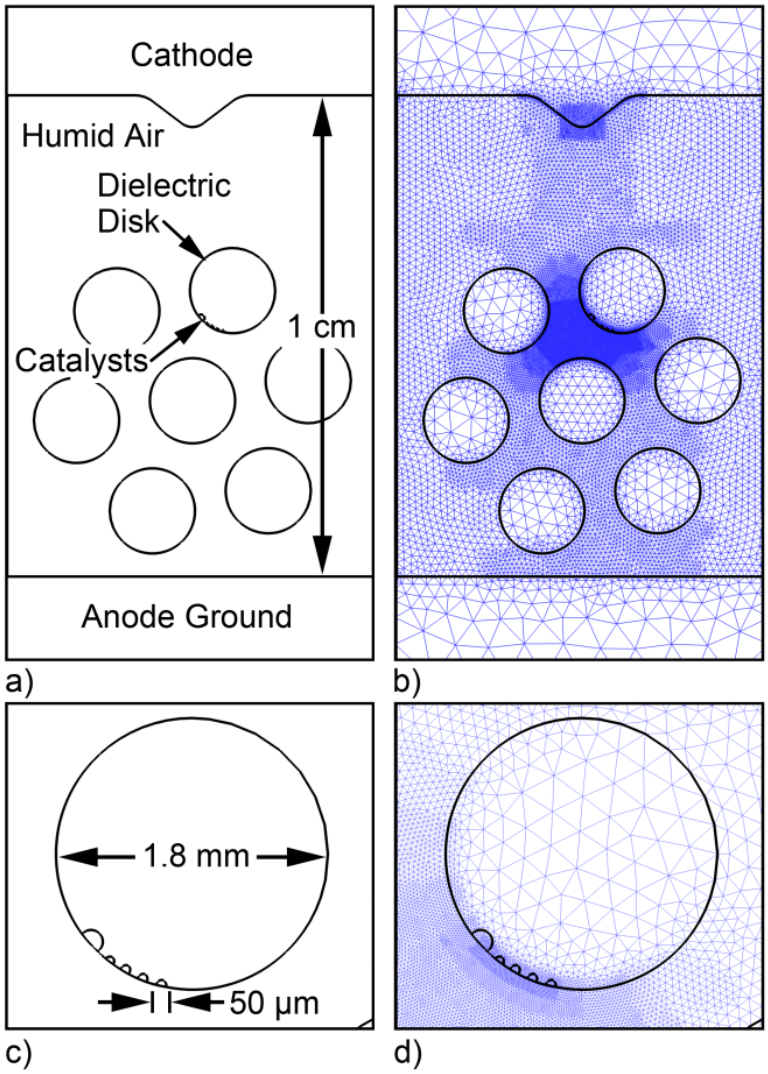

Fig. 5. 1 Geometry of the base case reactor. (a) Schematic of the entire reactor. b) Computational mesh, c) Enlargement of the topmost disk. d) Enlargement of numerical mesh.

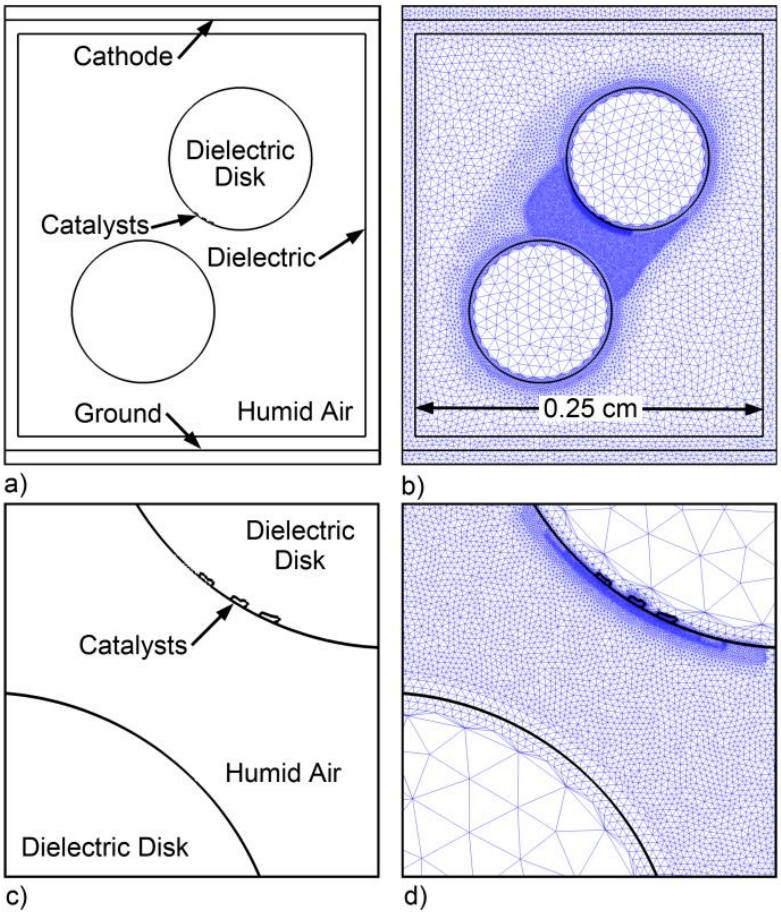

Fig. 5. 2 Geometry of the reduced scale reactor. (a) Schematic of the entire reactor. b) Computational mesh. c) Enlargement of inter-disk gap and catalysts. d) Enlargement of numerical mesh.

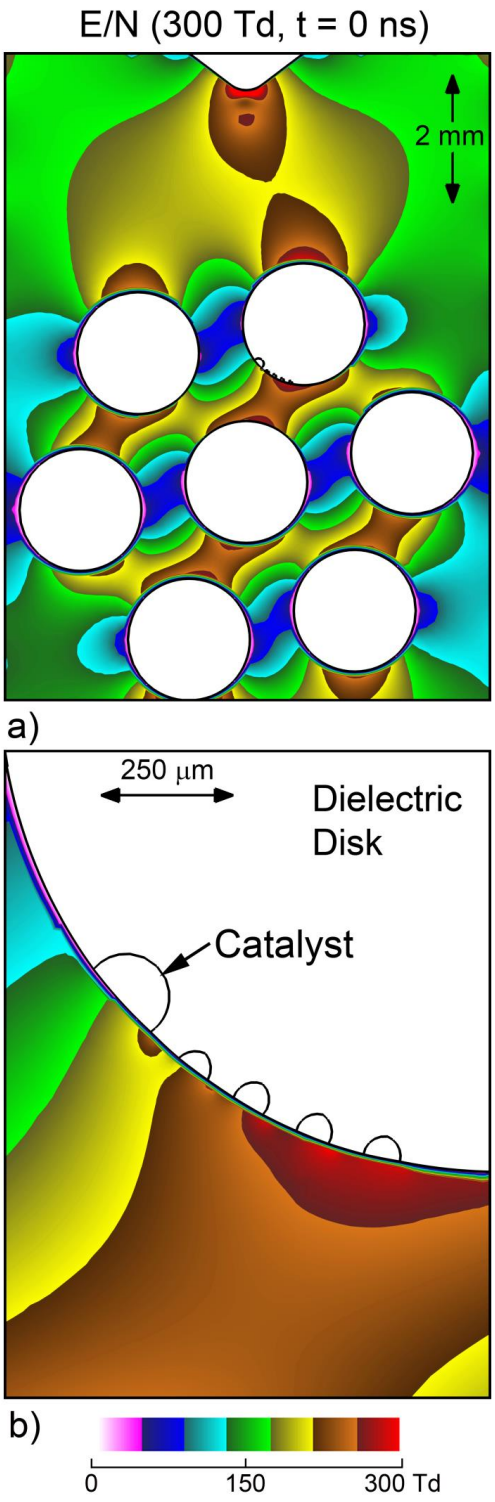

Fig. 5. 3 Reduced electric field (E/N) at t = 0 s for a) the full-size base-case geometry and b) enlargement near the catalysts.

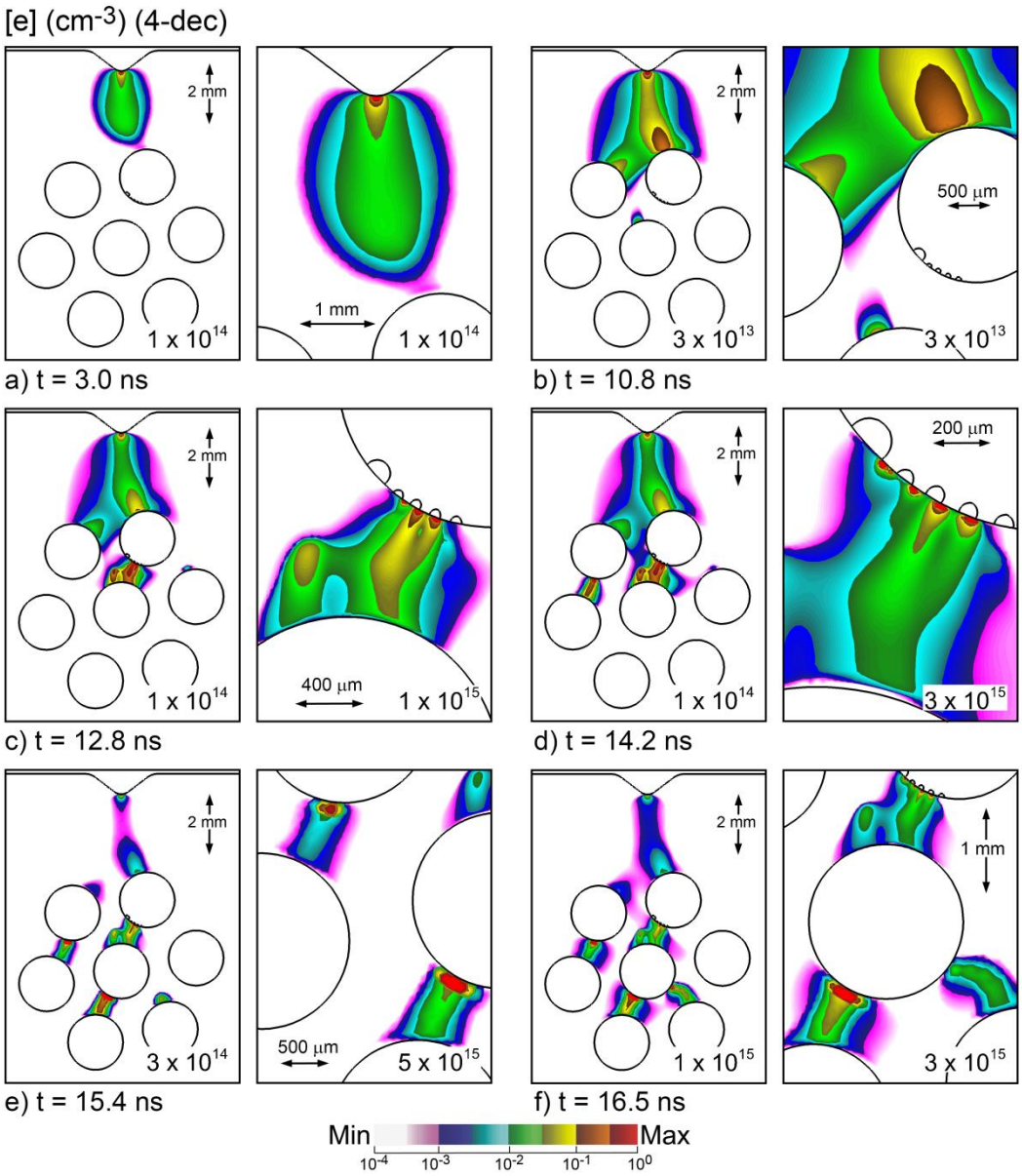

Fig. 5. 4 Time evolution of electron density in the full-size base-case. a) 3.0 ns; b) 10.8 ns; c) 12.8 ns; d) 14.2 ns; e) 15.4 ns; and f) 16.5 ns. At each time, images are shown for the (left) full reactor and (right) enlargements in regions of interests. Densities are plotted on a 4-decade log scale with the maximum value indicated in each frame.

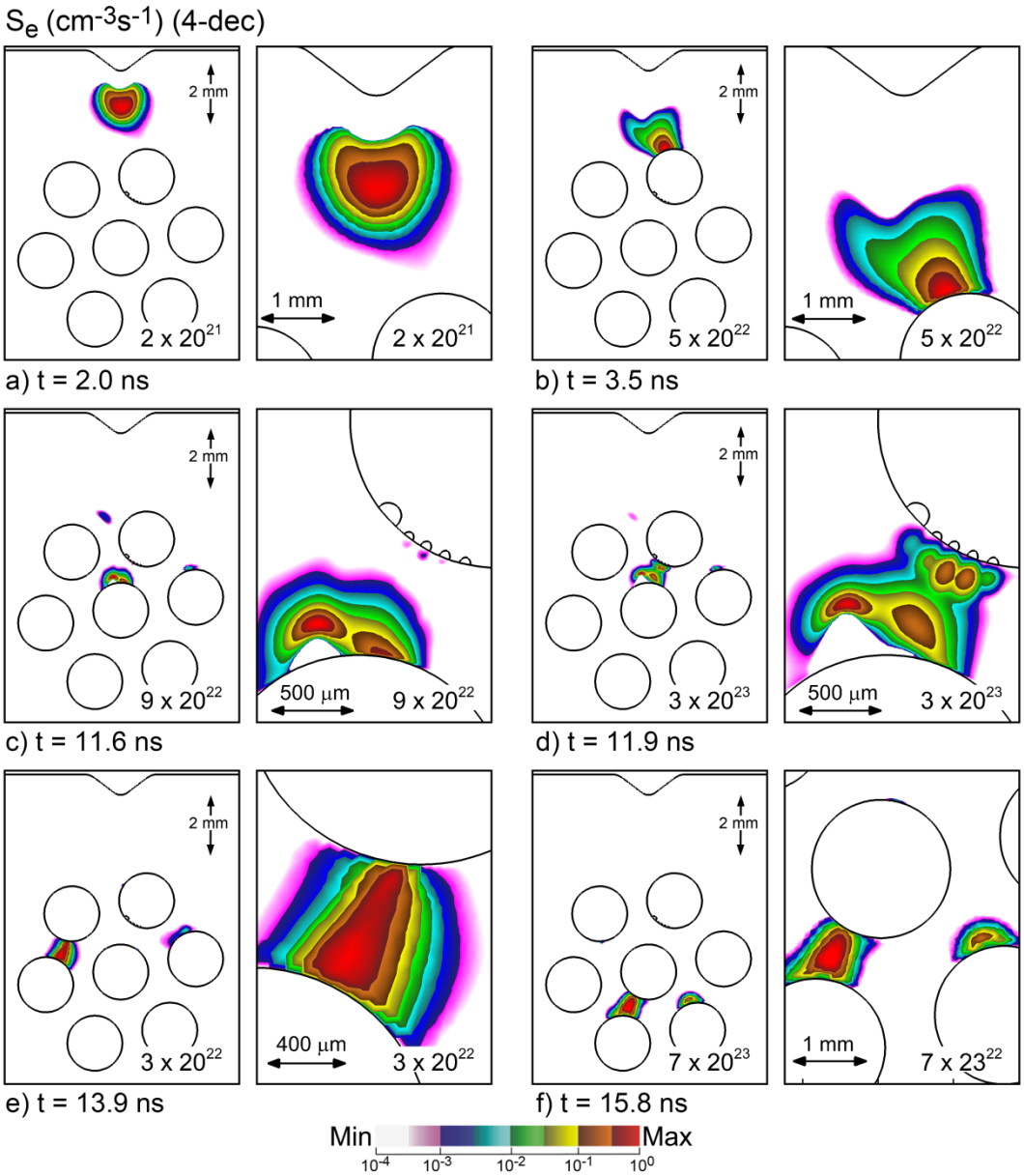

Fig. 5. 5 . Time evolution of electron impact source time in the full-size base-case. a) 2.0 ns; b) 3.5 ns; c) 11.6 ns; d) 11.9 ns; e) 13.9 ns; and f) 15.8 ns. At each time, images are shown for the (left) full reactor and (right) enlargements in regions of interests. Sources are plotted on a 4-decade log scale with the maximum value indicated in each frame.

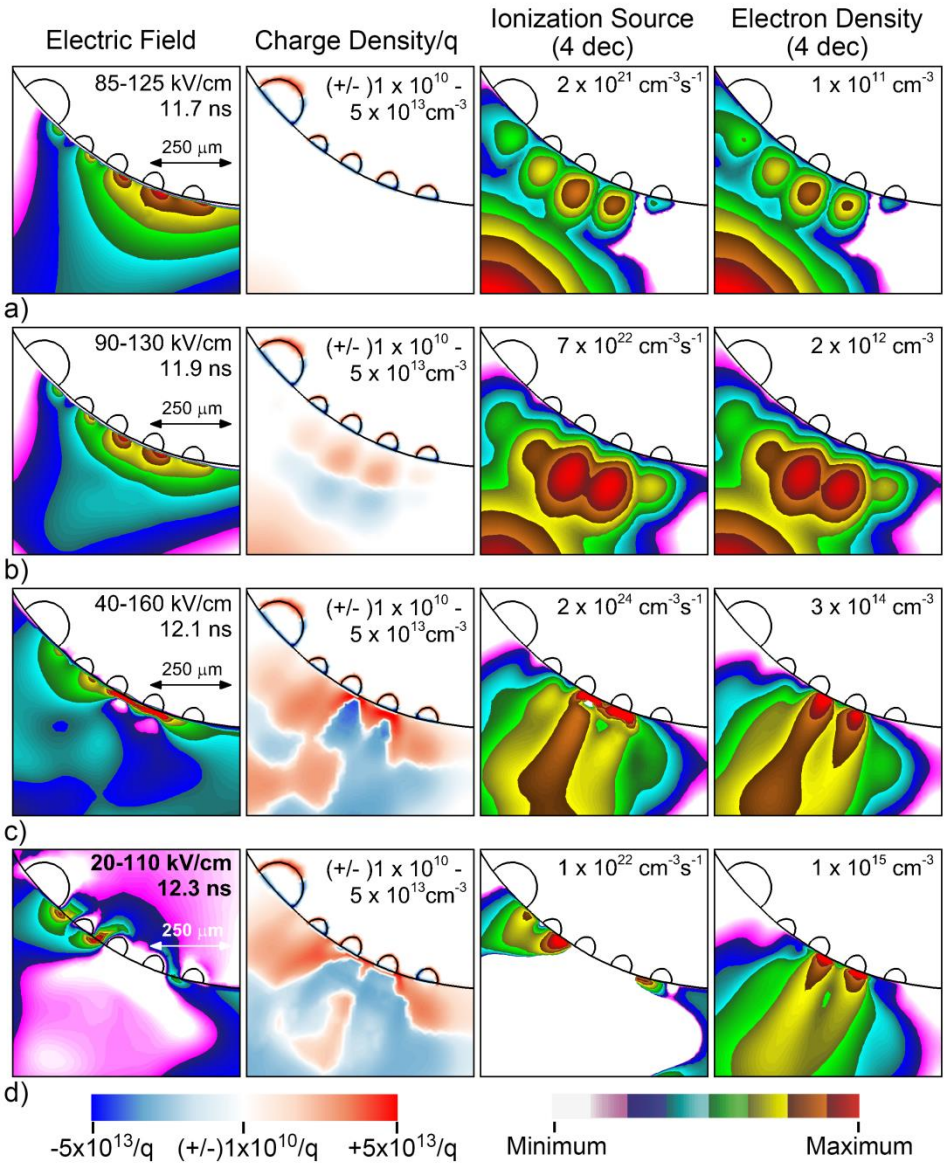

Fig. 5. 6 Plasma properties in the vicinity of the catalyst particles (left to right) electric field, charge density, ionization source term, and electron density at times of a) 11.7 ns; b) 11.9 ns; c) 12.1 ns; and d) 12.3 ns. These images are during streamer propagation toward the metallic catalysts. Gradients in charge density lead to the formation of strong electric fields and electric field emission of electrons from the surfaces of metals.

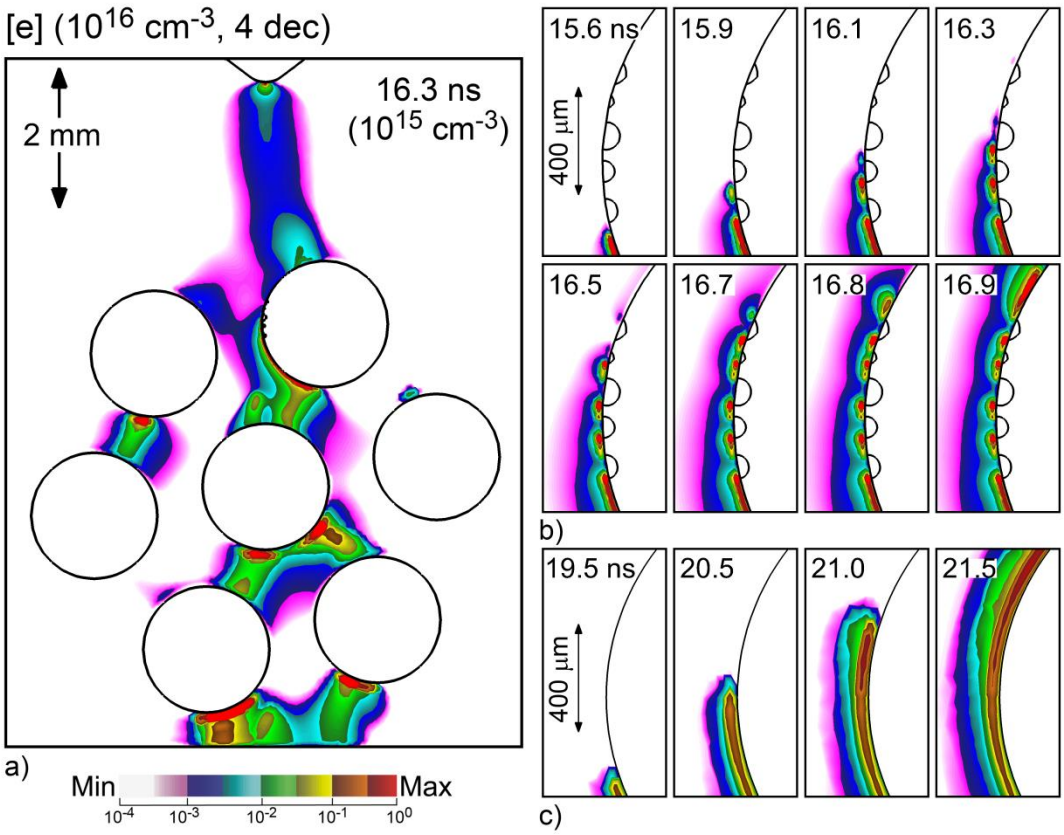

Fig. 5. 7 Electron density in the full-size geometry with catalysts arranged along the left pole of the topmost particle. a) Electron density in the entire reactor at 16.3 ns. b) Surface ionization wave (SIW) in the vicinity of the catalysts (15.6 ns to 16.9 ns) showing stagnation of SIWs approaching the catalysts and re-ignition on the other side. c) SIW for the same location without metallic catalysts. Densities are plotted on a 4-decade log scale.

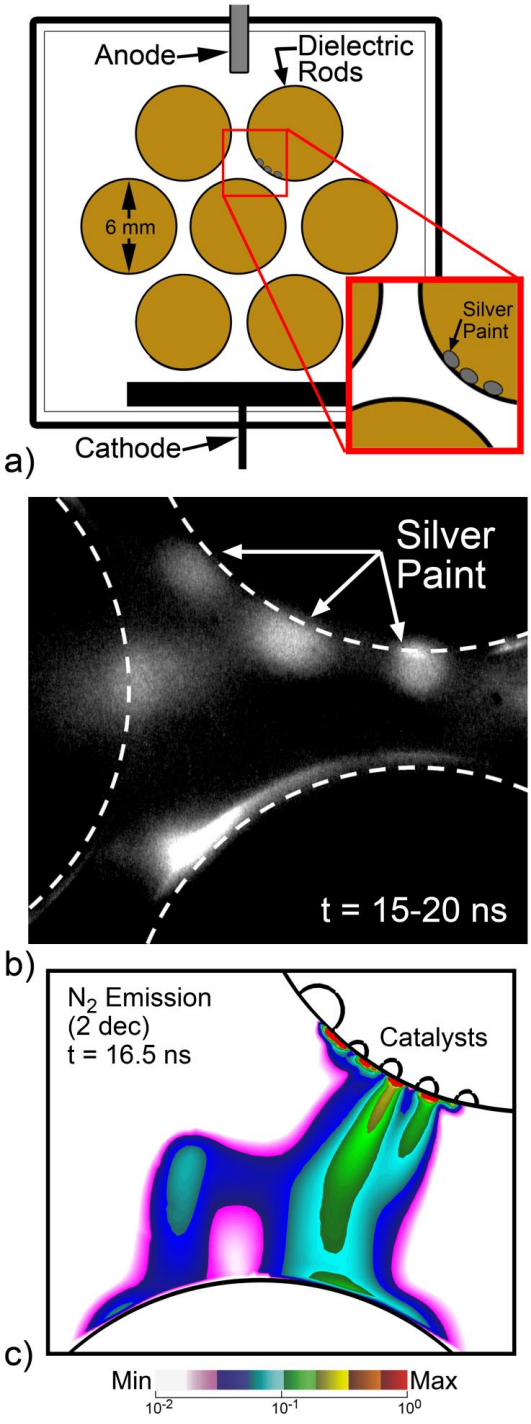

Fig. 5. 8 Experimental and computational comparison. a) Schematic experimental set-up of 2-dimensional packed bed reactor with silver film placed on the top-right dielectric disk. b) ICCD image of plasma emission near silver film. c) Computed densities of light-emitting species in a similar system.

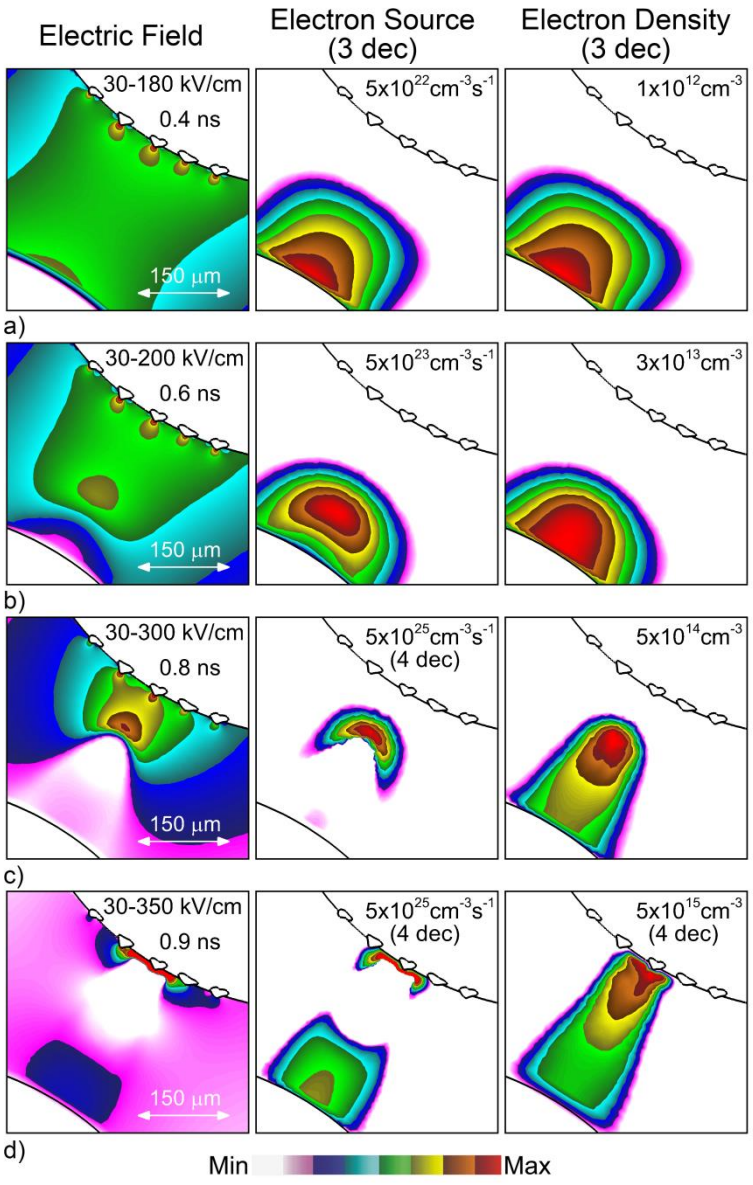

Fig. 5. 9 Plasma properties in the vicinity of protruding catalytic particles (left to right) electric field, electron impact ionization source, and electron density at times of a) 0.4 ns; b) 0.6 ns; c) 0.8 ns; and d) 0.8 ns. Electron density and source are plotted on a 3-decade log scale unless indicated otherwise. The maximum values or range of values plotted in each are indicated in each frame.

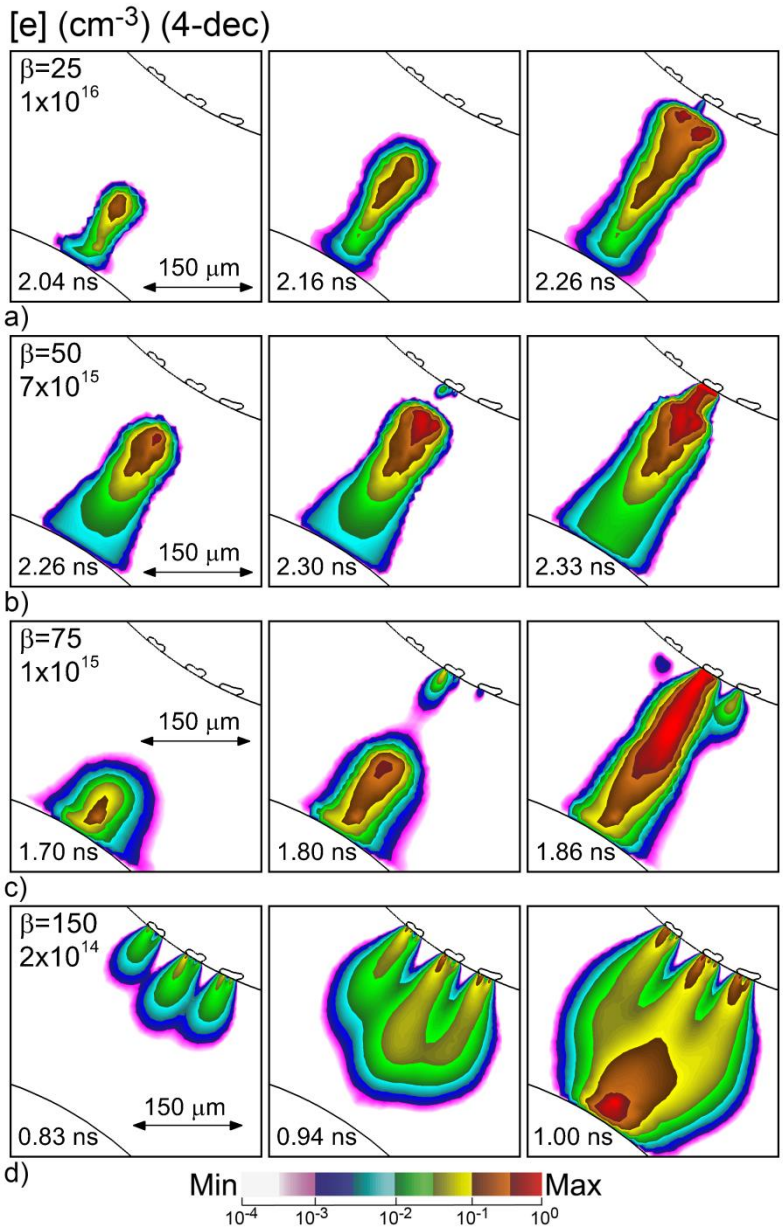

Fig. 5. 10 Electron densities at the end of the voltage pulse for different values of the electric field enhancement factor, β, in the reduced geometry at different times (left to right). β = a) 25; b) 50; c) 75; and d) 150. Densities are plotted on a 4-decade log-scale with maximum values noted in each frame. The mechanism of plasma formation changes from being volume- to surface-dominated with increasing β.

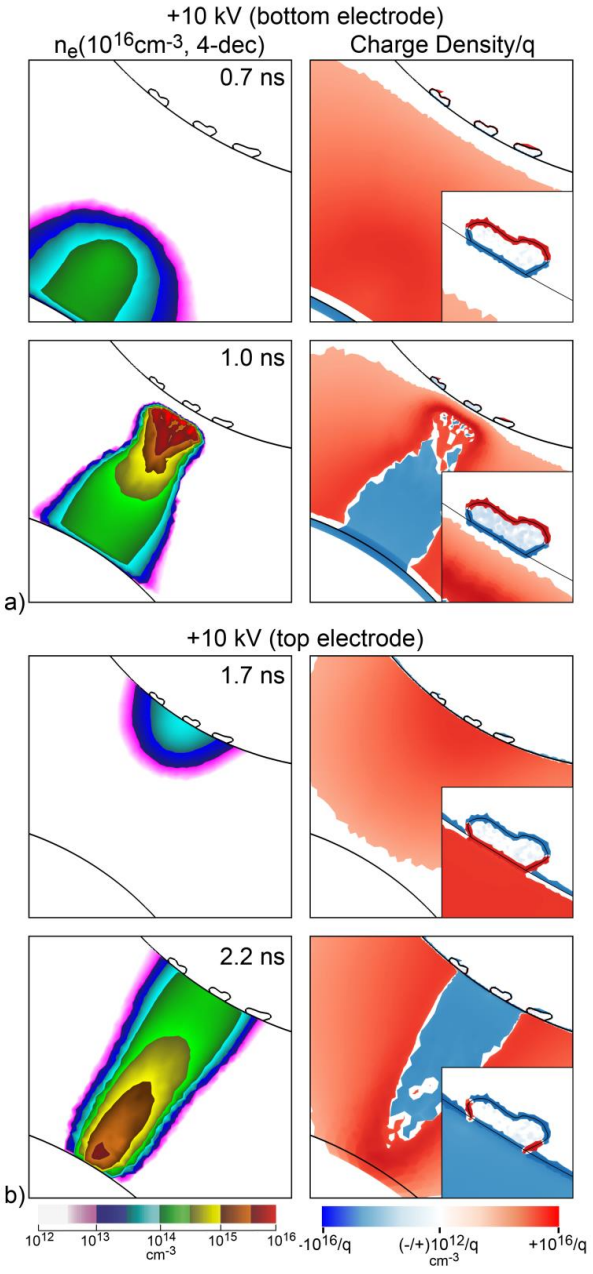

Fig. 5. 11 Electron density and charge density in positive-voltage cases where a) the top electrode is powered and b) the bottom electrode is powered. Both densities are plotted on a 4-decade log-scale. The charge density shows both negative and positive values. The discharge properties and effects of the catalysts are dependent on whether the metal inclusions serve in a cathodic role and not necessarily on the polarity of the pulse.

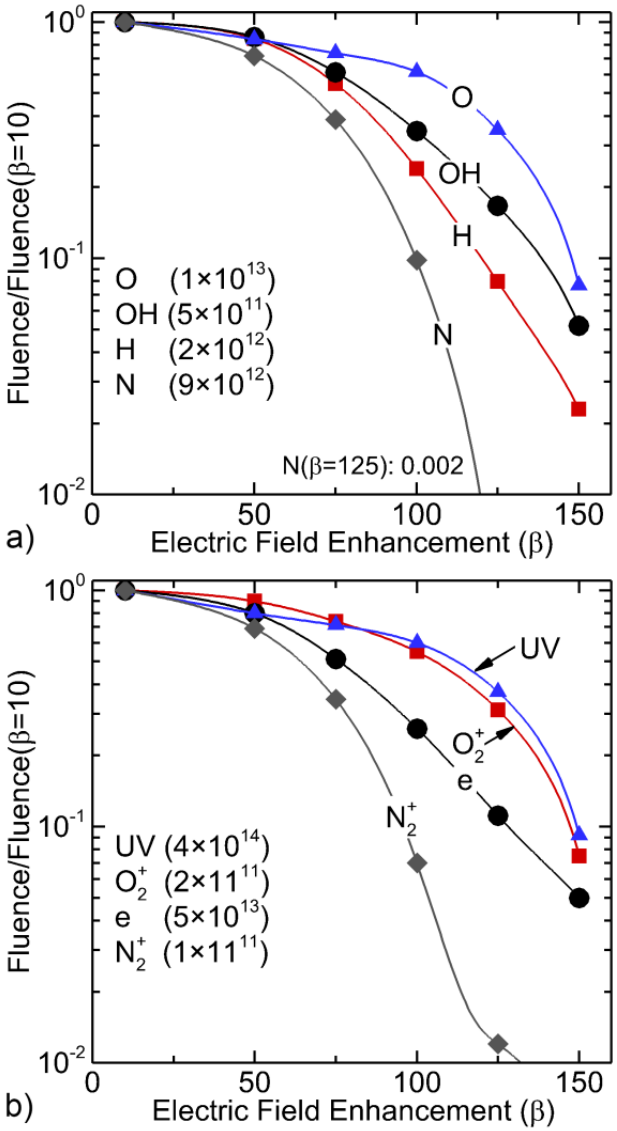

Fig. 5. 12 Fluences of selected species to the surfaces of the middle catalyst particle as a function of the electric field enhancement factor for the reduced-scale geometry. a) O, OH, H, N, and b) N_2^+, O_2^+, UV photons, and electrons. With the increase in conductivity due to electric field emission of electrons, the electric field in the adjacent plasma decreases, leading to a colder plasma and decreased fluences to the surface.

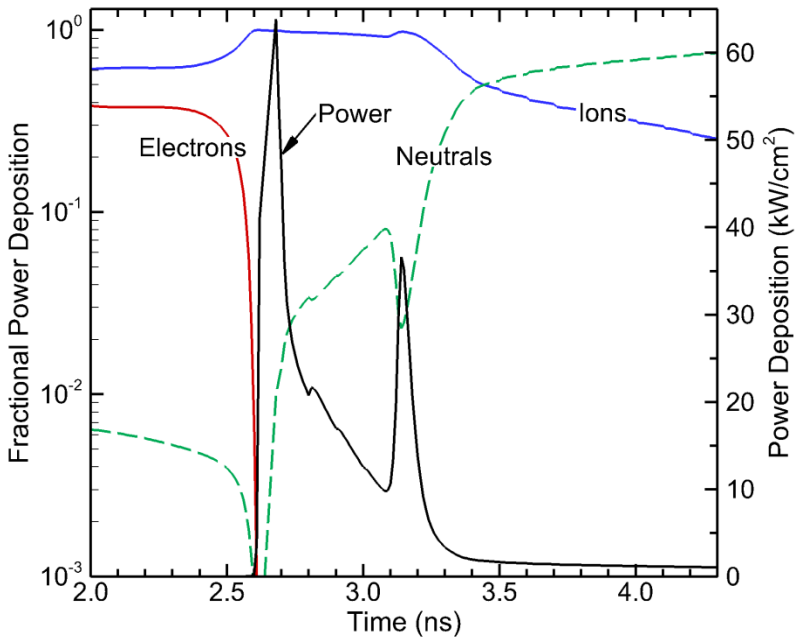

Fig. 5. 13 Total and fractional power deposition to the surface of the catalyst as a function of time for the reduced scale geometry base case. Power deposition by ions dominates, with neutral chemical reactions dominating in the afterglow.

5.8 References

[1] M. Besora and F. Maseras, WIREs Comput. Mol. Sci. **8,** 1372 (2018).

[2] H. Liu, Chinese J. Catal. **35,** 1619 (2014).

[3] A. Bogaerts, X. Tu, J. C. Whitehead, G. Centi, L. Lefferts, O. Guaitella, F. Azzolina-Jury, H. Kim, A. B. Murphy, W. F. Schneider, T. Nozaki, J. C. Hicks, A. Rousseau, F. Thevenet, A. Khacef and M. Carreon, J. Phys. D Appl. Phys. **53,** (2020).

[4] R. Snoeckx and A. Bogaerts, Chemi. Soc. Rev. **46,** (2017).

[5] S. Xu, S. Chansai, C. Stere, B. Inceesungvorn, A. Goguet, K. Wangkawong, S. F. R. Taylor, N. Al-Janabi, C. Hardacre, P. A. Martin and X. Fan, Nat. Catal. **2,** 142 (2019).

[6] R. Gholami, C. E. Stere, A. Goguet and C. Hardacre, Phil. Trans. R. Soc. A **376,** 20170054 (2017).

[7] J. G. Chen, R. M. Crooks, L. C. Seefeldt, K. L. Bren, R. Morris Bullock, M. Y. Darensbourg, P. L. Holland, B. Hoffman, M. J. Janik, A. K. Jones, M. G. Kanatzidis, P. King, K. M. Lancaster, S. V. Lymar, P. Pfromm, W. F. Schneider and R. R. Schrock, Science (80-.). **360,** 873 (2018).

[8] H. Puliyalil, D. Lašič Jurković, V. D. B. C. Dasireddy and B. Likozar, RSC Adv **8,** 27481 (2018).

[9] S. Liu, L. R. Winter and J. G. Chen, ACS Catal. **10,** 2855 (2020).

[10] Z. Wang, Y. Zhang, E. C. Neyts, X. Cao, X. Zhang, B. W. L. Jang and C. J. Liu, ACS Catal. **8,** 2093 (2018).

[11] A. Vesel, M. Mozetic, A. Drenik and M. Balat-Pichelin, Chem. Phys. **382,** 127 (2011).

[12] X. Tu, H. J. Gallon, M. V Twigg, P. a Gorry and J. C. Whitehead, J. Phys. D. Appl. Phys. **44,** 274007 (2011).

[13] U. Roland, F. Holzer and F. D. Kopinke, in Catalysis Today **73,** 315 (2002).

[14] H. Lee, D.-H. Lee, Y.-H. Song, W. C. Choi, Y.-K. Park and D. H. Kim, Chem. Eng. J. **259,** 761 (2015).

[15] F. Holzer, F. D. Kopinke and U. Roland, Plasma Chemistry and Plasma Processing **25,** 595 (2005).

[16] T. Nunnally, K. Gustol, A. Rabinovich, A. Fridman, A. Gustol and A. Kemoun, J. Phys. D Appl. Phys. **44,** 274009 (2011).

[17] K. Hensel, Eur. Phys. J. D. **54,** 141 (2009).

[18] K. Hensel, V. Martišovitš, Z. Machala, M. Janda, M. Leštinský, P. Tardiveau and A. Mizuno, Plasma Process. Polym. **4,** 682 (2007).

[19] E. C. Neyts and A. Bogaerts, J. Phys. D. Appl. Phys. **47,** 224010 (2014).

[20] P. Brault, J. M. Bauchire, F. James and C. Josserand, Defect Diffus. Forum **323–325,** 387 (2012).

[21] A. Bogaerts, Q. Z. Zhang, Y. R. Zhang, K. Van Laer and W. Wang, Catal. Today **337,** 3 (2019).

[22] J. Hong, S. Pancheshnyi, E. Tam, J. J. Lowke, S. Prawer and A. B. Murphy, J. Phys. D Appl. Phys. **51,** 109501 (2018).

[23] S. Matera, W. F. Schneider, A. Heyden and A. Savara, ACS Catal. **9,** 6624 (2019).

[24] A. Bogaerts, A. Berthelot, S. Heijkers, S. Kolev, R. Snoeckx, S. Sun, G. Trenchev, K. Van Laer and W. Wang, Plasma Sources Sci. Technol. **26,** 063001 (2017).

[25] F. Che, J. T. Gray, S. Ha, N. Kruse, S. L. Scott and J. S. McEwen, ACS Catal. **8,** 5153 (2018).

[26] H. Kim, Y. Teramoto, A. Ogata, H. Takagi and T. Nanba, Plasma Process. Polym. **36,** 45 (2016).

[27] B. S. Patil, Q. Wang, V. Hessel and J. Lang, Catal. Today **256,** 49 (2015).

[28] A. Bogaerts and E. C. Neyts, ACS Energy Lett. **3,** 1013 (2018).

[29] R. Brandenburg, A. Bogaerts, W. Bongers, A. Fridman, G. Fridman, B. R. Locke, V. Miller, S. Reuter, M. Schiorlin, T. Verreycken and K. K. Ostrikov, Plasma Process. Polym. **16,** 1700238 (2017).

[30] H.-H. Kim, Y. Teramoto, A. Ogata, H. Takagi and T. Nanba, Plasma Chem Plasma Process Relat. **36,** 45 (2015).

[31] J. Hong, S. Prawer and A. B. Murphy, ACS Sustain. Chem. Eng. **6,** 15 (2018).

[32] Y. X. Zeng, L. Wang, C. F. Wu, J. Q. Wang, B. X. Shen and X. Tu, Appl. Catal. B Environ. **224,** 469 (2018).

[33] W. Chung and M. Chang, Renew. Sustain. Energy Rev. **62,** 13 (2016).

[34] G. J. van Rooij, D. C. M. van den Bekerom, N. den Harder, T. Minea, G. Berden, W. A. Bongers, R. Engeln, M. F. Graswinckel, E. Zoethout and M. C. M. van de Sanden, Faraday Discuss. **183,** 233 (2015).

[35] A. Bogaerts, T. Kozák, K. van Laer and R. Snoeckx, Faraday Discuss. 217 (2015).

[36] I. Michielsen, Y. Uytdenhouwen, J. Pype, B. Michielsen, J. Mertens, F. Reniers, V. Meynen and A. Bogaerts, Chem. Eng. J. **326,** 477 (2017).

[37] H. H. Kim, Y. Teramoto, A. Ogata, H. Takagi and T. Nanba, Plasma Process. Polym. **14,** 1600157 (2016).

[38] J. C. Whitehead, J. Phys. D Appl. Phys. **49,** 243001 (2016).

[39] P. Mehta, P. Barboun, D. B. Go, J. C. Hicks and W. F. Schneider, ACS Energy Lett. **4,** 1115 (2019).

[40] S. Tanaka, H. Uyama and O. Matsumoto, Plasma Chem Plasma Process **14,** 4 (1994).

[41] D. Mei, X. Zhu, C. Wu, B. Ashford, P. T. Williams and X. Tu, Appl. Catal. B Environ. **182,** 525 (2016).

[42] A. M. Darr, A. M. Loveless and A. L. Garner, Appl. Phys. Lett. **114,** 014103 (2019).

[43] F. Schertz, M. Schmelzeisen, M. Kreiter, H. Elmers and G. Schönhense, Physi. Rev. Let. **108,** 237602 (2012).

[44] R. G. Forbes, J. Vac. Sci. Technol. B **26,** 2 (2008).

[45] A. M. Lietz and M. J. Kushner, J. Phys. D. Appl. Phys. **49,** 425204 (2016).

[46] J. Kruszelnicki, K. W. Engeling, J. E. Foster, Z. Xiong and M. J. Kushner, J. Phys. D Appl. Phys. **50,** 025203 (2017).

[47] K. W. Engeling, J. Kruszelnicki, M. J. Kushner and J. E. Foster, Plasma Sources Sci. Technol. **27,** 085002 (2018).

[48] K. Van Laer, S. Kolev and A. Bogaerts, Plasma Sources Sci. Technol. **25,** 015002 (2015).

[49] S. Nijdam, J. Teunissen, E. Takahashi and U. Ebert, Plasma Sources Sci. Technol. **25,** 044001 (2016).

[50] H. H. Kim and A. Ogata, Eur. Phys. J. Appl. Phys. **55,** 13806 (2011).

[51] T. S. Light, S. Licht, A. C. Bevilacqua and K. R. Morash, Electrochem. Solid-State Lett. **8,** E16 (2005).

[52] C. G. Malmberg and A. A. Maryott, J. Res. Natl. Bur. Stand. **56,** 2641 (1956).

[53] S. I. Grashchenkov and A. I. Grigoryev, Fluid Dyn. **46,** 437 (2011).

[54] P. D. Maguire, C. M. O. Mahony, C. P. Kelsey, A. J. Bingham, E. P. Montgomery, E. D. Bennet, H. E. Potts, D. C. E. Rutherford, D. A. McDowell, D. A. Diver and D. Mariotti, Appl. Phys. Lett. **106,** 224101 (2015).

[55] R. M. Young and D. M. Neumark, Chem. Rev. **112,** 5553 (2012).

[56] P. Rumbach, D. M. Bartels, R. M. Sankaran and D. B. Go, Nat. Commun. **6,** 7248 (2015).

[57] D. C. Taflin, T. L. Ward and E. J. Davis, Langmuir **5,** 376 (1989).

Chapter 6 Interactions Propagation of Atmospheric Pressure Plasmas Through Interconnected Pores in Dielectric Materials[4]

Transfer of plasma reactivity to solids can also influence the properties of the material itself. For example, porous ceramics and polymers are also used as scaffolding in tissue engineering to enable the re-growth of bone structures and cell regeneration, as well as for the growth of soft tissues [1–3]. The application of APPs has been shown to accelerate and stabilize the growth of cells on these scaffolds [2,4–7]. Plasmas have also been shown to sterilize these porous materials and have been used for this purpose in-vivo and ex-vivo during dental procedures [8]. Plasmas have been utilized to functionalize and coat porous materials, demonstrating the ability to penetrate into the interior of foams and to affect pore structure [9–11]. The method of the propagation of APPs through porous media is not well characterized. This chapter discusses the results from an investigation of humid air APPs propagating through short, fully interconnected pore-chains in a dielectric substrate. In this chapter, modeling of plasmas into micron-scale pore chains is also discussed.

6.1 Introduction

The propagation of plasmas on the surface of porous materials has been experimentally investigated in both the catalysis and medical fields [2,5,12–20]. The complexity of the geometry presents many challenges [16,21,22]. Fluid and particle-in-cell (PIC) modeling of plasma propagation into micron-scale pores indicates that, even in these small structures, transport is

[4] The results discussed and a portion of the text in this chapter have been previously published in J. Kruszelnicki, Runchu Ma and M. J. Kushner, "Propagation of Atmospheric Pressure Plasmas Through Interconnected Pores in Dielectric Materials", J. Appl. Phys., **129** 143302 (2021)

dominantly electric field driven drift, as opposed to diffusion dominated. Due to polarization of the pore materials and subsequent electric field enhancement, large electron densities are produced in the pores. While higher plasma densities near surfaces are observed, surface ionization waves are not, suggesting that the higher plasma densities are due to secondary electron emission. Photoionization has not been found to be impactful. Swanson and Kaganovich have investigated secondary electron emission from foam-like or fuzz-like surfaces using Monte-Carlo simulations and analytical models [23]. They find that secondary electron yield decreases from foam and fuzz-like surfaces compared to planar surfaces. Gu et al. have modeled surface discharges propagating into pores using PIC methods [24]. They find an enhanced plasma density near the interior surfaces of the pores, as compared to the volumetric discharge.

In this chapter, simulations of plasma propagation through short chains of inter-connected, 150-micron-diameter pores in dielectric materials will be presented. The size and interconnectivity of these structures are similar to those found in tissue scaffolding [25]. We found that plasma propagation from pore-to-pore depends heavily on photoionization, which allows for the seeding of electrons into regions of high electric fields in the next pore. This photoionization is particularly important when the opening between interconnected pores is small, a condition that decreases the ability of electrons and ions to follow electric field lines and continue propagating from pore to pore. The angle of the pore-chain with respect to the applied electric field is important to the manner of plasma propagation through the pore chain. Propagation changed from being dominated by microdischarges for vertically oriented pore-chains to surface ionization waves (SIWs) for pore-chains oriented at an angle. Depending on the angle of the pore-chains, fluxes of short-lived species (e.g., ions, electrons, hydroxyl radicals, and electronically excited states) to the inside surface of the pores were preferentially onto one side of the pore-chain. This asymmetry in

incident fluxes did not occur for long-lived species (e.g., ozone, hydrogen peroxide, and acids) over longer time scales, as diffusive transport in the pores during the afterglow following a discharge pulse homogenizes the fluxes.

A review of the initial conditions is provided in Section 6.2. A discussion of the plasma dynamics in the base-case, a vertically oriented pore-chain, is in Section 6.3. The influence of the size of openings between pores is discussed in Section 6.4. Plasma properties in pore-chains having an angle with respect to the applied electric field is discussed in Section 6.5. Concluding remarks are in Section 6.6.

6.2 Initial Conditions and Reaction Mechanism

The base case has initial conditions of 300 K and 760 Torr (1 atm). The gas is humid air ($N_2/O_2/H_2O$=78/21/1). Due to the short timescales in this study, gas heating was not considered. The reaction mechanism contains 67 species and 1512 reactions. The reaction mechanism is a modified version of that discussed in Ref. [25], taking into account only gas-phase species and eliminating several higher order positive and negative water cluster ions.

The base case geometry and numerical mesh are shown in Fig. 6.1. Nominally, the geometry is a coplanar dielectric barrier discharge reactor with a 1-mm gap. The bottom dielectric is 740 μm in height, and it is meant to represent the type of porous ceramic with a dielectric constant of 61 that is used for bone scaffolding[26,27]. The secondary electron emission coefficient for ions incident on the dielectric is 0.1. A chain of four vertically oriented inter-connected circular pores open to the gas gap is placed in the dielectric. Each pore has a diameter of 150 μm and an inter-pore opening of 50 μm.

The plasma conditions are the same for all cases. A -8 kV pulse is applied to the top electrode, while the bottom electrode is held at ground potential. The voltage pulse has a total

duration of 10 ns. The voltage rises linearly from zero to -8 kV in 5 ns, and it is held at -8 kV for an additional 5 ns before being brought to zero in a step function manner. A plasma seed with a peak density of 1×10^{10} cm^{-3} and a radius of 100 μm is then placed directly above the pore-chain opening near the top electrode in order to initialize the discharge. Following the 10 ns voltage pulse, a 10 ms afterglow period is simulated assuming quasi-neutral conditions. All surfaces are initially uncharged. So, these results address either the first discharge pulse through the porous network, or a low enough pulse repetition rate that the majority of surface charge will have dissipated prior to the next pulse.

During the inter-pulse pulse period, the Neutral Plasma option within *nonPDPSIM* is utilized. When the voltage is turned off, Poisson's equation is no longer solved. Plasma neutrality is enforced by setting electron densities to the difference between the positive and negative ion densities and setting the electron temperature equal to the gas temperature. (At atmospheric pressure, the electron thermalization time is only a few ns.) The transport of ions is then given by their thermal transport coefficients, since there is no electron mediated ambipolar enhancement to rates of diffusion. Although the solutions for charged and neutral transport are implicit, there are still limits to the time-steps that can be taken, for example, not exceeding multiplicative factors of the dielectric relaxation time or Courant limit, or times to deplete species by reactions. The time-step in the afterglow is determined primarily by the processes with the fastest rate of chemical reactions for depleting a species. In this study, the typical dynamically chosen time-steps during the plasma period are about 1 ps, while the time-steps in the neutral period following the discharge pulse start at 10^{-9} s and incrementally increase to 10^{-6} s.

At the surfaces, all ions neutralize and electrons neutralize, resulting in charging of the surface. All electronically excited states quench to their ground states with unity probability,

except for metastable states of homo-nuclear diatomic molecules that have lower quenching probabilities. The quenching coefficient of $O_2(^1\Delta)$ is 0.02 and that of $N_2(A)$ is 0.05. The quenching coefficients are unity for vibrationally excited species that are infrared-active, whereas those for homo-nuclear, non-infrared active species are lower. The quenching coefficient of $O_2(v)$ is 0.02 and that of $N_2(v)$ is 0.05. Photoionization of O_2 by photons emitted by excited nitrogen species ($N_2(b^1\Pi)$ and $N_2(b^1\Sigma)$) is included with a cross section of 1.5×10^{-17} cm^2.

6.3 Plasma Propagation into Vertical Pore-Chains

The evolution of the electron density as a function of time is shown Fig. 6.2 a) for a discharge pulse above a vertical pore chain. An enlargement of the pores with electron density is shown in Fig. 6.2 b). The times noted in all figures are relative to the beginning of the voltage pulse. Note that the scales of the contours are changed between frames. Upon application of voltage, the electron density drifts downward – reminiscent of a Townsend avalanche –at 3 ns, as shown in Fig. 6.2 a). Once the electrons intersect with the surface of the lower dielectric (5 ns, $n_e \approx 2 \times 10^{10}$ cm^{-3}), the surface charges negatively, which launches a positive space-charge streamer traveling upward towards the cathode (8 ns). The streamer head has a moderately high electron temperature ($T_e \approx 10$ eV) and is electropositive ($\rho/q \approx 10^{14}$ cm^{-3}). In crossing the 1-mm gap, the electron density in the head of the streamer reaches 3×10^{15} cm^{-3}. Once the microdischarge bridges the gap back to the cathode, the impedance of the plasma column is low, transferring the cathode potential to the surface of the dielectric. This transfer of potential to the surface produces sufficient intense lateral electric fields to launch Surface Ionization Waves (SIWs) across the top of the dielectric at 9.3 to 9.8 ns, as depicted in Fig. 6.2 a). The electron temperature in the leading portion of the SIW is approximately 5 eV, producing electron densities of 7×10^{14} cm^{-3}. The transfer of

the cathode potential to the surface of the dielectric and to the top of the pore chain also launches an electron avalanche into the pores.

The time evolution of the electron density through the pore-chain is shown in Fig. 6.2 b). Time sequences of plasma properties in the second pore from the top are shown in Fig. 6.3 – displaying electron source by photoionization, ionization source by electron impact, electric field/gas number density (E/N), and electron density. (Note that, in the enlarged images of the pores, the contour scale was chosen to emphasize plasma properties inside the pore of interest. As a result, the contour scale may be saturated outside the pore where values exceed the maximum of the plotted scale.) The plasma is initially seeded in the topmost pore by photoionization from the bulk plasma above the pore opening. These seed electrons then drift and avalanche in the applied axial electric field, intensified by polarization of the adjacent curved dielectric surfaces. Initiation of the plasma from pore-to-pore along the chain is dominated by photoionization.

In this orientation of the pores, the sharply rounded edges of the pore openings are in the horizontal direction. With the applied electric field oriented vertically, the polarization of the dielectric produces, at the edges, a minimum in the electric field in the horizontal direction. There is a maximum in electric field in the vertical direction above and below the edges of the pore openings. Once photoionization seeds electrons inside the pore, electron avalanche begins to dominate, particularly so in the polarized intensified electric fields below the edges of the openings. Ionization waves (IWs) are launched from those locations on each side of the pore from these locations of electric field enhancement. Electron densities up to 2×10^{15} cm^{-3} are produced inside the pore.

The electron avalanche in the pores tends to follow the electric field lines (in the downward direction), and negatively charge the bottom surfaces of the pores. The upper surfaces of the pores

become positively charged. This results in formation of E/N of up to 600 Td (1 Td = 10^{-17} V-cm^2), allowing for the formation of SIWs along the walls of the pores. Formation of SIWs is important for the surface functionalization of the porous media, as it enables the production of short-lived, reactive species and VUV photons to reach the surface. The formation of SIWs in pore-like structures was also reported by Gu et al. [24]. This process of seeding of electrons by photo-ionization through the narrow pore opening, followed by formation of plasma filaments and, finally, SIWs continues in each of the consecutive pores.

In principle, the propagation of plasma through the vertically oriented pores should be symmetric across the mid-plane. However, the structures appearing in Figs. 6.2 and 6.3 are not perfectly symmetric. This lack of symmetry is due, in part, to the plasma entering the pore being slightly asymmetric and the numerical mesh not being perfect mirror-images on either side of the pore. In extremely large electric fields (E/N > 500 Td) produced inside the pores, avalanche times are as short as tens of ps, which rapidly amplifies small differences in E/N of only a few Td.

The fluences (time-integrated fluxes) of charged species (electrons, N_2^+ and O_2^+) and reactive oxygen and nitrogen species, RONS (NO, OH, H_2O_2, and O_3), to the inside surfaces of the pores and top surface of the dielectric after the discharge pulse at 10 ns are shown in Figs. 6.4 a) and 4b. The peaks in fluences numbered in Fig. 6.4 a) correspond to the pore openings and bottom of the last pore, as labeled in Fig. 6.1 b). The bottom of the pore-chain is located between the dotted lines in Fig. 6.4. Moving left and right from the center is the equivalent of moving upward along the inside surface of the left and right side of the pore-chains and, finally, out the top of the pore. During the short discharge pulse, fluences to the surfaces are dominated by species produced within a few to tens of microns of the surface. Even on these short timescales, significant ion chemistry occurs. For example, in atmospheric pressure air plasmas, the three-body reaction

that converts N_2^+ to N_4^+ occurs within a few ns. Over the 10 ns duration of the voltage pulse, the majority of the gas phase N_2^+, which does not charge exchange with other species, is converted to N_4^+. The end result is that both the magnitude and shape of the fluence of N_2^+ and N_4^+ to the pore surfaces are nearly the same.

The fluences of both charged species and neutral RONS are symmetrical to both sides of the pore-chain after the discharge pulse. The local maxima in fluences correspond to the pore openings, where electric field enhancement leads to higher plasma densities. The minima in fluences between the peaks correspond to the curved walls of the pores, as well as the weaker SIWs that propagate along the walls. After 10 ns, the larger fluences of electrons compared to positive ions results from the negative polarity of the discharge that negatively charges the anode-covering dielectric surfaces. The fluences of charged species are higher than those of neutrals (2-3×10^{12} cm^{-2} as compared to 7-8 $\times 10^{10}$ cm^{-2}). For the same densities, fluxes of charged particles to surfaces are higher than the neutral RONS, either due to drift in the applied electric field (electrons) or due to the ambipolar electric field (ions).

The lower fluences of neutral RONS can also be attributed to the reaction sequence required for their creation. The production of O_3, NO, and H_2O_2 require additional gas phase reactions following the generation of primary radicals by electron impact dissociation (e.g., O, N, and OH). These additional reactions simply take time to occur, and so these species have not yet amassed large densities and fluences during the discharge pulse. Fluences are generally lower deeper into the pore-chain. This results from a general decrease in plasma density down the pore chain and shorter time for fluxes to reach the surface.

During the afterglow flowing the discharge pulse, neutral species produced in the interior of the pores have time to diffuse to the surfaces, and post-pulse chemistry takes place to either

deplete species or to generate new species. The fluences of neutral RONS to the pore surfaces 10 ms after the discharge pulse are shown in Fig. 6.4 c). The uniformity of the fluences of neutral RONS are greatly improved and greatly increased, as compared to their post-pulse values, though not in direct proportion to their post-pulse values. The improved uniformity and larger fluences are due not only to the slower diffusion of the neutral species from the volume of the pores to the surfaces, but also to the fact that low-reacting species with the surfaces simply accumulate fluence over time.

To allow for some moderate depletion of species during the afterglow, we specified a reaction probability on surfaces of 0.01 for O_3, H_2O_2, NO, and OH. These reaction probabilities should be interpreted as rates of consumption of these species on surfaces. The changes in the relative values of the fluences at 10 ms, as compared to the post-discharge values at 10 ns, are due to the gas phase reactivity consuming or generating these species. For example, after 10 ms, O_3 (10^{19} cm^{-2}) and H_2O_2 (5×10^{17} cm^{-2}), which require additional collisions to form, have the largest fluences; however, after the discharge pulse at 10 ns, they have the lowest fluences. Moreover, after 10 ms, NO (4-5 $\times$ 10^{16} cm^{-2}) and OH (3-4 $\times$ 10^{15} cm^{-2}) have the smallest fluences; yet, after the discharge pulse at 10 ns, they have the largest fluences. Species formed due to electron impact dissociation, such as OH, produce large fluences after the discharge pulse. However, these species also tend to be more reactive in the gas phase, being consumed in forming more stable species such as H_2O_2. These reactions lower the fluences of the reactive primary species, while increasing the fluences of the more stable product(s).

Surface reactivity is important in assessing these fluences since the surface to volume ratio is large for small pores. Surface sites are the locations at which catalytic reactions can take place. Surface sites have a density of about 10^{15} cm^{-2} – a typical value for metallic solids. Thus, the

cylindrical pores considered here with a diameter of 150 μm have about 4.7×10^{13} sites per cm of depth. These dimensions require a gas phase radical density of 2.7×10^{17} in order to enable the gas phase species to react with (and be consumed by) every surface site. The details of this reactivity with the surface are unique to each material.

The fluences of species to the walls of the pore-chain at 10 ns and 10 ms are listed in Table 6.1. During the discharge pulse, the fluences are dominated by excited nitrogen species because of the composition of the gas (78% N_2). These leading fluences are followed by the fluences of ionized oxygen (ionization potential $\approx$12 eV), atomic oxygen (dissociation energy $\approx$5 eV), and nitrogen atoms (dissociation energy $\approx$12 eV). As the discharge transitions to an afterglow, species requiring additional (and possibly multiple) reactions to form begin to dominate. In particular, O_3, H_2O_2, and acids (HNO_x) form over many ms. In order to provide some context for surface reactions and the functionalization of porous materials, we assume a surface reaction probability of 0.01 for all neutral species. With this reaction probability, the fraction of surfaces sites that are functionalized during the afterglow of the discharge pulse, also listed in Table I, ranges from 0.1 for O_3 and 0.004 for HNO_3, to as the minimum of 1×10^{-4} for NO. With few exceptions, tens to hundreds of discharge pulses would be required to functionalize the entire inner surface of the pores.

6.4 Impact of Inter-Pore Opening Size

The transport of species pore-to-pore is, in part, determined by the size of the opening between the pores. To investigate the consequences of this interconnectivity, the diameter of the openings between the pores, d_p, is varied from 37 μm to 150 μm. The diameter of the pores is held constant at 150 μm, meaning that the largest of the opening sizes produces a via or trench. The

evolution of electron densities with these pore openings is shown in Fig. 6.5.

As the size of pore openings decreases, the convective transport of electrons through the openings becomes progressively hindered by the charging of the pore surfaces in the vicinity of the opening which, in turn, creates a space-charge barrier. As a result, as the opening narrows, the propagation of the discharge from pore-to-pore becomes progressively more dependent on photoionization to seed plasma in the next pore. As the pore opening decreases in size, the electric field enhancement below the opening becomes more pronounced. Once plasma is seeded in a lower pore, the more intense electric field enhancement launches micro-streamers across the pores. With the smallest opening (d_p = 37 μm), the micro-streamers largely miss the sidewalls, and no SIW propagates in a restrike fashion. As d_p increases, electric field enhancement at the edges of the opening becomes directed more along the surface, and the plasma becomes more surface-hugging. At d_p = 150 μm with straight walls, the plasma propagates along the surfaces of the trench as singular SIWs, dependent on the self-generated electric field in the heads of the ionization front (peaking at E/N $\approx$ 420 Td, $T_e \approx$ 7 eV), instead of on geometric electric field enhancement. While the plasma does not uniformly fill the trench, fluxes of reactive species to the surface are uniform due to the complete plasma coverage.

The propagation of the plasma through the pore chain slows as the pore opening d_p increases. This is a counter-intuitive result. The small radii of curvature of the dielectric produces a larger surface capacitance which, in principle, should require a longer dwell time of the plasma to fully charge. By this logic, the speed of propagation of the discharge should slow as d_p decreases. However, in order to obey this scaling, the plasma should propagate dominantly as an SIW, whose motion is determined by the charging of the underlying capacitance of the surface. Instead, the SIW detaches from the surface as d_p decreases, a process that is just beginning to occur

with d_p = 112 μm. The evolution of the ionization wave from a SIW into a volumetric streamer eliminates the need for surface charging for the ionization to propagate, and so reduces the dependence of discharge propagation on the specific capacitance of the surface.

The fluences of electrons O_2^+ and N_2^+ to the pore surfaces during the voltage pulse for pore openings of 37 μm, 75 μm, 112 μm, and 150 μm are shown in Fig. 6.6. (The fluences for a pore opening of 50 μm are contained in Fig. 6.4.) As the pore opening decreases in size, the convective charged particle transport through the opening decreases, while the electric field enhancement at the edges of the opening increases. These trends result in more localized ionization near the openings, the launching of micro-streamers, and less intense SIWs. These combined effects produce more modulation in the charged particle fluences to the surfaces. With increasing pore opening, the local modulation in fluences decreases – that is, the fluences are locally more uniform. However, globally, the fluences are less uniform with larger pore openings. This lessening of global uniformity is due to the decrease in speed of the propagation of the plasma through the pores. For example, as noted, the plasma does not reach the bottom of the feature for the 150 μm opening.

6.5 Angle of the Pore-Chain

In actual porous material, the orientation of the pores with respect to the applied electric field is random, as is the manner of their interconnectivity. To investigate the consequences of the orientation of the pore-chain on discharge propagation, the angle of the pore-chain with respect to the surface normal of the electrodes is varied: – 0°, 22.5°, and 45.0°. The time evolution of electron density for these orientations is shown in Fig. 6.7. The electron impact ionization source and E/N in the 3rd pore for the chain oriented at 45° are shown in Fig. 6.8. The plasma cascades through

the pores in a different fashion as the angle moves away from the vertical. For all angles, photoionization is required to seed electrons in the next pore due to the constricting opening, which limits electron transport. With an increasing angle of the pore chain, the opening between pores is more aligned with the applied electric field. This alignment produces polarization induced electric field enhancement at the tips of the openings, as shown in Fig. 6.8a. The electric field at the tips of the opening reaches values as high as 1000 Td for an orientation of 45°. Recall that, for vertically oriented pores, there is instead a reduction in E/N at the tips of the opening. This progressive increase in E/N with an increasing angle produces ionization in the pore opening directly adjacent to the surface. On the other hand, with a shallow angle, the ionization is largely in the volume.

With the applied electric field progressively more normal to the walls of the pore chain with an increasing angle, as well as with ionization occurring more adjacent to the surface, the plasma becomes increasing asymmetric. The lower surfaces of the pores are charged negatively, a condition that supports SIWs that propagate along surface shown by the region of positive electron source and high E/N in Fig. 6.8. The trailing plasma column has densities reaching 2×10^{16} cm^{-3} with commensurately high conductivities that reduce E/N below self-sustaining. The electron source terms in the plasma column along the surface then become negative, dominated by attachment and recombination. With charging of the lower surface of the pore, a positive SIW is launched upwards along the top surface of the pore. However, this SIW stalls due to the shorting of the electric potential by the conductive plasma on the bottom surface. The end result is that, as the angle of the pore-chain increases from the vertical, the discharge through the chain becomes progressively dominated by SIWs along the lower surface.

The speed of propagation of SIWs depends, in part, on the effective surface capacitance

(C_s, F/cm^2). As discussed earlier, SIWs propagating on surfaces with larger C_s tend to propagate more slowly. The volumetric ionization waves are much less sensitive to the C_s of nearby surfaces. With increased C_s, due to the orientation of the pores and a more SIW dominated plasma, the discharge in the pores at a larger angle propagate more slowly.

The orientation of the pore chain embedded in the dielectric affects the discharge propagation in the gas gap above the dielectric in at least two ways. The first is that the effective surface capacitance at the top of the dielectric is a function of the material density and layout below the surface. With the vertically oriented pore-chain, C_s is the same on both sides of the center line. As the pore-chain angles to the right of center, C_s increases on the right side relative to the left side. The second is that, as the pore-chain fills with conductive plasma, the electric potential is shorted, bringing the cathode potential towards the top of the pore-chain. With an increasing angle of the pore-chain and an asymmetric sub-surface conductivity, the potential is arrayed asymmetrically above the dielectric.

For example, the electron density and electric potential at the end of the voltage pulse are shown in Fig. 6.9 for pore-chains oriented at 0^o, 22.5^o, and 45^o. With the pore-chain at 0^o, the micro-discharge streamer in the gap is essentially symmetrically arrayed above the pore-chain. The SIWs propagate with equal speeds to the right and left of the pore chain opening. The conductive plasma in the pore-chain reduces the electric potential at the top of the pores to -4.6 kV, whereas the potential is 3-4 kV higher beyond the edge of the SIWs. As the pore-chain tilts to the right at 22.5^o and 45^o, the micro-discharge in the gap tilts progressively to the left. There is a small asymmetry in the vacuum electric fields in the gap due to the spatially dependent permittivity below the surface, and this results in a small shift to the left of the initial streamer. However, the majority of the asymmetry is due to the warping of the electric potential as the pore-

chain fills with conductive plasma. The SIW on the top of the dielectric propagates to the left more quickly and with a higher electron density than does the SIW propagating to the right. The slowing of the SIW to the right is likely a result of the surface capacitance C_s being larger to the right due to the orientation of the pore chain.

As the pore chain tilts to the right, the plasma coverage favors the lower surfaces of the pores. This directly translates to non-uniform fluxes of reactive species to the pore surfaces after the discharge pulse. The fluences of reactive species after 10 ns and 10 ms for the pore-chain oriented at 22.5^o are shown in Fig. 6.10. Fluences for the pore chain oriented at 45^o are shown in Fig. 6.11. (Fluences for the pore-chain oriented at 0^o are shown in Fig. 6.4.) With an increasing angle of the pore-chain, the fluences at the end of the discharge pulse at 10 ns for both the ions and neutrals increase on the left wall and decrease on the right wall. The deficit in fluences along the right wall near the bottom of the chain worsens with increased angle. This is, in part, due to the slower propagation speed of the SIWs over a longer distance. For the 45^o orientation, the discharge fails to reach the bottom of the pore-chain by the end of the voltage pulse. The fluence of electrons is approximately an order of magnitude lower to the right-side wall, as compared to the fluence to the left-side wall at a tilt of 22.5^o. This disparity increases to approximately 2-orders of magnitude for a tilt of 45^o.

After 10 ms, diffusion of the neutral species has, in large part, mediated the non-uniform fluences to the surface produced by the angled pore chains. However, there is a limit (at least, on these time scales) to this mediating diffusion. With the plasma not having fully reached the bottom of the pore chain for the 45^o orientation, few neutral radicals are produced in the bottom pore. As a result, there is a deficit of neutral reactive fluence to the walls of the bottom pore. Either the radical is depleted by the gas phase or surface reactions before diffusing to the last pore, which is

the case for OH and NO, or there has not been enough time for the stable species (O_3 and H_2O_2) to diffuse through the chain.

6.6 Concluding Remarks

Propagation of atmospheric-pressure plasmas into and through chains of dielectric pores (150 μm diameter) was computationally investigated. These pores are of the size that are typically found in materials used for tissue engineering and that often require functionalization of their surfaces for biocompatibility. Propagation of plasma into pores and pore-to-pore typically relies on photoionization to seed electrons in regions of high electric fields. For pore-chains that are oriented parallel to the applied electric field, polarization of the dielectric below the openings then avalanches these seed electrons to form micro-streamers that cross the majority of the pore diameter. Upon intersection with and charging of the surfaces of the pores, surface ionization waves (SIW) then propagate along the walls of the pores.

The size of the openings between pores significantly impacts the method of plasma formation and propagation of plasma through the pore-chain. With small pore openings, photoionization is generally required to seed electrons in the next pore. Electric field enhancement at the edges of the openings then launches micro-streamers through the volume which, in turn, initiates SIWs. As the size of the openings increases, photoionization becomes less necessary to propagate the plasma, as convective transport through the opening is less restricted. There is also less geometrical electric field enhancement due to fewer sharp edges of the opening. It is this electric field enhancement that typically launches volume micro-streamers. As a result, SIWs begin to dominate. With SIWs dominating, the fluences of reactive species become increasingly more uniform along the pore walls.

The angle of the pore-chain with respect to the applied electric field has a significant impact both on plasma formation and on the uniformity of the fluence of ions and radicals to the inside surfaces of the pores. Even with a vertically oriented pore-chair, the fluence of ions to the pore surfaces is non-uniform due not only to the electric field enhancement at the pore openings, but also the mix of volumetric micro-streamers and SIWs in the pores. This non-uniformity is, however, symmetric on both sides of the pore-chain. As the angle of the pore-chain increases, enhancement of the electric field at the pore openings becomes more pronounced, leading to formation of high-density microdischarges that launch SIWs on the lower surfaces of the pore-chains. There is little plasma directly formed on the upper surfaces, leading to non-uniform fluences of plasma generated species to the two sides of the pore at the end of the discharge pulse. Non-uniformities in the fluences of charged species generally do not significantly improve during the afterglow that follows the discharge pulse. Diffusion of neutral species during the afterglow does improve the uniformity of their fluences to pore surfaces. Given the random orientation of pore-chains in most porous materials, obtaining uniform surface functionalization, which requires a large ion component, will be challenging. However, it will be far less challenging to obtain uniform surface functionalization that is dominated by neutral species, though several hundred to thousands of discharge pulses will be required to fully functionalize the relevant surfaces.

Pore chains in industrial and biomedical materials have 3-dimensional (3D) features that are not captured in the results from the 2-dimensional (2D) simulations discussed here. Although we hesitate to quantitatively comment on how these 3D effects manifest themselves in plasma propagation through pore chains, as these simulations have not been done, we can make some general comments. The electric field enhancement that results from sharp edges having the same radius of curvature is typically larger in 3D than in 2D, as well as larger in a cylindrically

symmetric structure that is off-axis than in the equivalent Cartesian representations. In this regard, we expect that plasma propagation that relies on geometric electric field enhancement will be more intense in 3D. These features would include the micro-streamers that are launched from the edges of pore-openings in tilted pore chains. The solid angle subtended by a pore-opening in 3D is smaller than in 2D for otherwise equivalent dimensions. As a result, convective plasma transfer from pore-to-pore would likely be even more restricted in 3D than it is in 2D and diffusion of ions would become even less important. This increase in restriction would then make the contributions of photoionization to propagating the plasma pore-to-pore even more important in 3D.

6.7 Tables

Table 6. 1 Surface-averaged Fluences of Reactive Species to the Pore-Chain Walls

Species	Average Fluence (cm^{-2}) at 10 ns	Average Fluence (cm^{-2}) at 10 ms	Fraction Surface Sites Reacted
	Short-Lived Species		
$N_2(A)$	1.1×10^{12}	7.2×10^{12}	1.1×10^{-7}
$N_2(v)$	7.4×10^{11}	1.4×10^{14}	2.2×10^{-6}
O_2^+	2.0×10^{11}	3.7×10^{13}	6.3×10^{-7}
O	1.4×10^{11}	2.5×10^{16}	3.0×10^{-3}
OH	3.8×10^{8}	1.3×10^{15}	4.8×10^{-6}
N	1.4×10^{11}	6.3×10^{14}	7.0×10^{-6}
N_2^+	1.3×10^{11}	6.0×10^{12}	9.5×10^{-8}
N_4^+	1.1×10^{11}	1.8×10^{12}	4.0×10^{-8}
$O_2(v)$	6.1×10^{10}	2.5×10^{13}	4.2×10^{-7}
N_2**	3.3×10^{10}	7.6×10^{11}	1.2×10^{-8}
$O_2(^1\Delta)$	2.3×10^{10}	7.6×10^{16}	1.3×10^{-3}
N_3^+	1.1×10^{10}	1.3×10^{12}	2.5×10^{-8}
	Long-Lived Species		
O_3	3.4×10^{6}	5.2×10^{18}	1.1×10^{-1}
H_2	1.1×10^{8}	1.4×10^{18}	5.3×10^{-3}
HNO_2	2.6×10^{5}	6.7×10^{17}	1.6×10^{-2}
N_2O_5	4.0×10^{-3}	4.0×10^{17}	1.2×10^{-3}
H_2O_2	6.1×10^{7}	2.5×10^{17}	4.6×10^{-3}
HNO_3	1.0×10^{3}	1.7×10^{17}	4.0×10^{-3}
HO_2NO_2	1.1×10^{-2}	8.0×10^{16}	2.3×10^{-3}
N_2O	5.2×10^{8}	6.0×10^{16}	7.9×10^{-3}
NO_2	6.1×10^{7}	1.9×10^{16}	4.5×10^{-4}
NO	4.7×10^{8}	6.3×10^{15}	1.0×10^{-4}

6.8 Figures

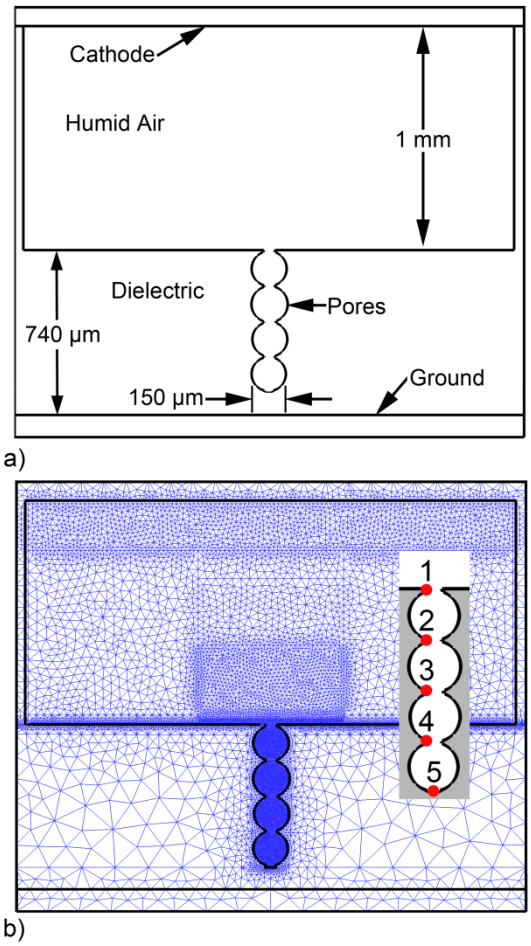

Fig. 6 1 Geometry for the base case. a) Schematic of the computational domain. b) Numerical mesh. The inset shows the locations of the labels used to map fluence to the surface of the pores. Four pores with diameters of 150 μm, with 50 μm openings, are embedded into a 600-μm thick dielectric. The powered electrode is located 1 mm above the dielectric. The numbers in the inset identify locations at which fluences are collected in later figures.

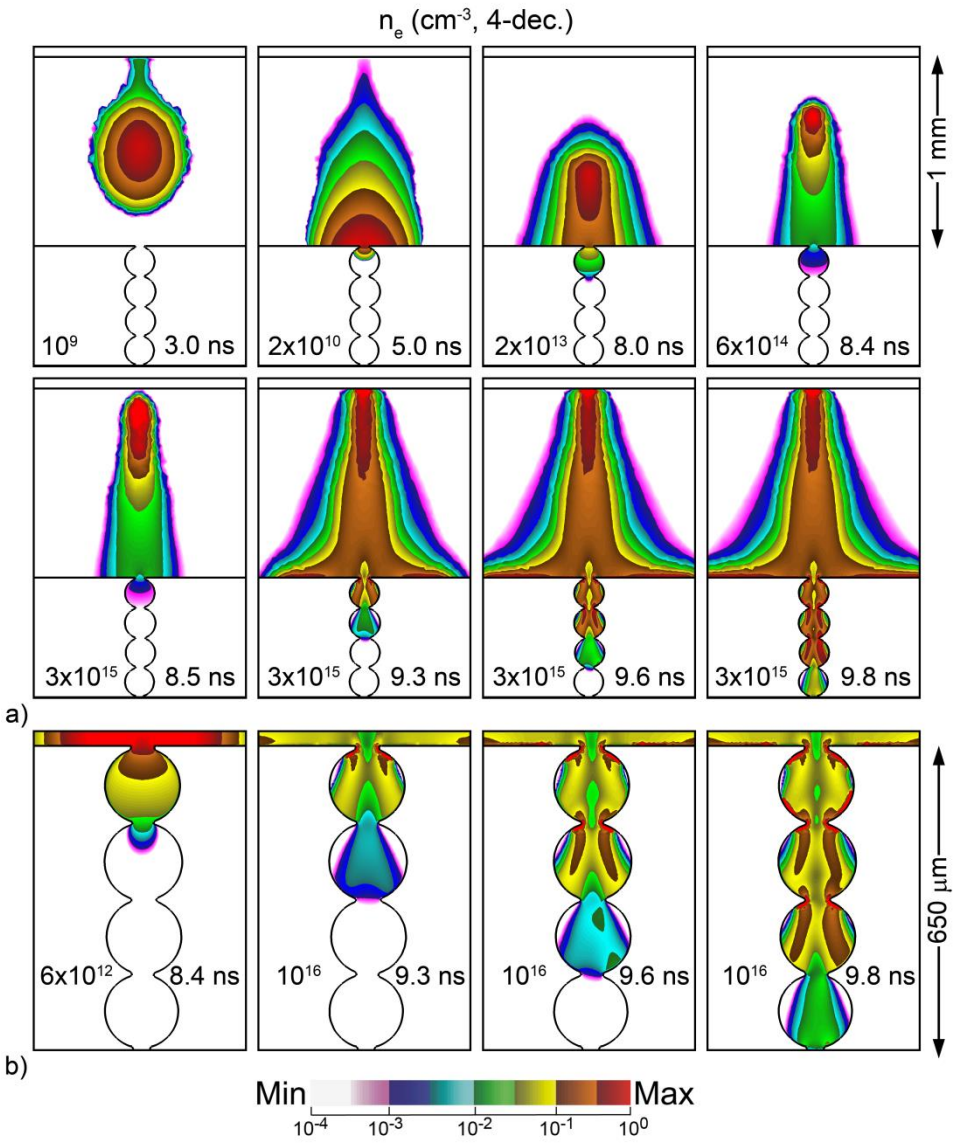

Fig. 6 2 Time evolution of electron density in the base case plotted over 4 decades on a long-scale. a) Streamer in the gas phase and pore-chain. b) Enlargement of the pore-chain. The maximum value and time of the image are noted in each frame.

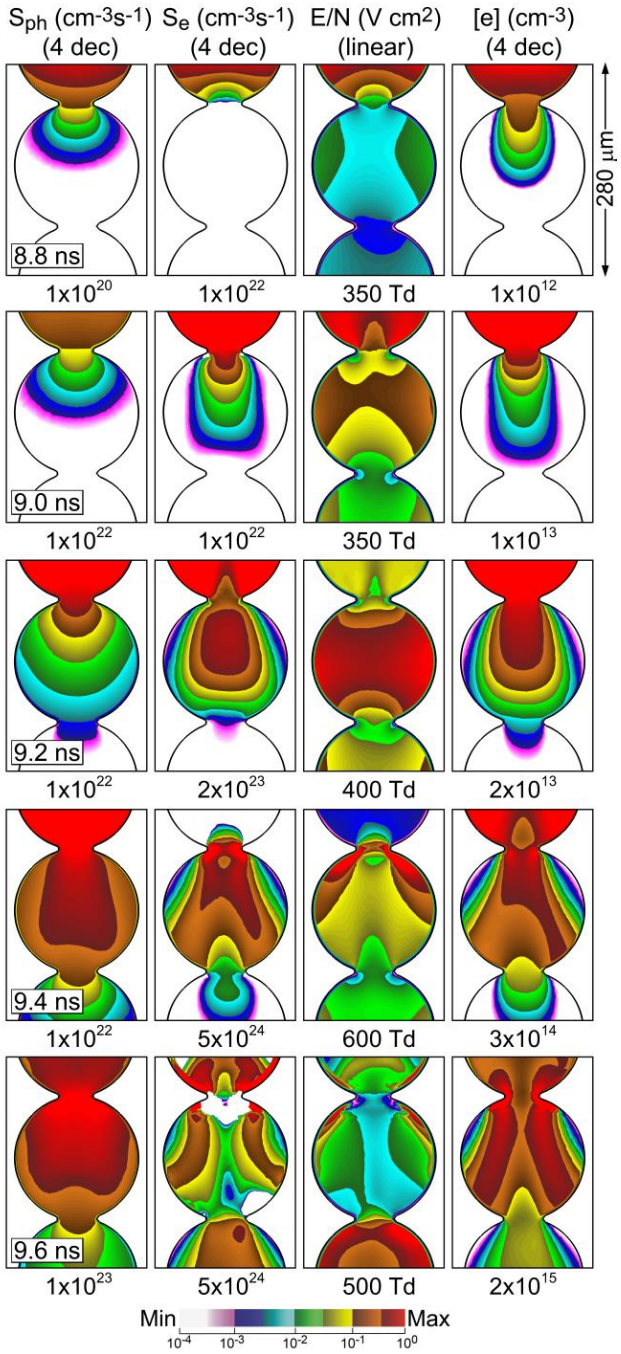

Fig. 6 3 Time sequence (top to bottom) of plasma properties in the 2nd pore from the top. (left-to-right) Photoionization source (S_{ph}), electron impact ionization source (S_e), electric field/gas number density (E/N), and electron density ([e]). Except for E/N, quantities are plotted on a 4-decade log-scale. The maximum value in each image is noted below the frame. The ranges of the values plotted were chosen to emphasize the plasma properties in the pore of interest. This resulted in some images being saturated in the pore above.

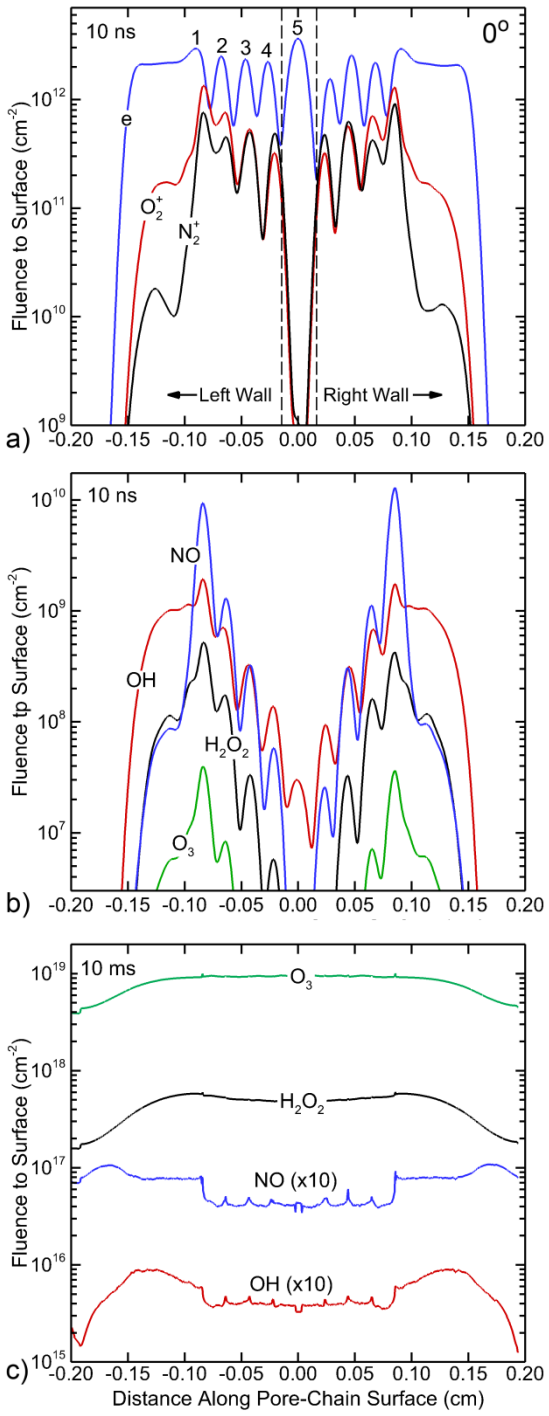

Fig. 6 4 Fluences of plasma generated species to the inside surfaces of the vertically oriented pore-chain. a) Electrons and ions after 10 ns b) Neutral species after 10 ns c) Neutral species after 10 ms. The maxima in fluences correspond to the pore openings. The numbering of the peaks correlates with the locations cited in Fig. 1. The dotted lines are the boundaries of the floor of the bottom pore.

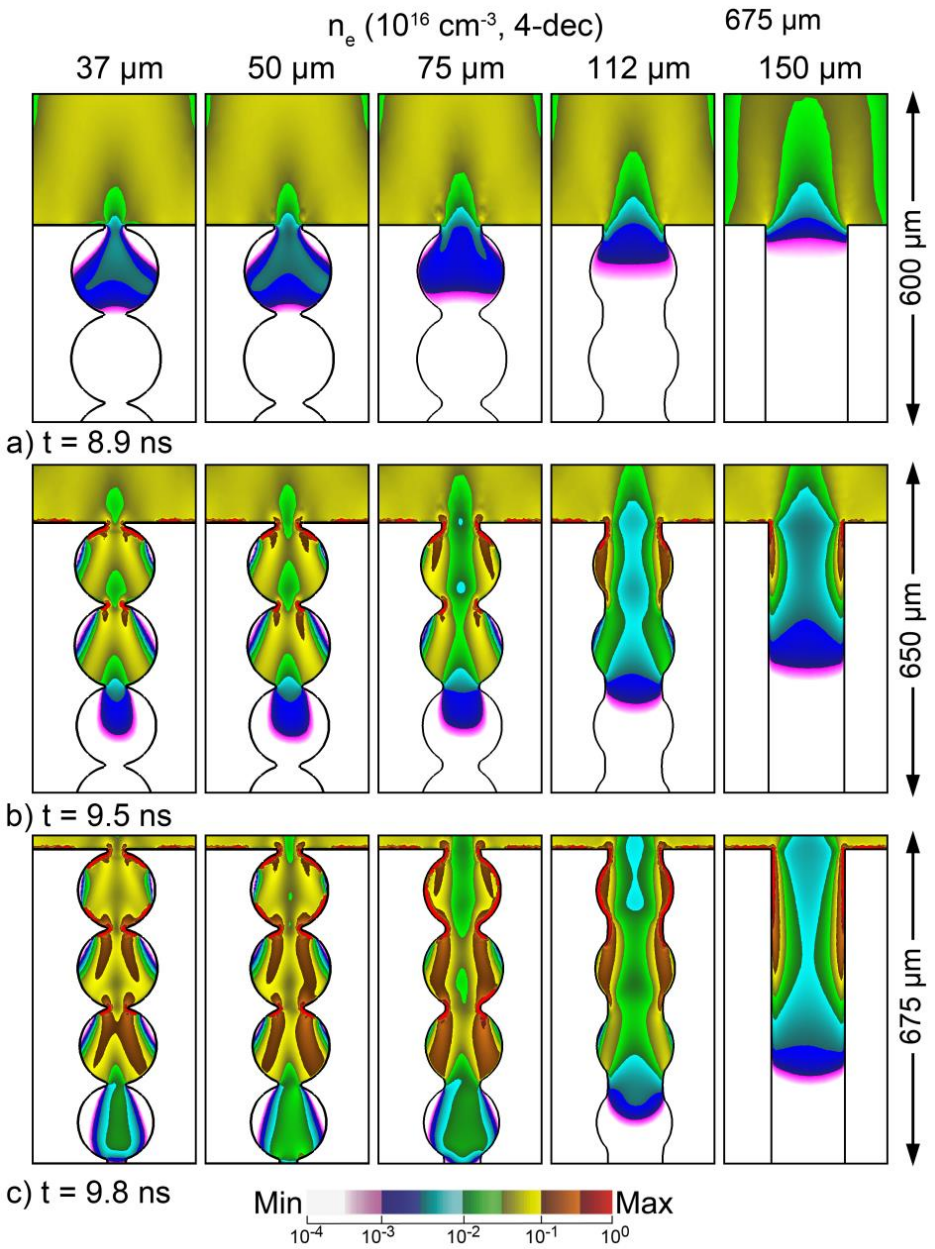

Fig. 6 5 The time sequence of electron density in pore-chains with varying pore-opening sizes (left-to-right) of 37, 50, 75, 112, and 150 µm. a) 8.9 ns; b) 9.5 ns; and c) 9.8 ns. Plasma formation becomes surface-discharge dominated as the openings become larger. The density is plotted on a log-scale over 4 decades.

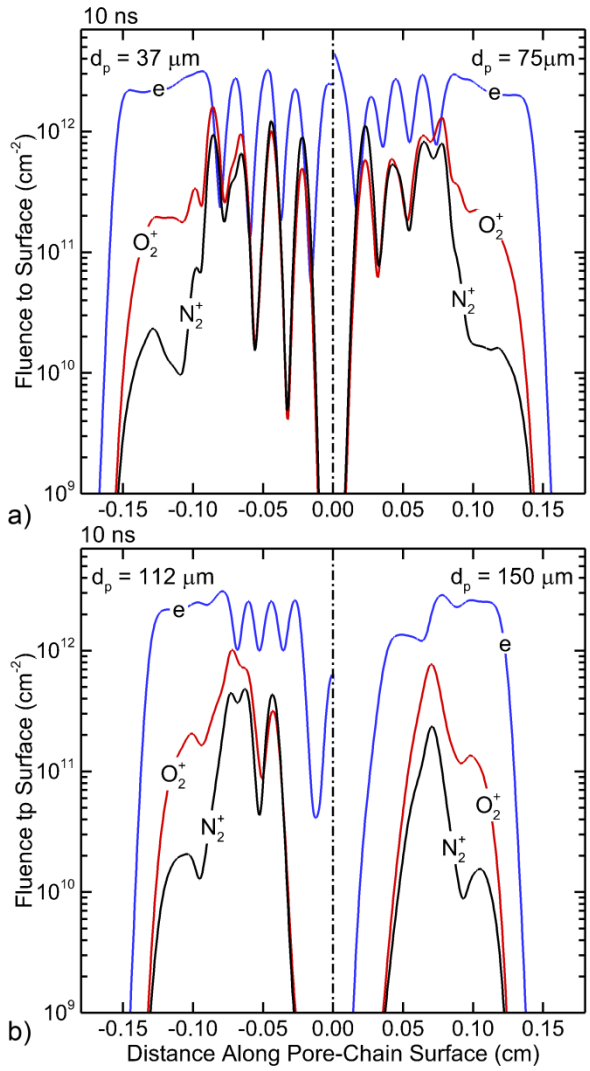

Fig. 6 6 Fluences of electrons and ions after 10 ns to the inside surfaces of the vertically oriented pore-chain for different pore openings. a) 37 μm and 75 μm. b) 112 μm and 150 μm. For each opening the fluences are shown for only one wall (left or right). The maxima in fluences correspond to the pore openings.

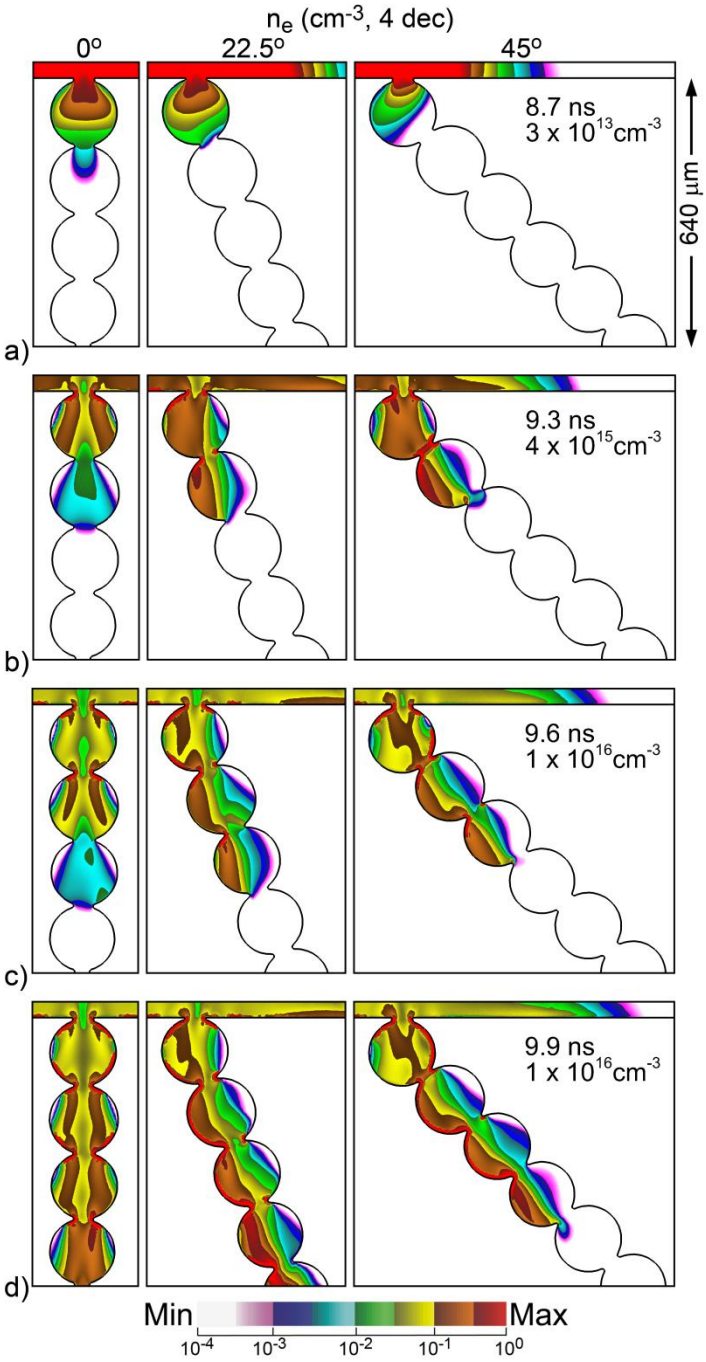

Fig. 6 7 The time sequence of electron density in pore-chains with varying angles (left-to-right) of 0°, 22.5°, and 45°. a) 8.7 ns; b) 9.3 ns; c) 9.6 ns; and d) 9.9 ns. Plasma formation becomes surface-discharge dominated as the angle increases. The electron density is plotted on a log-scale over 4 decades. The maximum value for each time is noted in the third frame.

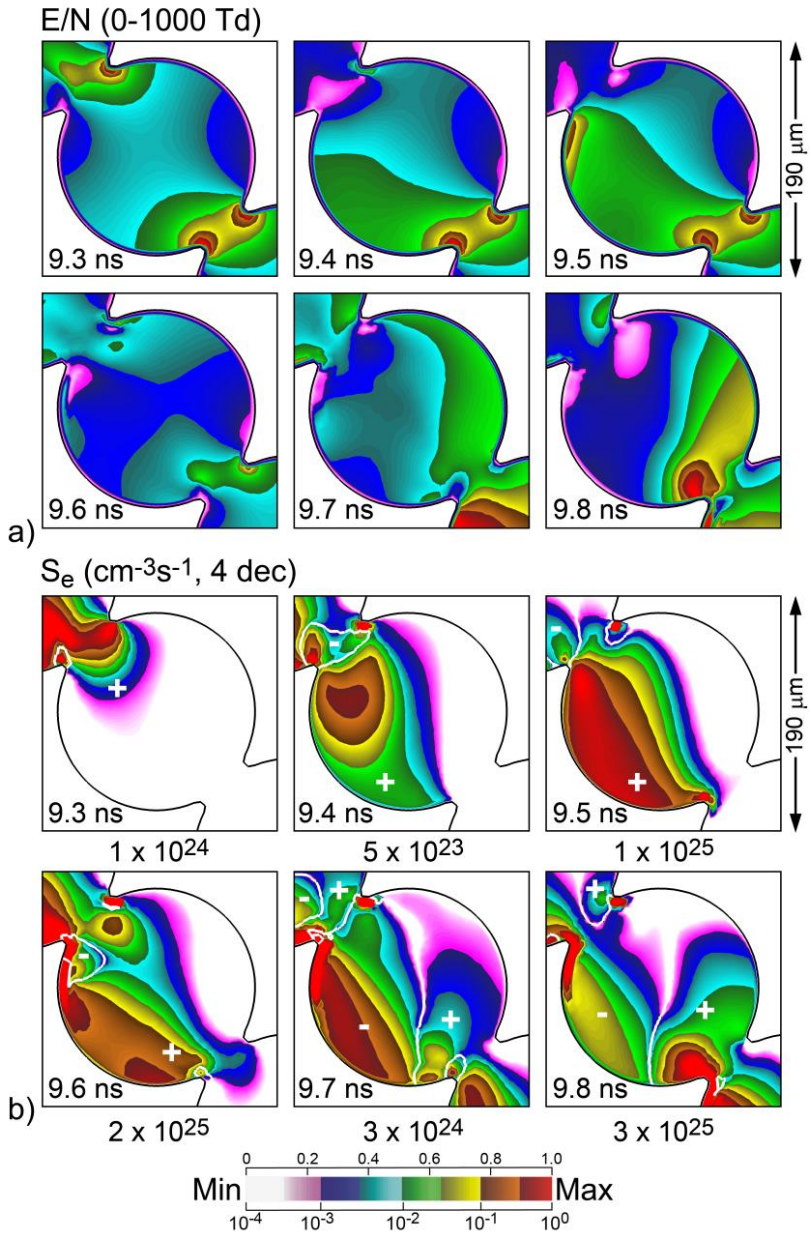

Fig. 6 8 Time sequences of plasma properties in the 3rd pore in the pore-chain oriented at 45°. a) E/N on a linear 0-1000 Td scale. (1 Td = 10^{-17} V-cm^2). b) Electron impact ionization source plotted on a 4-decade log-scale with the maximum value noted below each frame. The absolute value of the ionization source is plotted, with white lines separating regions of electron impact producing positive gains in electron density (noted with "+") and regions in which electron impact produces losses (noted with "-").

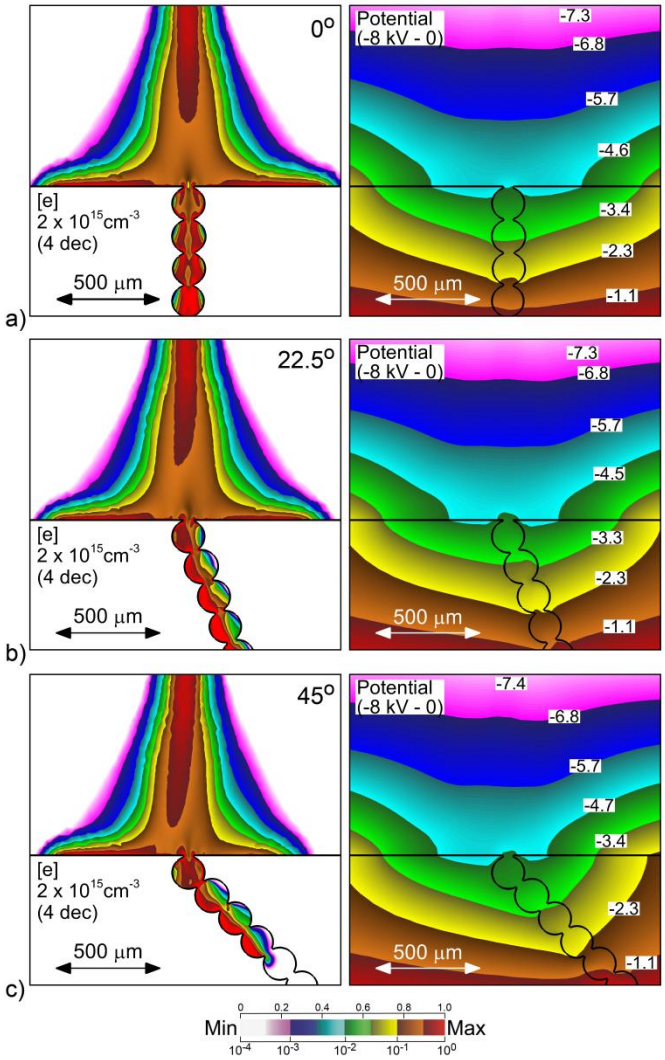

Fig. 6 9 Electron density and electric potential at the end of the discharge pulse for pore-chains at different angles. a) 0°; b) 22.5°; and c) 45°. Electron density is plotted on a 4-decade log scale. Contour labels for electric potential have units of kV.

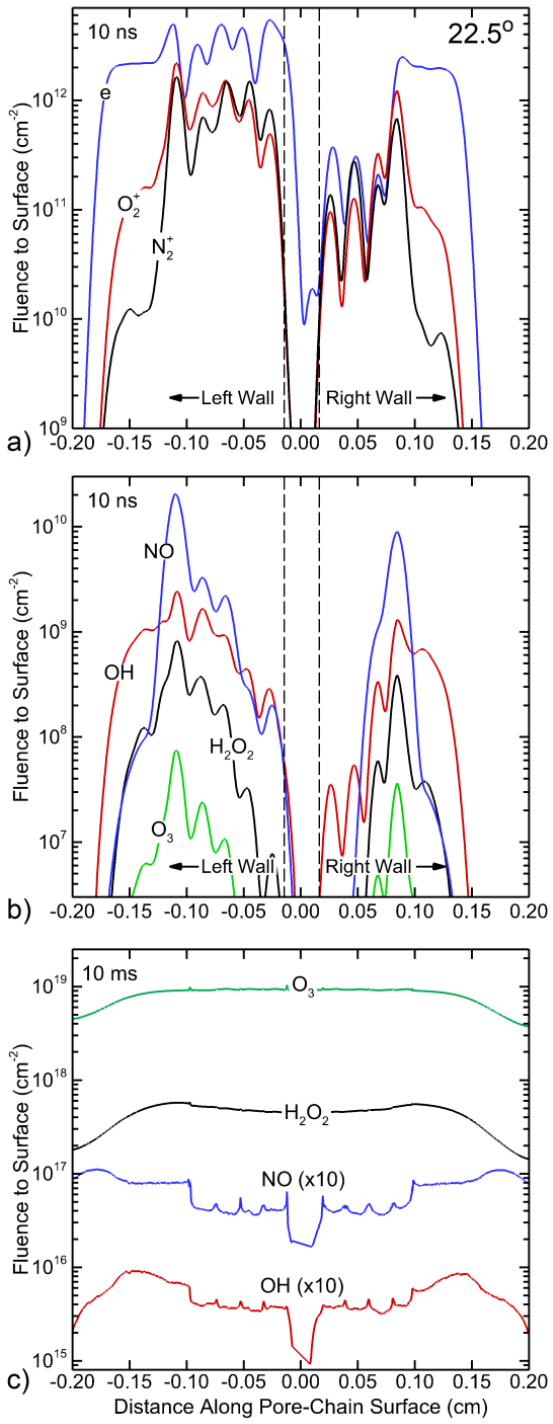

Fig. 6 10 Fluences of plasma-generated species to the inside surfaces of the pore-chain oriented at 22.5°. a) Electrons and ions after 10 ns b) Neutral species after 10 ns c) Neutral species after 10 ms. The maxima in fluences generally correspond to the pore openings. The dotted lines are the boundaries of the floor of the bottom pore.

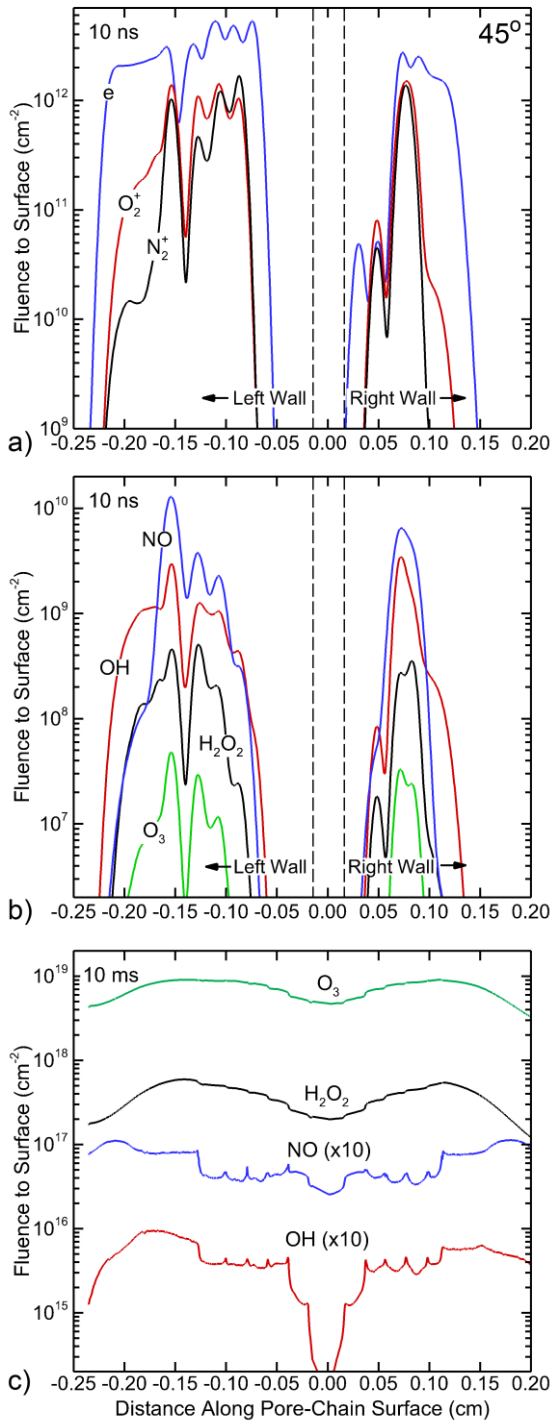

Fig. 6 11 Fluences of plasma-generated species to the inside surfaces of the pore-chain oriented at 45°. a) Electrons and ions after 10 ns b) Neutral species after 10 ns c) Neutral species after 10 ms. The maxima in fluences generally correspond to the pore openings. The dotted lines are the boundaries of the floor of the bottom pore.

6.9 References

[1] C. Shuai, G. Liu, Y. Yang, W. Yang, C. He, G. Wang, Z. Liu, F. Qi and S. Peng, Colloids Surfaces B Biointerfaces **185,** 110587 (2020).

[2] H. Amani, H. Arzaghi, M. Bayandori, A. S. Dezfuli, H. Pazoki-Toroudi, A. Shafiee and L. Moradi, Adv. Mater. Interfaces **6,** 13 (2019).

[3] B. P. Chan and K. W. Leong, Eur. Spine. J. **17,** S467 (2008).

[4] A. Lipovka, R. Rodriguez, E. Bolbasov, P. Maryin, S. Tverdokhlebov and E. Sheremet, Surf. Coatings Technol. **388,** 125560 (2020).

[5] H. Rebl, B. Finke, J. Schmidt, H. S. Mohamad, R. Ihrke, C. A. Helm and J. B. Nebe, Mater. Sci. Eng. C **69,** 1116 (2016).

[6] M. Wang, Y. Zhou, D. Shi, R. Chang, J. Zhang, M. Keidar and T. J. Webster, Biomater. Sci. **7,** 2430 (2019).

[7] G. Lutzweiler, J. Barthes, G. Koenig, H. Kerdjoudj, J. Mayingi, F. Boulmedais, P. Schaaf, W. Drenckhan and N. E. Vrana, ACS Appl. Mater. Interfaces **11,** 19819 (2019).

[8] M. Gherardi, R. Tonini and V. Colombo, Trends Biotechnol. **36,** 583 (2018).

[9] X. Qiao, Y. M. Wang, W. X. Weng, B. L. Liu and Q. Li, Ceram. Int. **44,** 21564 (2018).

[10] C. X. Wang, M. Du and Y. P. Qiu, Surf. Coatings Technol. **205,** 909 (2010).

[11] Y. Sun, M. Krishtab, H. Struyf, P. Verdonck, S. De Feyter, M. R. Baklanov and S. Armini, Langmuir **30,** 3832 (2014).

[12] J. Kim, S. A. Park, J. Kim and J. Lee, Materials (Basel). **12,** 9 (2019).

[13] U. Roland, F. Holzer and F. D. Kopinke, Appl. Catal. B Environ. **58,** 217 (2005).

[14] F. Holzer, U. Roland and F. D. Kopinke, Appl. Catal. B Environ. **38,** 163 (2002).

[15] Y. Moriguchi, D. S. Lee, R. Chijimatsu, K. Thamina, K. Masuda, D. Itsuki, H. Yoshikawa, S. Hamaguchi and A. Myoui, PLoS One **13,** 1 (2018).

[16] Y. Zhang, H. Y. Wang, Y. R. Zhang and A. Bogaerts, Plasma Sources Sci. Technol. **26,** (2017).

[17] K. Hensel, V. Martišovitš, Z. Machala, M. Janda, M. Leštinský, P. Tardiveau and A. Mizuno, Plasma Process. Polym. **4,** 682 (2007).

[18] S. Singh, C. Prakash, H. Wang, X. feng Yu and S. Ramakrishna, Eur. Polym. J. **118,** 561 (2019).

[19] E. Simoncelli, D. Barbieri, R. Laurita, A. Liguori, A. Stancampiano, L. Viola, R. Tonini, M. Gherardi and V. Colombo, Clin. Plasma Med. **3,** 77 (2015).

[20] A. Stancampiano, D. Forgione, E. Simoncelli, R. Laurita, R. Tonini, M. Gherardi and V. Colombo, J. Adhes. Dent. **21,** 229 (2019).

[21] Y. R. Zhang, K. Van Laer, E. C. Neyts and A. Bogaerts, Appl. Catal. B Environ. **185,** 56 (2016).

[22] Q. Z. Zhang and A. Bogaerts, Plasma Sources Sci. Technol. **27,** 035009 (2018).

[23] C. Swanson and I. D. Kaganovich, J. Appl. Phys. **123,** 023302 (2018).

[24] J. G. Gu, Y. Zhang, M. X. Gao, H. Y. Wang, Q. Z. Zhang, L. Yi and W. Jiang, J. Appl. Phys. **125,** 153303 (2019).

[25] A. M. Lietz and M. J. Kushner, J. Phys. D. Appl. Phys. **49,** 425204 (2016).

[26] P. R. Prezas, B. M. G. Melo, L. C. Costa, M. A. Valente, M. C. Lança, J. M. G. Ventura, L. F. V. Pinto and M. P. F. Graça, Appl. Surf. Sci. **424,** 28 (2017).

[27] J. P. Gittings, C. R. Bowen, I. G. Turner, A. C. E. Dent, F. R. Baxter and J. Chaudhuri, Acta Biomater. **5,** 743 (2009).

Chapter 7 Summary and Future Work

The impact of plasma reactivity on its surroundings was discussed in this work, with primary focus given to dielectric barrier discharges at atmospheric pressure and in air. The transfers of this reactivity to gases, solids, and liquids were computationally investigated, revealing several physical and chemical processes that influence efficiency and selectivity. In several cases, the results were validated experimentally by collaborators, lending further credibility to the results.

7.1 Summary

In Chapter 1, an overview of low-temperature plasmas (LTP) and their properties was presented. The challenges and opportunities involved in deploying LTPs for environmental (gas processing, pollutant removal, water treatment), agricultural (increased plant viability via direct and indirect interactions with plasmas), and medical (cancer treatment, dentistry, dermatology) applications were discussed. Furthermore, a review of the current literature in the field was provided. Finally, the difficulties in computational modeling complex plasma systems were briefly discussed.

In Chapter 2, the model used in this work, a 2-dimensional fluid plasma simulator called *nonPDPSIM,* was described. The principle equations being solved in *nonPDPSIM* were overviewed, including the Poisson's, Boltzmann's, electron temperature, Green's (radiation transport), charge and neutral particle continuity, gas and surface temperature, and Navier-Stokes equations. The basics of the model's operation – such as input files, mesh, and matrix structure – were also summarized. Last, the author's contributions to the development of *nonPDPSIM* were

reviewed. These included additions to the surface heating algorithm, inclusion of OpenMP parallelization, deployment of new meshing software, and addition of periodic fluid boundary conditions. These updates increased the model's capabilities and efficiency.

Chapter 3 reviewed the results from several studies of plasma packed bed reactors (PPBRs). First, the principle mechanism for plasma development in PPBRs was uncovered. In a PPBR, two or more dielectric media bind the plasma. This is because the dielectric materials become polarized, providing electric field enhancement in the regions between them. Electrons in those regions are then accelerated along the electric field lines and leave behind regions of positive space-charge. Upon impacting the up-field bounding dielectric, the electrons charge the material's surface, further increasing the local electric field and inventories of positive space-charge. The positive charges left behind in the gas then lead to the formation of positive streamers between the dielectrics. The positive streamers "connect" with the down-field bounding dielectric and form what are commonly known as Filamentary Microdischarges. Finally, the positive streamers also positively charge the surface of the down-field dielectric. The high degree of charge non-uniformity then leads to the formation of surface ionization waves (SIWs). This process was found to occur regardless of the dielectric material being used, polarity and amplitude of the applied voltage, composition of the background gas, geometry, or operating pressure (as long as the gap between the dielectrics is much greater than the electrons' mean free path). The formation of various reactive species was also found to be dependent on the type of discharges present within the reactor. For example, SIWs involve high energy electrons in the ionization front. As a result, dissociation of nitrogen (vs, for example, oxygen) preferentially took place in regions where SIWs occurred due to the higher binding energy of N_2.

Here, the work on packed bed reactors was extended to include metallic catalyst particles. The investigation focused on the synergistic interactions between plasmas and thermal catalysts – an example plasma reactivity transfer to solids. Metallic particles were found to significantly impact plasma formation in PPBRs. As voltage is applied, the high-conductivity catalysts expel electric fields, leading to formation of very high electric fields in the immediate proximity. Depending on the surface roughness of the particles, these fields can overcome their work function, leading to electric field emission of electrons. This phenomenon leads to plasma preferentially forming near the catalysts, as well as formation of plasmas at lower applied voltages. Furthermore, due to increased plasma densities near the catalysts, higher fluxes of electrons, ions, and reactive neutrals to their surfaces were observed. These enhanced fluxes can increase the surface temperatures and surface reaction rates, leading to higher efficiencies.

In Chapter 5, plasma/surface interactions were further investigated in the context of porous media. Plasma propagation through interconnected microscopic pore-chains has applications within medicine and catalysis. Plasma was found to first form within pores due to propagation of photoionization deep in the chain structure. Once gas in the pores was pre-ionized, the topology of the dielectric led to local electric field enhancement and formation of microdischarges and SIWs. Uniformity of reactive fluxes to the surface of the pores is an important factor in sterilization and functionalization of materials. As the chain becomes more tangential to the applied electric field, plasma forms preferentially on the up-field surfaces. Uniformity of fluxes to the surface is therefore significantly impacted. Similarly, as the openings between pores increase in size, plasma propagation becomes less dependent on radiation transport and microdischarges. Rather, SIWs become dominant, increasing overall fluxes and coverage uniformity.

Finally, in Chapter 6, interactions between liquid water and plasmas for medical applications were investigated. Transfer of reactive species to the microdroplets was found to be heavily dependent on the individual species' Henry's Law constant, *h*. Low-*h* liquid species (e.g., O_3) came to an equilibrium quickly and did not deplete the local densities of their gas-phase equivalents. Simultaneously, high-*h* species (e.g., H_2O_2) required longer plasma-exposure times to reach a steady state due to the liquid's ability to sustain their higher relative densities. Furthermore, it was found that the gas-phase densities of high-*h* species quickly became locally depleted, leading to slower solvation rates. To counteract this phenomenon, plasma-produced species must be resupplied via additional plasma pulses. Another important criterion impacting the rates of solvation was the surface-to-volume ratio (SVR) of the liquid. Smaller droplets have an increased SVR, allowing for higher relative solvation rate, and therefore faster equilibration. Under identical conditions, a smaller droplet had a higher density of high-*h* species compared to a larger droplet. The densities of low-*h* species, however, remained unchanged, regardless of the droplet diameter.

As part of the work of this dissertation, several previously underexplored means of plasma formation were identified. Knowledge of the basic processes underlying complex systems like plasma catalytic reactors enabled new avenues for control of reactivity. Increases in efficiency, selectivity, activation, and coverage uniformity all depend on numerous system parameters discussed in this work. Principally, the impact of material properties and topology, applied voltage, background gas, and pressures were investigated.

The types of discharges present at any given point within a packed bed reactor have significant impact on the species being produced. This is primarily due to variations in electron temperatures in the ionization heads, which translate to the ability to increase selectivity. More diffuse, uniform

plasmas tend to preferentially produce those principle species requiring lower energies. For example, in air, dissociation of oxygen in microdischarges can then lead to high densities of ozone and hydrogen peroxide. On the other hand, dissociation of nitrogen present in the proximity of streamers or SIWs leads to formation of acids and nitrous/nitric oxides. The work presented in this dissertation further elucidates the means by which experimental settings can induce formation of one type of plasma over another.

Similarly, the choice of materials impacts plasma processes in multiple ways. Most studies substitute dielectrics within a PBR and only account for shape and dielectric constant. In fact, work presented in this thesis shows that surface roughness of catalysts, for example, can cause formation of additional plasma due to electric field emission. This process has significant influence on microscopic processes, which then combine to change macroscopic results. Instead of increasing applied voltages (and therefore energy costs), it is therefore recommended that rough-surfaced catalysts be utilized.

Liquid activation is perhaps the most complex application of low-temperature atmospheric pressure plasmas. Through this work, the impact of local effects on rates of solvation were uncovered. Prior investigations primarily focused on 0-dimensional or steady-state effects. Here, the depletion of high-*h* species in the gas phase was shown to decrease the average densities inside microdroplets. Rather than increasing applied voltage or pulse lengths, it was shown that increasing pulse repetition rates results in increased activation. Similarly, a decreased radius of microdroplets increased the surface-to-volume ratio, which allowed for higher relative fluxes of reactive species to the surfaces. This insight can lead to a more efficient and more selective production of plasma-activated media.

7.2 Future Work

Several improvements to *nonPDPSIM* could further enable future studies. To improve performance, additional profiling of the code would highlight inefficient regions of the code. These sections could then be either rewritten or parallelized. In particular, during the plasma-on period, the majority of the simulation time is spent in the sparse matrix solver. Even though significant work went into deploying parallel solvers (Intel MKL), the best performance was still achieved by using a single-threaded, non-parallelizable algorithm. The performance of *nonPDPSIM* could therefore be greatly improved if a different, more capable parallel solver were developed.

Further development of meshing strategies could also improve code performance. In particular, dynamic meshing would allow the code to adjust node sizes in the moment, based on given sets of parameters (for example, electron temperature, charge density, field strength). Such a capability would decrease the time required to construct a "proper" mesh before a case was run. Furthermore, it would limit formation of "hot spots" (mesh nodes with abnormally high fields/densities resulting from mesh imperfections). Hot spots contribute significantly to decreases in code performance and can result in unphysical results. Last, dynamic meshing could allow for changes in the initial geometries. This could be applied, for example, in a study of plasma's impact on wake formation on the surface of liquid water. Results in Chapter 6 would also be enhanced by such an update, as it would allow for the tracking of droplet radius decrease due to evaporation.

The *nonPDPSIM* algorithm would also benefit from coupling the fluid and liquid modules. Currently, the liquid regions within the model are static and no Navier-Stokes equations are solved within them. Gas flow present above the water surface would cause movement within the liquid itself. As a result, the transport of reactive species within water would be impacted. Furthermore,

because plasma deposits a significant amount of energy into the liquid, local circulation patterns would likely develop due to water heating. These phenomena were not considered in this work and would be a fruitful area for further exploration.

The work presented in this dissertation could be further expanded in several ways. Surface processes (surface catalytic reaction) other than those presented in Chapter 6 could be included in all studies. *NonPDPSIM* in uniquely situated to simultaneously calculate local electric fields and simulate their impact on surface reaction rates via surface energy bending. This could provide further insights into causes for the plasma/catalyst synergies discussed in Chapter 4. Additionally, knowledge of fluxes incident on surfaces would provide insight into which catalysts should be deployed in a given system.

Further and systematic exploration of the variable space on work presented in Chapter 5 would be useful. Operating parameters, such as applied voltage amplitude and polarity, and the dielectric constant could have a significant impact on the results. A study exploring these impacts could provide a guide for experimental work going forward. The scientific community would benefit from increased knowledge of the means of maximizing plasma coverage uniformity within pores. An investigation of the impact of interconnectivity and plasma formation in completely separated pores would also be of great interest. Finally, the work presented in Chapter 5 only concerned a single plasma pulse. In a commercial setting, the pores would be treated by hundreds or thousands of pulses. The impact of surface charging on subsequent pulses could provide further insights into means of plasma propagation.

As is always the case in modeling studies, further experimental validation of the theoretical findings would be extremely useful. In particular, the validation of the solvation rates of species based on the Henry's Law constant could have an impact on the field. Such an experiment has

several obstacles. First, many of the reactive species being tracked by *nonPDPSIM* are short-lived. Measurements would therefore have to be made on small timescales, so the densities of intermediate species would not be depleted. Second, the droplets would have to be accumulated in a larger liquid vessel in order to be tested. This necessarily leads to the mixing of newly-activated and more "stagnant" volumes of water. Third, direct interrogation of the liquid is likely impossible. Scavenger chemicals would therefore have to be used to infer densities of various species. Presence of these scavengers is likely to change aqueous kinetics and would have to be done very carefully.

Lastly, throughout this work, only up to three photons were tracked. This was done on the assumption that photons primarily serve as means of seeding electrons ahead of positive ionization waves. However, liquids and catalysts alike have shown numerous interactions with background VUV photons – these include dissociation of species within liquids, killing of bacteria, and activation of surface sites. While photo-reactions are expensive calculations to perform, the insight gained into the mean-free-paths, reaction rates, and surface effects would be extremely useful to the low-temperature plasma community. This is especially true as optical emission is one of the best means of probing plasmas without disturbing them.